



The
University
Of
Sheffield.

Quantitative Electron Energy-loss Spectrum Data Processing for Hyperspectral Imaging in Analytical Transmission Electron Microscopy

Author:

Veerendra C ANGADI

*A thesis submitted in fulfilment of the requirements for the degree of
Doctor of Philosophy*

in the

**Department of Electronic and Electrical Engineering
Faculty of Engineering
The University of Sheffield**

4th April 2018

Declaration of Authorship

I, Veerendra C ANGADI, declare that this thesis entitled, 'Quantitative Electron Energy-loss Spectrum Data Processing for Hyperspectral Imaging in Analytical Transmission Electron Microscopy' and the work presented in it are my own. I confirm that:

- This work was done wholly while in candidature for a research degree at this university.
- Where any part of this thesis has previously been submitted for a degree or any other qualification at this University or any other institution, this has been clearly stated.
- Where I have consulted the published work of others, this is always clearly attributed.
- I have worked purely on simulation and data processing of analytical EELS. The experimental data acquisition has been conducted by **Dr. Thomas Walther** (for multi-junction solar cell, gallium nitride and silicon studied in the JEOL 2010F FEG-TEM) and **Dr. Toshihiro Aoki** (for indium gallium nitride and aluminium nitride doped with terbium studied in the Nion UltraSTEM), all of whom are acknowledged individually in the experimental chapter.
- Where I have quoted from the work of others, the source is always given. With the exception of such quotations, this thesis is entirely my own work.
- I have acknowledged all main sources of help.
- Where the thesis is based on work done by myself jointly with others, I have made clear exactly what was done by others and what I have contributed myself.

Signed:

Date:

'We reap what we sow. We are the makers of our own fate. The wind is blowing; those vessels whose sails are unfurled catch it, and go forward on their way, but those which have their sails furled do not catch the wind. Is that the fault of the wind?..... We make our own destiny.'

SWAMI VIVEKANANDA

The University of Sheffield

Abstract

Faculty of Engineering
Department of Electronic and Electrical Engineering

Doctor of Philosophy

Quantitative Electron Energy-loss Spectrum Data Processing for Hyperspectral Imaging in Analytical Transmission Electron Microscopy

by Veerendra C ANGADI

In this thesis, a comprehensive automated quantification process of some of the features in electron energy-loss spectroscopy (EELS) is described.

For high-loss spectra, two algorithms have been proposed for automated ionization core-loss edge onset detection and quantification. The robustness of the edge detection by estimated exponent method is tested with respect to various parameters for different values of such size of the detection window, specimen thickness and an average white Gaussian noise. For quantification, the pre-edge regions and the integration ranges are automatically chosen based on the edges detected and elemental maps are calculated. A novel way of modelling background in post-edge regions is explored for GaAs high-loss spectra. However, simple post-edge background extrapolation tends to give an overestimation of the net core-loss. Hence, an optimum background is calculated from the error bars of the Poissonian statistics of net core-losses subtended by backgrounds modelled from pre- and post-edge regions. The Richardson-Lucy deconvolution method is explored at high-loss spectra to iteratively reconstruct the single scattering distribution. The ringing artefacts are studied with respect to number of iterations. A baseline correction to conventional linear least-squares method of core-loss quantification is proposed. An example of a high-loss spectrum image (SI) from a Ge based solar cell is used to test the relative quantification of Ga, As and Cu. The improvement from $\sim \pm 8\%$ to less than $\lesssim \pm 3\%$ in the quantification of Cu, Ga and As compared to other least-squares fit models are noticed. In some regions due to overlapping of core-losses, the large errors produced by standard least-squares methods was reduced from $\sim \pm 15\%$ to $\lesssim \pm 9\%$.

The thesis has also explores the joint fitting of bulk plasmons (InN, GaN and $\text{In}_x\text{Ga}_{1-x}\text{N}$) and core-losses of $4d$ and $3d$ transitions of In and Ga respectively in the low-loss range < 50 eV. The effective In content in phase separated $\text{In}_x\text{Ga}_{1-x}\text{N}$ is quantified from two different fit ranges. A correction factor

is proposed to correct the effects of a limited fit range arising due to inclusion of a truncated In reference spectrum in joint fitting. In both short and truncation corrected extended fit ranges the values of effective In content has been quantified $\sim \pm 10\%$ with both bulk plasmons and core-losses. Chemical profiling of different regions in an EELS SI is done by mapping the positions of bulk plasmons. The full width at half maximum (FWHM) of bulk plasmon, W_p , is also studied by fitting a Lorentzian function. Regions with (surface) oxide formation or imperfection in the crystal structures due to formation of Tb–O complexes revealed an increase in W_p .

The blind measurement of bandgap for a wide-bandgap material, GaN, has also been studied. The bandgap onset detection is compared for different methods such as by fitting a square-root function, derivative method and a novel approach based on the centroids of clusters identified when fit ranges are systematically varied. The square-root fitting and derivative method was applied to density of state (DOS) region between 0 eV to 12 eV to variously modelled backgrounds such as exponential tail extrapolation of ZLP, Richardson-Lucy and Fourier-log deconvolutions etc. The blind measurement of bandgap with square-root fitting to ZLP subtracted GaN spectrum was found to be at 3.28 eV with an R^2 of 0.91 and for derivative method it was at 3.31 eV which is in agreement with the literature. The square-root fit applied to different DOS background modelling was able to determine bandgap at 3.52 ± 0.91 eV where as from derivative method it was 3.52 ± 0.41 eV. The bandgap measured using centroid of the highest R^2 in the clusters detected using k -means clustering analysis was found to be at 3.52 ± 0.91 eV which is comparable to square-root fits. The blind measurement of bandgap was applied to test for GaAs spectrum. The determined values with derivative and k -means cluster analysis was found to be at 1.40 eV and 1.20 eV, respectively. The precise measurement of bandgaps from EELS for an unknown material is found to be difficult ($\lesssim \pm 0.41$ eV) when compared to optical spectroscopy.

Acknowledgements

There have been a lot people involved in the process of this project, not just in terms of direct contribution but also the moral support throughout my research. First and foremost I would like to thank my supervisor, Dr. Thomas Walther, who has guided me through the whole project and also been extremely supportive and encouraging. Coming from a signal processing background, material research was a complete alien to me. Thomas has been very patient and I got to learn a lot from him. He made this project very interesting and enjoyable for me. I would also like to extend my gratitude to the Department of Electronic and Electrical Engineering for the financial support to fund my PhD, without which this project wouldn't have been possible.

I would like to thank my second supervisor, Dr. Charith Abhayaratne, who has been incredibly supportive right from my masters degree. He has provided valuable inputs to this project. I was very lucky to have both Thomas and Charith as my supervisors. Last but not the least, I would also like to show my gratitude to the Institute of Physics, Royal Microscopical Society and the Learned Society Fund of the University of Sheffield for funding conference attendances in Cambridge, Oxford (MSM 2015, 2017), Manchester, Durham (EMAG 2015, 2016), Lyon (EMC 2016).

I gratefully acknowledge Thomas along with Dr. Toshihiro Aoki for conducting all the experiments and providing data which have been used in this research. I am grateful to the Kroto Centre for High Resolution Imaging and Analysis at the University of Sheffield and the LeRoy Eyring Center for Solid State Science at the Arizona State University. These facilities were used along with facilities in the Sorby Centre at the University of Sheffield to conduct EELS experiments.

I would like to thank my colleagues Xiaoyi Wang and Ran Guo. It was really amazing to work with them. Finally, I am grateful to Appaji, Amma, Pratibha Akka, Vidya Akka and their little ones Gubbi, Subbi, Tuppi, who always cheer me up and support me unconditionally, and my friends here in Sheffield, who have been very supportive and kind.

Contents

Abstract	vii
Acknowledgements	ix
List of Figures	xv
List of Tables	xxiii
1 Introduction	1
1.1 Aim and Objectives	1
1.2 Structure of thesis	3
1.3 Contributions	4
1.4 Published work	6
1.4.1 Journal publications	6
1.4.2 Conference proceedings	6
2 Background literature	9
2.1 Microscopy	9
2.1.1 Transmission Electron Microscope	11
2.1.2 Gatan Imaging Filter	13
2.2 Electron energy-loss spectroscopy (EELS)	15
2.3 EELS quantification	18
2.4 Core-loss pre-processing	21
2.5 Modelling plural scattering	23
2.6 Fourier-ratio deconvolution	25
2.7 Fourier-log deconvolution	28
2.8 Angular convergence correction	29
3 Automated ionization core-loss analysis	33
3.1 Introduction	33
3.2 Detection of ionization core-loss edges	34
3.2.1 Cluster detection by counting positive slope angles	35
3.2.2 Cluster detection through peak detection	39
3.3 Quantification by background subtraction	49
3.4 Results from multi-junction solar cell	50
3.5 Results from InGaN	57
3.6 Results from AlN:Tb	58
3.6.1 Tb–O co-segregation in annealed AlN:Tb	61
3.7 Summary	63

4	Advanced automated high-loss analysis of EELS	67
4.1	Introduction	67
4.2	Selection of background models	68
4.3	Optimal fit	69
4.3.1	Background model in pre-edge region	69
4.3.2	Background model in post-edge region	70
4.3.3	Background model with optimal fit	70
4.3.4	Considerations for background modelling	72
4.4	Richardson-Lucy deconvolution	72
4.5	Considerations while applying deconvolution	77
4.6	Baseline correction to background fit	78
4.6.1	Comparison with standard routines	87
4.7	Summary	88
5	Automated low-loss analysis	91
5.1	Introduction	91
5.2	Modelling $\text{In}_x\text{Ga}_{1-x}\text{N}$ low-loss EELS	92
5.2.1	Modelling bulk plasmons of $\text{In}_x\text{Ga}_{1-x}\text{N}$	92
5.2.2	Modelling core-losses of $\text{In}_x\text{Ga}_{1-x}\text{N}$	95
5.2.3	Joint fitting of bulk plasmons and core-losses	97
5.3	Effective composition in $\text{In}_x\text{Ga}_{1-x}\text{N} / \text{GaN}$	101
5.4	Results from joint fitting	106
5.5	Truncation correction for core-losses	107
5.6	Quantification from plasmon peaks	111
5.7	Relative specimen thickness from modelling	115
5.8	Summary	118
6	Automated VEELS for bandgap measurements	123
6.1	Introduction	123
6.2	Limitations in determination of bandgap onset	124
6.3	Modelling ZLP	126
6.3.1	Modelling ZLP in 1D	127
6.3.2	Modelling ZLP in 2D	128
6.3.3	Deconvolution of 1D ZLP	130
6.4	Determination of Bandgap from 1D Spectra	132
6.4.1	Method I	133
6.4.2	Method II	135
6.4.3	Method III	135
6.4.4	Method IV	135
6.4.5	Method V	135
6.4.6	Discussion of 1D spectrum processing	135
6.5	Determination of bandgap from 2D SI	139
6.5.1	Discussion of 2D spectrum processing	141
6.6	Bandgap determination by cluster analysis	141
6.7	Summary	143
7	Conclusion	147
7.1	Future work	148

A	EELS experiments	149
A.1	Multi-layer solar cell	149
A.2	InGaN thin films	151
A.3	AlN thin film doped with Tb	154
A.4	GaN	156
B	User manual for the EELSAnalyser	159
B.1	Import EELS data into EELSAnalyser	159
B.2	Visualization in EELSAnalyser	161
B.3	Quantification of EELS Spectrum Image	162
	Bibliography	165

List of Figures

2.1	Electron interaction with material producing other types of radiation	10
2.2	Electron scattering	11
2.3	A Cross-sectional diagram of TEM (Graham, 2009).	12
2.4	GIF component interface to TEM and control path (Gatan, 1996).	13
2.5	Standard procedures for EELS acquisition in TEM (A) TEM with a magnetic-prism spectrometer below the viewing screen, (B) TEM incorporating an in-column imaging filter and (C) scanning-transmission (STEM) system (Egerton, 2009).	16
2.6	A low-loss electron energy-loss spectrum of polycrystalline Si. a) ZLP b) bulk plasmon peak c) Si $L_{2,3}$ ionization core-loss edge on top of exponential decaying background. Experimental conditions: voltage = 197 kV, dispersion = 0.5 eV per channel, spectrum offset = 0 eV, exposure time = 0.1 s.	17
2.7	Comparison of noise suppression methods applied to an EEL spectrum. The term w describes the width (in pixels) of the filter mask. PCA is not effective in suppressing spike noise as the reconstruction of spectrum based on first 17 significant components (shown at the top) still contains noise. The median filter works best.	22
2.8	(A) Two models of low-loss spectrum of plasmon location, $E_p = 20$ eV. (B) Simulated hydrogenic model of single scattering core-loss ionization edge and its plural scattered version with respect to low-losses modelled in (A). (C) Cumulative sum of intensity as a function of integration range (Δ).	26
2.9	(A) Effective collection semi-angle correction for $\beta = 15$ mrad. (B,C) are the convergence corrected integrated cross-sections, $\sigma(E, \Delta, \beta^*, E_0)$, and differential cross-sections, $\frac{\partial}{\partial E}\sigma(E, \Delta, \beta^*, E_0)$ from hydrogenic model for O K edge at 532 eV.	31
3.1	Original spectrum of Si $L_{2,3}$ edge and C K edge (in dark blue) and angle as defined in eqn. 3.7 (in red) showing the presence of clusters in the latter correlates with the onset of ionization edges.	35
3.2	Flow chart for edge detection in spectra that consist of N channels. c is the count of channels with positive gradient, i is the energy channel, j is the loop count, w is the window width and mod is modulo operator (remainder after division).	36

3.3	The location of core-loss (here: Si L _{2,3} edge) is detected from the look-up table and fine-tuned to a value of 99 eV as per eqn. 3.9.	37
3.4	Histogram distribution of edge onsets detected for EELS SI from semiconductor heterostructure shown in fig. A.1 for 80 eV offset (A), 250 eV offset (B) and 950 eV offset (C). The edges are later identified in table 3.2.	40
3.5	Flow chart for edge detection in spectra that consist of N channels. $\bar{\theta}_i$ is the mean value of angles, i is the energy channel, j is the loop count, w is the window width and mod is modulo operator (remainder after division).	41
3.6	Simulated GaAs spectra using two Hartree-Slater cross-sections for Ga L and As L respectively with (A) $t/\lambda = 0$ (B) $t/\lambda = 0.9$, $w = 25$, $A = 3.75 \times 10^{10}$, $r = 2.45$, $a = b = 25$. Dependence of Ga L and As L edge detection (C) with variable size of the window, w for $t/\lambda = 0$. (D) as a function of relative thickness.	43
3.7	Simulated GaAs spectra using two Hartree-Slater cross-sections for Ga L and As L respectively with (A) 30 dB, (B) 30 dB and smoothed using averaging filter of window 10 twice. $t/\lambda = 0$, $w = 25$, $A = 3.75 \times 10^{10}$, $r = 2.45$, $a = b = 25$. Dependence of Ga L and As L edge detection (C) with addition of white Gaussian (AWG) noise at varying SNR for $w = 25$ and $t/\lambda = 0$ and (D) the smoothed AWG noisy spectrum filtered with an averaging filter of width 10 pixels at varying SNR. . .	44
3.8	The edge detection by cluster method ($w = 25$) applied to sum spectrum from regions 8, 5, 3 and region without sample of multi-junction solar cell described in section A.1. Each $\bar{\theta}$ spectra have vertical range between $-\pi/2$ to $\pi/2$	46
3.9	The edge detection algorithm ($w = 25$) is applied to In _x Ga _{1-x} N phase separated material. Sum spectrum is extracted from In rich and Ga rich region from EELS SI. Each $\bar{\theta}$ spectra have vertical range between $-\pi/2$ to $\pi/2$	47
3.10	The edge detection algorithm is applied to Tb doped AlN EELS SI. The sum spectrum (~ 3741 spectra) are taken from AlN region 1 as in fig. A.4(B) and another sum spectrum (~ 1131 spectra) from Si substrate region which is indicated as region 2.	48
3.11	Block diagram of ionization core-loss edge selection and background subtraction.	51
3.12	The persistence of an artefact at 72–85 eV in spectra from all locations (3 single spectra are displayed) shows that the Al L _{2,3} edge (nominally starting at 73 eV) cannot be evaluated from spectra acquired with 80 eV offset after spectra without offset had been acquired previously with the ZLP located at channel #100.	54

3.13	(E) Definition of regions in the EELS SI. Regions indicated by blue dotted lines are thicker regions, while red lines denote interfaces. A sum spectrum is extracted from each region for further quantification in table 3.2. Set of maps generated with EELS SI of 80 eV offset (A–D), with 250 eV offset (F–H) and with 950 eV offset (I–M). The elemental maps show the spatial distribution of Al L _{2,3} , Si L _{2,3} , Al L ₁ , P L _{2,3} , C K, In M _{4,5} , O K, Cu L _{2,3} , Ga L _{2,3} , Ge L _{2,3} , As L _{2,3} and Al K edges. Al L _{2,3} is a false positive detection due to an artefact. Maximum intensity values in counts after background subtraction, integration and scaling according to eqn. 3.16 with constant = 1. The minimum intensity in all the maps is 0.	55
3.14	Screen shot of program output showing pre-edge regions and integration windows dynamically assigned by the algorithm for SI with 80 eV offset (A), 250 eV offset (B) and 950 eV offset (C).	56
3.15	(A) Rotated HAADF-STEM image of cross-sectioned In _{0.62} Ga _{0.38} N film at high magnification, about 10 nm above the GaN substrate, showing (0002) lattice fringes. Growth direction points upwards. Elemental maps of (B) indium from In M _{4,5} edge, (C) gallium from Ga L _{2,3} edge and (D) nitrogen from N K edge recorded at 100 kV and calculated using (B & D) integration after inverse power law subtraction, (C) integration after exponential background extrapolation. All intensities are normalized to a sum of unity to calculate at.%. .	59
3.16	Background subtracted net intensities after the edge onsets have been integrated and normalised with respect to the corresponding scattering cross-sections and exposure times. Elemental maps of Al L _{2,3} (A) and Si L _{2,3} (B) in the low-loss region. Elemental maps of N K (C), O K (D), and Tb M _{4,5} (E) in the high-loss region. (F) HAADF.	60
4.1	Power-law background fit crossing spectrum	68
4.2	Experimental EELS of GaAs with $t/\lambda \approx 1$ with different background fits with error bars for As L _{2,3} (Ga L _{2,3} is more straight forward).	71
4.3	(A) Simulated low-losses (black) pure Poissonian, (blue) mixture of Gaussian and Lorentzians weighed according to Poisson statistics and (orange) a pure Gaussian. (B) Saw-tooth (hydrogenic model) edge. The plural scatter is generated by convolving the single scattered hydrogenic edge with pure Poissonian low-loss. The RL deconvolution is applied to recover the single scattering distribution.	74

4.4	(A) RL deconvolution method applied to the plural scattered saw-tooth (hydrogenic) edge. The plural scattered saw-tooth is generated by convolving the single scattered hydrogenic edge with low-loss simulated from a mixture of Gaussian and Lorentzian weighed according to Poissonian statistics. (B) Trace of position and amplitude of the first 4 ringing artefacts with increase in number of iterations during RL deconvolution of plural scattered edge in (A).	75
4.5	(A) RL deconvolution method applied to a plural scattered saw-tooth (hydrogenic) edge. The plural scattered saw-tooth is generated by convolving the single scattered hydrogenic edge with low-loss simulated from a pure Gaussian. (B) Trace of position and amplitude of the first 4 ringing artefact with increase in number of iterations during RL deconvolution of plural scattered edge in (A).	75
4.6	Least-squares fits for all the proposed models. (A) eqn. 4.16. (B) eqn. 4.17. (C) eqn. 4.18. (D) eqn. 4.19 and (E) eqn. 4.20. (F) Location of pixel (35, 21) in region 3 shown in STEM image.	84
4.7	Elemental maps obtained from baseline corrected eqn. 4.20. (A–C) maps are from EELS SI with 80 eV offset. (D–F) from EELS SI with 250 eV offset and (G–I) from EELS SI with 950 eV offset.	85
5.1	$\text{In}_x\text{Ga}_{1-x}\text{N}/\text{GaN}$ layers overview image with coloured boxes in (A) indicating location of extracted spectra in (B).	93
5.2	The FWHM of bulk plasmon peak of ternary alloy as a function of x (Wang et al., 2016).	94
5.3	(A) Lorentzian functions which model the bulk plasmons for InN [$E_p(x = 1) = 15.53 \text{ eV}$, $W_p(x = 1) = 3.83 \text{ eV}$], GaN [$E_p(x = 0) = 19.55 \text{ eV}$, $W_p(x = 0) = 4.19 \text{ eV}$] and $\text{In}_x\text{Ga}_{1-x}\text{N}$ [$E_p(x = 0.5) = 17.54 \text{ eV}$, $W_p(x = 0.5) = 5.28 \text{ eV}$]. (B) Core-losses of In N_5 , Ga M_5 and simulated $\text{In}_{0.5}\text{Ga}_{0.5}\text{N}$, as shown in eqn. 5.7. The truncation of $\text{In N}_{4,5}$ and $\text{In}_x\text{Ga}_{1-x}\text{N}$ core-losses can be observed.	94
5.4	The offset energy, ΔE , in eV between plasmon and the first core-loss (Wang et al., 2016).	95
5.5	Simulated $\text{In}_x\text{Ga}_{1-x}\text{N}$ spectra for $x \in [0, 1]$ for step size, $\Delta x = 0.1$. The reference spectra for In and Ga edges are extracted from EELS data acquired from Nion USTEM (Walther et al., 2017).	98
5.6	Model fit in the range of 13 eV to $\sim 23 \text{ eV}$ and individual components of three bulk plasmons and three core-losses in (A) $\text{In}_x\text{Ga}_{1-x}\text{N}$ region at pixel (41, 16) (region 2 in fig. A.3(B)) with $R^2 = 0.9709$ and (B) GaN buffer layer at pixel (60, 30) (region 5 in fig. A.3(B)) with $R^2 = 0.9871$	99

5.7	Model fit in the range of 13 eV to 27 eV and individual components of three bulk plasmons and three core-losses in (A) $\text{In}_x\text{Ga}_{1-x}\text{N}$ region at pixel (41, 16) (region 2 in fig. A.3(B)) with $R^2 = 0.9709$ and (B) GaN buffer layer at pixel (60, 30) (region 5 in fig. A.3(B)) with $R^2 = 0.9871$	99
5.8	Results from fitting each spectrum from the SI in fig. A.3(B) by a linear superposition of three reference spectra, one for GaN, one for InGaN and one for InN film. Shown are the weight parameters attributed to (A,D) GaN, (B,E) InN and (C,F) $\text{In}_x\text{Ga}_{1-x}\text{N}$ where x was varied from 0.05 to 0.95 in steps of 0.05 ($\Delta x = 0.05$). Top row: fit for plasmons, middle row: fit for core losses. (G) plots the best fitting x value of the ternary component only. (H) shows the R^2 parameter of the fit for each spectral data point. (I) Rotated ADF image of the area investigated where the apparent slight tilt from vertical growth is due to drift during the acquisition of SI.	102
5.9	Results from fitting each spectrum from the SI in fig. A.3(B) by a linear superposition of three reference spectra, one for GaN, one for InGaN and one for InN film. Shown are the weight parameters attributed to (A,D) GaN, (B,E) InN and (C,F) $\text{In}_x\text{Ga}_{1-x}\text{N}$ where x was varied from 0.001 to 0.999 in steps of 0.001 ($\Delta x = 0.001$). Top row: fit for plasmons, middle row: fit for core losses. (G) plots the best fitting x value of the ternary component only. (H) shows the R^2 parameter of the fit for each spectral data point. (I) Rotated ADF image of the area investigated where the apparent slight tilt from vertical growth is due to drift during the acquisition of SI.	103
5.10	Maps of In content, x , calculated for data from fig. 5.8(G) from weights of fitting (A) plasmon losses, (B) low core-losses, (C) difference map (B)–(A).	104
5.11	Maps of In content, x , calculated for data from fig. 5.9(G) from weights of fitting (A) plasmon losses, (B) low core-losses, (C) difference map (B)–(A).	105
5.12	(A) In and constructed $\text{In}_x\text{Ga}_{1-x}\text{N}$ at $x = 0.5$ reference spectra. The constant extrapolation after the truncation is shown in orange dotted horizontal line. The black dotted vertical line is bifurcating the available spectra and the extrapolated spectra. (B) Truncation correction for $\text{In}_x\text{Ga}_{1-x}\text{N}$ as a function of x	107
5.13	The maps of truncation correction factors for (A) reference InN spectrum, $f_{cor}(x = 1)$. (B) constructed $\text{In}_x\text{Ga}_{1-x}\text{N}$ spectrum, $f_{cor}(x)$ and (C) reference GaN spectrum, $f_{cor}(x = 0)$	109
5.14	Truncation corrected weights calculated in eqns. 5.22–5.24 for (A) GaN (B) InN and (C) $\text{In}_x\text{Ga}_{1-x}\text{N}$ core-loss.	110
5.15	Maps of In content, x , calculated for data from fig. 5.9(G) from truncation corrected weights from fig. 5.14 of fitting (A) plasmon losses, (B) low core-losses, (C) difference map (B)–(A).	110

- 5.16 (A) The locations of random spectrum extracted from regions 2 (red), 3 (green) and 4 (blue) of multi-junction solar cell. (B) Spectrum extracted from region 2 of multi-junction solar cell (Cu) and a Lorentz function is fitted to the bulk plasmons. $E_p = 22.11$ eV and $W_p = 18.07$ eV. 112
- 5.17 Lorentz function is fitted to the bulk plasmons from (A) region 3 (GaAs), ($E_p = 15.54$ eV and $W_p = 5.50$ eV) and (B) region 5 (AlGaInP), ($E_p = 15.08$ eV and $W_p = 5.61$ eV) of multi-junction solar cell. 113
- 5.18 (A,C) maps and (B,D) profiles of bulk plasmon peak position, E_p (in eV), and FWHM, W_p (in eV), determined by Lorentz fitting. (E) and (F) are maps of bulk plasmon peak position, E_p (in eV), and FWHM, W_p (in eV), determined by Lorentz fitting. 114
- 5.19 The AlN:Tb spectrum from EELS SI in fig. A.4(A) is chosen as an example and fits described in eqns. 5.30 & 5.33 are shown on log-scale. Orange line: spectrum modelled using bulk plasmons as Lorentz functions. Yellow line: Voigt function is used to model the bulk plasmons. In both cases, ZLP is modelled using a Gaussian function. 117
- 5.20 (A) HAADF. t/λ values calculated using (B) eqn. 5.28, (C) low-loss fitting as described in eqn. 5.30 and the R^2 values of both the fit using Lorentzian and Voigt as bulk plasmons are described in (D). Similarly, (E, F) are the t/λ and R^2 values calculated from low-loss fit using eqn. 5.33. 119
- 6.1 Clusters of E_g vs. R^2 for EELS of GaN Series 1. The square-root fitting is applied to the raw experimental spectrum in fig. A.5(B) with varying fit ranges from 0.5 eV to 3 eV between 0–10 eV at every 0.5 eV increment, (A) without subtracting any background and (B) and with bulk-plasmon subtraction. . . . 126
- 6.2 1D modelling of ZLP of EELS for (GaN from fig. A.5(B) and $t/\lambda = 0.25$) by distribution fitting of Gaussian ($R^2 = 0.995$) and Voigt ($R^2 = 0.998$) functions in the fitting range -5 eV to 5 eV or exponential tail extrapolation. 128
- 6.3 (A) Modelled 2D ZLP with multivariate pseudo-Voigt function (Counts on log-scale), $V_p(\mathbf{x}, \mu, \Sigma, C)$ to experimental GaN 2D EELS Series 1 shown in fig. A.5(A). (B) Profiles of spectrum and multivariate pseudo-Voigt function model. (C) Non-dispersive axis profile of multivariate pseudo-Voigt function model to ZLP. 129
- 6.4 (A) RL deconvolution applied to bulk plasmon subtracted to GaN low-loss EELS from fig. A.5(B) at different iterations to demonstrate the effects of ringing artefacts and non-negative nature due to Poissonian statistics. (B) ZLP background removal for DOS using RL and Fourier-log deconvolution. RL deconvolution is applied for 3 iterations then an exponential function is used to extrapolate the tail and subtract with RL deconvoluted spectrum. 131

6.5	(A) The background is by three exponentials extrapolation and the bulk plasmon by a Lorentz function. (B) The difficulty in choosing the fit range for reliable determination of bandgap is illustrated by fitting a $300 \times \sqrt{E - E_g}$ function fit at onset and a square-root function after the edge.	133
6.6	Bandgap maps of $\text{In}_x\text{Ga}_{1-x}\text{N}$ determined by (A) derivative method. (B) modelling background as an offset and fitting eqn. 6.7. (D) Rotated ADF image of the area investigated where the apparent slight tilt from vertical growth is due to drift during the acquisition of SI. (E) subtracting ZLP and bulk plasmons, and modelling the residual spectrum with eqn. 6.7. (C,F) are R^2 maps of eqn. 6.7 fitting (B,E) respectively.	134
6.7	The square-root function fit applied to residual spectrum of GaN (A–E) Series 1. The fit range is from 0 eV to 12 eV.	136
6.8	Fourier-log deconvolution applied to GaAs low-loss spectrum. The onset of DOS could be seen at ~ 1.40 eV.	139
6.9	(A) 2D RL deconvolution applied to 2D EELS SI of GaN Series 1. (B) Profiles of GaN Series 1, pseudo-Voigt function model to ZLP and 2D deconvoluted spectrum.	140
6.10	k -means cluster assignments and centroids for bandgap determination by square-root fits for all possible fit windows with a change in step window of 0.5 eV for GaN 1D (A) raw (B) plasmon subtracted (C) Fourier-log deconvoluted spectrum. The limits of the fit range are 0 eV to 10 eV. The similar fitting analysis is used to get the cluster for (D) Fourier-log deconvoluted GaAs spectrum.	142
A.1	(A) An ADF image showing an overview of the layer structure analysed and indicating the rectangular regions selected for spatial drift (yellow) and SI acquisition (green). (B) Definition of regions in the EELS SI. Regions indicated by blue dotted lines are thicker regions, while red lines denote interfaces. A sum spectrum is extracted from each region for further quantification in table 3.2. (C) Relative thickness map (t/λ).	150
A.2	(A) Rotated HAADF-STEM image of cross-sectioned $\text{In}_{0.62}\text{Ga}_{0.38}\text{N}$ film at high magnification, about 10 nm above the GaN substrate, showing (0002) lattice fringes. Growth direction points upwards. (B) Relative thickness map (t/λ) in multiples of the inelastic mean free path, λ	153
A.3	(A) Rotated ADF image of the area investigated where the apparent slight tilt from vertical growth is due to drift during the acquisition of SI. (B) Definition of regions 1–4 in the InGaN and region 5 in the GaN buffer used later in analysis. (C) Relative thickness map for spectrum imaging at 60 kV, with mean values of $t/\lambda = 1.52 \pm 0.14$ in the top carbon region, 0.43 ± 0.02 in the InGaN layer (which is, hence, almost uniformly thin) and 0.59 ± 0.13 in the GaN buffer.	153

A.4	(A) HAADF. (B) Box 1 area in AlN used for the calculation of cross-correlation between elemental maps. Box 2 includes the Si substrate. (C) Relative thickness map (t/λ).	155
A.5	The spatially resolved EELS (Counts on log-scale) acquired with a drift tube offset of (A) 10 eV with a 0.6 mm entrance aperture. (B) is the profile of spatially resolved EELS integrated across 40 non-dispersive channels from (A).	157
B.1	Visual time report of distributed tasks using two workers on MacBook Pro.	163

List of Tables

3.1	A look-up table used for edge detection.	38
3.2	Quantification in atomic percent (at.%) of each region of the three SIs recorded. The sum of all concentrations has been normalised to 100% according to eqn. 3.17.	52
3.3	Relative quantification of Cu, Ga and As elemental maps with DigitalMicrograph™ in different regions shown in fig. 3.13(E) (GaAs).	54
3.4	Background fitting details. All numerical values are in eV.	57
3.5	Calculated mean free paths (λ), mean atomic number ($\langle Z \rangle$), mean atomic mass ($\langle A \rangle$) and mean energy-loss ($\langle E \rangle$).	58
3.6	Background fitting details. All numerical values are in eV.	61
3.7	Elemental quantification (at.%) in AlN:Tb and Si region for top 40 rows (Box 1) and lowest 15 rows (Box 2) respectively as shown in fig. A.4(B).	61
3.8	Cross-correlation between elemental maps in AlN region marked by box in fig. A.4(B).	63
4.1	The attributes associated with each formulas from eqn. 4.16 to 4.19.	81
4.2	Relative quantification of elemental maps at region 3 as shown in fig. 4.7(D) (GaAs).	81
4.3	Relative quantification of elemental maps at region 5 as shown in fig. 4.7(D) (GaAs).	82
4.4	Relative quantification of elemental maps at region 8 as shown in fig. 4.7(D) (GaAs).	82
4.5	Quantification in atomic percent (at.%) of region 3, 5 and 8 of the three GaAs multi-junction solar cell SIs recorded as discussed in section A.1. The sum of all concentrations has been normalised to 100% according to eqn. 3.17.	86
4.6	Relative quantification of Cu, Ga and As elemental maps with Hyperspy, DigitalMicrograph™ and EELSAnalyser in region 3 shown in fig. 4.7(D) (GaAs).	87
4.7	Relative quantification of Cu, Ga and As elemental maps with Hyperspy, DigitalMicrograph™ and EELSAnalyser in region 5 shown in fig. 4.7(D) (GaAs).	88
4.8	Relative quantification of Cu, Ga and As elemental maps with Hyperspy, DigitalMicrograph™ and EELSAnalyser in region 8 shown in fig. 4.7(D) (GaAs).	88

5.1	Comparison of effective In content from different regions identified in fig. A.3(B) for fitting range from 13 eV to \sim 23 eV.	105
5.2	Comparison of effective In content from different regions identified in fig. A.3(B) for an extended fitting range from 13 eV to 27 eV.	106
5.3	The total intensity of the reference spectrum of InN, synthesised $\text{In}_x\text{Ga}_{1-x}\text{N}$ and the extrapolated spectrum are used to calculate the truncation correction at each value of x	108
5.4	Comparison of effective In content from different regions identified in fig. A.3(B) for an extended fitting range from 13 eV to 27 eV.	110
5.5	The modelled bulk plasmon position, E_p , from Lorentz function described in eqn. 5.27 for the low-loss EELS of multi-junction solar cell in fig. 5.16(A).	112
5.6	The modelled bulk plasmon position, E_p , from Lorentz function described in eqn. 5.27 for the low-loss EELS of AlN doped with Tb in fig. A.4(B).	115
5.7	AlN doped with Tb	117
6.1	Modelling multivariate Gaussian function to experimental 2D EELS of GaN. The values of μ and Σ are in pixels and not in eV.	129
6.2	Bandgap determined by all the proposed methods for 1D GaN spectrum.	137
6.3	Bandgap determined for method II and method V for adjusted fit range of 0 eV to 10 eV for 1D GaN spectrum.	138
6.4	The co-ordinates of the centroids with highest R^2	142
A.1	EELS data acquisition parameters for the four SIs acquired from the same area, indicated by the green rectangle in fig. A.1(A)	151
A.2	EELS data acquisition parameters for the two SIs acquired from InGaN, indicated by fig. A.2(A) and fig. A.3(A).	152
A.3	EELS data acquisition parameters for the two SIs acquired from the same area.	154
A.4	EELS low-loss data acquisition parameters for the 2D SI acquired in TEM mode.	157

List of Abbreviations

TEM	Transmission Electron Microscopy
EELS	Electron Energy-loss Spectroscopy
HREELS	High Resolution Electron Energy-loss Spectroscopy
VEELS	Valence Electron Energy-loss Spectroscopy
EDXS	Energy Dispersive X-ray Spectroscopy
CLS	Cathodoluminescence Spectroscopy
STEM	Scanning Transmission Electron Microscopy
HAADF	High-angle Annular Dark Field
ADF	Annular Dark Field
GIF	Gatan Imaging Filter
SI	Spectrum Image
eV	electron Volt
RL	Richardson-Lucy
PSF	Point Spread Function
FWHM	Full Width at Half Maximum
HWHM	Half Width at Half Maximum
ZLP	Zero-loss Peak
FEG	Field Emission Gun
FN	Fowler-Nordheim
MB	Maxwell-Boltzmann
DOS	Density Of States
CRT	Cathode Ray Tube
AlN	Aluminium Nitride
Tb	Terbium
AlN:Tb	Aluminium Nitride doped with Terbium
O	Oxygen
N	Nitrogen
Al	Aluminium
UV	Ultra-Violet
LED	Light Emitting Diode
P	Phosphorous
Si	Silicon
Er	Erbium
Eu	Europium
In	Indium
GaAs	Gallium Arsenide
InN	Indium Nitride
GaN	Gallium Nitride
InGaN	Indium Gallium Nitride
InGaAs	Indium Gallium Arsenide

RBS	R utherford B ack-scattering S pectrometry
ICP-OES	I nductive C oupled P lasma- O ptical E mission S pectroscopy
DC	D irect C urrent
CCD	C harge- C oupled D evice
SNR	S ignal-to- N oise R atio
MLLS	M ultiple L inear L east S quares
at.%	a tomic p ercent
AWGN	A dditive W hite G aussian N oise

Physical Constants

Speed of Light	$c_0 = 2.997\,924\,58 \times 10^8 \text{ m s}^{-1}$
Electron charge	$e = 1.602 \times 10^{-19} \text{ C}$
Electron rest mass	$m_0 = 9.110 \times 10^{-31} \text{ kg}$
Electron rest energy	$m_0 c^2 = 511.00 \text{ eV}$
Atomic mas unit ($1/N_A$)	$u = 1.661 \times 10^{-27} \text{ kg}$
Bohr radius ($4\pi\epsilon_0\hbar^2(m_0e^2)^{-1}$)	$a_0 = 5.292 \times 10^{-11} \text{ m}$
Rydberg energy ($\hbar^2(2m_0a_0^2)^{-1}$)	$R = 13.61 \text{ eV}$
Photon energy \times wavelength	$hc/e = 1.240 \text{ eV } \mu\text{m}$
Avogadro number	$N_A = 6.022 \times 10^{23} \text{ mol}^{-1}$
Boltzmann constant	$k = 1.381 \times 10^{-23} \text{ J K}^{-1}$
Permittivity of space	$\epsilon_0 = 8.854 \times 10^{-12} \text{ F m}^{-1}$
Permeability of space	$\mu_0 = 1.257 \times 10^{-6} \text{ H m}^{-1}$
Planck constant	$h = 6.626 \times 10^{-34} \text{ J s}$
$\hbar/2\pi$	$\hbar = 1.055 \times 10^{-34} \text{ J s}$

To my parents, sisters and beloved nieces

Chapter 1

Introduction

1.1 Aim and Objectives

The aim of this work is automated electron energy-loss spectra (EELS) quantification without user bias from the discrete objectives involved for low/high energetic core-losses, bulk plasmon losses and valence electron energy-loss spectra (VEELS).

Presently, techniques for quantification of EELS is subject to bias because the quantification process involves user intervention and is not extensive in a manner that thousands of spectra can be processed automatically. Manual processing of multi-dimensional data is time consuming. Hence there is a need for automatic, generic, objective and effective processing of spectra from scanning transmission electron microscopy (STEM). Typically, an EELS spectrum has a very large background. The intensity of ionization edges compared to this background is very small. An automated detection of the ionization onset would be required to model the spectra without human bias. The traditional way of choosing pre-edge regions and integration ranges for quantification manually are heavily biased and sometimes difficult to reproduce if these parameters aren't mentioned. Modelling the background using statistical tools such as least-squares fit, distribution fit and different signal processing techniques can provide a very effective way for quantification and mapping high-loss spectrum images (SIs). Effects of systematic and statistical errors have been difficult to assess for core-loss quantification as there is no single model that can determine the extent of systematic errors. Hence, in high-loss least-squares modelling of ionization edges, a model accounting for the systematic error needs to be proposed and should be compared to the traditional quantification by background subtraction. The elimination of plural scattering in the quantification process can lead to unforeseen errors such as artefacts arising from Fourier based deconvolution methodologies. However, some of the machine learning tools such as maximum likelihood

estimation are seldom explored for high-loss EELS with regards to artefacts or its convergence. Hence a model is needed to understand these artefacts. In almost all the cases, the background is modelled in the pre-edge region. An alternative approach of modelling the background in post-edge region seems feasible. A baseline correction to traditional linear least-squares fits is explored to minimize the systematic error arising due to background extrapolation under the core-losses at higher energy. Sometimes a background model chosen such as inverse power-law function or exponential function may not be optimal. Hence, a linear baseline correction and small alterations in the way of modelling could alter the quantification results further.

The quantification of phase separated ternary alloys such as $\text{In}_x\text{Ga}_{1-x}\text{N}$ are only studied in high-loss regions. But the low-energetic core-losses such as In $4d$ and Ga $3d$ transitions along with the bulk plasmon could be used to study the phase separation. The challenges in extracting reference spectra for In $4d$ and Ga $3d$ transitions will be discussed. These reference spectra do not have proper theoretical cross-sections (for $4d$ transitions) assigned to them; extrapolating and/or fitting these reference spectra is challenging. Also, the dependence of fit ranges in low-loss for determination of phase separation needs to be addressed. The bulk plasmons can be modelled using pure Lorentz functions or Voigt functions. The position of the bulk plasmon can compliment the quantification of high-loss EELS, and maps of width of bulk plasmons can sometimes reveal information on crystallinity.

Automated bandgap measurement is a challenging task. Visual determination of the onset is not a comprehensive way of determining the bandgap in EELS. The apparent values of a bandgap heavily rely on the type of background subtraction and fit ranges for the density of states (DOS). There is need to deal with the dominating zero-loss peak (ZLP) and bulk plasmons. Hence a proper methodology is needed to reliably measure the bandgap with error margins for an unknown material. A highly energy resolved spectra from a monochromator could be a better way to determine the bandgap onset. However, for a low-loss spectrum obtained in a normal TEM, the bandgap computation is challenging. The measurement of bandgap from a deconvoluted (1D) spectrum can be compared with the measurement of bandgap from spatially resolved (2D) EELS. Apart from the square-root function fitting, other methods will be explored such as derivative and k -means clustering.

1.2 Structure of thesis

This thesis is divided into four technical chapters. Following a general literature review the analysis of EELS is discussed from higher to lower energy-loss. Energy-losses > 100 eV can be considered as high-loss. The analysis of low-loss spectra is more complex due to the presence of the ZLP, inter and intra-band scattering, bulk and surface plasmon losses, core losses due to edges with low ionization energies (eg. M and N shells), and plural scattering due to finite thickness of the sample, which results in bulk plasmons being replicated at higher energies. Low-loss spectra are usually dominated by ZLP and plasmon losses. The quantification of ionization edges in high-losses is relatively straight forward as they are superimposed on a monotonically decaying background. This makes it possible to automatically identify the core-loss ionization edges. Chapter 3 proposes two methods of automated core-loss ionization edge detection. The improved edge detection algorithms are applied to simulated spectra with varying window sizes, thickness, noise and to a smoothed spectrum using simple averaging filter. The same method is tested with different experimental EELS spectra such as high loss of multilayer heterostructure of a solar cell, $\text{In}_x\text{Ga}_{1-x}\text{N}$ and AlN doped with Tb. In chapter 4 various background fitting methods and the factors that affect the quantification processes are discussed. Deconvolution methods are studied and the limit of their efficiency is discussed. A baseline correction to the linear least-squares fit of the theoretical model to an experimental spectrum is proposed. Hence, high-loss spectra (> 100 eV) are analysed in chapters 3 and 4, followed by analysis of bulk plasmon and low-energetic core-losses (10 eV to 100 eV) in chapter 5. The quantification of spectra from the ternary semiconductor alloy $\text{In}_x\text{Ga}_{1-x}\text{N}$ by jointly fitting bulk plasmons and $4d$ transitions of In and $3d$ transitions for Ga are discussed with two different fit ranges. A truncation correction factor that improves the quantification of In core-loss in the extended fit ranges has been proposed. The reliability of bandgap determination in low-loss ($\lesssim 12$ eV) VEELS of InGaN and GaN is analysed in chapter 6. The various methodologies are applied to determine the bandgaps of GaN and $\text{In}_x\text{Ga}_{1-x}\text{N}$ ternary alloys. Different methodologies such as square-root function fitting, derivative method and cluster classification methods are applied and their reliability is studied. The effects of underlying intensities of ZLP and bulk plasmons are discussed in chapter 6.

1.3 Contributions

- Chapter 3:
 - Proposal of two automated ionization core-loss edge onset detection algorithms. First algorithm uses look-up table to identify the core-losses by counting positive slope-angle clusters. The second algorithm uses the standard peak detection algorithms to detect the peaks formed by the exponent of the background at each point of the spectrum.
 - The limits of the edge detection algorithm by peak detection is tested by choosing different window lengths, specimen thickness, additive white noise and effects of smoothing using an averaging filter.
 - Automated quantification of dynamically selected pre-edge regions for fitting and integration ranges is proposed.
- Chapter 4:
 - The disadvantage of the most commonly used inverse power-law function for high-loss EELS quantification is discussed with mathematical inferences. An alternative approach of background modelling in post-edge regions is discussed in the case where the pre-edge modelled background extrapolation is crossing the spectrum at higher energy-losses. An optimal extrapolation of background for an overestimated net core-loss from post-edge and underestimated net core-loss from pre-edge background models using their respective Poissonian error bars is proposed.
 - Richardson-Lucy deconvolution (Maximum-Likelihood estimation) is discussed for core-loss spectrum processing to retrieve the single scattering distribution. The deconvolution algorithm is tested for a simulated plural scattering distribution and the relationship between ringing artefacts and the number of iterations is discussed.
 - A large change in the quantification of EELS by slightly modifying the least-squares model parameters is demonstrated for an example case of overlapping Cu, Ga and As L-edges. A baseline

corrected linear least-squares modelling of EELS spectrum is proposed to handle the systematic error posed by background extrapolation to higher energy-losses. The plural scattering is included in the analysis by convolving the single scattering theoretical cross-section from Hartree-Slater or hydrogenic models with the low-loss EELS.

- Chapter 5

- Phase separation in $\text{In}_x\text{Ga}_{1-x}\text{N}$ is studied by fitting three bulk plasmons and low-energetic Ga $M_{4,5}$ and In $N_{4,5}$ edges for spectra of $\text{In}_x\text{Ga}_{1-x}\text{N}$, InN and GaN in two different fit ranges (from 13 eV to 23 eV and 13 eV to 27 eV).
- Due to experimental problems in recording the experimental reference spectrum of the In $4d$ transition over a sufficiently wide interval, the quantification of core-losses with extended fit ranges shows discrepancies. These were rectified by proposing a truncation correction parameter for extrapolation of the truncated InN reference spectrum.
- The modelling of bulk plasmons by Lorentz functions and Voigt functions is discussed to verify the quantification of high-loss EELS. The position and width of bulk plasmons are analysed.
- A novel method of measurement of relative thickness of the material from low-loss fitting is proposed and the results are compared with the traditional log-ratio method.

- Chapter 6

- The reliability of bandgap measurement from VEELS is studied assuming the material under observation is unknown but has a direct bandgap. The modelling of background for DOS such as, tail of ZLP and bulk plasmons, influences the measurement of bandgap. Hence bulk plasmon and ZLP modelling by subtraction and deconvolution in traditional 1D EELS and spatially resolved EELS is studied by using multivariate statistical distribution modelling. This modelling is compared with results from a simple extrapolation of the tail of ZLP.
- Automated bandgap measurements are compared using different square-root function fits and a derivative method for monochromated low-loss EELS SI of $\text{In}_x\text{Ga}_{1-x}\text{N}/\text{GaN}$ material.

- Various methods are proposed for measurement of bandgap for GaN. The statistics of the bandgap measured are tabulated. The methodology is extended to lower bandgap material such as GaAs to check the reliability of the method.
- A novel approach of measurement of bandgaps by cluster analysis is proposed based on k -means clustering. The relationship between formation of clusters over various fit ranges and R^2 values are studied. The centroid, mean and median of the cluster with the highest R^2 is found to approximate the bandgap.

1.4 Published work

1.4.1 Journal publications

Angadi, V. C., Benz, F., Tischer, I., Thonke, K., Aoki, T. and Walther, T. (2017). 'Evidence of Terbium and Oxygen Co-segregation in Annealed AlN:Tb'. *Appl. Phys. Lett.* 110.22, p. 222102. DOI: [10.1063/1.4984237](https://doi.org/10.1063/1.4984237).

Walther, T., Wang, X., **Angadi, V. C.**, Ruterana, P., Longo, P. and Aoki, T., (2017). 'Study of Phase Separation in an InGaN Alloy by Electron Energy-loss Spectroscopy in an Aberration Corrected Monochromated Scanning Transmission Electron Microscope'. *J. Mater. Res.* 32.05, pp. 983–995. DOI: [10.1557/jmr.2016.447](https://doi.org/10.1557/jmr.2016.447).

Angadi, V. C., Abhayaratne, C. and Walther, T. (2016). 'Automated Background Subtraction Technique for Electron Energy-loss Spectroscopy and Application to Semiconductor Heterostructures'. *J. Microsc.* 262.2, pp. 157–166. DOI: [10.1111/jmi.12397](https://doi.org/10.1111/jmi.12397).

1.4.2 Conference proceedings

Angadi, V. C., Abhayaratne, C. Walther, T. 'Determination of Bandgap Onset by Richardson-Lucy Deconvolution of Electron Energy-loss Spectra (EELS): 1D EELS vs 2D EEL spectrum images'. *The 20th Microsc. Semicond. Mater.*, Oxford, UK; April 2017.

Angadi, V. C., Walther, T. 'Influence of Background Subtraction and Deconvolution on Calculation of EELS Core-loss Intensities'. *The 16th Euro. Microsc. Congr.*, Lyon, France; August 2016. DOI: [10.1002/9783527808465.EMC2016.6237](https://doi.org/10.1002/9783527808465.EMC2016.6237).

Angadi, V. C., Walther, T. 'Systematic study of background subtraction technique for EELS'. *Electron Microsc. Analysis Group*, Durham, UK; April 2016. DOI: [10.13140/RG.2.1.4020.6320](https://doi.org/10.13140/RG.2.1.4020.6320).

Angadi, V. C., Abhayaratne, C., Walther, T. 'Development of Automated Background Subtraction for Electron Energy-loss Spectroscopy'. *Electron Microsc. Analysis Group*, Manchester, UK; July 2015. DOI: [10.13140/RG.2.1.2972.0566](https://doi.org/10.13140/RG.2.1.2972.0566).

Angadi, V. C. and Walther, T. 'Core-Loss Edge Detection and Background Subtraction Techniques for EELS'. *Hyperspec. Imaging Applic. Conf.*, Coventry, UK; October 2014. DOI: [10.13140/2.1.4887.4565](https://doi.org/10.13140/2.1.4887.4565).

Chapter 2

Background literature

2.1 Microscopy

Before going in detail into EELS and its computational challenges due to its complex structure, a very brief and generic background of electron scattering in electron microscopy and cross-section of transmission electron microscopy (TEM) is discussed. Electrons are a form of radiation that can ionize the material under observation. When a high-energy electron interacts with the material, it produces a stream of secondary electrons by ionizing the material. The secondary electrons produced are important in analysing some of the properties of the material itself. When a beam of electrons is incident on a thin specimen, the non-scattered electrons which do not undergo any angular deviation and pass through the thin specimen in a straight direction, are called direct beam. The scattered electrons which are reflected back in almost the direction of incident beam are called backscattered electrons. The incident electrons, when passing near-by a charged particle, will experience a change in the kinetic energy which can lead to the emission of a photon or secondary electron, hence preserving the law of conservation of energy and momentum. This type of scattering is called bremsstrahlung scattering, as indicated in fig. 2.1. This scattering has very high characteristic angle, θ_E , and hence cannot be detected (Baier et al., 1999; Brydson et al., 2001; Fuggle et al., 1991). Also it cannot ionize the inner-shell and hence does not contribute to core-losses. The bremsstrahlung scattering (Blumenthal et al., 1970) is a continuous spectrum which extends across the axis in hyper-spectral data. Some of the incident electrons from the beam may be absorbed by the material in the specimen itself. Auger electrons (Jablonski, 1987) are an alternative to the release of X-ray photons, when an ionized atom returns to the ground state. This effect is used to study surface features and property of the surfaces (Harris, 1968). In semiconductor materials with direct band-gap, if an electron beam is incident on it the formation of electron-hole pair takes place.

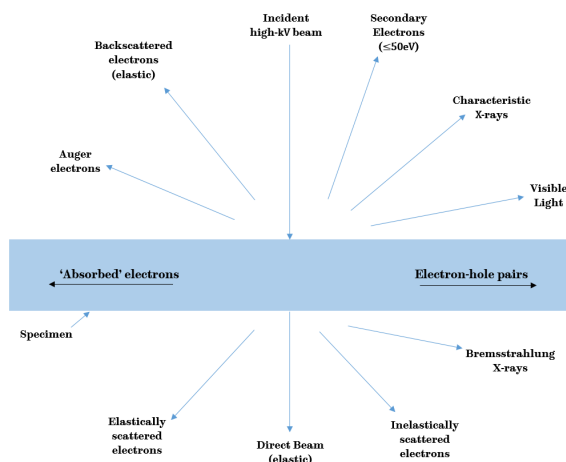


FIGURE 2.1: Electron interaction with material producing other types of radiation

They recombine to give out light. This is called cathodoluminescence (CLS) (Xie et al., 2012) and can also be used, among other types of radiation, in hyperspectral data analysis of the material. The electrons in the microscope can be classified as primary or secondary scattered electrons. The secondary electrons are called so because they are released from the bound electrons of the material. The primary electrons are the incident electrons and the secondary are the electrons produced by the interaction of primary electrons with the material/specimen. The incident electron beam interacts with the outer shell electrons, which require less energy to be ejected from valence band. If the incident electron beam interacts with inner shell electrons which require much higher energy to be released, the incident electron beam loses significant energy. For slow secondary electrons the energy threshold is typically around 50 eV. In fig. 2.1, Auger electrons, Bremsstrahlung electrons, Cathodoluminescence etc are all secondary electron scattering effects. The other classification of electron scattering is elastic vs inelastic scattering. The incident electron beam undergoes interactions with the atoms in the material. The electron deviates from its incident path due to positively charged nucleus. The deviation in its path could be from 0° to 180° . The incident beam with fast electrons can also interact inelastically with the material producing the secondary electrons or X-rays or Auger electrons. Phonon scattering is a type of inelastic scattering in which secondary electrons can be produced due to thermal vibrations of surface or bulk states of the material. Phonon scattering has a very small energy-loss which is $\ll 0.1\text{ eV}$ and it cannot be resolved using usual typical electron spectrometer systems (Egerton, 2011b). But may be with better spectrometers it can be resolved (Krivanek et al., 2013). Phonon scattering along with elastic scattering constitutes the ZLP in EELS.

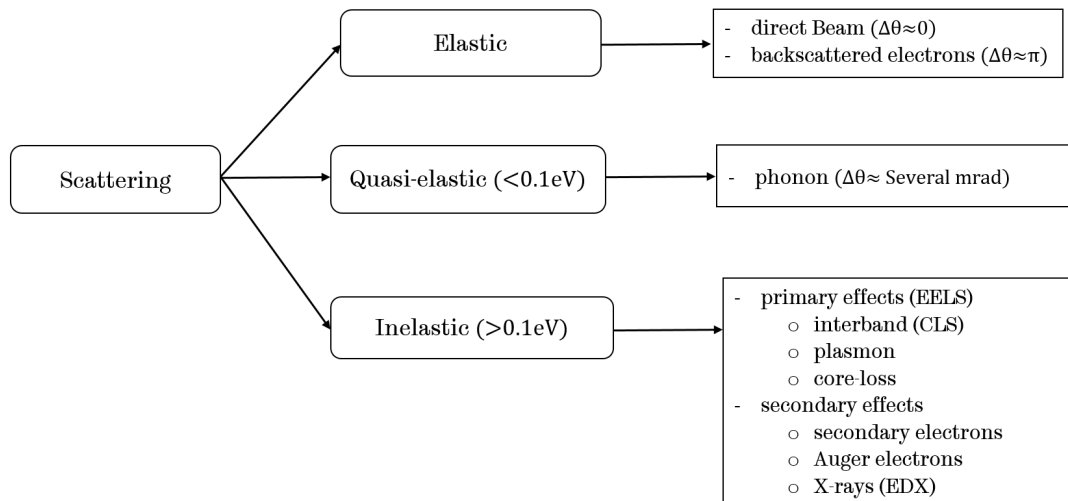


FIGURE 2.2: Electron scattering

2.1.1 Transmission Electron Microscope

The TEM is a very important instrument in characterizing semiconductor materials. This is useful in understanding the applications of nano structures of the semiconductor. The spatial resolution of the microscope can be from a few μm down to $\sim\text{\AA}$ for high-resolution TEM (HRTEM) (Amari et al., 2012; den Dekker et al., 2002). This makes it ideal for studying nano structures, defects etc. With the help of a wide variety of spectrometers, hyperspectral data can be acquired. A scanning transmission electron microscope (STEM) of 60 kV to 300 kV are used to scan the specimen and produce maps using detectors that collect intensity or a spectrum at each point. A STEM with a spectrometer has the capability to analyse the ionized sample using the scattered electrons and can provide chemical information of the sample. State-of-the-art TEMs operate in several modes such as energy filtered TEM (EFTEM) (Thomas et al., 2002), Bright field (BF) or Dark field (DF) imaging, electron energy-loss spectroscopy (EELS), energy dispersive X-ray spectroscopy (EDXS), convergent beam electron diffraction (CBED) etc. A cross-section of a TEM is shown in fig. 2.3. A high voltage of 60 keV–3 MeV is applied to a tip. Electrons are emitted from the electron gun by thermionic emission or field emission (Nion UltraSTEM 100) or combination of both effects called Schottky field emission gun (FEG) (Otten et al., 1993) (JEOL 2010F). Thermionic emission occurs when a material is heated at high enough temperature it emits electrons and field emission occurs when an electric field is applied to a small tip of the material it emits electrons due to the tunnelling effect. Schottky emission is the combination of both and hence it is thermally

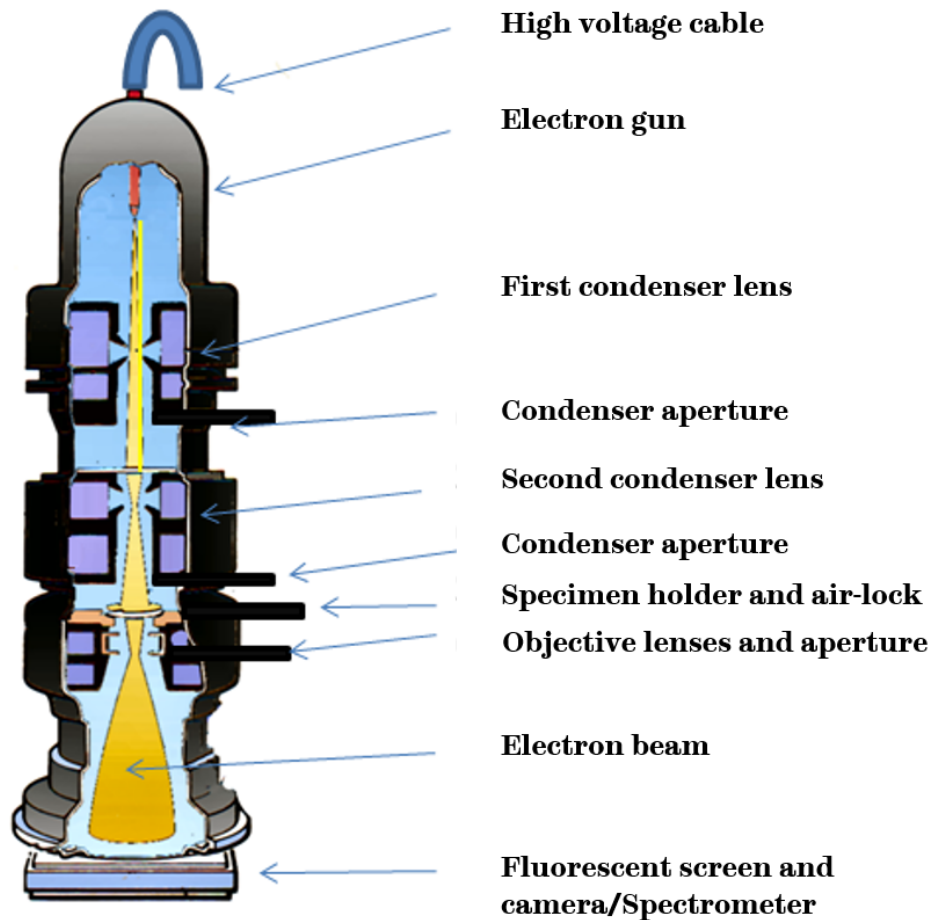


FIGURE 2.3: A Cross-sectional diagram of TEM (Graham, 2009).

assisted field emission (a.k.a enhanced field emission). Inside the TEM, vacuum is maintained to facilitate electrons to move in the microscope without the hinder from gas molecules. Liquid nitrogen and pumps are used to pump out the air continuously to create and maintain the vacuum conditions. The electrons emitted by the electron gun need to be focused to form a beam. A combination of lenses and apertures are used to focus the beam on the sample. The sample under observation is clamped to a specimen holder inserted in the TEM using an air-lock system. Three types of lens systems are used in TEM,

- **Condenser lens system** : It is used to focus the electrons emitted by the electron gun on to the specimen. The system has 2 or 3 single lenses.
- **Objective lens system** : These lenses are used to form a diffraction pattern in their back focal plane. It is usually a split lens, so a system of 2 single lenses.

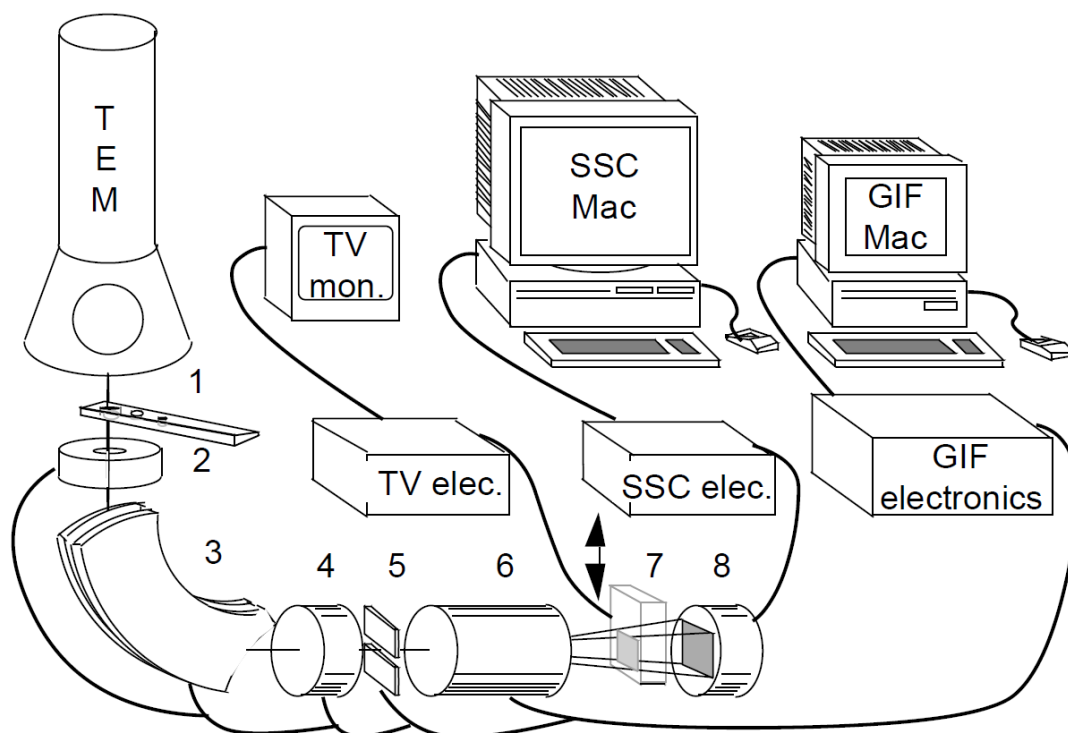


FIGURE 2.4: GIF component interface to TEM and control path (Gatan, 1996).

- **Projector lens system** : It magnifies the image or diffraction pattern onto screen or detector. It usually has 3 to 5 round lenses.

A fluorescent screen is used to see the electron beam interaction with the material. In STEM, a Gatan imaging filter (GIF) interface could be used instead of a 2D camera to record the image. In EELS spectrometer, a magnetic field is used to form an image of the dispersed beam on a detector, based on the dispersion of kinetic energy of the scattered electrons.

2.1.2 Gatan Imaging Filter

The GIF is attached to the imaging chamber of the TEM. The sophistication of the GIF system allows to acquire TEM images or diffraction patterns into energy-filtered images. It adds the additional capability of EELS and electron spectroscopic imaging (ESI) to the TEM. The hardware interface of a GIF is shown in fig. 2.4. The interface consists of 8 parts (Gatan, 1996):

1. **Entrance aperture:** The entrance aperture sizes are 3.0 mm, 2.0 mm or 0.6 mm. The 3.0 mm entrance aperture is typically used for energy-filtered imaging, whereas the 2.0 mm and 0.6 mm apertures are typically used for EEL spectroscopy.

2. **Pre-prism focusing and alignment coils:** Comprising a dipole, two quadrupoles and two sextupoles.
3. **Magnetic prism:** It has a 10 cm bending radius and the beam is bent by 90° to enter the charge-coupled device (CCD) camera.
4. **Spectrum-magnifying quadrupole assembly:** Comprising two quadrupoles (not present on GIF100).
5. **Energy-selecting slit:** It is pneumatically insertable and adjustable under computer control.
6. **Quadrupole-sextupole imaging assembly:** Comprising four quadrupoles and five sextupoles.
7. **Pneumatically retractable TV-rate CCD camera:** This interface is based on Gatan Model 694 TV-rate Camera. It uses powdered phosphorous to increase the sensitivity as compared to single crystal YAG scintillator. It is used for alignment and can be pneumatically retracted to allow images to be recorded on multi scan CCD.
8. **Multi-Scan CCD camera:** This interface is based on Gatan Model 694 Multi-Scan Camera. It has a 1024×1024 pixel CCD chip with $24 \mu\text{m}$ square pixels. A vacuum is maintained to prevent damages to CCD chip and scintillator. Note: R005 has 2048×2048 pixel with $14 \mu\text{m}$ square pixels.

The software packages that run in collaboration with hardware,

- **Filter control:** Controls the operations of GIF electronics.
- **Digital Micrograph:** A software interface which can acquire images from multi scan camera and display them.
- **Image filter suite:** It is one of the plug-ins for the Gatan Micrograph Suite (GMS) in Digital Micrograph. It is used to automatically compute ratio maps or can acquire EEL spectra and pass it on to EELS analyser (Gatan, 2015).

With the help of a wide variety of spectrometers, hyperspectral data can be acquired like EELS (Arenal et al., 2008), EDXS (Horita et al., 1989) and CLS (Xie et al., 2012).

2.2 Electron energy-loss spectroscopy (EELS)

EELS is ideal for quantification of the elements present in a material at near atomic resolution (Reimer, 1995). The intensity of core-loss edges of an element in EELS is via the ionization cross-section related to the number of atoms of that element. The amount of kinetic energy that is lost by an incident electron to excite an electron inelastically from an inner atomic shell is the cause for the formation of core-loss edges (Egerton, 2011b). The minimum incident energy of an electron required to ionize an electron from a particular shell produces the ionization edge onset for that shell. However, any excessive incident energy will also cause the ionization and still retain excessive kinetic energy. In EDXS where the edges are the difference between two ionization shells and hence a detected electrons are of discrete energies. Hence in EDXS, the ionization edges are peaks while in EELS it is an exponential decay after the ionization edge. The EEL spectrometer sorts the scattered electrons according to their kinetic energy. Some of the standard imaging techniques used in acquisition of EELS are shown in fig. 2.5. The most common system is a TEM fitted with magnetic prism. The beam entering the prism is elastic and inelastic (energy-loss) that occurred in the specimen. The magnetic prism is used to sort the electrons according to their kinetic energies and the electrons are collected by a spectrometer at 90° to the optical axis. The instrumental arrangement is shown in fig. 2.5(A). An alternative setting is to arrange the spectrometer to be in the TEM column. To get the imaging stability there are multiple prisms that bend the beam in the shape of Omega (Ω). The image is formed on the CCD camera. A slit can be introduced to act as an energy-filter. The arrangement of the equipment is shown in fig. 2.5(B). A third kind of system is based on STEM. A field emission source is used to form a probe that can raster scan the specimen. A dark field image is generated by highly scattered electrons that are collected at a ring-shaped (annular) detector. The annular detector read-out should be synchronous to the scanning probe. The system is shown in fig. 2.5(C). The spectrum is due to both multiple elastic and inelastic scattering of the electrons by the sample. EELS spectra are complex in nature due to the presence of the ZLP, energy-loss near edge structure (ELNES), extended electron energy-loss fine structure (EXELFS) (Ahn, 2005), plasmon inter-band transitions (Raether, 1980) and phonon scattering etc. These influence the extraction of core-loss edges through background subtraction. In the low-loss region (Browning et al., 2011) of an EELS the

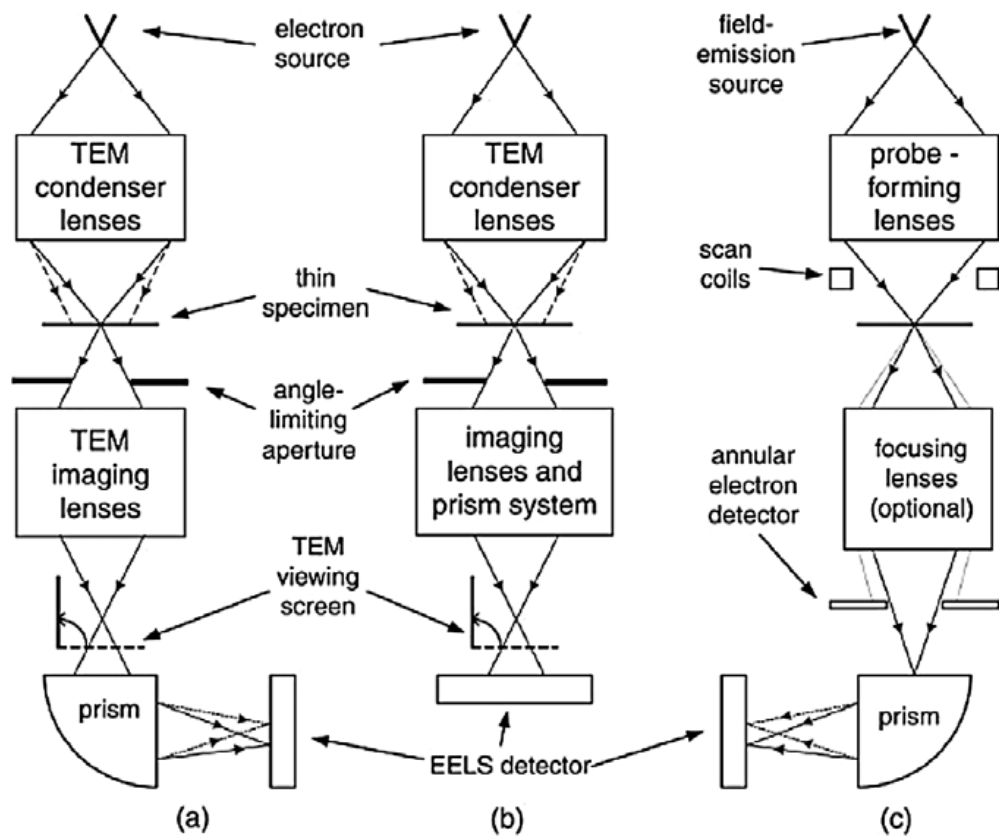


FIGURE 2.5: Standard procedures for EELS acquisition in TEM (A) TEM with a magnetic-prism spectrometer below the viewing screen, (B) TEM incorporating an in-column imaging filter and (C) scanning-transmission (STEM) system (Egerton, 2009).

predominant feature is the ZLP due to the combination of both elastic scattering and phonon scattering. The energy-loss of phonon scattering is so low that it is almost impossible to resolve in conventional spectrometers (Baden et al., 1981) and only very recently highly stabilized spectrometers with energy resolution <30 meV have become available (Krivanek et al., 2013). In recent years, phonon extraction from ZLP has been proposed (Egoavil et al., 2014) by either subtracting or dividing the modelled ZLP to the experimental spectra. The ZLP is mostly forward scattered and very intense so sometimes it tends to saturate the CCD due to its high intensity. The other prominent feature in the low-loss range is the plasmon loss as shown in fig. 2.6. This is

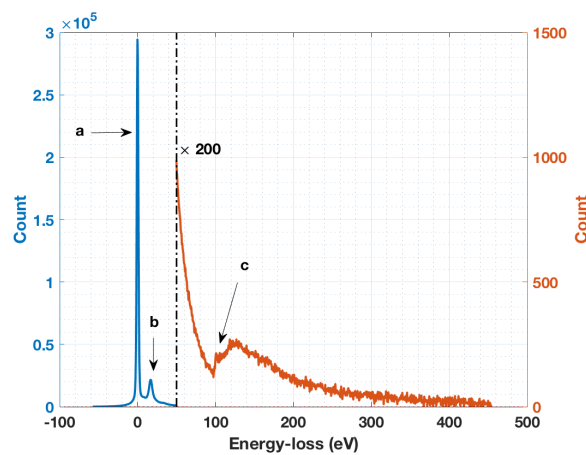


FIGURE 2.6: A low-loss electron energy-loss spectrum of polycrystalline Si. a) ZLP b) bulk plasmon peak c) Si $L_{2,3}$ ionization core-loss edge on top of exponential decaying background. Experimental conditions: voltage = 197 kV, dispersion = 0.5 eV per channel, spectrum offset = 0 eV, exposure time = 0.1 s.

due to polarisation of the material by the passing high-energy electrons. The typical range of energy-loss of bulk plasmon peaks is from 1 eV to ~ 30 eV (Williams et al., 1996). Multiple bulk plasmon losses can occur if the sample is thicker. Also surface plasmons in very thin films can occur (Scholl et al., 2012). Since the surface plasmon effects are only due to polarisation on surface. Hence it is a 2D effect unlike bulk plasmon which is due to bulk material (3D). This also mean the location of surface plasmon can be approximated if bulk plasmon is known. i.e. $E_p \approx E_s \times \sqrt{2}$. The peak of a plasmon shifts with respect to the dielectric properties of the material and the complex dielectric constant can be extracted from the single scattering distribution via Kramers–Kronig transform. The study of bulk plasmon peaks is important in the study of shifts in bulk plasmons rather than actual peak positions in alloy (Williams et al., 1996). The change in peak position with respect to composition, x , can be modelled as shown in eqn. 2.1. Where, x , is the composition ratio in an

alloy.

$$E_p(x) = E_p(x=0) + x \cdot \left(\frac{dE_p}{dx} \right) \quad (2.1)$$

The peak position of the bulk plasmon can be interpolated by least squares fittings as was proposed by Hunt et al., (1995). The ELNES provides the bonding information which can be used to calculate chemical shifts (Kimoto et al., 1997; Mayer et al., 1996; Reimer, 1995; Wang et al., 2018) and the maps of these shifts can be obtained (Thomas et al., 1999a, 2001a; Walther et al., 1995), whereas the EXELFS provides the diffraction effects surrounding the ionized atom due to excess energy of the ionized electron. In the high-loss region EEL spectra have a background that is decaying almost exponentially. The core-loss edges superimposed on this background can be extracted and the influence of multiple plasmon scattering can be removed by Fourier-based deconvolution (Thomas et al., 1999b, 2001b) with the low-loss function, yielding single scattering distribution. The extracted core-losses can be mapped to obtain relative concentration maps (Cooper et al., 2011; Muller et al., 2008) or absolute atomic density distribution maps (Colliex et al., 1994; Colliex et al., 2010; Pennycook et al., 2011).

2.3 EELS quantification

EELS has become a standard tool for identification and sometimes also quantification of chemical elements in materials science. It is important for understanding the chemical and/or structural composition of natural or processed materials. The elemental quantification in high-loss spectra is based on ionization core-losses superimposed on an approximately exponentially decaying background. The net ionization edges can be extracted by modeling the background in the pre-edge region below the ionization threshold by an inverse power-law function (eqn. 2.2) or an exponential decay function (eqn. 2.3) and then subtracting an extrapolated background from the post-edge region.

$$f(E) = AE^{-r} \quad (2.2)$$

$$f(E) = \sum_{j=1}^k \begin{bmatrix} A_1 \\ \cdot \\ \cdot \\ A_j \end{bmatrix} \exp \left(- \begin{bmatrix} r_1 \\ \cdot \\ \cdot \\ r_j \end{bmatrix} E \right) \quad (2.3)$$

where A_j and r_j are fitting parameters with a constraint that $r_j \geq 0 \forall j$. The value of k decides the number of exponentials used in the background modelling (most studies use only $k = 1$). The residual spectrum after subtracting the modelled background contains the ionization core-loss intensity (I) integrated from edge onset over a window (Δ). The absolute quantification of EELS core-loss edges (areal densities x in number of atoms/nm²) without considering plural scattering is shown in eqn. 2.4 for a given collection semi-angle (β).

$$x = \frac{I(\beta, \Delta)}{I_0(\beta)\sigma(E, E_0, \beta, \Delta)} \quad (2.4)$$

where I_0 is the intensity of the elastic peak. If the effect of plural scattering is large due to sample thickness and the absolute quantification can only be approximated without removing plural scattering by eqn. 2.5. Low-loss, I_{low} , is integrated over a window of Δ eV to compensate for the redistribution of the core-loss intensity.

$$x \approx \frac{I(\beta, \Delta)}{I_{low}(\beta, \Delta)\sigma(E, E_0, \beta, \Delta)} \quad (2.5)$$

In a spectrum, relative quantification can be performed by calculating atomic percentages (at.%). For example, if pure GaAs is being quantified then we know that Ga should make up 50 at.% and As 50 at.% . Generally, EELS quantification can be done using two procedures:

- background subtraction methods (Egerton, 1978),
- multiple linear (or non-linear) least-squares fitting methods. (Door et al., 1995; Shuman et al., 1987; Steele et al., 1985; Wang et al., 1992)

In background subtraction methods, the x from eqn. 2.4 is calculated from the residual spectrum after background subtraction with a differential cross-section known from theory or experiment. In multiple linear least-squares (MLLS) fitting (Hofer et al., 1993; Thomas et al., 2012), x is estimated by fitting the theoretical differential cross-section calculated from either Hartree-Slater or hydrogenic models or experimental calibration (model) spectra to the spectrum, along with a modelled background. The model used for the calculation of the integrated cross-section are taken from Egerton, (1989) as shown in eqn. 2.6.

$$\sigma(E, E_0, \beta, \Delta) = \frac{4a_0^2 R^2}{ET} \cdot f(\Delta) \cdot \left[\ln \left(1 + \beta^2 / \bar{\theta}_E^2 \right) + G(\beta, \gamma, \bar{\theta}_E) \right] \quad (2.6)$$

$$T = \frac{E_0 (1 + E_0/2m_0c^2)}{(1 + E_0/m_0c^2)} \quad (2.7)$$

$$\gamma = 1 + \frac{E_0}{m_0c^2} \quad (2.8)$$

where R is the Rydberg energy, a_0 is Bohr radius, $\bar{E} = [E_c(E_c + \Delta)]^{1/2}$ is the mean energy-loss in the energy range of integration for an ionization edge (E_c), E_0 is the kinetic energy of the incident electrons, m_0 is electron rest mass and $\bar{\theta}_E = \bar{E}/(2\gamma T)$ is the characteristic scattering angle. $f(\Delta)$ is the integrated oscillator strength and its calculations depends on the atomistic models (Reilman et al., 1979; Saloman et al., 1988) and $G(\beta, \gamma, \bar{\theta}_E)$ is the retardation term and is given by eqn. 2.9, where ν is the velocity of the electron. The retardation term has maximum effect when $\beta \approx \theta_E$.

$$G(\beta, \gamma, \bar{\theta}_E) = 2 \ln \gamma - \ln \left(\frac{\beta^2 + \theta_E^2}{\beta^2 + \theta_E^2/\gamma^2} \right) - \frac{\nu^2}{c^2} \left(\frac{\beta^2}{\beta^2 + \theta_E^2/\gamma^2} \right) \quad (2.9)$$

In this thesis, the theoretical cross-section is calculated by numerically differentiating the eqn. 2.6 with respect to E . The conventional method of quantification by manually selecting a pre-edge region to extract ionization edges is exhaustive and leads to inconsistency for thousands of spectra. State-of-the-art software tools like Hyperspy (de la Peña et al., 2017b), Cornell Spectrum Analyser (CSI) (Cueva et al., 2011, 2012; Hovden et al., 2013), EELS-Model (Bertoni et al., 2006, 2008; Verbeeck, 2015; Verbeeck et al., 2004, 2006, 2008a,b) and Gatan DigitalMicrograph™ (Gatan, 2015) remove such inconsistency partly by applying manually selected quantification routines to entire EELS SI data sets. Similarly, a model-based approach to EELS quantification has been presented by Verbeeck et al., (2004). The quantification parameters of the experimental data for the EELSMODEL software have been discussed by Verbeeck et al., (2008b). These authors later discussed standard-less quantification of EELS, which they claim provided better results (Verbeeck et al., 2008a). None of these software packages, however, detects an ionization edge and quantifies it automatically without any human intervention: Hyperspy can perform an independent component analysis (ICA) (de la Peña et al., 2011) but the physical interpretation of the statistically significant components in terms of element-specific core-losses still needs to be provided by the user for any type of multivariate statistical analysis (Trebbia et al., 1996). A multivariate analysis approach of end member hyperspectral unmixing using Bayesian linear unmixing (BLU) was proposed by Dobigeon et al., (2012). Both BLU and ICA algorithms need to know the number of

end member. i.e. number of ionization core-loss edges in the high-loss spectra. Principle component analysis (PCA) (Härdle et al., 2012; Ilin et al., 2010; Jackson, 1991; Krzanowski, 2000) was used to get an initial guess of number of ionization edges by observing variance plot (de la Peña, 2010; Spiegelberg et al., 2017a). DigitalMicrograph™scripts such as Oxide Wizard (Yedra et al., 2014) typically work on the basis of the user first assigning regions of interest and identifying edges manually, which the algorithm can then track and quantify in similar spectra of larger data sets. The aim is to subtract the EELS background and provide elemental maps and profiles of thousands of spectra in an extended SI without any prior knowledge of the ionization edges. Noise and/or spikes due to X-rays or read-out errors of individual detector pixels in the spectrum can lead to false positive detection of ionization edges. Before proceeding to the quantification process, it is therefore important to pre-process the spectrum.

2.4 Core-loss pre-processing

The noise in a spectrum arises due to a combination of low electron count numbers and read-out noise of the CCD camera (Ishizuka, 1993). A further problem arises as the detector point spread function (PSF) blurs the resulting shot noise over several adjacent pixels so it is often not directly apparent. The objective is to detect and quantify the core-loss edges after the acquisition of the spectrum image in the presence of noise. The noise in the spectra is a mixture of Poisson noise (or shot noise) and Gaussian noise (de la Peña, 2010). The ionization cross-section decreases with increasing energy-loss. As the signal-to-noise ratio (SNR) decreases with energy-loss, the intensity of high-loss ionization edges becomes comparable to the noise level. This emphasises the necessity of preprocessing signals before calculating the gradient of the spectra. An averaging filter is always inefficient (Boyle et al., 1988; Davies, 2012; Justusson, 1981) as it does not consider the type of noise and spikes (or pulses) are not completely removed (fig. 2.7). The number of spectral channels selected as filter width, w , influences the residual noise after smoothing but will also suppress the core-loss signal to some degree, in particular for sharp edges. An averaging filter gives good noise suppression when multiple spectra are averaged, providing a collective representative spectrum with reduced noise. PCA is a form of multivariate analysis, using orthogonal eigenfunctions (Fukunaga, 2013; Jolliffe, 2002; Lichtert et al., 2013; Manly et al., 2016; Pearson, 1901; Potapov, 2016). A multivariate

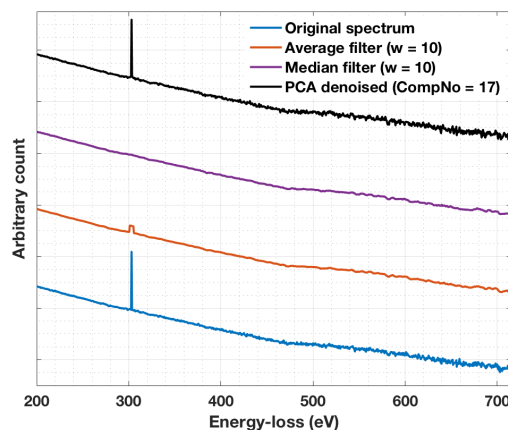


FIGURE 2.7: Comparison of noise suppression methods applied to an EEL spectrum. The term w describes the width (in pixels) of the filter mask. PCA is not effective in suppressing spike noise as the reconstruction of spectrum based on first 17 significant components (shown at the top) still contains noise. The median filter works best.

analysis tool (simply called `pca()` function in Matlab R2017b) has been used to analyse datasets in an unsupervised manner. The dataset in this case is the SI. The components of the PCA are spectral components ranked in order of significance. The lower order components with high local variance represent all the components needed to describe most features of the spectrum apart from the noise (low variance because it is present in all channels and everywhere). Hence, PCA can in principle be used for denoising the spectrum, and a Poisson-weighted PCA algorithm that properly accounts for the variance in shot noise has been used to reduce noise in Time-of-Flight Secondary Ion Mass Spectrum images (Keenan et al., 2004). Spiegelberg et al., (2017b) have proposed the singular value decomposition (SVD) to remove noise from EELS spectra and to estimate the background. Although the authors suggest that this should be applied as the last step after all the noise removing algorithm have been applied. If the noise is Poissonian however, a morphological filter such as a median filter is the most effective way of improving the SNR (Ataman et al., 1980), as shown in fig. 2.7. In 2D (images), a median filter has been proven to be best filter in case of ‘salt and pepper noise’, which corresponds to Poisson noise in images (Ahmad et al., 1987; Lim, 1990; Perreault et al., 2007; Pratt, 2007). Here, it preserves the shape of the spectrum. Fig. 2.7 shows the performance of different filters in terms of removing an artificial spike in a spectrum with a delayed In $M_{4,5}$ edge from

InGaAs. As the SNR is decreasing with energy almost exponentially, a median filter is chosen as defined in eqn. 2.10.

$$S'(E) = \exp(\text{median}(\ln([S_{i-w}, \dots, S_{i+w}]))) \quad (2.10)$$

where S is the spectrum, w is a window over which the median filter is applied. In the following, all spectra were median filtered first to help identify the core-loss edges, then the quantification routines for background fit, extrapolation and signal integration were applied to the unfiltered spectra. Median filtering will not remove noise due to CCD gain variations. This can lead to false positive identification of apparent ionization edges. If the pre-processing is needed only to remove spikes arising due to dead pixels in the CCD detector of the spectrometer, a good outlier identifying filter can be used. A hampel identifier (Liu et al., 2004; Suomela, 2014) uses median absolute deviation to identify outliers and replaces the outlier with the median value as shown in eqns. 2.11-2.14.

$$S = \{s_1, s_2, \dots, s_n\} \quad (2.11)$$

$$m_i = \text{median}\{s_{i-w}, s_{i-w+1}, s_{i-w+2}, \dots, s_i, \dots, s_{i+w}\} \quad (2.12)$$

$$\sigma_i = \kappa \cdot \text{median}\{|s_{i-w} - m_i|, \dots, |s_i - m_i|, \dots, |s_{i+w} - m_i|\} \quad (2.13)$$

$$\kappa = \frac{1}{\sqrt{2} \text{erfc}^{-1} 1/2} \approx 1.4826 \quad (2.14)$$

Given a spectrum of S , a local median (m_i) in a window (w) and standard deviation (σ_i) are calculated. The σ_i/κ parameter is called median absolute deviation. If a pixel in the spectrum $|s_i - m_i| > n_\sigma \times \sigma_i$, then it will be considered as an outlier and will be replaced with a local median, m_i . Usually, the value of n_σ will be 3, which indicates the threshold for an outlier as 3 times the standard deviation, $3 \times \sigma_i$.

2.5 Modelling plural scattering

The residual spectrum after background subtraction includes systematic error at higher losses from the edge onset. Hence using a large integration range (Δ) will affect the quantification of EELS. But using a small integration range means that the quantification is strongly affected by statistical errors. Hence, there has to be a trade-off in using an optimal integration range (Δ). The quantification ($N_{(\text{at.}\%)}$) of EELS for a give collection semi-angle (β)

by background subtraction is a function of integration range, as shown in eqn. 2.15. While calculating relative quantification, if the integration ranges for two edges to be compared are not the same (for eg. Δ_A & Δ_B), then each residual spectrum is affected by different statistical errors as well as the effects from the plural scattering.

$$N_A \text{ (at.\%)} = \frac{\frac{I_A(\Delta_A)}{\sigma_A(\Delta_A)}}{\frac{I_A(\Delta_A)}{\sigma_A(\Delta_A)} + \frac{I_B(\Delta_B)}{\sigma_B(\Delta_B)} + \dots + \frac{I_n(\Delta_n)}{\sigma_n(\Delta_n)}} \times 100 \quad (2.15)$$

The incident beam that scatters inelastically can be modelled by assuming electrons undergo collisions independently. The probability, $P(n, t/\lambda)$, of a number of inelastic scattering events (n) by an electron is given by the Poisson equation in eqn. 2.20 where t is the thickness of the sample, λ is the mean distance between successive inelastic scattering events (inelastic mean free path for inelastic scattering) and is given by eqn. 2.16.

$$\lambda \approx \frac{106F(E_0/E_m)}{\ln(2\beta E_0/E_m)} \quad (2.16)$$

$$E_m \approx 7.6Z_{eff}^{0.36} \quad (2.17)$$

The atomic fraction, f_i , of an atomic number, Z_i , is used to calculate the effective atomic number, Z_{eff} as defined by eqn. 2.18.

$$Z_{eff} \approx \frac{\sum_i f_i Z_i^{1.3}}{\sum_i f_i Z_i^{0.3}} \quad (2.18)$$

The λ calculation is approximated by Malis et al., (1988), where F is the relativistic factor defined by eqn. 2.19.

$$F = \frac{1 + E_0/1022 \text{ keV}}{(1 + E_0/511 \text{ keV})^2} \quad (2.19)$$

Hence t/λ is the mean number of inelastic collisions by an electron through the specimen. The probability, $P(n, t/\lambda)$, can also be defined as the ratio of total intensity of n -fold inelastic scattering (I_n) to the total intensity of the spectrum (I_t) as shown in eqn. 2.20.

$$P\left(n, \frac{t}{\lambda}\right) = \frac{I_n}{I_t} = \left(\frac{1}{n!}\right) \left(\frac{t}{\lambda}\right)^n \exp\left(-\frac{t}{\lambda}\right) \quad (2.20)$$

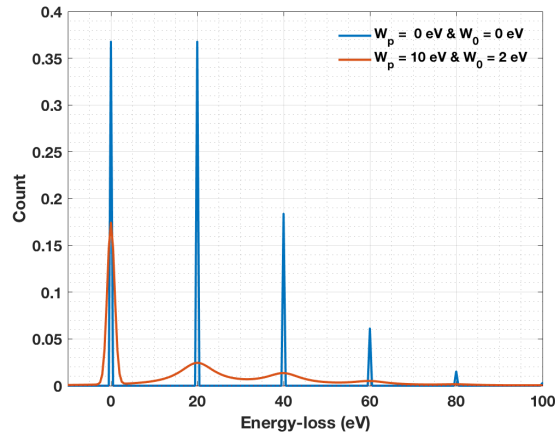
Hence, as the thickness of the sample increases the intensity is redistributed from the edge onset to higher energies according to Poissonian statistics. A

simulated low-loss spectrum is shown in fig. 2.8(A) with plasmon peak (E_p) at 20 eV, plasmon width (W_p) of 0 eV (in blue) & 10 eV (in orange) and zero-loss width (W_0) of 0 eV (in blue) & 2 eV (in orange) as an example. As can be observed from eqn. 2.20, as t/λ increases the multiple plasmons start becoming more dominant. This is replicated in higher losses as a convolution with the low-loss spectrum. As higher order plasmons become dominant, the intensity at ionization edge onset is shifted to higher losses as it is evident in fig. 2.8(B). The integration range (Δ) affects the quantification as the intensity is shifted. Fig. 2.8(C) demonstrates the reduction in intensity for lower Δ ranges. The plural scattering will also affect the background modelling for the consecutive ionization edges. Hence, the following points have to be considered for quantification,

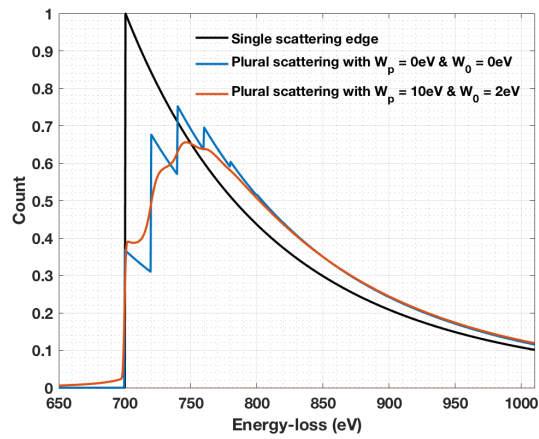
- Using same integration range (Δ) for all the core-loss edges. It is worth noting that all the theoretical cross-section models such as Hartree-Slater and/or Hydrogenic models assume single scattering distribution. Hence, using the same integration range would systematically avoid errors in relative quantification.
- Using large integration ranges of at least $5 \times E_p$ for all the core-loss edges. Plural scattering redistributes the intensity close to the edge onset towards higher energy, but the total integrated intensity will remain unchanged, and the effects from higher order multiple plasmons are typically very low. This approach has disadvantage of a large systematic error while integrating the residual spectrum due to the extrapolation of the background to higher energy.
- Using deconvolution methods (Verbeeck et al., 2009) such as Fourier-log (Johnson et al., 1974), Fourier-ratio deconvolution (Egerton et al., 2008) methods. These methods recover the single scattering distribution of the spectrum through deconvolution with low-loss (a spread function). Richardson-Lucy (RL) deconvolution method (Biggs et al., 1997) is explored in high-loss region later in section 4.4.

2.6 Fourier-ratio deconvolution

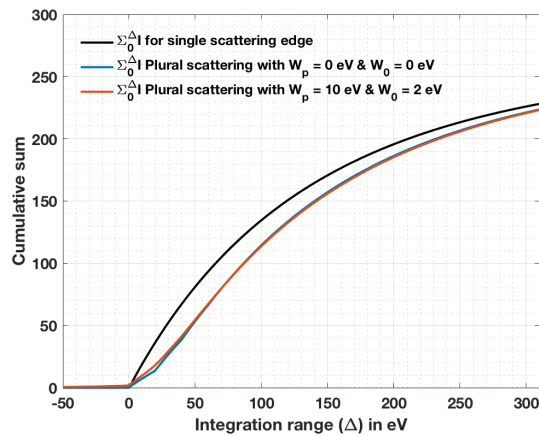
Fourier-ratio deconvolution is a standard method of deconvolution in signal processing. From a spectrum with plural scattering, $S_{PSD}(E)$, the single



(A)



(B)



(C)

FIGURE 2.8: (A) Two models of low-loss spectrum of plasmon location, $E_p = 20$ eV. (B) Simulated hydrogenic model of single scattering core-loss ionization edge and its plural scattered version with respect to low-losses modelled in (A). (C) Cumulative sum of intensity as a function of integration range (Δ).

scattering distribution, $S_{SSD}(E)$, can be retrieved as shown in eqn. 2.21.

$$S_{SSD}(E) = \mathcal{F}^{-1} \left\{ \frac{\mathcal{F}\{S_{PSD}(E)\}}{\mathcal{F}\{S_{PSF}(E)\}} \right\} \quad (2.21)$$

The notation \mathcal{F} and \mathcal{F}^{-1} indicate Fourier and inverse Fourier transform operator, respectively. $S_{PSF}(E)$ is a low-loss spectrum with its total intensity normalised to unity. This ensures conservation of total intensity as discussed in eqn. 4.10. Fourier-ratio method heightens noise. This is because the values of high frequency Fourier coefficients are low in the denominator. Care should be taken that values in the denominator are not exactly 0. Hence an extremely small offset ($\sim 1 \times 10^{-10}$ or even lower) is commonly added to the denominator to avoid division by 0. The amplified noise can be suppressed by re-convolving the Fourier-ratio with a smoothing kernel, $R(E)$, such as a Gaussian or the ZLP peak itself, as shown in eqn. 2.22. Sometimes this may not sufficient. a modulus operator is applied to bring any negative values to > 0 .

$$S_{SSD}(E) = \mathcal{F}^{-1} \left\{ \mathcal{F}\{R(E)\} \cdot \left[\frac{\mathcal{F}\{S_{PSD}(E)\}}{|\mathcal{F}\{S_{PSF}(E)\}| + \text{constant}} \right] \right\} \quad (2.22)$$

The spectrum must be extrapolated to avoid kinks. Hence a Hann window as described in eqn. 4.13 or an inverse power law extrapolation can be applied. The length of extrapolation does not affect the ringing artefact as long as the left and right side of the spectrum are at same level (≈ 0). Many implementations of the fast Fourier transform (FFT) the length of the spectrum must be a power of 2. A Fourier transform is implemented in most software package as an FFT, which uses vectorised versions of butterfly diagrams. An FFT is usually referred to as N -point FFT.

$$N = 2^n \quad \forall n \in \mathbb{N}^+ \quad (2.23)$$

If the length of the spectrum is not equal to N , then by default some routines pad zeros to make the length of the spectrum meet the next largest power of 2 criterion. But padding zeros would introduce a sharp kink in the spectrum which is equivalent to a *sinc* function (ripples) in frequency domain. Hence, whenever extrapolating, the extrapolation must be carried out to make the length equal to N and try to minimise kinks in the spectrum. This has been implemented by Egerton, (2011a) as `Frat()` routine¹.

¹Egerton, (2011a)'s `Frat` routine uses inverse cosine function as shown in eqn. 4.13 for extrapolation to a length N .

2.7 Fourier-log deconvolution

As the thickness of the sample increases the effect of plural scattering increases as per eqn. 2.20. This implies that higher multiple bulk plasmons become more prominent in the low-loss spectrum. In typical (S)TEM the effect of multiple bulk plasmons becomes prominent up to as high as $5 \times E_p$ in energy-loss. Any core-losses that are present at low-losses are difficult to quantify due to the fact that the background is not monotonic. Hence, a single scattering low-loss spectrum is needed to extract and analyse the core-losses. Johnson et al., (1974) proposed the Fourier-log deconvolution method² as shown in eqn. 2.24.

$$S_{SSD}(E) = \mathcal{F}^{-1} \left\{ \mathcal{F}\{R(E)\} \cdot \ln \left[\frac{\mathcal{F}\{S_{PSF}(E)\}}{\mathcal{F}\{Z_0(E)\}} \right] \right\} \quad (2.24)$$

where the $Z_0(E)$ is the extracted ZLP from $S_{PSF}(E)$. $Z_0(E)$ is extracted until the minimum point (E_k) between the ZLP and the first plasmon of the $S_{PSF}(E)$, then the right tail is extrapolated by an inverse power-law function. Instead of extracting from $S_{PSF}(E)$, $Z_0(E)$ can be also be simulated as a Gaussian function, $\mathcal{N}(E, 0, W_0)$, with full width at half maximum (FWHM), W_0 , same as the ZLP in $S_{PSF}(E)$. The Gaussian can be scaled to the intensity of ZLP (I_0) of $S_{PSF}(E)$, works only if the ZLP is symmetric, i.e. in case of low-loss acquired in monochromator, as shown in eqn. 2.25.

$$\int^{E_k} S_{PSF}(E) = \int^{E_k} Z_0(E) = I_0 \cdot \int^{E_k} \mathcal{N}(E, 0, W_0) \quad (2.25)$$

The log-ratio term in eqn. 2.24 calculates the single scattering distribution. But due to the presence of Fourier coefficients that are close zero, the noise is heightened. Hence, one needs to re-convolve the log-ratio with a smoothing function $R(E)$. The re-convolving function can either be a Gaussian kernel or the ZLP itself, $Z_0(E)$. If the re-convolving function, $R(E)$, is normalised to unity then the intensity is preserved, as in case of eqn. 4.10. If the intensity of $Z_0(E)$ is not normalised. The resulting single scattered distribution is absolutely quantified. The removal of kinks and the extrapolation must be carried out similar to Fourier-ratio deconvolution method described in section 2.6.

²Similar to Frat, Egerton, (2011a)'s routine for Fourier-log deconvolution is `Flog`. The uses same methods for extrapolation.

2.8 Angular convergence correction

The deconvolution methods discussed in section 2.5 assume that all the intensity is captured by the spectrometer CCD. However, this is not the case. The detected intensity is limited by a finite collection semi-angle (β). The systematic study by Egerton et al., (1990), which showed the effects of β on obtaining single scattering distribution and hence quantification of EELS. If the angular spread defined by the convergence semi-angle (α) is limited by a collection semi-angle (β) even more intensity is not recorded by the spectrometer CCD. A correction factor, F_1 , can be calculated from the ratio of intensity of spectrum $I(\alpha, \beta, \Delta)$, with an α comparable with β , and intensity of spectrum $I(0, \beta, \Delta)$ where $\alpha \approx 0$ or $\beta \gg \alpha$. With the help of Scheinfein et al., (1984), the ratio can be solved analytically³ as shown in eqn. 2.26.

$$F_1 = \frac{I(\alpha, \beta, \Delta)}{I(0, \beta, \Delta)} = \frac{2/\alpha^2}{\ln[1 + (\beta/\theta_E)^2]} \int_0^\beta \ln \left[\frac{\psi^2 + (\psi^4 + 4\theta^2\theta_E^2)^{1/2}}{2\theta_E^2} \right] \theta d\theta \quad (2.26)$$

where θ_E is the characteristic scattering angle as defined in eqn. 2.27.

$$\theta_E \approx \frac{E_k + \Delta/2}{(\gamma m_0 \nu)} \quad (2.27)$$

$$\psi^2 = \alpha^2 + \theta_E^2 - \theta^2 \quad (2.28)$$

The F_1 is a function of characteristic scattering angle (θ_E), implying that it is a function of energy-loss. Hence, the correction factor is different for all core-loss edges. It is also worth noting that $F_1 \leq 1$ as $I(0, \beta, \Delta) > I(\alpha, \beta, \Delta)$. Hence elemental quantification ratio from eqn. 2.15 can be corrected as shown in eqn. 2.29.

$$N_1 \text{ (at.\%)} = \frac{\frac{I_1(\beta, \Delta_1)}{\sigma_1(\beta, \Delta_1) \cdot F_{1,1}}}{\sum_{j=1}^n \frac{I_j(\beta, \Delta_j)}{\sigma_j(\beta, \Delta_j) \cdot F_{1,j}}} \times 100 \quad (2.29)$$

For absolute quantification in eqn. 2.4, the convergence correction for low-loss and high-losses are different. Hence, another convergence correction, F_2 (eqn. 2.30), can be introduced for absolute quantification as shown in eqn. 2.31.

$$F_2 \approx \begin{cases} F_1, & : \alpha \leq \beta \\ (\alpha/\beta)^2 \cdot F_1, & : \alpha \geq \beta \end{cases} \quad (2.30)$$

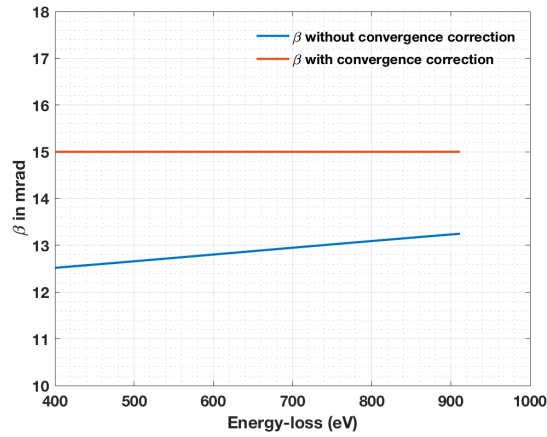
³The routine for calculating the correction factors F_1 , F_2 and β^* is Concor2 (Egerton, 2011a).

$$X = \frac{I(\beta, \Delta)}{I_0(\beta) \cdot \sigma(\beta, \Delta) \cdot F_2} \quad (2.31)$$

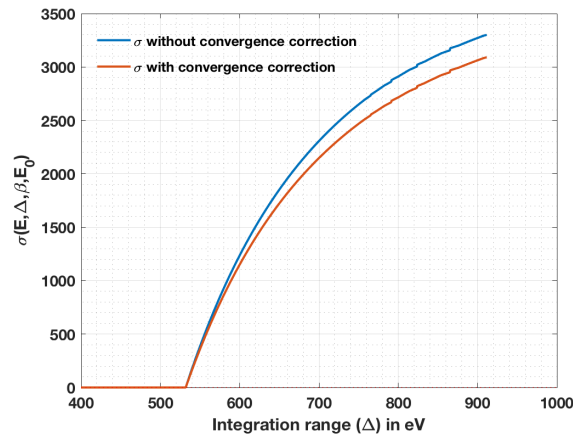
In eqn. 2.29, the term $\sigma(\beta, \Delta) \cdot F_1$ can be treated as the correction to theoretical cross-section rather than to the intensity. Hence, an effective collection semi-angle $\beta^*(E)$ can be used as a correction to the collection semi-angle as shown in eqn. 2.32.

$$\sigma_A(\beta^*, \Delta) = \sigma_A(\beta, \Delta) \cdot F_{1A} : \beta^* < \beta, \forall \alpha \gtrsim \beta \quad (2.32)$$

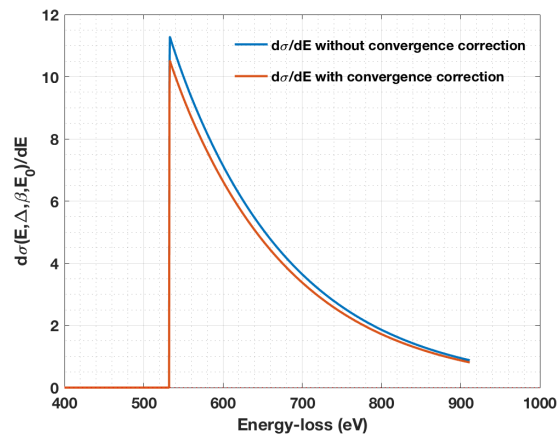
This is useful in linear least-squares fitting as correction by lowering the β of theoretical cross-section, increasing the fitting precision. This correction is effectively increasing the collection semi-angle of the spectrum. Figs. 2.9(A–C) demonstrate the values of β^* , convergence corrected integral, $\sigma(E, \Delta, \beta^*, E_0)$, and differential $(\frac{\partial}{\partial E}\sigma(E, \Delta, \beta, E_0))$ cross-sections for $\alpha = 16.6$ mrad and $\beta = 15$ mrad.



(A)



(B)



(C)

FIGURE 2.9: (A) Effective collection semi-angle correction for $\beta = 15$ mrad. (B,C) are the convergence corrected integrated cross-sections, $\sigma(E, \Delta, \beta^*, E_0)$, and differential cross-sections, $\frac{\partial}{\partial E}\sigma(E, \Delta, \beta^*, E_0)$ from hydrogenic model for O K edge at 532 eV.

Chapter 3

Automated ionization core-loss analysis

3.1 Introduction

The process of automated ionization edge analysis can be explained in two parts: ionization core-loss edge detection and background subtraction for quantification of individual ionization edges detected. The quantification of EELS used in this chapter follows the standard integration method (Egerton, 1978). To quantify a spectrum there are a lot of challenges in terms of artefacts, noise and gain correction problems of the CCD camera. Hence, a pre-treatment of spectra is necessary before the process of edge detection and background subtraction. If the background is exponentially decaying, there is no ionization edge and the SNR is high, then the gradient of a spectrum should be negative everywhere. As the spectrum is preprocessed, positive gradients indicate the presence of core-loss edges. A look-up table can be used to accurately identify the corresponding core-losses of the elements. An inverse power-law (eqn.2.2) or exponential decay function (eqn.2.3) will be used to fit a curve, $B(E)$, in the pre-edge region to fit, extrapolate and subtract the background. The extracted core-loss edges are used for further quantification using integration after background subtraction. All programming was performed in Matlab using the current version, R2017b (MathWorks, 2017). A spectrum $S(E)$ with ionization edges superimposed on a background modelled by $B(E)$ at higher losses as a function of energy-loss (E) and integration range (Δ) is shown in eqn. 3.1. I is the intensity and σ the ionization cross-section for the j^{th} shell of i^{th} element in the spectrum.

$$S(E, \beta, \Delta) = B(E) + \sum_{i,j} I_{i,j}(\beta, \Delta) \sigma_{i,j}(\beta, \Delta) \quad (3.1)$$

3.2 Detection of ionization core-loss edges

For automation of background subtraction, a novel approach of core-loss edge detection is proposed. For an EELS SI, $S(x, y, E)$, the gradient of SI can be defined as shown in eqn. 3.2.

$$\nabla \mathbf{S} = \left[\frac{\partial}{\partial x} \hat{x} + \frac{\partial}{\partial y} \hat{y} + \frac{\partial}{\partial E} \hat{E} \right] S(x, y, E) \quad (3.2)$$

where $\nabla \mathbf{S}$ is the gradient of the SI (data cube) with regard to spatial \hat{x} , \hat{y} directions and energy-loss direction \hat{E} . The gradient of the EELS SI, $S(x, y, E)$, in the direction of energy loss is determined by eqn. 3.3.

$$\nabla \mathbf{S} \cdot \hat{E} = \frac{\partial}{\partial E} S(x, y, E) \quad (3.3)$$

Numerically, a gradient is the central difference for the inner channels in the \hat{E} direction as shown in eqn. 3.4.

$$(\nabla \mathbf{S})_{E_n} \cdot \hat{E} = \frac{1}{2} \cdot \{S(x, y, E_{n+1}) - S(x, y, E_{n-1})\} \quad (3.4)$$

where $n \in \mathbb{N}_1 : 1 < n < N$ and $N \in \mathbb{N}$ is the number of channels (or length of the spectrum). The gradient of the spectrum at the end of channels are single sided differences as shown in eqn. 3.5 for $n = 1$ and eqn. 3.6 for $n = N$.

$$(\nabla \mathbf{S})_{E_1} \cdot \hat{E} = S(x, y, E_2) - S(x, y, E_1) \quad (3.5)$$

$$(\nabla \mathbf{S})_{E_N} \cdot \hat{E} = S(x, y, E_N) - S(x, y, E_{N-1}) \quad (3.6)$$

The gradient of EELS has to be negative for ranges beyond multiple plasmon losses and without any core-losses, falling asymptotically towards zero. The only points that are positive must be due to the presence of noise or ionization edges. If the EELS SI is denoised, the probability of a positive gradient being due to noise is low, although clearly dependent on the type of denoising method used. The angle (θ) between the EELS and horizontal energy axis is determined by eqn. 3.7 and can be plotted, as shown for an example spectrum of Si with C in fig. 3.1.

$$\theta = \arctan \left\{ \nabla \mathbf{S} \cdot \hat{E} \right\}, \quad -\frac{\pi}{2} < \theta < \frac{\pi}{2} \quad (3.7)$$

The arctan (a.k.a \tan^{-1}) function can bifurcate the gradients by flushing them

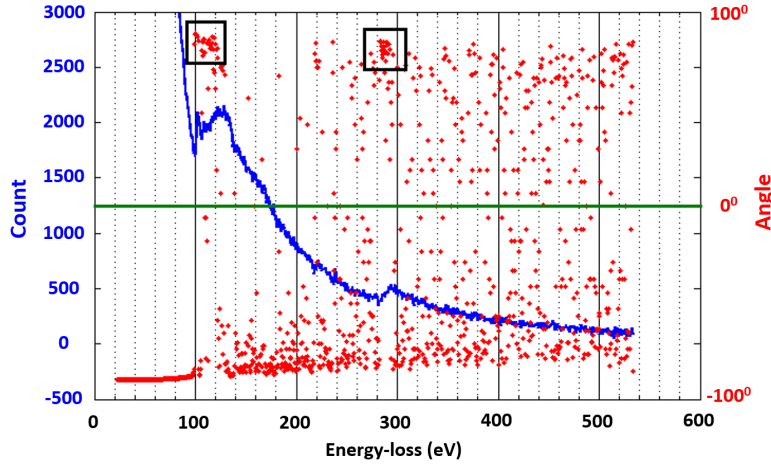


FIGURE 3.1: Original spectrum of Si $L_{2,3}$ edge and C K edge (in dark blue) and angle as defined in eqn. 3.7 (in red) showing the presence of clusters in the latter correlates with the onset of ionization edges.

far apart to $-\pi/2$ for background gradient and $\pi/2$ for gradient at edge onset making the detection more reliable. Only positive angles are considered further, as negative values are due to the background of EELS. A cluster of positive angles is formed if a core-loss edge is present. Positive angle values without a cluster are due to noise. A similar gradient approach of ionization edge detection by applying derivatives to log of spectrum was proposed by Kundmann et al., (1991) and was extended to EELS SI by Thomas, (2001). The algorithm had problems with sever heightened noise level, ELNES and EXELFS. Hence the it was unable to find the unique solution to the close by ionization edges.

3.2.1 Cluster detection by counting positive slope angles

Clusters are detected by counting the positive angular data points within a window, compared to the size of the window. The flow chart for the process implemented in Matlab is shown in fig. 3.2. The mod (or modulo operator) is defined in eqn. 3.8 (Knuth, 1973). If the length of the spectrum, $N \in \mathbb{N}$, is not a multiple of the size of the window, $w \in \mathbb{N}$, there will be a few pixels left at the end of last iteration. These reminder pixels, $r \in \mathbb{N}$, can be taken as window size at the end of the spectrum, or they can be ignored. But if the dispersion has been binned to a large value or the chosen window size is larger, then the reminder pixels should not be ignored.

$$r = N - w \cdot \left\lfloor \frac{N}{w} \right\rfloor \quad (3.8)$$

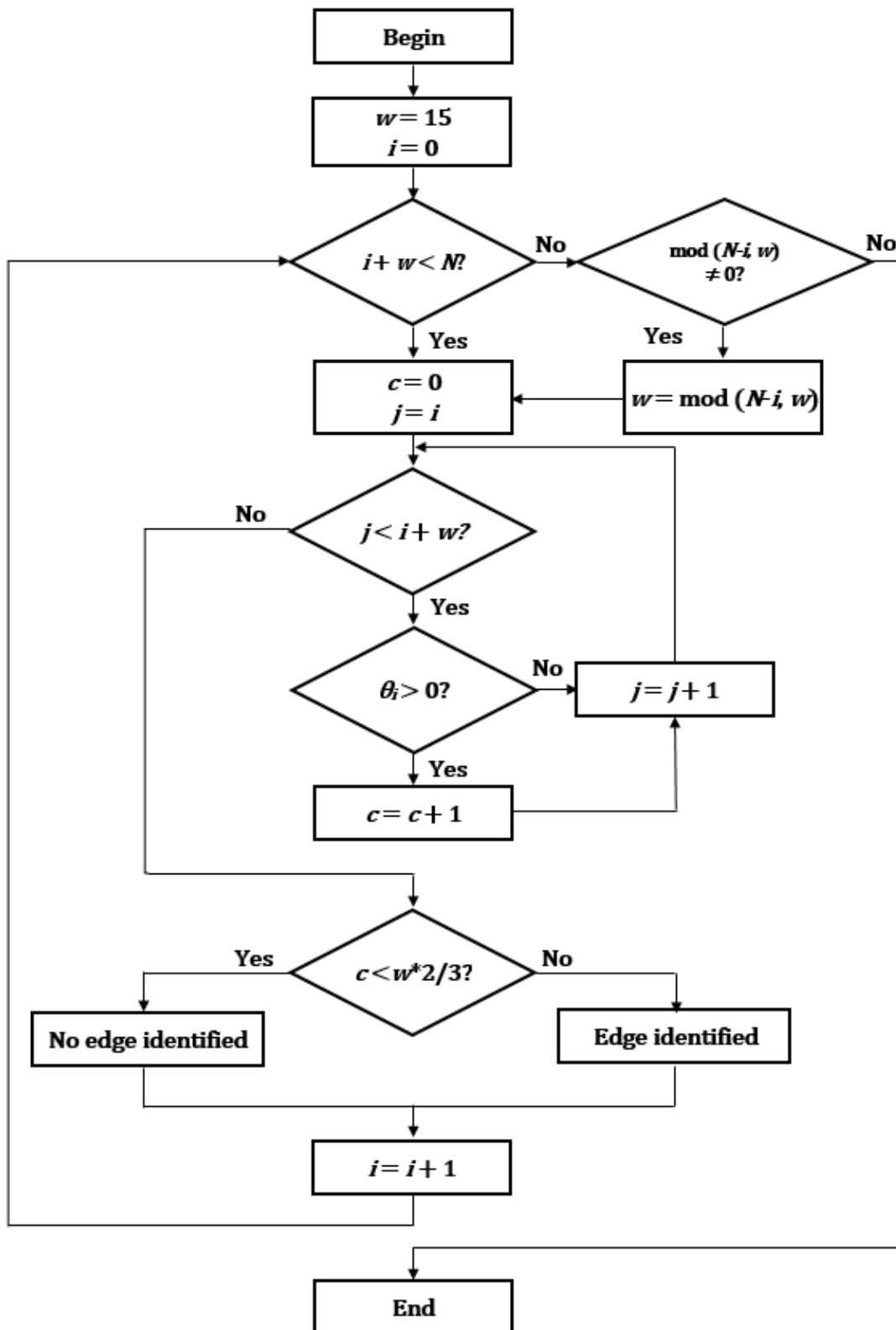


FIGURE 3.2: Flow chart for edge detection in spectra that consist of N channels. c is the count of channels with positive gradient, i is the energy channel, j is the loop count, w is the window width and mod is modulo operator (remainder after division).

The floored division operator $\lfloor \cdot \rfloor$ gives the integer part of $\frac{N}{w} \in \mathbb{R}$. The size of the window is chosen such that it should be comparable to the sharpness of the onset of typical edges (a few eV for sharp hydrogenic and up to 10 eV for delayed edges). Similarly, the window size should not be too small (< 5 channels), to avoid false positives due to noise. Typically, the window sizes selected in this study were between 5 and 25 channels wide (the default is $w = 15$), and clusters are identified as intervals of that given width wherein at least $2/3$ of all channels have angular values $\theta > 0$. Due to near edge structures or/and chemical shifts the edges detected may not be at the exact location of the ionization onset predicted for free atoms. It may also happen that 2 or 3 consecutive windows might detect positive angles. To refine the results from ionization edge identification, a look-up table is used containing onset values of some of the major ionization edges (Ahn et al., 1983; Egerton, 2011b) as shown in table 3.1¹. The exact edge onset is identified from the predicted edge positions (clusters) by finding the nearest ionization edge in the look-up table that agrees with position of the beginning of the window, as shown in eqn. 3.9:

$$Edge_i = E_{(\min||E_n - Cluster_i||)} \quad (3.9)$$

where E_n is the list of all n ionization edges from the look up table, $Cluster_i$ is the list of all predicted ionization edge onsets (numbered consecutively by index). The ionization edge detection and correction can be visualized as shown in fig. 3.3. Histograms of the detected edges in three different EELS SI

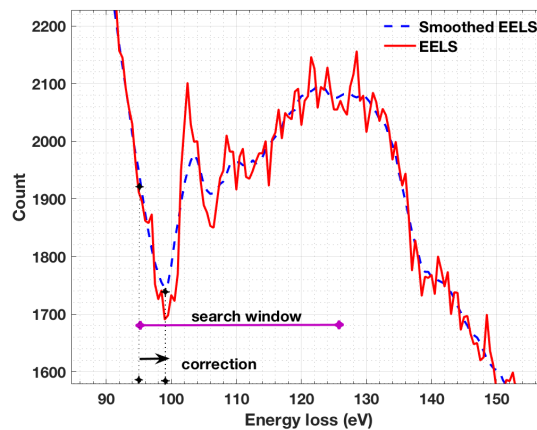


FIGURE 3.3: The location of core-loss (here: Si $L_{2,3}$ edge) is detected from the look-up table and fine-tuned to a value of 99 eV as per eqn. 3.9.

¹Note: The table only lists some of the major semiconductor ionization onsets. Due to anomalies in the CCD gain correction, some of the ionization onsets were wrongly detected. Hence few of the uncommon and semiconductor material were not considered.

TABLE 3.1: A look-up table used for edge detection.

Z	Edges	Onset in eV	Edge shape	Edge type
5	B K	188	<i>h</i>	K
6	C K	284	<i>h</i>	K
7	N K	400	<i>h</i>	K
8	O K	532	<i>h</i>	K
9	F K	685	<i>h</i>	K
13	Al K	1560	<i>h</i>	K
13	Al L ₁	118	<i>h</i>	L
13	Al L ₃	73	<i>d</i>	L
14	Si L ₃	100	<i>h</i>	L
15	P L ₁	189	<i>h</i>	L
15	P L ₃	135	<i>d</i>	L
16	S L ₁	229	<i>h</i>	L
16	S L ₃	165	<i>h</i>	L
17	Cl L ₁	270	<i>h</i>	L
17	Cl L ₃	200	<i>d</i>	L
19	K L ₁	377	<i>h</i>	L
19	K L ₃	294	<i>w</i>	L
29	Cu L ₃	931	<i>h</i>	L
30	Zn L ₃	1020	<i>d</i>	L
31	Ga L ₃	1115	<i>d</i>	L
32	Ge L ₃	1217	<i>d</i>	L
33	As L ₃	1323	<i>d</i>	L
47	Ag M ₅	367	<i>d</i>	M
49	In M ₅	443	<i>d</i>	M
65	Tb M ₅	1242	<i>w</i>	M

of a cross-sectioned multi-junction solar cell are shown in fig. 3.4. Although edge onset identification may fail in individual spectra due to noise the histograms clearly show that the identification of the edges is unambiguous when thousands of spectra from all locations in SI are considered. The efficiency of the edge detection is also dependent on the quality of the gain correction of the CCD. Long exposures of the ZLP might yield artefacts in successively acquired spectra due to gain changes induced by over exposures. This could potentially lead to false positive detection of ionization edges in EELS acquired with energy offsets. Such artefacts can, however, be identified by varying the energy offset as they remain fixed at that channel (usually around #100) where the ZLP had been placed before. A multi-junction solar cell is used for the detection and quantification of all the ionization core-losses using cluster detection thorough counting later in section 3.4.

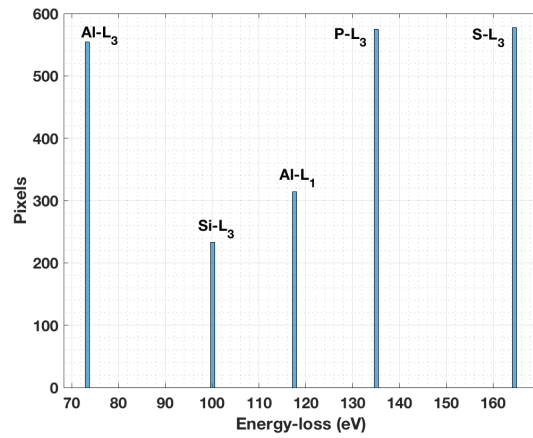
3.2.2 Cluster detection through peak detection

Another method of detecting the clusters is by predicting the kind of statistics these clusters exhibit. As discussed in subsection 3.2.1, the clusters are formed due to the presence of edge onsets and tend to have positive slope angles. All the negative values are due to the presence of strong background. This indicates that the mean value of the group of clusters is always higher than the rest of the pixels and can be detected by an overlapping sliding window of size $w \in \mathbb{N}$. The implementation of this algorithm is shown in fig. 3.5 as a flowchart. Unlike θ from eqn. 3.7, slope angles are calculated by estimating the exponent r from inverse power-law function (or exponent from exponential decay function) at each channel if the pre-edge region is already known (eqn. 3.11). The value of r is estimated as shown in eqn. 3.10.

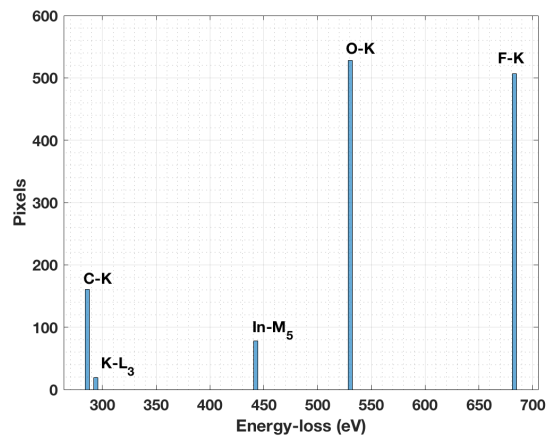
$$\hat{r}(E) \approx \frac{\nabla \mathbf{S} \cdot \hat{E}}{B(E)} \quad (3.10)$$

$$\theta = \arctan \{\hat{r}\}, \quad -\frac{\pi}{2} < \theta < \frac{\pi}{2} \quad (3.11)$$

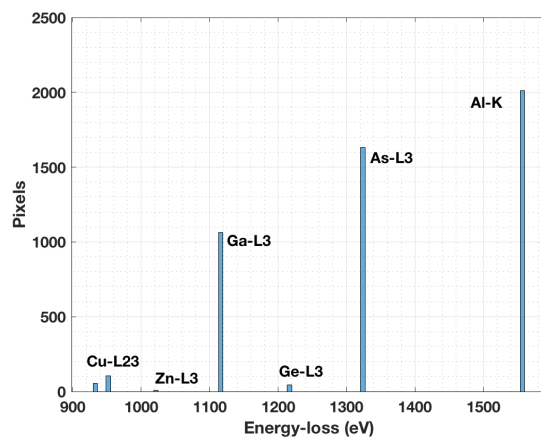
$\bar{\theta}$ can be viewed as the θ value smoothed over a window of w . It is important to apply a Hampel filter to remove single pixel noise which may be misinterpreted as an ionization edge prior to the above evaluation. Applying a Hampel filter ensures that θ values only contain features from core-loss edges. Consider the example of a spectrum as described in eqn. 3.1, with two ionization edges $\sigma_1(E, \beta)$ and $\sigma_2(E, \beta)$ and an inverse power-law function as



(A)



(B)



(C)

FIGURE 3.4: Histogram distribution of edge onsets detected for EELS SI from semiconductor heterostructure shown in fig. A.1 for 80 eV offset (A), 250 eV offset (B) and 950 eV offset (C). The edges are later identified in table 3.2.

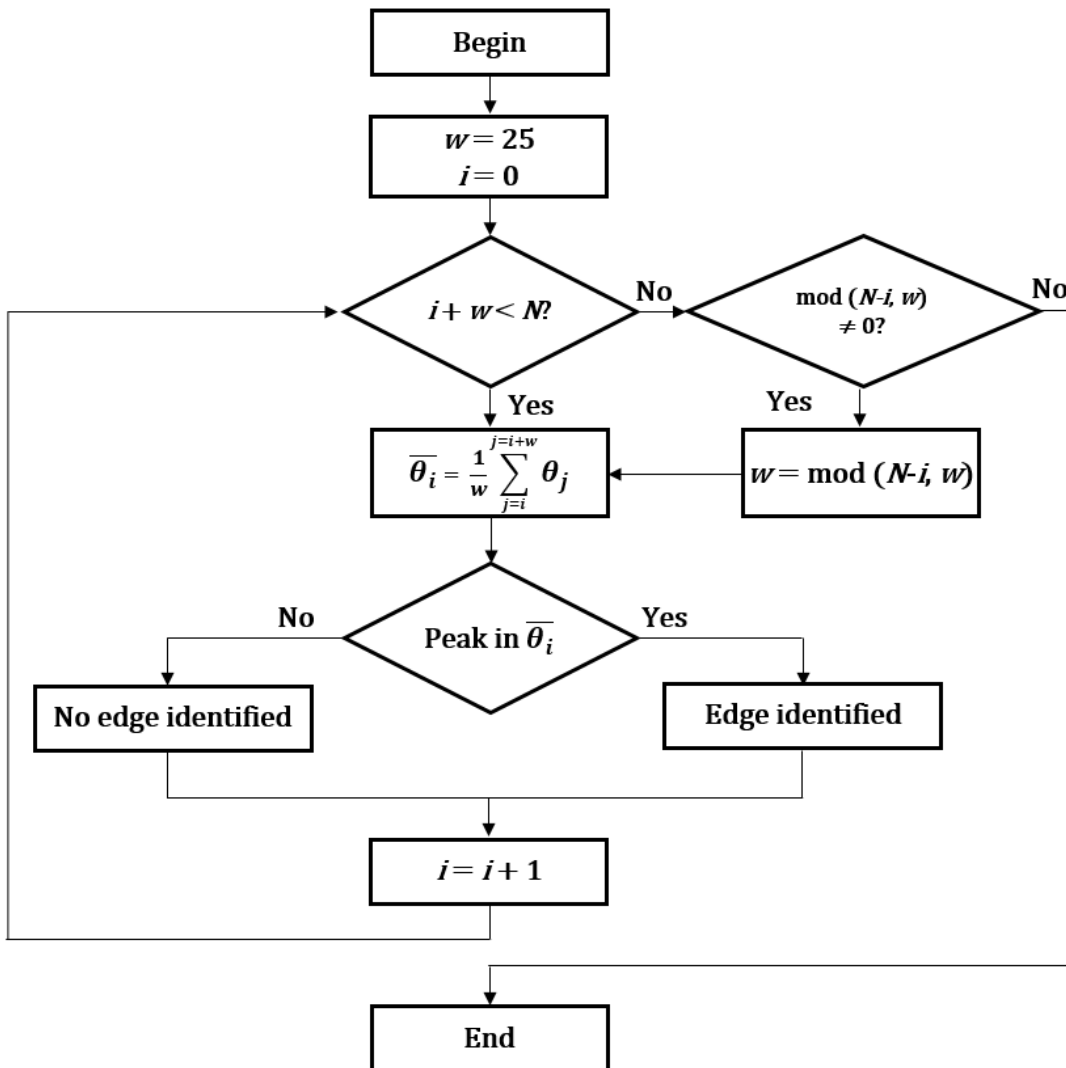


FIGURE 3.5: Flow chart for edge detection in spectra that consist of N channels. $\bar{\theta}_i$ is the mean value of angles, i is the energy channel, j is the loop count, w is the window width and mod is modulo operator (remainder after division).

a model for the background as described in eqn. 3.12.

$$S(E, \beta) = A \cdot E^{-r} + I_1 \cdot \sigma_1(E, \beta) + I_2 \cdot \sigma_2(E, \beta) \quad (3.12)$$

The term $-E^{-1}$ in eqn. 3.13 provides the baseline for $\hat{r}(E)$ and it is almost constant at high enough energy-losses. The term after the addition sign in eqn. 3.13 provides the features describing the edge onset as shown in fig. 3.6 and fig. 3.7. The r term is the exponent of the background of the spectrum, $S(E, \beta)$.

$$\hat{r}(E) \approx r \cdot -E^{-1} + A^{-1} \cdot E^r \left[I_1 \frac{\partial}{\partial E} \sigma_1(E, \beta) + I_2 \frac{\partial}{\partial E} \sigma_2(E, \beta) \right] \quad (3.13)$$

If there is no knowledge of pre-edge regions, then θ can be calculated as previously described in eqn. 3.7. The window size is typically chosen from $w = 5$ to 35. At each sliding window a mean value of slope angles $\bar{\theta}$ is calculated at each energy channel i . The window sliding is done one channel at a time. A similar technique of including residue channels in subsection 3.2.1 are incorporated using the `mod` operator. The position of falling edge of the peak in $\bar{\theta}_i$ is the nearest estimate of the onset of the core-loss ionization edge. The robustness of the technique can be studied by simulating a GaAs high-loss spectrum and applying the method described in fig. 3.5 with varying size of the sliding window (w), relative thickness (t/λ) and the noise level. A spectrum, $S(E, \beta)$, is simulated by an inverse power-law function (AE^{-r}) and the theoretical cross sections of Ga $L_{2,3}$ and As $L_{2,3}$ ². To test the effect of varying window size, w , a spectrum has been simulated with $t/\lambda = 0$ without noise. Fig. 3.6(C) shows that the position of the peak which indicates the ionization core-loss remains at the same position as the size of the window, w , is increased from 5 to 35 channels. However, the peak is broadened towards lower energy-loss with increase in w . This is because the window slides from left to right of the energy-loss axis. A similar effect of peak spreading towards higher energy-loss is observed when sliding the window instead from right to left of the energy-loss axis. However, the falling edge of the peaks remain approximately at the edge onset (Ga L at 1115 eV and As L at 1323 eV) and rising edge for window sliding from right to left. In fig. 3.6 (C), it appears as if, using a smaller w is better because the peak remains unambiguously

²Modelling of theoretical cross-section of ionization edges using least squares method is discussed in section 4.6. The parameters of inverse power law background, $A = 3.7 \times 10^{10}$, $r = 2.5$ and scaling parameters for theoretical cross-sections were ~ 23 for both Ga L and As L edges.

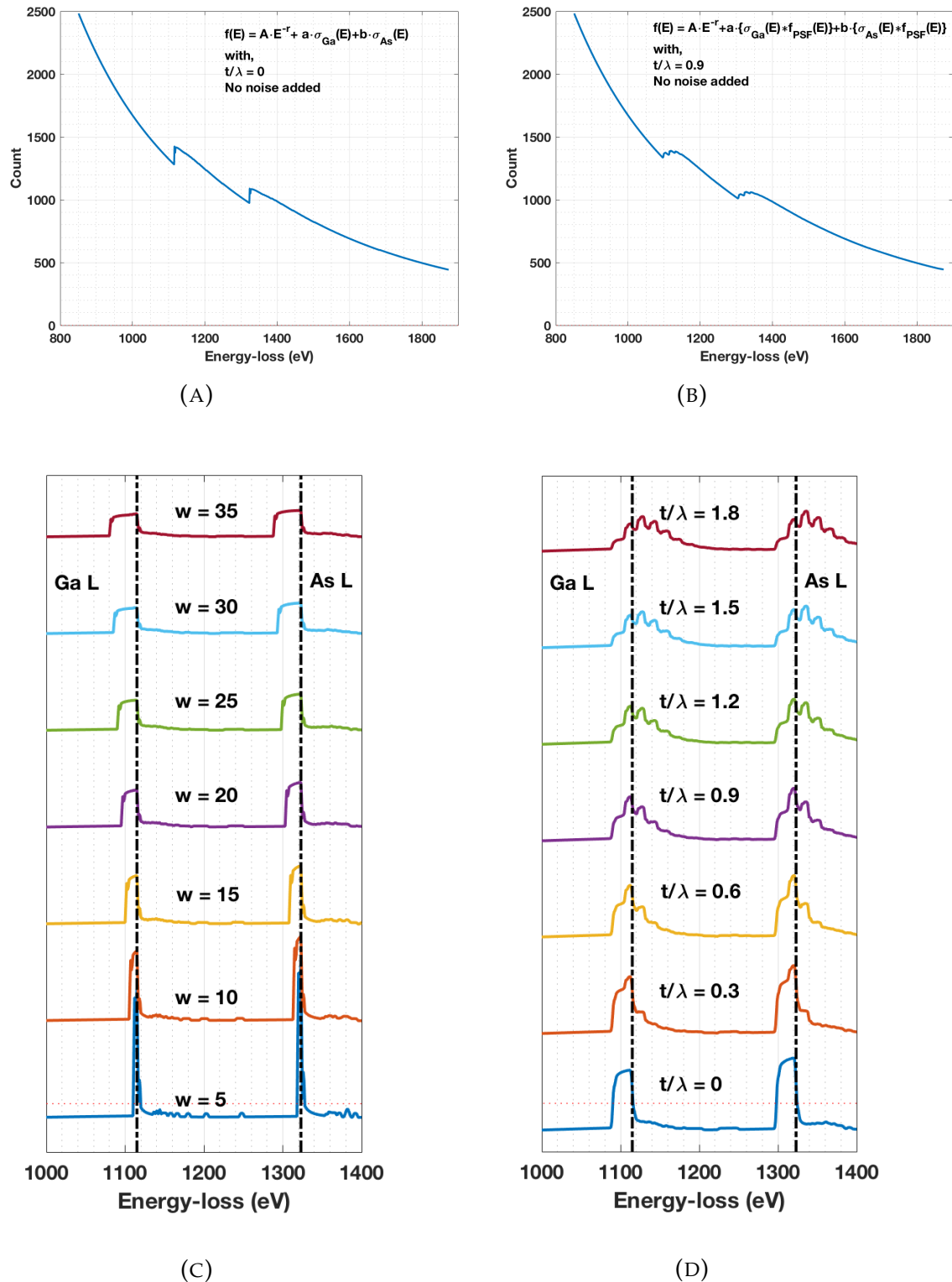


FIGURE 3.6: Simulated GaAs spectra using two Hartree-Slater cross-sections for Ga L and As L respectively with (A) $t/\lambda = 0$ (B) $t/\lambda = 0.9$, $w = 25$, $A = 3.75 \times 10^{10}$, $r = 2.45$, $a = b = 25$. Dependence of Ga L and As L edge detection (C) with variable size of the window, w for $t/\lambda = 0$. (D) as a function of relative thickness.

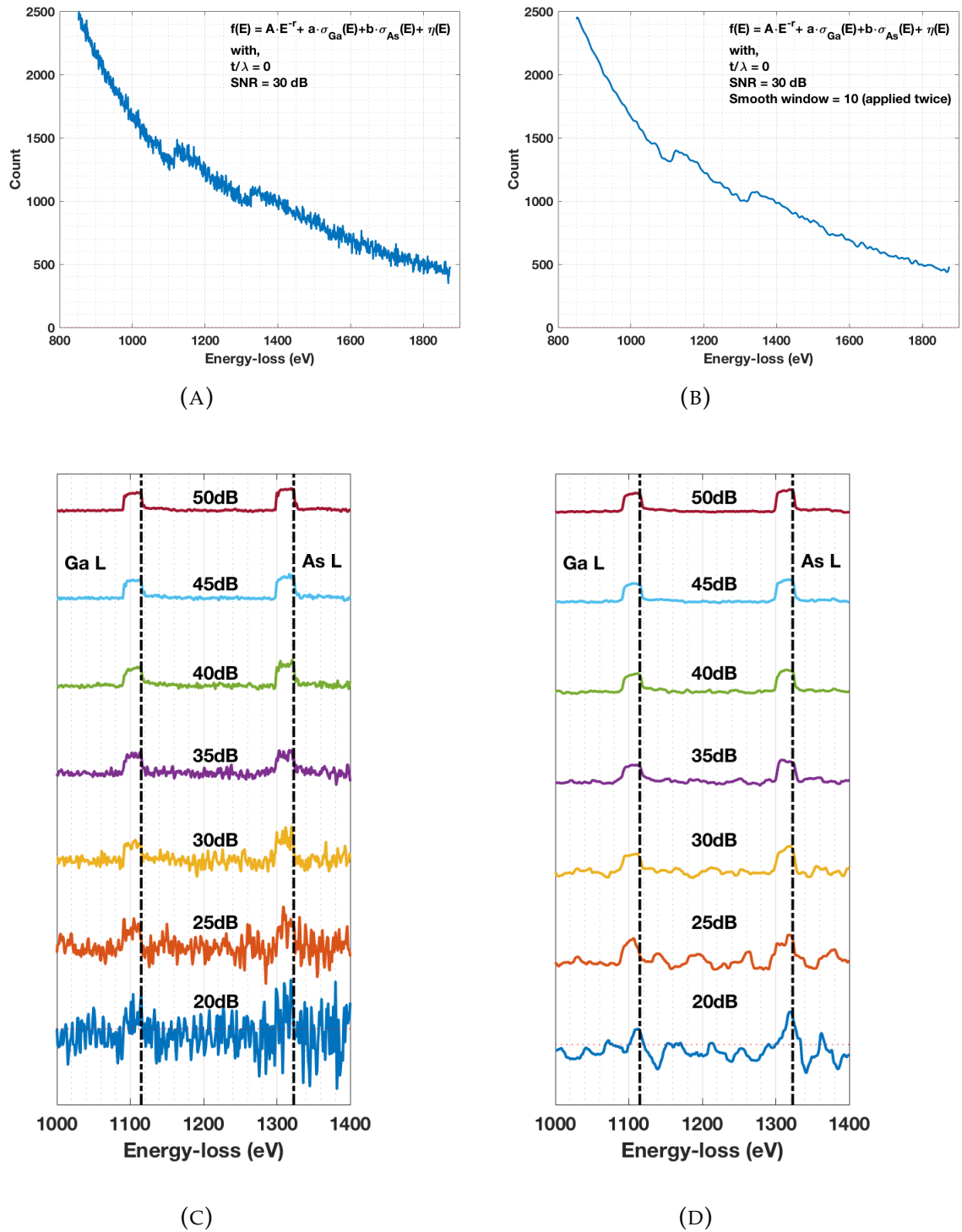


FIGURE 3.7: Simulated GaAs spectra using two Hartree-Slater cross-sections for Ga L and As L respectively with (A) 30 dB, (B) 30 dB and smoothed using averaging filter of window 10 twice. $t/\lambda = 0$, $w = 25$, $A = 3.75 \times 10^{10}$, $r = 2.45$, $a = b = 25$. Dependence of Ga L and As L edge detection (C) with addition of white Gaussian (AWG) noise at varying SNR for $w = 25$ and $t/\lambda = 0$ and (D) the smoothed AWG noisy spectrum filtered with an averaging filter of width 10 pixels at varying SNR.

located at the edge onset. However, due to noise present in the experimental spectrum, using smaller w will have a noises $\bar{\theta}_i$ and the detection of peak becomes more unreliable. If the SNR of the spectrum is high, it is possible to detect L₂ and L₃ edges, as seen in fig. 3.6(C) for $w = 5$. To test the effect of varying relative thickness, t/λ , the simulated GaAs single scattering spectrum (with no noise added) is convoluted with a low-loss, $f_P SF(E)$, to simulate a spectra from thicker GaAs. The relative thickness, t/λ , is varied from 0 to 1.8, in steps of 0.3. The low-loss is simulated by a Gaussian for ZLP and Lorentzian functions for bulk plasmon peaks weighed according to Poissonian statistics³. Fig. 3.6(D) shows that for $t/\lambda = 0$, the peak detected at ionization onset has same energy spread as the FWHM of ZLP. As t/λ is increased to 1.8, the multiple peaks that appear in fig. 3.6(D) are peaks due to multiple scattering. Hence for a thicker specimen, mere detection of maximum peak location is not a precise detection of edge onset. These peaks due to multiple scattering are spaced at multiples of the bulk plasmon energy ($E_p = 15.7$ eV). Hence, for a thicker sample the ionization edge detection might be off by multiples of E_p . The single scattering spectrum can be obtained by deconvolution which is discussed in section 2.5. The edge correction can be applied as discussed in previous subsection 3.2.1 at high-loss ionization edges. This is because at high-loss the ionization edges are far apart and the efficiency of the precise edge detection will be higher. The SNR of the EELS spectrum decreases with increase in energy-loss. This will have a large effect on detecting edges as the heights of the ionization edges become comparable with the amplitude of noise. An additive white Gaussian noise (AWGN), $\eta(E)$, is added to the simulated spectrum to test the effect of noise level on the detection of Ga L_{2,3} and As L_{2,3}. The SNR is calculated using eqn. 3.14.

$$\text{SNR} = 10 \cdot \log_{10} \left(\left| \frac{\sum_{i=1}^n S_i(E)^2}{\sum_{i=1}^n (S_i(E) - \eta_i(E))^2} \right| \right) \quad (3.14)$$

From fig. 3.7(C), it is evident that peak detection gets almost impossible for spectrum with SNR <30 dB. Once the simple averaging filter is applied the peak detection can be made reliable up to ~ 25 dB, as shown in fig. 3.7(D). To make sure the spectrum has high enough SNR for detecting core-loss edges, one way is to get the sum spectrum (or mean spectrum) from regions of EELS SI and calculate the $\bar{\theta}$ as in eqn. 3.7. Getting sum spectrum can be automated if the overview image has distinct contrasts. Then the sum spectrum can be obtained from regions identified by image segmentation algorithms. This

³The detailed description of low-loss simulation is described in later sections in chapter. 5

improves the counting statistics for the spectrum and reduces Poissonian noise significantly. The edge detection by cluster method by means of finding peak position has been applied to different semiconductors described in section A.1, A.2 and A.3. The sum spectrum from regions 8, 5, 3 and region with no material (all spectra above region 1) from multi-junction solar cell with SI of 950 eV spectrum offset are considered in order to check if all the edges are identified. The edges that are expected from 950 eV offset SI are Ga $L_{2,3}$ edge at 1115 eV, As $L_{2,3}$ edge at 1323 eV and Al K edge at 1560 eV. As expected both Ga $L_{2,3}$ and As $L_{2,3}$ are identified from GaAs regions (regions 3 and 8). Region 5 is expected to be AlGaInP. Hence no As $L_{2,3}$ is identified. All the $\bar{\theta}$ spectrum from fig. 3.8 show the features of ionization edge except for the $\bar{\theta}$ spectrum with no material. It is interesting to note the features shown in the pink box in fig. 3.8 which are artefacts present in all regions of the SI. These are specific to particular channels of the spectrum and probably due to anomalies in the gain correction. Minute changes in the $\bar{\theta}$ can be observed across all the spectra in fig. 3.8 for all regions. But the large peaks are observed at channel numbers 824, 898 and 939. These artefacts will also mask a possible Al K edge at 1560 eV which is in close approximation. Hence, Al K edge cannot be detected. The edge detection algorithm from fig. 3.5 is tested with

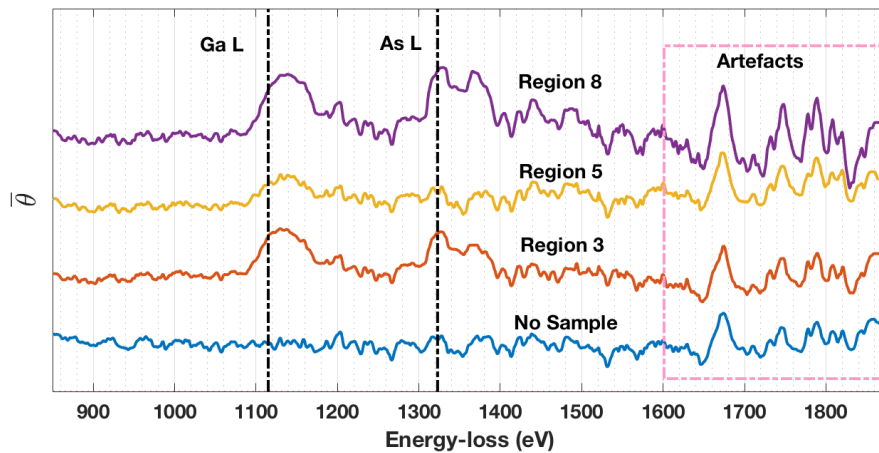


FIGURE 3.8: The edge detection by cluster method ($w = 25$) applied to sum spectrum from regions 8, 5, 3 and region without sample of multi-junction solar cell described in section A.1. Each $\bar{\theta}$ spectra have vertical range between $-\pi/2$ to $\pi/2$.

$\text{In}_x\text{Ga}_{1-x}\text{N}$ material with sum spectrum extracted separately from In and Ga rich regions⁴ to check the extent of variation in edge detection with varying concentration of In and Ga. The $\bar{\theta}$ spectra for both In and Ga rich are superimposed in fig. 3.9. Similar to previous findings, the $\bar{\theta}$ is affected by anomalies

⁴The In and Ga rich regions can be seen in elemental maps shown in fig. 3.15(B,C).

in in the gain correction. It is noticeable in both spectra. In $\text{In}_x\text{Ga}_{1-x}\text{N}$ material, the percentage of N would be constant but the percentages of In and Ga can change. This is also reflected in $\bar{\theta}$ spectra as N K edges overlap almost perfectly in both spectra from In and Ga rich $\text{In}_x\text{Ga}_{1-x}\text{N}$. The Ga $L_{2,3}$ edge in the In rich spectrum is difficult to identify due to effects from gain correction and the intensity of the edge onset is very low. However, in Ga the rich region, the Ga $L_{2,3}$ edge is clearly identifiable and the In $M_{4,5}$ intensity is lower. Hence the stoichiometry also plays an important role in identifying the ionization edges from clusters. It is also worth noting that if the ionization edge

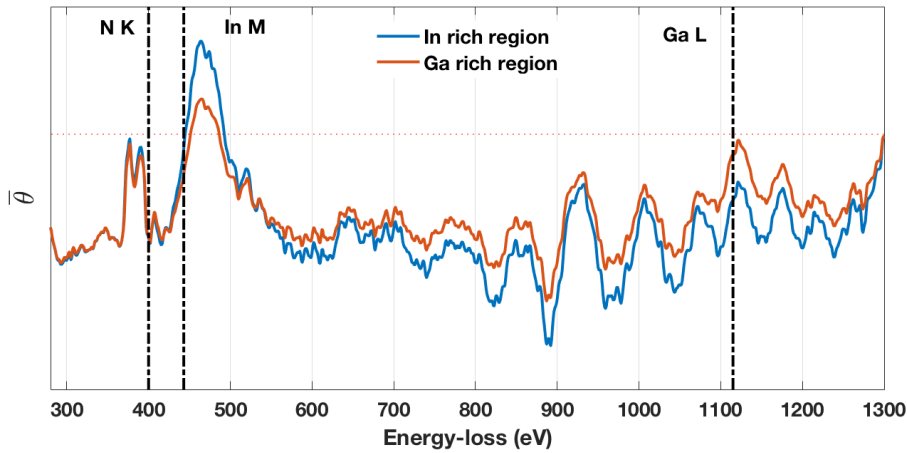


FIGURE 3.9: The edge detection algorithm ($w = 25$) is applied to $\text{In}_x\text{Ga}_{1-x}\text{N}$ phase separated material. Sum spectrum is extracted from In rich and Ga rich region from EELS SI. Each $\bar{\theta}$ spectra have vertical range between $-\pi/2$ to $\pi/2$.

onset is hydrogenic (as in case of N K edge) or sharp is in single scattering (as in shown in fig. 3.6(C)) then the edge onset is the falling edge of peaks in $\bar{\theta}$ spectrum which was observed in fig. 3.6(C). However, if the edges are delayed (as in In $M_{4,5}$) and/or plural scattered then the edge onset is rising edge which was observed in fig. 3.6(D). The thicker the sample, the more intensity is redistributed to higher energies hence the onset must be changed to rising edge instead of falling edge. The algorithm has finally been applied to Tb doped AlN material described in section A.3. Two sum spectra are extracted⁵ from region 1 (AlN) and 2 (Si substrate) as shown in fig. A.4(B). The span of the energy-loss is from 340.8 eV to 1614.8 eV. Hence, the large energy-loss span is responsible visible background which is following $-E^{-1}$ trend from eqn. 3.13. The N K and O K are sharp hydrogenic edges, hence the edge onset is at the falling edge of the peaks. Tb $M_{4,5}$ edge at 1242 eV is present but it is

⁵In the high-loss SI of AlN doped with Tb, first #10 and last #50 channels have been distorted to zero value while acquisition. This could be due to the energy slit introduced. Hence all the spectra are considered from channel numbers #11 to #467 only.

not detectable due to the fact that its concentration in AlN is ~ 2 at.% (Benz et al., 2013a) and the height of edge onset is comparable with noise at high-loss. Also, during acquisition, the spectra were binned by a factor 4 to reduce the size of data set in energy-loss direction from 2048 to 512 channels making the dispersion to 2.8 eV/channel rather than 0.7 eV/channel. The white lines from $M_{4,5}$ transition of Tb_2O_3 complex are at 1243 eV for M_5 and 1274 eV for M_4 about 30 eV apart with FWHM of ~ 4 eV. The energy dispersion of the spectrum is 2.8 eV/channel. Benz et al., (2013a) have shown high-loss EELS spectra with 800 eV spectrum offset, 1 eV/channel dispersion and 100 s exposure time for 2% Tb doped in AlN. The ionization edge height is still very low for even 100 s. Hence, for 2.8 eV/channel dispersion with 0.1 s exposure time, there is about 1 or 2 pixels that might describe the white lines. Also as discussed earlier, the stoichiometry also plays major role in identifying the edge onset. The algorithm detects the cluster not a single pixel. Hence, the single pixels are treated as an outlier, i.e. noise. Apart from white lines, the ionization edge property of Tb $M_{4,5}$ is wide and delayed. Hence, Tb $M_{4,5}$ is not detectable in this particular SI. The sum spectrum from AlN region has been obtained by averaging ~ 3741 spectra, whereas sum spectrum from Si substrate is obtained by averaging ~ 1131 spectra. This means that the SNR of the AlN sum spectrum should be higher than the one from the Si sum spectrum. The noisy artefacts present for the latter in fig. 3.10 is evidence of SNR being lower. $In_xGa_{1-x}N$ and AlN doped with Tb are used to test the cluster detection by finding the peak.

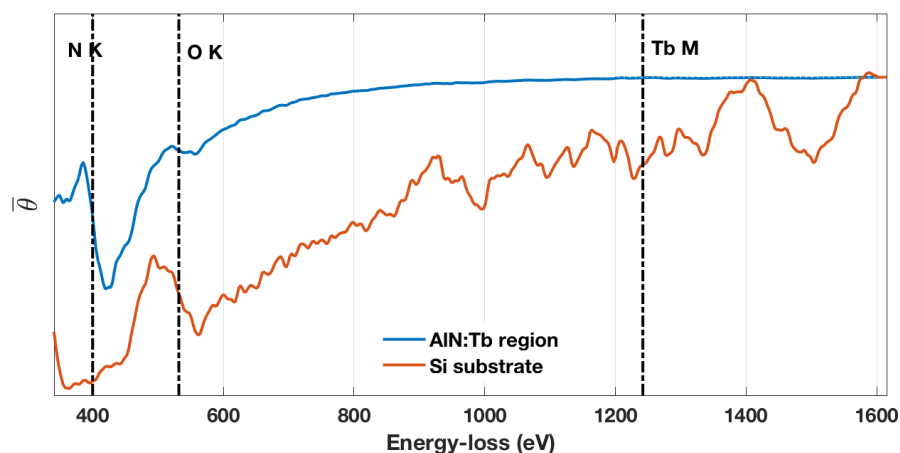


FIGURE 3.10: The edge detection algorithm is applied to Tb doped AlN EELS SI. The sum spectrum (~ 3741 spectra) are taken from AlN region 1 as in fig. A.4(B) and another sum spectrum (~ 1131 spectra) from Si substrate region which is indicated as region 2.

3.3 Quantification by background subtraction

The presence of the ZLP and plasmon losses in low-loss spectra makes it difficult to model the background for energies below about 100 eV. The inverse power-law is used to model the background in pre-edge regions for individual ionization core-loss edges above this threshold. This may be justified in our case as table A.1 demonstrates we have generally used high dispersions for lower energy losses and lower dispersions at higher offsets. So wide regions extending from low to high energy losses, wherein the shape of the background often departs significantly from the slope expected from a simple inverse power-law function (Leapman, 2005), have been avoided. A linear model of spectrum $S(E)$ with ionization edges superimposed on a background modelled by an inverse power-law at higher losses with an error, $\varepsilon(E, \Delta)$, as a function of energy-loss (E) and integration range (Δ) is considered, as shown in eqn. 3.15.

$$S(E, \beta, \Delta) = AE^{-r} + \sum_{i,j} I_{i,j}(\beta, \Delta) \sigma_{i,j}(\beta, \Delta) + \varepsilon(E, \Delta) \quad (3.15)$$

The pre-edge regions for the background modelling should be selected as large as possible to minimize systematic errors. A larger pre-edge region provides more data points for modelling of the background and chemical shifts that could shift the edge onset by up to ~ 8 eV are less prone to influence the background modelling. Due to the possible presence of near edge structure, the pre-edge region should ideally end well before the edge onset. Hence, the pre-edge region is selected dynamically by the algorithm over all the core-loss edges and across the EELS SI. The pre-edge region extends typically from half the distance between two consecutive core-loss edges to a few channels before the nominal edge onset. Standard integration methods are used for the quantification of background subtracted EELS spectra (Egerton, 1978). If the integration window exceeded the experimental energy-loss axis limit then the edge would be omitted (in the semiconductor multilayer example presented later, the integration window for the P L_{2,3} edge was manually reduced to 37.4 eV to avoid this). The selection of integration window and the systematic and statistical errors (Bevington et al., 1969) influencing quantification have been discussed by Leapman, (2005). Two core-loss edges close to each other will be partially overlapping and are not accurately quantifiable by this integration method. The accuracy of the quantification also depends on the shape of the ionization edges. If the onset

of an ionization edge is delayed, small integration windows give high statistical errors. Hence the initially specified integration window (Δ) is applied only to hydrogenic edges. In case of delayed edge onsets, the spectrum is integrated up to the next ionization edge onset, providing better statistics for delayed maximum edge shapes, but at the cost of slightly higher systematic errors. EELS is usually performed with a spectrometer entrance aperture, and the integration of the spectrum intensity is a function of collection semi-angle (β) and integration window (Δ) (Egerton, 2011b). The values of partial cross-sections are evaluated from the `SIGMAK3`, `SIGMAL3` and `SIGPAR` Matlab routines written by Egerton, (2011a). The overall process of core-loss edge selection and background subtraction is shown in the form of a block diagram in fig. 3.11. The implementation of the algorithm in Matlab R2017b (MathWorks, 2017) means the code can be distributed not only to multiple processing cores (presently a windows 10 PC with 4 cores and MacBook Pro with 2 cores has been tested) but to multiple computers using the Matlab parallel computing tool box as discussed in appendix B.

3.4 Results from multi-junction solar cell

Again, sum spectra are extracted from each individual region for quantification. Elemental concentrations (x) are calculated using eqn. 3.16. The concentrations (x_j) are normalised to yield the at.% of all detected elements. The normalised X values thus provide a relative quantification. The sum of all N_n adds up to unity (or 100%) in eqn. 3.17. Quantification results for each region are shown in table 3.2. Specimen thickness (t) values in terms of multiples of the mean free path (λ) of inelastic scattering can be extracted from the first EELS SI which contains the ZLP and plasmon peaks. These t/λ values are ~ 1 (except in the top thin layer of region 1) indicating an average specimen thickness around $t \approx 130$ nm, which corresponds to the inelastic mean free path calculated according to Egerton, (2011b) for GaAs under the conditions listed in table A.1.

$$x_j = \frac{I_j(\beta, \Delta)}{\sigma_j \cdot t_j \cdot \tau} \quad (3.16)$$

$$N_1 \text{ (at.\%)} = \frac{x_1}{\sum_{j=1}^n x_j} \times 100 \quad (3.17)$$

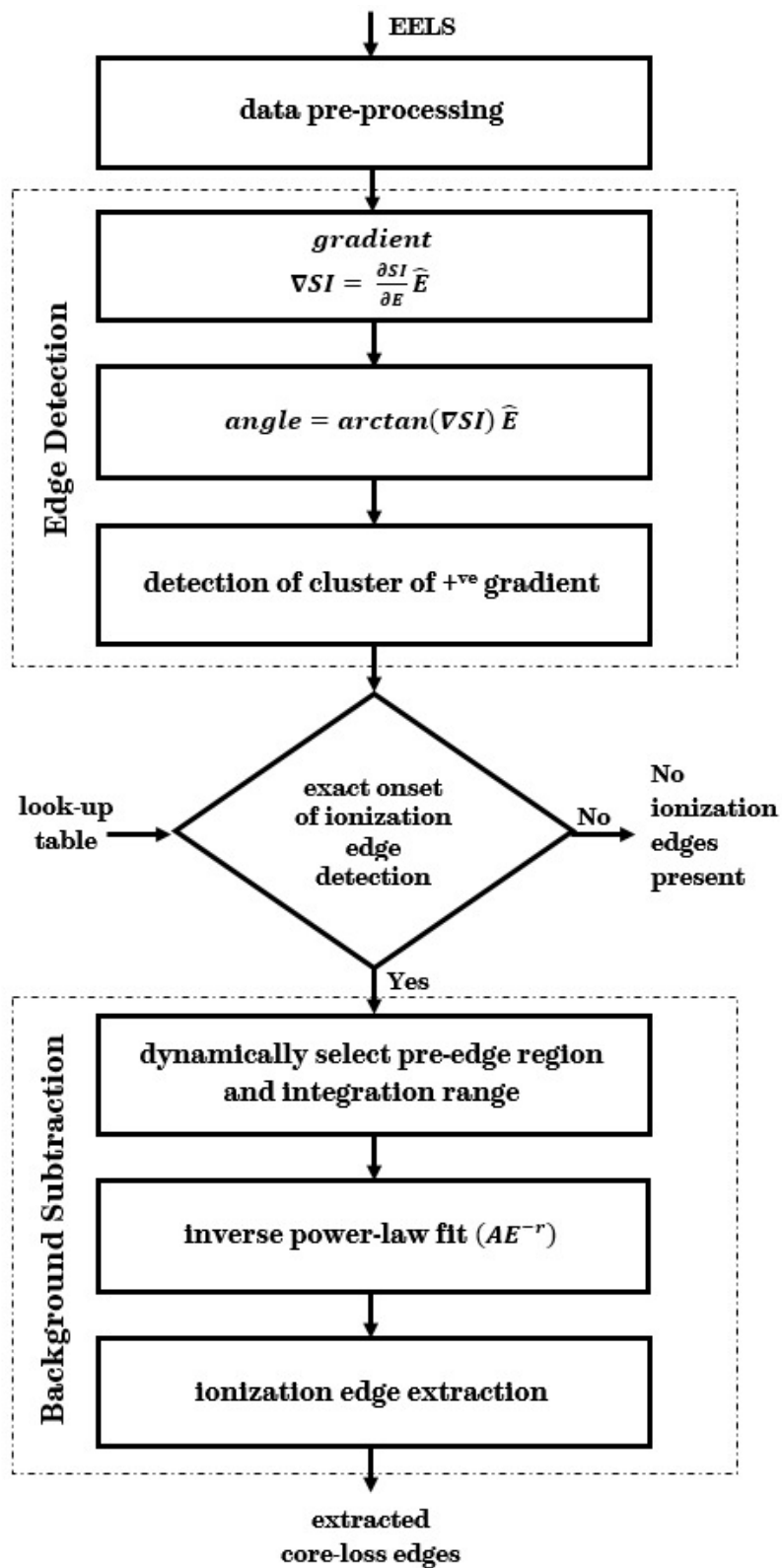


FIGURE 3.11: Block diagram of ionization core-loss edge selection and background subtraction.

TABLE 3.2: Quantification in atomic percent (at.%) of each region of the three SIs recorded. The sum of all concentrations has been normalised to 100% according to eqn. 3.17.

	t/λ	80 eV offset			250 eV offset			950 eV offset		
		Si L ₂₃	Al L ₁	P L ₂₃	CK	In M ₄₅	OK	Cu L ₂₃	Ga L ₂₃	As L ₂₃
Dispersion (eV/channel)		0.10	0.10	0.10	0.50	0.50	0.50	1.00	1.00	1.00
Exposure time (τ) (s)		0.5	0.5	0.5	0.5	0.5	0.5	2	2	2
Integration range (Δ) (eV)		15	15	37.4	50	89	50	200	200	200
Region 1	0.52	1.44	3.22	5.47	44.09	2.37	43.40	0.00	0.00	0.00
Region 2	0.96	1.51	2.08	3.89	30.03	0.00	38.30	24.18	0.00	0.00
Region 3	0.95	7.87	0.00	6.26	9.29	0.00	2.41	0.00	41.46	32.72
Region 4	0.95	8.53	1.63	40.73	18.61	10.37	0.00	0.00	10.07	10.05
Region 5	1.01	0.00	3.99	43.48	10.10	16.90	0.00	0.00	25.02	0.50
Region 6	1.04	3.82	1.62	29.97	4.84	3.61	0.00	0.00	22.80	33.35
Region 7	1.04	1.57	3.17	49.16	7.87	19.08	0.00	0.00	8.92	10.23
Region 8	1.11	8.07	0.00	1.92	0.00	0.00	1.50	0.00	42.94	45.57

The values in table 3.2 are normalised with respect to relative thickness (t/λ) and exposure time (τ). The parameters in table A.1 are used for the calculation of partial cross-sections, $\sigma(\beta, \Delta)$, using SIGMAK3, SIGMAL and SIGMAPAR routines that take into account the finite collection semi-angle but neglect any corrections due to the angular spread of the incident beam that may play a role as soon as $\alpha \gtrsim \beta$ (Egerton, 2011b) or due to multiple scattering. In the sense that the index j runs over all elements detected, this performs what is usually called a relative compositional quantification in at.% (rather than an absolute quantification in terms of atomic areal density). As the scattering cross-sections in eqn. 3.16 are for single scattering, whereas plural scattering is known to affect the edge shape, moving intensity from the onset towards higher energies, a reliable quantification would require either deconvoluting each spectrum in the SI to recover the single inelastic scattering contribution or integrating all net edge intensities over similar energy ranges so that all edges would be affected by multiple (plasmon) scattering to the same degree (Walther et al., 1995). Large integration windows can be used for edges at high energy losses that typically lie far apart from each other (here, Ga L_{2,3} and As L_{2,3}), whereas small integration windows must be used at lower energies (here, Si L_{2,3} and P L_{2,3}). Small integration ranges, Δ , tend to underestimate intensity considerably if thicknesses are large and the spectra are not deconvolved for multiple inelastic scattering. This has indeed been observed here, as deconvolution was not applied (see below). The algorithm generates maps which provide the spatial distributions of the elements in the material. The maps are generated by integration of background subtracted spectra at each point according to eqn. 3.16. The background subtraction may not work perfectly for some spectra due to high noise or near-edge structures which would contribute to inferior curve-fitting. Also, the EELS SI with 80 eV offset revealed an artefact at around channel #100 due to the previous exposure of this area of the CCD to the ZLP. This is shown in fig. 3.12. Hence, the map of the Al L_{2,3} edge can only be evaluated with caution. Some elemental maps in fig. 3.13 are very noisy, but the overall spatial distribution of elements can be clearly evaluated. Screen shots of the program outputs are shown in fig. 3.13 and 3.14. It can be observed that the algorithm automatically detects the core-losses and dynamically selects pre-edge regions and integration windows for each core-loss of the SI and that the output maps yield a quick visual feedback on the relative strengths of the chemical signals detected. The quantified values are compared with the standard background subtraction routines such as Hyperspy and CSI as shown in table 3.3. The values were almost

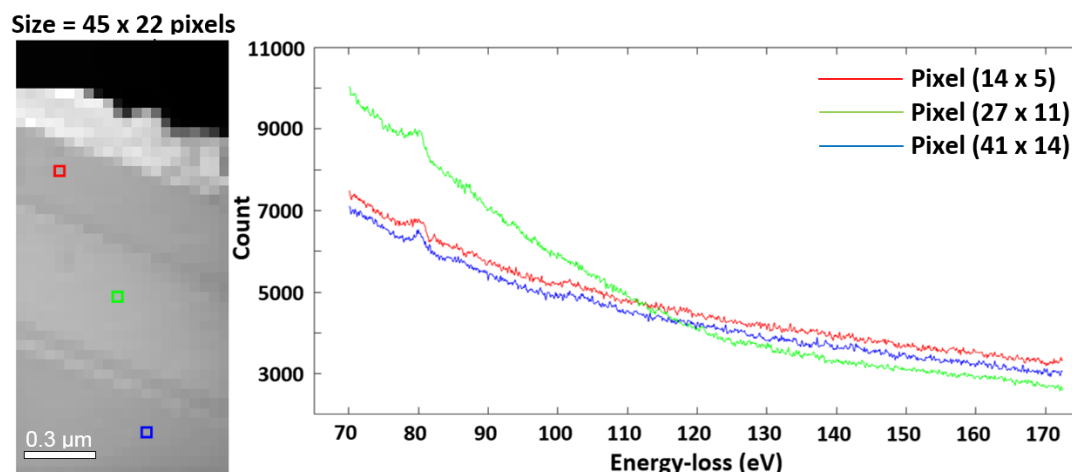


FIGURE 3.12: The persistence of an artefact at 72–85 eV in spectra from all locations (3 single spectra are displayed) shows that the Al $L_{2,3}$ edge (nominally starting at 73 eV) cannot be evaluated from spectra acquired with 80 eV offset after spectra without offset had been acquired previously with the ZLP located at channel #100.

similar to the values quantified by our algorithms hence, only mean-squared error (MSE) between our values and the standard routine values are shown for x_j . As expected the Al $L_{2,3}$ is affected due to the presence of artefact and

TABLE 3.3: Relative quantification of Cu, Ga and As elemental maps with DigitalMicrograph™ in different regions shown in fig. 3.13(E) (GaAs).

MSE		80 eV offset				
		Al $L_{2,3}$	Si $L_{2,3}$	Al L_1	P $L_{2,3}$	
CSI	368.93	0.13	0.01	0.52		
Hyperspy	1066.92	3.12	0.06	2.92		
MSE		250 eV offset				
		C K	In $M_{4,5}$	O K		
CSI	1.20	0.17	1.21			
Hyperspy	1.81	12.73	7.86			
MSE		950 eV offset				
		Cu $L_{2,3}$	Ga $L_{2,3}$	Ge $L_{2,3}$	As $L_{2,3}$	Al K
CSI	1.29	0.53	1.44	5.13	8.08	
Hyperspy	2.36	1.24	3.14	18.56	151.46	

different routines tend to give different results due to the inherent constraints might have applied to deal with noise while fitting the background.

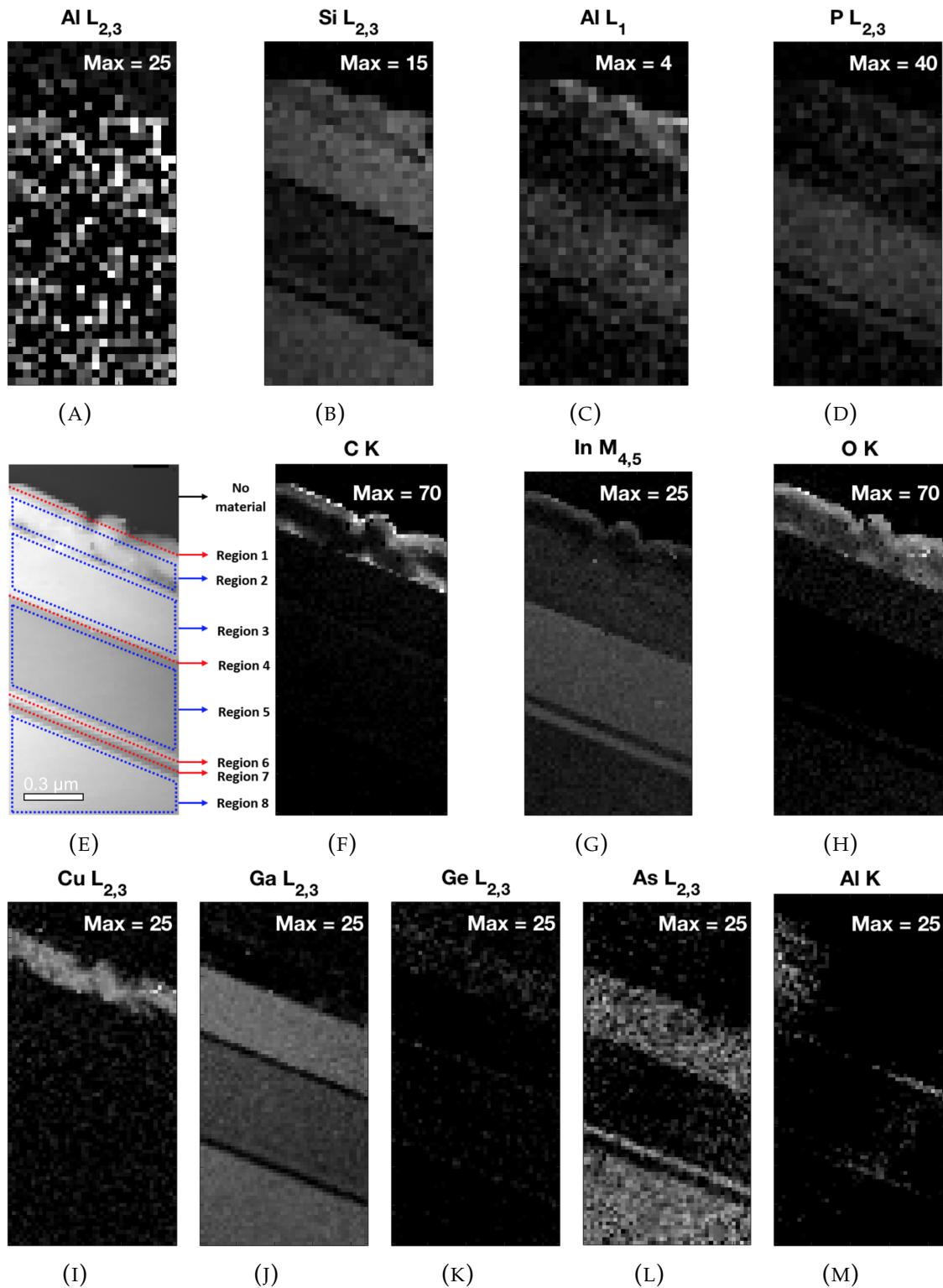


FIGURE 3.13: (E) Definition of regions in the EELS SI. Regions indicated by blue dotted lines are thicker regions, while red lines denote interfaces. A sum spectrum is extracted from each region for further quantification in table 3.2. Set of maps generated with EELS SI of 80 eV offset (A–D), with 250 eV offset (F–H) and with 950 eV offset (I–M). The elemental maps show the spatial distribution of Al $L_{2,3}$, Si $L_{2,3}$, Al L_1 , P $L_{2,3}$, C K, In $M_{4,5}$, O K, Cu $L_{2,3}$, Ga $L_{2,3}$, Ge $L_{2,3}$, As $L_{2,3}$ and Al K edges. Al $L_{2,3}$ is a false positive detection due to an artefact. Maximum intensity values in counts after background subtraction, integration and scaling according to eqn. 3.16 with constant = 1. The minimum intensity in all the maps is 0.

Detected edges :
73 100 118 135 165
Delta for edge 165eV is exceeding energy-loss axis limit (172.4eV)
Edge considered for quantification :
73 100 118 135

-----Pre-edge region-----

Range eV	Begin eV	End eV	Onset eV
1	72	72.8	73
14	86	99.8	100
9	109	117.8	118
9	126	134.8	135

-----Integration region-----

Onset eV	Element	Begin eV	End eV	Integration Range eV
73	'Al-L3'	73	100	27
100	'Si-L3'	100	115	15
118	Al-L1'	118	135	15
135	'P-L3'	135	172.4	37.4

Detected edges :
284 294 443 532 685
Delta is overlapping with next edge. Edge 294eV is omitted
Delta for edge 685eV is exceeding energy-loss axis limit (712eV)
Edge considered for quantification :
284 443 532

-----Pre-edge region-----

Range eV	Begin eV	End eV	Onset eV
42	242	283	284
80	363	442	443
45	487	531	532

-----Integration region-----

Onset eV	Element	Begin eV	End eV	Integration Range eV
284	'C-K'	284	334	50
443	'In-M5'	443	532	89
532	O-K'	532	582	50

Detected edges :
931 951 1020 1115 1217 1323 1560
Delta is overlapping with next edge. Edge 951eV is omitted
Delta is overlapping with next edge. Edge 1020eV is omitted
Edge considered for quantification :
931 1115 1217 1323 1560

-----Pre-edge region-----

Range eV	Begin eV	End eV	Onset eV
40	891	929	931
92	1023	1113	1115
51	1166	1215	1217
53	1270	1321	1323
119	1441	1558	1560

-----Integration region-----

Onset eV	Element	Begin eV	End eV	Integration Range eV
931	'Cu-L3'	931	1031	100
1115	'Ga-L3'	1115	1217	102
1217	'Ge-L3'	1217	1323	106
1323	'As-L1'	1323	1560	237
1560	'Al-K'	1560	1660	100

FIGURE 3.14: Screen shot of program output showing pre-edge regions and integration windows dynamically assigned by the algorithm for SI with 80 eV offset (A), 250 eV offset (B) and 950 eV offset (C).

3.5 Results from InGaN

The images in figs. 3.15(B–D) are elemental maps of the distribution of the three elements indium (from In $M_{4,5}$ edge), gallium (from Ga $L_{2,3}$ edge) and nitrogen (from N K edge) calculated by fitting the data, using pixel-wise automated edge detection routines described in section 3.2 with inverse power-law or exponential background fit, subtraction in the pre-edge regions and net integration over certain ranges. Details of the fitting are reported in table 3.4. The relative quantification has been normalised to a sum of unity

TABLE 3.4: Background fitting details. All numerical values are in eV.

SI	edge	fit begin	fit end	onset	Δ	fit type
	N K	287	398	400	51	Pow ¹
high-loss	In $M_{4,5}$	410	441	443	247	Pow
	Ga $L_{2,3}$	600	1113	1115	189	Exp1 ²

¹ Inverse power-law function (eqn. 2.2).

² Exponential decay function (eqn. 2.3).

taking into account only these three elements. There was a very faint O signal (from O K) from the surface which has been neglected. The quantification of the Ga content from the Ga $L_{2,3}$ edge (15.2 ± 5.9 at.%), which would imply an average x value for $\text{In}_x\text{Ga}_{1-x}\text{N}$ of $x = 0.7 \pm 0.1$. The Ga $L_{2,3}$ edge starts at very high energy (1115 eV) so its intensity is weak and the maps will be mainly limited by shot noise, while background subtraction is relative straight-forward (due to large pre-edge region) and implies small systematic errors. For the quantification of the N K edge and the In $M_{4,5}$ edge the situation is reversed: these edges lie at lower energies and so have plenty of intensity but they partially overlap (the N K edge starts at 400 eV, the In $M_{4,5}$ edge at 443 eV) so they are more difficult to separate. A higher apparent In signal would predicts less N in relative quantification. Deconvolution of the spectra could change the relative quantification further but has not yet been attempted here, as it would have been difficult to record low and high-loss spectra without the dual-EELS option (Scott et al., 2008) and we use integration ranges sufficiently wide for the N and Ga edges to include plasmon replicas so (multiple) plasmon scattering would cancel out in the ratio approach taken. However, it should be stated that the relative quantification of $\text{In}_x\text{Ga}_{1-x}\text{N}$ is a real challenge, firstly, as it implies evaluating three ionization edges of different types (K, L, and M) and, secondly, because two edges of these overlap significantly. The standard deviations of the N map

in fig. 3.15(D) is very small, as would be expected for a constant group-V sub-lattice consisting of N only. The maps for In and Ga show much larger scatter, with 2–3 times higher standard deviations. The lateral scale of the In-rich regions visible in fig. 3.15(B) extends to only 0.5–3 nm, which would be in agreement with findings by other groups (Jinschek et al., 2006). Given the projection through the ~ 40 nm thick specimen such In-rich clusters, should they exist and not be an artefact from electron irradiation (Doppalapudi et al., 1998; Lin et al., 2000; Park et al., 2005; Singh et al., 1997), must consist of almost pure InN. The low-loss EELS SI of $\text{In}_x\text{Ga}_{1-x}\text{N}$ from table A.2 is quantified by simultaneously fitting plasmon losses (those of InN, $\text{In}_x\text{Ga}_{1-x}\text{N}$ and GaN) along with core-losses of In N edge ($4d$ transition), Ga M edge ($3d$ transition) and ternary alloy $\text{In}_x\text{Ga}_{1-x}$ of group-III sub-lattice later in chapter. 5.

3.6 Results from AlN:Tb

AlN doped with Tb was studied in Angadi et al., (2017) and Benz et al., (2013a) with regards to the formation of Tb–O complexes. Similar rare-earth doped AlN was studied by Wieg et al., (2015). The nominal concentration of Tb in AlN is expected to be 2 at.%. The inelastic mean free path (λ) values in Si (substrate), AlN:Tb region and SiO_2 region at 60 kV are ~ 49 nm, ~ 52 nm and ~ 54 nm, respectively. The values of the relative thickness (t/λ) map in fig. A.4(C) and the mean free paths (λ) calculated in table 3.5 (Craven et al., 2016; Malis et al., 1988) can thus be directly related to absolute specimen thickness (t) in the range of 13–20 nm. Elemental maps are shown in figs. 3.16.

TABLE 3.5: Calculated mean free paths (λ), mean atomic number ($\langle Z \rangle$), mean atomic mass ($\langle A \rangle$) and mean energy-loss ($\langle E \rangle$).

Composition at.%	AlN:Tb,O 48 : 49 : 2 : 1	SiO_2 33.3 : 66.7	Si:O 99 : 1
$\langle Z \rangle$	11.05	10.00	13.94
$\langle A \rangle$	23.15	20.03	27.97
$\langle E \rangle$ (eV)	18.0	17.4	19.6
λ (nm)	52.4	54.0	48.9

The background fitting details are listed in table 3.6 along with the integration ranges (Δ). The functions used to fit the background are exponential decay (eqn. 2.3) or inverse power-law functions (eqn. 2.2). The value of $k = 1$ from eqn. 2.3 for fit type ‘Exp1’, and $k = 2$ for fit types ‘Exp2’ and ‘Pow’ as indicated in table 3.6. The Si $L_{2,3}$ edge and Al $L_{2,3}$ core-losses are extracted

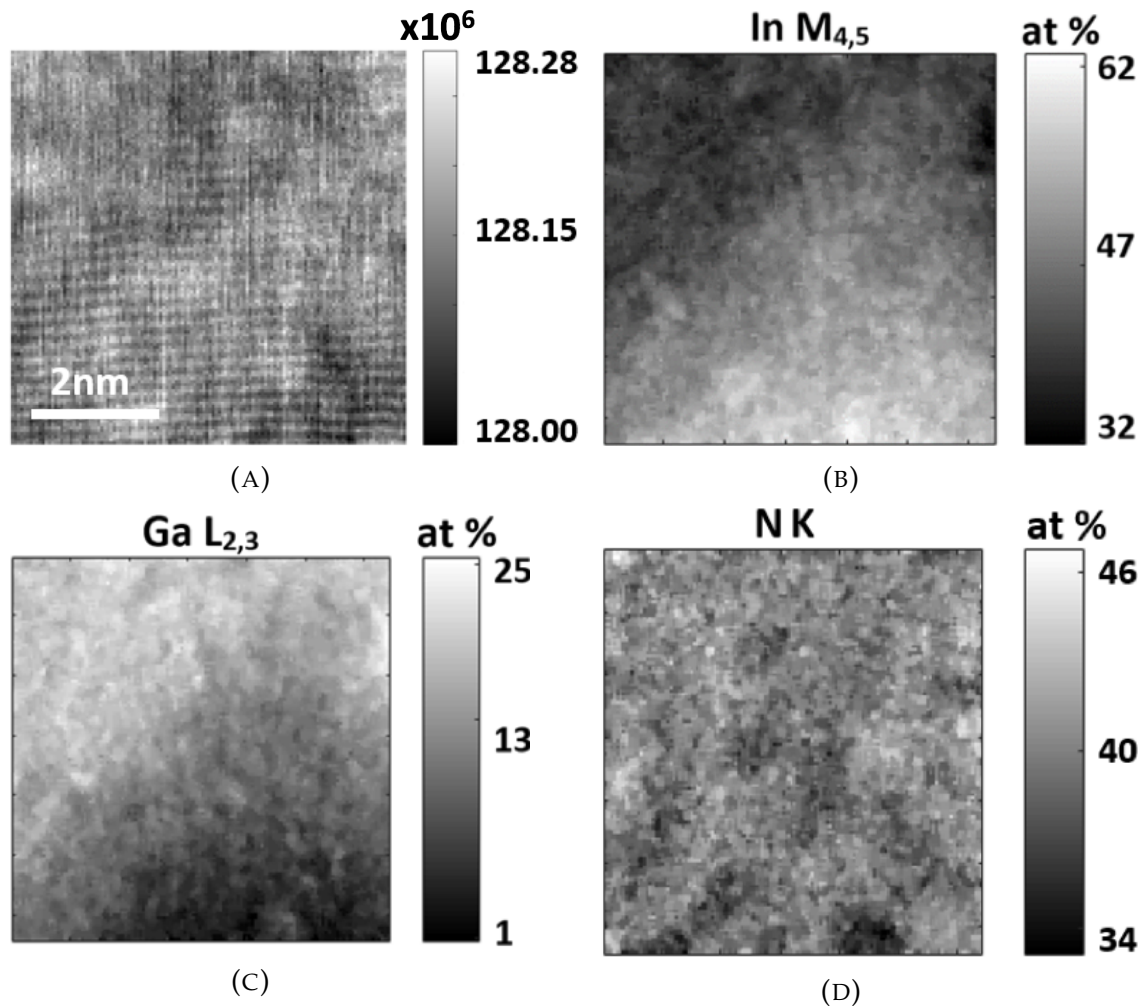


FIGURE 3.15: (A) Rotated HAADF-STEM image of cross-sectioned $\text{In}_{0.62}\text{Ga}_{0.38}\text{N}$ film at high magnification, about 10 nm above the GaN substrate, showing (0002) lattice fringes. Growth direction points upwards. Elemental maps of (B) indium from In M_{4,5} edge, (C) gallium from Ga L_{2,3} edge and (D) nitrogen from N K edge recorded at 100 kV and calculated using (B & D) integration after inverse power law subtraction, (C) integration after exponential background extrapolation. All intensities are normalized to a sum of unity to calculate at.%.

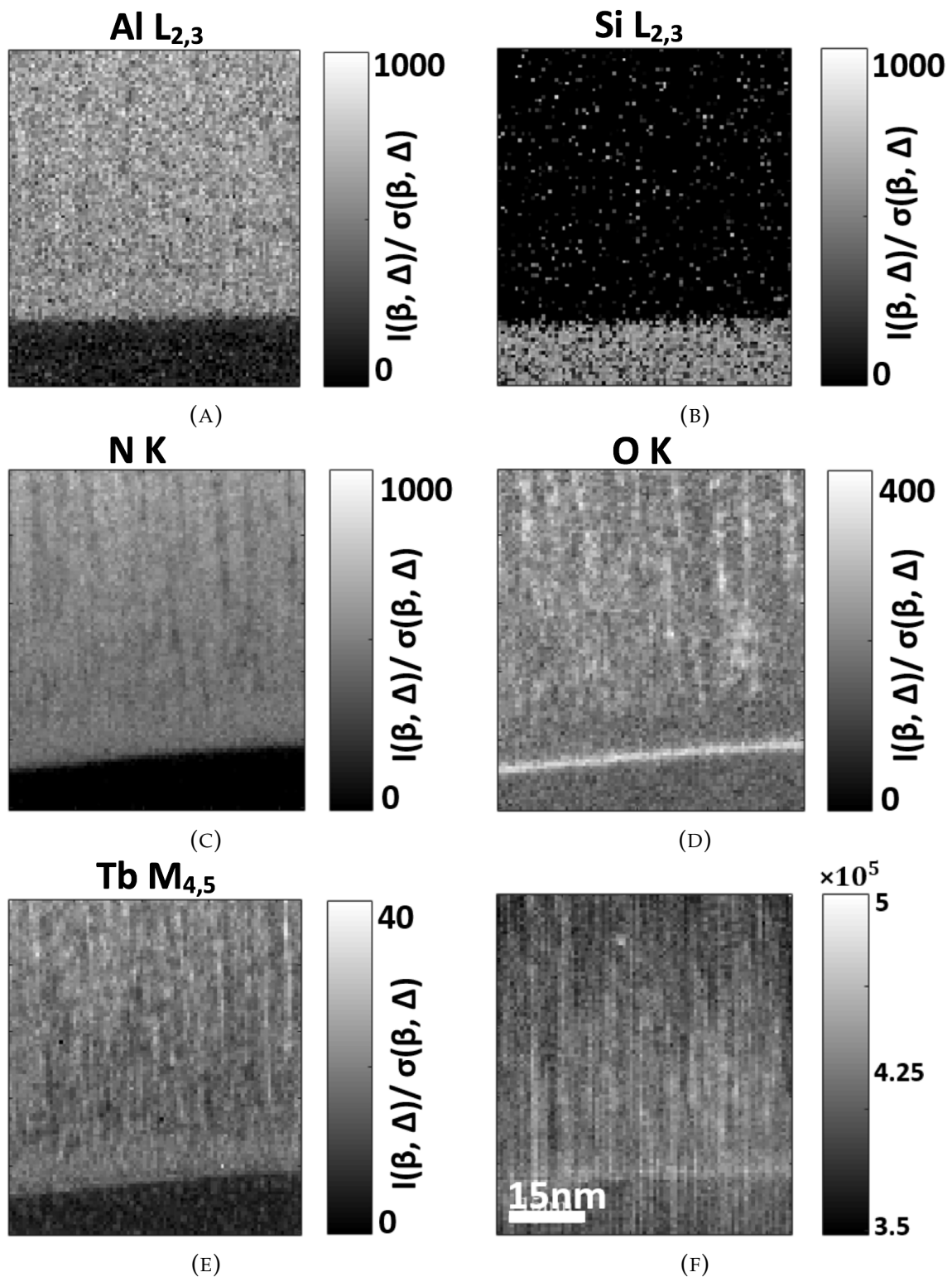


FIGURE 3.16: Background subtracted net intensities after the edge onsets have been integrated and normalised with respect to the corresponding scattering cross-sections and exposure times. Elemental maps of Al L_{2,3} (A) and Si L_{2,3} (B) in the low-loss region. Elemental maps of N K (C), O K (D), and Tb M_{4,5} (E) in the high-loss region. (F) HAADF.

from low-loss SI (table A.3). N K, O K and Tb M_{4,5} edges are extracted from

TABLE 3.6: Background fitting details. All numerical values are in eV.

SI	edge	fit begin	fit end	onset	Δ	fit type
low-loss	Al L _{2,3}	23.8	70	72.8	27.3	Exp2 ¹
	Si L _{2,3}	41.3	98	99.4	105	Exp2
high-loss	N K	343.6	385.6	385.6	112	Pow ²
	O K	427.6	517.2	525.6	112	Exp1 ³
	Tb M _{4,5}	727.2	1147.2	1211.6	246.4	Exp1

¹ Superposition of two exponential decay functions (eqn. 2.3).

² Inverse power-law function (eqn. 2.2).

³ Exponential decay function (eqn. 2.3).

high-loss SI (table A.3). The integration range (Δ) for Al L_{2,3} is limited by overlap with the Si L_{2,3} edge. The maps of Al L_{2,3} and Si L_{2,3} in figs. 3.16(A,B) are relatively noisy due to the low exposure time and hence low SNR. Large negative values in the Si L_{2,3} map are due to poor background fitting in the AlN region due to the preceding Al L_{2,3} ionization edge. Deconvolution is not applied because of the low SNR in the spectrum: deconvolution by Fourier-ratio or RL methods would increase the noise even further. The interface in the high-loss maps as in figs. 3.16(C–E) appears to be inclined with respect to the horizontal by an angle of $\sim 4.6^\circ$ due to drift during the long time of acquisition. Due to this mismatch in the interface, the at.% values have been calculated only in the regions indicated in fig. A.4(B) and shown in table 3.7.

TABLE 3.7: Elemental quantification (at.%) in AlN:Tb and Si region for top 40 rows (Box 1) and lowest 15 rows (Box 2) respectively as shown in fig. A.4(B).

Box	Region	Al	N	Tb	O	Si
1	AlN:Tb	43.2	38.7	1.4	15.8	0.01
2	Si	17.2	0	0.8	20.3	62.3

3.6.1 Tb–O co-segregation in annealed AlN:Tb

In general, rare-earth metal dopants (Kenyon, 2002, 2003) produce narrow optical emission lines almost insensitive to temperature. Hence, they find application in cathode ray tubes (CRTs), optical fibres, electroluminescence, etc.(Aitasalo et al., 2003) Tb is a very important rare-earth metal dopant in semiconductors and is used for green emission. A common application of Tb is tuning the green light component in incandescent lamps which give

white light. Over the years, there has been a lot of research on creating UV light emitting diodes (LEDs). In principle, AlN with a 6.2 eV bandgap should be able to give an emission at ~ 200 nm, but there are difficulties to overcome to make such UV emitters commercially available. This large bandgap makes AlN an ideal matrix for rare-earth ions which typically have emission wavelengths much longer than 200 nm. AlN combines high thermal conductivity with low electrical conductivity, which makes it ideal for certain electronic applications, e.g., as heat sinks and substrates for devices with low leakage currents. The Tb–Tb ionic interactions in semiconductors can be exploited to tune the emission from green to blue (Benz et al., 2013b). While segregation of P dopants in Si can constitute a problem for electronic devices, (Keizer et al., 2015) segregation of rare-earth atoms in lanthanide doped semiconductors may be beneficial: Rutherford Back-Scattering (RBS) has been used to show that Er ions in GaAs occupy displaced tetrahedral interstitial sites, (Takahei et al., 1994; Zavada et al., 1995) and there has been speculation about co-segregation with O and other impurities co-doping of which is known to enhance the luminescence intensity in Si (Michel et al., 1991), GaAs (Zavada et al., 1995), and AlN (Oliveira et al., 2004). For Er and O co-doped (Al)GaAs, a structural model of the defect consisting of one Er^{3+} and two O^{2-} ions with C_{2V} symmetry has been suggested based on the number of emission lines observed (Takahei et al., 1994), but no direct evidence could be put forward, and such complexes would need further vacancies to remain electrically neutral. While Eu doped anatase (Pal et al., 2012) and Eu doped magnesia (Rastogi et al., 2015) show series of strong luminescence lines in the range of 550–720 nm, Tb doped AlN (Penilla et al., 2013) and Tb doped but otherwise pure AlN (Wieg et al., 2012) both display similar emission triplets at around 490 nm and 540 nm. This differs from the seven emission lines in CL we observe for Tb doped and annealed AlN where we directly observe Tb and O co-segregation by STEM. The segregation of Tb in AlN and the local cluster arrangements can be studied and observed by spectroscopy methods like CL and EELS. The possible formation of Tb complexes in Tb doped AlN has been conjectured based on CL (Benz et al., 2013a). The concentration of Tb in our AlN sample is ~ 2 at.% as estimated by inductive coupled plasma-optical emission spectroscopy (ICP-OES) and energy dispersive X-ray spectroscopy (EDXS). A high resolution analytical STEM is needed to confirm directly segregation of single atoms into small complexes. In case of N K and O K in figs. 3.16(C,D), the contrast of the maps indicates anti-correlation, i.e. in the AlN region, O is replacing N (group V

TABLE 3.8: Cross-correlation between elemental maps in AlN region marked by box in fig. A.4(B).

X_{corr}	Al	N	Tb	O	Si
Al	1.0000	0.0802	0.0337	0.0012	-0.0920
N	0.0802	1.0000	-0.0366	-0.3694	-0.0060
Tb	0.0337	-0.0366	1.0000	0.3466	0.0064
O	0.0012	-0.3694	0.3466	1.0000	0.0188
Si	-0.0920	-0.0060	0.0064	0.0188	1.0000

sub-lattice). Tb must be replacing Al in the group III sub-lattice, although the corresponding decrease in local Al contrast is too small to be clearly visible in fig. 3.16(A). Table 3.8 lists the cross-correlation values (X_{corr}) between the elemental maps in the top half of AlN marked in fig. A.4(B), calculated using MATLAB function `corr2(x, y)`, where x and y are the elemental maps from figs. 3.16(A–E) at region A marked in fig. A.4(B). The cross-correlation of N and Tb map is negative. Similar observations can be made between N and O. The cross-correlation between Tb and O maps is positive, indicating the formation of Tb–O complexes. In conclusion, the STEM analysis demonstrates co-segregation of the Tb ions together with O ions (which are a common impurity of AlN) in AlN. These experimental results are consistent with atomistic simulations by Benz et al., (2013a,b) (Angadi et al., 2017).

3.7 Summary

Apart from the traditional and well known methods of dealing with noise, such as averaging, median filtering or PCA, an alternative approach to remove spikes arising due to dead pixels in the CCD detector is proposed. The Hampel filter used performs median absolute deviation to identify outliers locally and only replaces outliers with the local median whereas traditional smoothing filters tend to smooth the ionization edges which would adversely affect the ELNES. If the absolute residue between spectrum and the local median, $|s_i - m_i|$, is greater than three times the standard deviation (σ_i), then the local median, m_i , is substituted in place of an outlier. Two novel ionization edge detection algorithms are proposed to blindly detect core-losses even if the material is unknown. In the first method, the clusters of points with positive gradients near edge onset are detected by counting them. The method also makes use of a look-up table as in table 3.1 to make fine adjustment in

the edges detected. Cluster detection can detect edges efficiently when the core-loss has a clear, noise-free and positive onset. It was observed in case of Al L₃, that the edge overlapped with an artefact at channel number #100 due to a previously acquired ZLP. In such cases, even though the edge is clearly detected, the quantification maps will be noisy, as in fig. 3.13(A). At lower energies, ionization edge onsets are much closer. Hence, use of smaller counting windows might lead to false positive detection of core-loss edge onsets. The lookup table is modified in this particular case, where Al L₁ is added even though there is no reliable partial cross-section available for quantification. This was done to get an approximate elemental map of Al. The Al K elemental maps were showing large negative values due to the pre-edge region fitting for Al K being severely affected by EXELFS of the preceding As L_{2,3} edge and the Al K intensity was extremely feeble. The ionization edge was detected despite due to noise comparable to the Al K ionization onset but quantification failed. A similar effect was observed for Ge L_{2,3}. The Ge L_{2,3} is falsely detected due to a combination of noise and the EXELFS from the preceding Ga L_{2,3} edge. The look-up table method assumes the energy calibration is done correctly before applying edge detection routine. If the energy-loss is not well calibrated then there could be possible false positive detection of edge onsets, especially at lower energies where the edge onsets are close to each other. The P L_{2,3} quantification was affected by limited integration ranges. The edge detection method by counting the positive slope-angle gradient is a novel approach but ineffective when the onset does not have a definitive positive gradient at edge onset. Kundmann et al., (1991)'s approach of log-derivative had similar drawbacks. Hence the second method of edge detection was developed where the arctan function is applied to estimate the exponent for each channel of the spectrum, as in eqn. 3.11, rather than calculating the gradient itself, as in eqn. 3.7. This is a robust way for detecting edge onsets. The results from simulations used simulated or experimental spectra. The efficiency of the edge detection was tested for a variety of parameters, such as window length, noise, specimen thickness and simple averaging filter applied to spectra of various noise level, calculated as shown in eqn. 3.14. The detected edges were used to quantify the experimental EELS SIs, with a channel width, $w = 25$ pixels. It was observed in figs. 3.8, 3.9 and 3.10 that the distortion in gain correction has a large impact on determination of edge onset. Both edge detection algorithms work best when the high-loss spectrum has high SNR (> 30 dB), with constant/linear CCD gain correction, high dispersion (to reduce the effect of $-E^{-1}$ background in $\bar{\theta}$) and single

scattering distribution (i.e. deconvolved spectra). The automated selection of pre-edge regions and integration regions proposed avoids any user bias and when an unknown EELS SI is used as input, the output will be the elemental maps (areal density, x_j). The selection of pre-edge region is sometimes tricky at lower energies as the core-loss onsets are close to each other and the background fitting is affected by EXELFS of underlying core-losses as well as the long tails of the Poissonian distribution of bulk plasmon peaks. The EELS quantification is applied to three different test materials, such as GaAs (Ge-based) multi-junction solar cell (section A.1), $\text{In}_x\text{Ga}_{1-x}\text{N}/\text{GaN}$ thin films (section A.2) and AlN doped with Tb (section A.3). For the solar cell sample, the core-losses were acquired in three different SIs of different spatial sizes, as shown in table A.1. Sum spectra were extracted from each region described in fig. 3.13(E) for quantification and results have been tabulated in table 3.2. It is evident that regions 1, 2, 4, 6 and 7 are thin layers and data for them are limited by statistics. Hence, for further detailed analysis only regions 3, 5 and 8 were considered in table 3.2. Although the map of the Al $L_{2,3}$ edge is affected by the artefact as described above and can only be evaluated in so far as to rule out significant Al enrichment in any of the thicker regions, the Al K edge at 1560 eV is rather noisy but yields an Al K map in fig. 3.13(M) that indicates that Al may be present in parts of interfacial regions 4 and 6. The Al L_1 edge is very weak and for quantification the corresponding map in fig. 3.13(C) cannot be directly used. For computation of the Al fraction in table 3.2 we tentatively applied a partial scattering cross-section to Al L_1 one order of magnitude smaller than for Al $L_{2,3}$. The weak intensity in the Ge $L_{2,3}$ map is completely due to noise. The quantification of individual spectra generally lacks statistics due to noise. Considering instead the sum of spectra from sub-regions as labelled in fig. 3.13(E) not only provides better SNR but a computationally viable method for quantification. Each inclined row marked by red lines in fig. 3.13(E) consists of 24 spectra (for EELS SI_1) or 47 spectra (for all other SIs), whereas the wider regions numbered 3, 5 and 8 all contain several hundred spectra. Neglecting the signals from C (mainly surface contamination) and O (due to surface oxidation) the nominal values from table 3.2 for wider regions 3, 5 and 8 would indicate chemical compositions of the underlying thin layers of compound semiconductors of $\text{GaAs}_{0.84}\text{P}_{0.16}:\text{Si}$, $\text{Al}_{0.09}\text{In}_{0.37}\text{Ga}_{0.54}\text{P}:\text{As}$ and $\text{GaAs}:\text{P}, \text{Si}$, respectively, where the elements listed after the colon refer to minority elements in the detection range of 1 – 2 at.%, which however seems somewhat high for dopants. If we check the ratio of group III/V elements in these three compounds, that is, $(x_{\text{Al}} + x_{\text{In}} + x_{\text{Ga}})/(x_{\text{P}})$

+ x_{As}), the values of 1.06, 1.04 and 0.91 obtained from the above three regions are in reasonably good agreement with the expected value of unity for a stoichiometric III/V compound semiconductor. As previously stated, the proposed method is mainly a demonstration of automated background subtraction by identifying core losses, and plural scattering has not been taken into account in table 3.2. The effect from plural scattering could be pronounced for Al, Si and P $L_{2,3}$ edges as these display slightly delayed onsets while the integration ranges are small. Hence the effect of plural scattering will move intensity from the edge onsets to values beyond the range of the actual EELS measurement (for P) or the integration range (for Al and Si), so the measured intensities in the experiment may be significantly lower than the measured cross-sections calculated for single scattering would predict. A quick estimate based on the small widths of the integration ranges used here (15 eV for Al and Si, and 37.4 eV for P) relative to the plasmon energy of GaAs (~ 16 eV) shows that plural scattering could have reduced intensities of the Al and Si $L_{2,3}$ edges over the measured interval by factors of up to 2 for $t/\lambda \approx 1$, however, the concentrations for Al and Si are rather low anyway and so the precise values are perhaps not so relevant here, whereas the effect on the P $L_{2,3}$ edge will be much weaker. The effect of plural scattering could in principle be minimised by deconvolution with the low-loss spectrum, which is explored in chapter 4. The identification of the chemical composition in the smaller regions and at interfaces is strongly limited by counting statistics as well as a potential undersampling of the thinnest layers given the pixel sizes reported in table A.1.

Chapter 4

Advanced automated high-loss analysis of EELS

4.1 Introduction

The background modelling in EELS is predominantly done with an inverse power-law function as in eqn. 2.2 (Egerton, 2011b). At higher energy-losses an inverse power-law does not decay as rapidly as an exponential function. Hence, it can be seen in fig. 4.1 that an inverse power-law function crosses the spectrum. However, an exponential function, decays towards zero rapidly and the extracted core-losses do not have large zero crossings (or large negative residues). It is evident from eqn. 2.2 that at higher energy-loss the ‘base’ increases whereas the ‘exponent’ is constant, resulting in the overall function to flatten at higher energy whereas in exponential functions as in eqn. 2.3, the overall exponent is decreasing more rapidly towards zero. In energy-loss regions around ~ 100 eV, Tenailleau et al., (1992) have looked into the optimal length of pre-edge fit range for the traditional inverse power-law and exponential functions. Due to the presence of dominant bulk plasmon peak and plural scattering, the error in quantification is large. Hence Tenailleau et al., (1992) proposed a new background model, based on three parameters (eqn. 4.1), of the form:

$$I(E) = \exp [a \ln(E) + b + c f(E)] \quad (4.1)$$

where a , b and c are fitting parameters. It is similar to inverse power-law but an additional term, $f(E) = E^{-1}$, within an exponential. If eqn. 4.1 is reduced to shown in eqn. 4.2, it can be seen that an additional term added is nothing but an exponential decay function multiplied by an inverse power-law function:

$$I(E) = \text{const.} \cdot E^a \cdot \exp [c f(E)] \quad (4.2)$$

where constant term is $\exp b$, $b < 0 < E$ and $f(E) = E^{-1}$. Eqn. 2.3 is the sum of exponentials, where the number of exponentials are defined by the value of k . However, there are alternative models like n^{th} order log-polynomial function as shown in eqn. 4.3. The function has total of $n + 1$ fitting parameters, where n is the number of exponent, r , and one scaling parameter, A .

$$I(E) = A \cdot \exp(r_n E^n + r_{n-1} E^{n-1} + \dots + r_j E^j + \dots + r_1 E) \quad (4.3)$$

In higher energy-loss regions, typically greater than ~ 100 eV, some constraints has to be made to make the background model not to cross the spectrum. If a pre-edge region fit range is greater than 100 channels and the beginning channel number is below 25% of the length of the spectrum, then there is less chance of an inverse power-law crossing the spectrum (because the rate of decay is lower for inverse power-law function at high energy-losses), but a definite and analytical model is needed to improve the background fitting and quantification of the spectra. An example of this is shown in fig. 4.1.

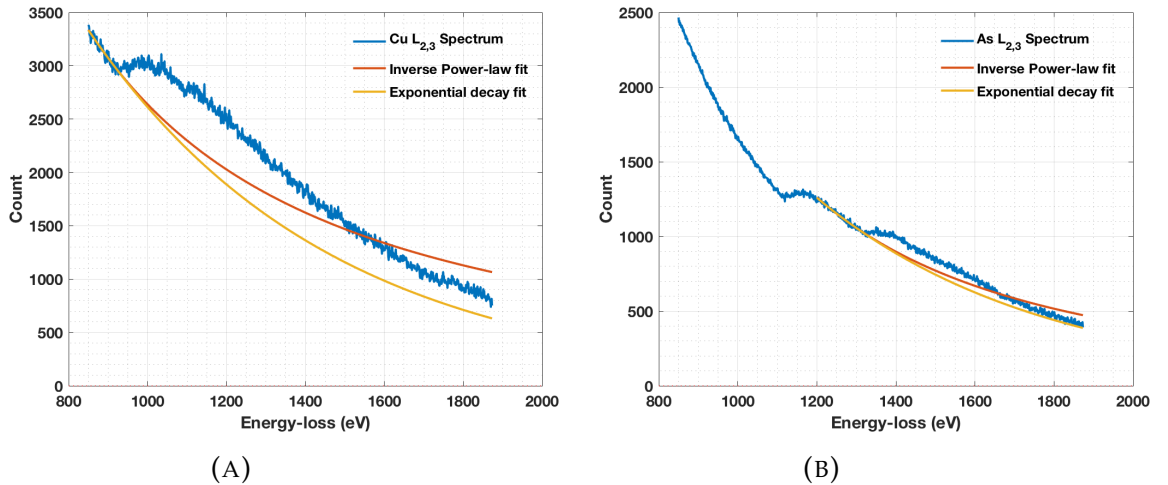


FIGURE 4.1: Power-law background fit crossing spectrum

4.2 Selection of background models

EELS is complex in nature due to the presence of the ZLP including phonons, plasmon scattering, near-edge structures (ELNES) and extended fine structures (EXELFS). These influence the extraction and quantification of core-loss edges through background subtraction. For extraction of core-losses

the conventional method of modelling the background only in pre-edge region is sometimes problematic and can even cross the spectrum, as shown in fig. 4.1. Therefore, we need to explore and study the applicability of the inverse power-law background (AE^{-r}) models as a function of energy-loss. In background subtraction, there is always a trade-off between systematic and statistical errors in quantification of core-losses. In some cases, either due to noise, near edge or extended fine structures in preceding edges, the extrapolated background can cross the spectrum, which leads to a large systematic under-estimate of the core-loss intensity. Background subtraction techniques with exponential fitting can be explored more systematically and a new approach on how the quantification can be improved by choosing different functions to fit in pre-edge regions is explored.

4.3 Optimal fit

The precision of EELS quantification with respect to spectrometer entrance aperture has been discussed by Bertoni et al., (2008). Modelling the background can also be explored more extensively by fitting an inverse power-law or exponential fit to the post-ionisation edge and shifting the background curve fitted downwards to pass through the edge onset. This leads to an over-estimate of the core-loss intensity. The best background fit and its reliability can be calculated from the error bars associated with the under and over-estimated intensities.

4.3.1 Background model in pre-edge region

Inverse power-law fits are modelled in the pre-edge region (range >30 eV). For the As $L_{2,3}$ edge, even though the R^2 values are good, the modelled background is crossing the spectrum as shown in fig. 4.2, due to the preceding Ga $L_{2,3}$ edge. A background crossing the spectrum predicts a negative core-loss intensity, which would be un-physical, although the As $L_{2,3}$ edge could still be quantified by integrating only the positive core-loss range. The Ga $L_{2,3}$ edge is straight forward as it has a very wide pre-edge region and the extrapolated background model will have negligible systematic errors. However, the background fits in pre-edge region for As $L_{2,3}$ are highly associated with large systematic errors if the integration ranges are large.

4.3.2 Background model in post-edge region

Inverse power-law fits can be extrapolated in the post-edge range from the end of the spectrum and offset vertically to cross through the edge onset. With post-edge background modelling, the As L_{2,3} edge has very large apparent cross-section, as shown in fig. 4.2. This indicates an over-estimate of the core-loss edge intensity. The Poissonian statistical error bars are, however, large. The Ga L_{2,3} edge is not straight forward to deal with in this way as it has very narrow post-edge region with varying gradient compared to the pre-edge region. To extrapolate by inverse power-law the post-edge region of the Ga L_{2,3} edge from end of the spectrum, the As L_{2,3} edge will have to be subtracted from the spectrum first. The background fit in post-edge regions are associated with large statistical errors if the integration ranges are small but large systematic errors if the integration range are wide. For post-edge modelling, statistical errors are difficult to assess from the knowledge of R^2 .

4.3.3 Background model with optimal fit

The inverse power-law fits in pre-edge and post-edge regions provide under-estimate (B_u) and over-estimate (B_o) of the core-loss edge intensity, respectively. The solution is to select backgrounds which are physically meaningful (yield positive core-loss intensity) and have small error bars. Hence, an optimal background (B_{opti}) may be given by eqn. 4.4.

$$B_{opti} = \frac{(B_u - \sqrt{I_u(\Delta)}) + (B_o + \sqrt{I_o(\Delta)})}{2} \quad (4.4)$$

$$I_u(\Delta) = \sum_{k=1}^{\Delta} S(k) - B_u(k) \quad (4.5)$$

$$I_o(\Delta) = \sum_{k=1}^{\Delta} S(k) - B_o(k) \quad (4.6)$$

where $\forall \Delta \in \mathbb{N}$, $I_u(\Delta)$ and $I_o(\Delta)$ are the cumulative intensity as a function of Δ for the net core-losses after subtracting modelled background in pre-edge and post-edge regions, respectively. $\sqrt{I_u(\Delta)}$ and $\sqrt{I_o(\Delta)}$ are the statistical error bars associated with under- and over-estimate, respectively. The upper (ε_u) and lower (ε_l) error bars associated with optimal background fit are given

by eqns. 4.7 and 4.8.

$$\varepsilon_u = \left(B_o + \sqrt{I_o(\Delta)} \right) - B_{opti} \quad (4.7)$$

$$\varepsilon_l = B_{opti} - \left(B_u - \sqrt{I_u(\Delta)} \right) \quad (4.8)$$

The error bars associated with optimal background are smaller than Poissonian statistics. The quantification of the Ga/As ratio in GaAs is then close to unity, with smaller systematic and statistical errors. The optimal background fitting yields Ga/As = 1.2759 when compared to 1.4101 with inverse power-law fitting in fit ranges and integration ranges described in fig. 3.14 for Ga and As only. Hence, it indicates that the improvements in R^2 values do not guarantee more accurate quantification. The optimal background can be used to extract core-losses from a spectrum and the underlying core-losses can be quantified with better statistics using larger integration ranges. The overestimated background is affected by thickness of the sample and

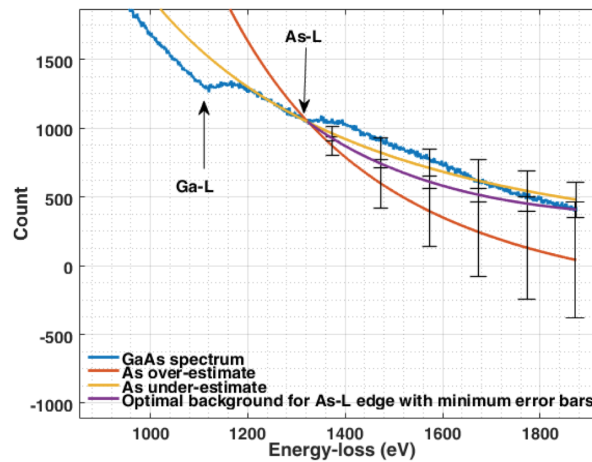


FIGURE 4.2: Experimental EELS of GaAs with $t/\lambda \approx 1$ with different background fits with error bars for As $L_{2,3}$ (Ga $L_{2,3}$ is more straight forward).

EXELFS. The optimal fit method is reliable for the thin sample (or single scattered spectrum) and post-ionization edge decays monotonically. This is the case for K edges. L and M edges are superposition of L_2 , L_3 and M_4 , M_5 respectively. The plural scattering effects on top of superimposed partial cross-section would mean that post-edge modelling other than K edges would not be reliable.

4.3.4 Considerations for background modelling

As discussed in section 4.1, the inverse power-law function is sometimes not ideal in describing the decaying background. In a modelled background using inverse power-law function at high-loss spectra, the *base* of the function (E , energy-loss) is increasing while the *exponent* is constant. This makes the function not to decay rapidly at higher loss. However, in the exponential decay functions, the *exponent* ($-rE$, from eqn. 2.3) is not constant. The magnitude ($| -rE |$) of the exponent is increasing linearly with energy-loss, while the *base* is constant, e . This is the reason why at energy-losses, exponential decay functions describe core-losses more effectively after the extrapolation when compared to the inverse power-law function. The EEL spectra are also limited by the finite collection semi-angle (β). Hence the number of counts in the spectra at higher-energies are lower than expected. This is another reason why an inverse power-law function crosses the spectrum at higher energy-losses as shown in figs. 4.1 and 4.2. There are some thumb rules that to be followed to ensure better modelling of the EELS background and hence reliable quantifications.

- In a given spectrum with two or more ionization core-loss edges, a combination of background models can be used, instead of using only inverse power-law (or other) functions to model background in pre-edge regions.
- Inverse power-law function is reliable if the pre-edge region is large (> 100 channels) and the pre-edge region is in the left most part of a given high-loss spectra. For e.g. if the spectrum has 1024 channel, the inverse power-law will be a reliable model in the first 256 channels, while the length of pre-edge is > 100 channels.
- At higher energy-loss part of high-loss spectra, an exponential decay function can be used to avoid, extrapolation crossing the spectrum. The pseudo code for the selection of background models shown in pseudo code.

4.4 Richardson-Lucy deconvolution

RL deconvolution is an iterative method of finding the maximum likelihood solution. The plural scattering spectrum, $S_{PSD}(E)$, is due to the convolution of the low-loss spectrum containing multiple bulk plasmons with the single

```

b ← model_begin_channel
e ← model_end_channel
E ← energy_loss
S ← spectrum
N ← length_of_E
procedure MODEL_SELECTION(b, e, E, S)
  if  $e - b + 1 > 100 \wedge b < N/4$  then
    back = iPower_law( $E[b : e], S[b : e]$ )
  else
    back = Exp_decay( $E[b : e], S[b : e]$ )
  end if
end procedure

```

scattering distribution spectrum, $S_{SSD}(E)$ as in eqn. 4.9. The normalised low-loss spectrum can be considered as a PSF, $S_{PSF}(E)$, which satisfies eqn. 4.10.

$$S_{PSD}(E) = S_{SSD}(E) * S_{PSF}(E) \quad (4.9)$$

$$\int_{-\infty}^{\infty} S_{PSF}(E) = 1 \implies \int_{-\infty}^{\infty} S_{PSD}(E) = \int_{-\infty}^{\infty} S_{SSD}(E) \quad (4.10)$$

The maximum likelihood estimation, $S_{est}(E)$, of single scattering distribution is shown in eqn. 4.11. The value of j indicates the current iteration number. The initial estimate, $S_{est}^{(0)}(E)$, can be initialised to plural scattered edge, $S_{PSD}(E)$. The term $\hat{S}_{PSF}(E)$ is the spatially reversed PSF, $S_{PSF}(E)$. The whole term in the parentheses is the error estimate at each iterations.

$$S_{est}^{(j+1)}(E) = S_{est}^{(j)}(E) \cdot \left[\frac{S_{PSD}(E)}{S_{est}^{(j)}(E) * S_{PSF}(E)} * \hat{S}_{PSF}(E) \right] \quad (4.11)$$

The RL deconvolution method assumes the spreading function, $S_{PSF}(E)$, complies with Poisson statistics. In implementations of RL deconvolution in standard routines like Hyperspy v1.3 (de la Peña et al., 2017b) or MATLAB¹ (MathWorks, 2017), the deconvolved spectrum (or data) will not have any negative values. All negative values are clipped at 0. Hence, the noise statistics arising from the RL deconvolution is biased, eqn. 4.12.

$$\int_{-\infty}^{\infty} S_{est}(E) = \int_{-\infty}^{\infty} S_{SSD}(E) + \epsilon, \epsilon \geq 0 \quad (4.12)$$

¹The standard routine in MATLAB for RL deconvolution is `SSD = ... deconvlucy(PSD, PSF, iter)`.

There are ways to work around this by adding and subtracting an offset before and after deconvolution, respectively but RL deconvolution works best when the spreading function is pure Poisson statistics, as shown in figs. 4.3(A,B). In fig. 4.3(A), the description of simulation of three low-losses are:

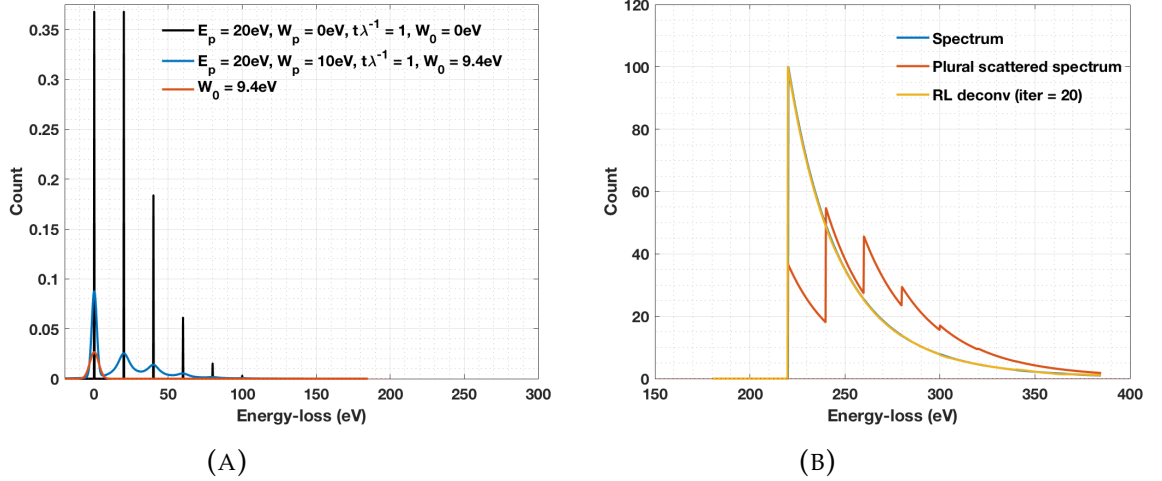


FIGURE 4.3: (A) Simulated low-losses (black) pure Poissonian, (blue) mixture of Gaussian and Lorentzians weighed according to Poisson statistics and (orange) a pure Gaussian. (B) Saw-tooth (hydrogenic model) edge. The plural scatter is generated by convolving the single scattered hydrogenic edge with pure Poissonian low-loss. The RL deconvolution is applied to recover the single scattering distribution.

- Black line: Simulated low-loss, $S_{PSF}(E)$, with pure Poissonian statistics as shown in eqn. 2.20 at every $E = n \cdot E_p$ where $n \in \mathbb{N}_0$ with relative thickness, $t/\lambda = 1$, bulk plasmon width, $W_p = 0$ eV, plasmon position, $E_p = 20$ eV and ZLP FWHM, $W_0 = 0$ eV².
- Blue line: Simulated low-loss, $S_{PSF}(E)$, with relative thickness, $t/\lambda = 1$, plasmon width, $W_p = 10$ eV, plasmon position, $E_p = 20$ eV and ZLP FWHM, $W_0 = 9.42$ eV. At $n = 0$, $S_{PSF}(0)$ is a Gaussian with FWHM of W_0 and $n \in \mathbb{N}$, $S_{PSF}(n \cdot E_p)$ are Lorentz functions weighed according to eqn. 2.20.
- Orange Line: Simulated low-loss, $S_{PSF}(E)$, with a pure Gaussian function at $S_{PSF}(0)$ of FWHM, $W_0 = 9.42$ eV. The low-loss has no bulk plasmon loss just to test the behaviour of RL deconvolution in the presence of non Poissonian spreading functions.

²Note: The ZLP FWHM, $W_0 = 9.42$ eV is taken as wide as possible only to test the extreme cases.

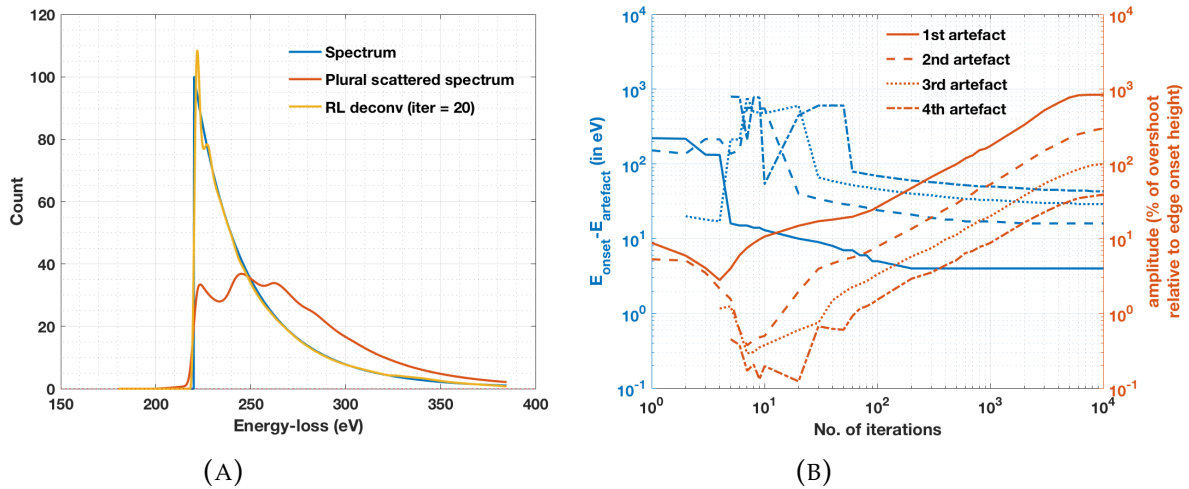


FIGURE 4.4: (A) RL deconvolution method applied to the plural scattered saw-tooth (hydrogenic) edge. The plural scattered saw-tooth is generated by convolving the single scattered hydrogenic edge with low-loss simulated from a mixture of Gaussian and Lorentzian weighed according to Poissonian statistics. (B) Trace of position and amplitude of the first 4 ringing artefacts with increase in number of iterations during RL deconvolution of plural scattered edge in (A).

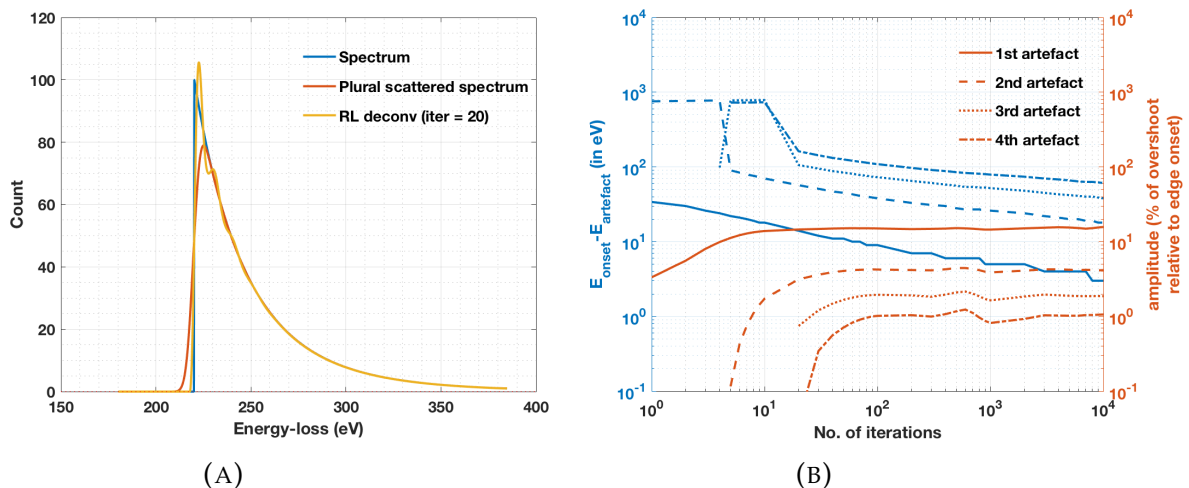


FIGURE 4.5: (A) RL deconvolution method applied to a plural scattered saw-tooth (hydrogenic) edge. The plural scattered saw-tooth is generated by convolving the single scattered hydrogenic edge with low-loss simulated from a pure Gaussian. (B) Trace of position and amplitude of the first 4 ringing artefact with increase in number of iterations during RL deconvolution of plural scattered edge in (A).

In fig. 4.3(B), it is evident that the RL deconvolution almost perfectly recovers the single scattering distributed spectrum (hydrogenic model). This is due to the fact that the spreading function has pure Poissonian statistics. However, if other components are present in the spreading function, such as a Gaussian, then the deconvoluted spectrum, $S_{est}(E)$, is affected by ringing artefacts, as can be observed in figs. 4.4(A) and 4.5(A). The position and amplitude of the first 4 dominant ringing artefacts with respect to number of iterations of RL deconvolution are shown in figs. 4.4(B) and 4.5(B). These are the ringing artefacts present in figs. 4.4(A) and 4.5(A), respectively. As the number of iterations increases the amplitude of the ringing artefacts increases and their positions are closing in towards the edge onset. High frequency components arising due to discontinuities at the end of the spectrum. The standard extrapolations by any finite impulse response (FIR) filters like Hann³ (or cosine, eqn. 4.13) windows or inverse power-law can be used to make the beginning and end of the spectrum converge to the same intensity level (≈ 0).

$$w(n) = \frac{1}{2} \left(1 - \cos \left(\frac{2\pi n}{N} \right) \right) : 0 \leq n \leq N \quad (4.13)$$

The extrapolation (of both end of the spectrum) by inverse power-law or exponential function fails if the tails of the edge are ending at higher counts at the end of the spectrum. Hence, the best way to extrapolate is by mirroring the whole spectrum before applying the deconvolution. This way, the discontinuities at the end of spectrum can be avoided. This is valid irrespective of the tail height of the edge and there is no complexity involved in selecting the size of the window as in case of extrapolation. Hence the ringing artefacts during RL deconvolution are due to the presence of Gaussian components which RL fails to model. Related to the ringing artefacts, a major disadvantage of the RL deconvolution method is the selection of an appropriate number of iterations. The amplitude of the ringing artefacts are increasing with the number of iterations. As it can be noted in figs. 4.4(B) and 4.5(B), the 2nd through 4th artefact are very low until at least iteration #15. As the number of iterations is increased beyond \sim #20, the artefacts are creeping in towards the edge onset and their amplitude is also increasing. This is true for any experimental spectrum, as the low-loss is a mixture of Poissonian and Gaussian statistics.

³The standard routine in MATLAB for Hann window is $w = \text{hann}(L)$, where L is the length of the window and $L = N + 1$

4.5 Considerations while applying deconvolution

The energy dispersion (eV/channel) of both plural scattered, $S_{PSD}(E)$, and normalised low-loss function, $S_{PSF}(E)$, must be the same. If the dispersions are not same then the normalised low-loss can be interpolated to match the dispersion of the plural scattered spectrum. But while applying deconvolutions, the lengths of $S_{PSD}(E)$ and normalised low-loss function, $S_{PSF}(E)$, must be the same. This is because of element-wise division of Fourier coefficients. This will be considered as an additional advantage of extrapolation. The extrapolation of signal will not only remove discontinuities in the signal but also help in matching the lengths of the spectra. As discussed in sections 4.4, 2.6 and 2.7, to minimise boundary discontinuities, multiplication by an inverse cosine or inverse power-law function are common extrapolation methods. These extrapolation functions, $f_{ext}(E)$, are generally quite efficient way to extrapolate because there is no discontinuity of the n^{th} derivative of these function as described in eqn. 4.14. Other extrapolation functions can be used such as a Gaussian, which approaches zero rapidly and its n^{th} derivative is also a Gaussian and continuous, as described in eqn. 4.14.

$$\lim_{n \rightarrow +\infty} \frac{d^n}{dE^n} f_{ext}(E) \neq \pm\infty \quad (4.14)$$

If the length of the plural scattering distribution and normalised low-loss are same, then instead of extrapolation, flipping both spectra is a better way to avoid discontinuity and the computational complexity decreases. The situations where the intensity of the plural scattered core-loss is truncated due to end of the spectrum (as is the case of P L_{2,3} for 80 eV offset EELS SI of multi-junction solar cell), the mere extrapolation and deconvolution cannot redistribute intensity from extrapolated part and recover the single scattering signal. If the plural scattering distribution is flipped over, then the truncated intensity can be recovered from the flipped spectrum. A continuous spectrum appended by its flipped version is always continuous. The point of contact between the spectrum and flipped version can be smoothed with a Gaussian to avoid any kink should it exists. The flipping extrapolation also complies with eqn. 2.23.

$$\mathcal{F}\{S_{PSF}(E - E_k)\} = e^{-j\omega E_k} \cdot \mathcal{F}\{S_{PSF}(E)\} \quad (4.15)$$

In $S_{PSF}(E)$, conventionally the maximum of the spectrum ($\|S_{PSF}(E)\|_{+\infty}$) is considered as the peak of the zero-loss. The ZLP must be rotated circularly

to bring the position of the maximum to channel #1. This is because all routines by default consider #1 (or #0) as the location of ZLP. If the zero-loss is not shifted to channel #1, then as per discrete Fourier transform (DFT) lateral-shift property⁴ as in eqn 4.15, a complex exponential is multiplied to the recovered single scattering spectrum, as shown in eqn. 4.15. Hence, there is a need to ensure that while applying FFT, there is no energy-shift in the deconvoluted spectrum.

4.6 Baseline correction to background fit

An alternative background subtraction method for quantification is by linear/non-linear least-squares methods. In these methods a reference spectrum is used to model the experimental spectrum and the fitting (scaling) parameters are used to express the relative weights in at.%. The reference spectrum can either be obtained experimentally or can be modelled using standard hydrogenic models or Hartree-Slater differential cross-sections. The major advantage of least-squares fit methods of quantification is to avoid errors due to deconvolution. As discussed in previous sections, the noise level is always increased by deconvolution. The reference (or modelled) single scattering spectrum can be convoluted with the low-loss spectrum to get the spectrum modelled with plural scattering. This can be used to compensate for the errors arising due to approximations used in eqn. 2.5 due to plural scattering. The exponent of the background fit, which describes the rate at which the background decays, is not same at every pixel in the SI. It is evident from fig. 3.12 that each row of spectra in SI has a different decay rate of the background even though all spectra have been acquired with same collection semi-angle (β) and exposure time (τ). However, the decay of the background in the proximity of the ionization edge is influenced by the specimen thickness. Various least-square fitting models can be used to quantify a spectrum. However, not all the models are consistent and may not produce the same results. In this section, we study five different models for GaAs along with Cu edge to check the consistency of the models. The eqn. 4.16 fits only $n \in \mathbb{N}$ differential cross-sections, $\sigma_n(E, \Delta, \beta, E_0)$, to the residual spectrum, $S_{res}(E)$,

⁴DFT is an infinite signal system. But FFT is an N -point spectrum. Hence shifting by E_k actually wraps the pixels at the end of the spectrum to the beginning of the spectrum.

where $p = [p_1, \dots, p_n] \in \mathbb{R}$ are the fitting parameters.

$$S_{res}(E) = \begin{bmatrix} p_1 \\ \cdot \\ \cdot \\ p_k \end{bmatrix}^\top \left\{ S_{PSF}(E) * \frac{\partial}{\partial E} \begin{bmatrix} \sigma_1(E, \beta, E_0) \\ \cdot \\ \cdot \\ \sigma_n(E, \beta, E_0) \end{bmatrix} \right\} \quad (4.16)$$

where k is the number of fitting parameters and n is number of cross-sections. The residual spectrum, S_{res} , is obtained by subtracting the background from the left most ionization edge. This indicates that the background needs to be subtracted prior to the quantification. Hence a pre-knowledge of background region is necessary for the quantification. The disadvantage of modelling with eqn. 4.16 is due to the presence of potentially large systematic errors arising from extrapolation of modelled background, $B(E)$, based on only small numbers of channels if the lowest ionization edge occurs close to the left side of the spectra. The systematic errors add additional offsets to the higher energy core-losses, hence, create an over- or under-estimates to the quantification of all other ionization edges at higher energies.

$$S(E) = p_1 B(E) + \begin{bmatrix} p_2 \\ \cdot \\ \cdot \\ p_k \end{bmatrix}^\top \left\{ S_{PSF}(E) * \frac{\partial}{\partial E} \begin{bmatrix} \sigma_1(E, \beta, E_0) \\ \cdot \\ \cdot \\ \sigma_n(E, \beta, E_0) \end{bmatrix} \right\} \quad (4.17)$$

Eqn. 4.17 is similar to the eqn. 4.16, but in this case, a known background in the pre-edge region, $B(E)$, is used in the model to fit along with the ionization core-losses. The fitting parameter p_1 is used as a scaling parameter for $B(E)$. This makes small improvements in minimizing the systematic errors. The fitting parameters, $[p_2, \dots, p_k]$, are used to quantify, ionization core-losses in at.%.

$$S(E) = p_1 B(E) + \begin{bmatrix} p_2 \\ \cdot \\ \cdot \\ p_{k-2} \end{bmatrix}^\top \left\{ S_{PSF}(E) * \frac{\partial}{\partial E} \begin{bmatrix} \sigma_1(E, \beta, E_0) \\ \cdot \\ \cdot \\ \sigma_n(E, \beta, E_0) \end{bmatrix} \right\} + p_{k-1} E + p_k \quad (4.18)$$

The scaling of pre-modelled background, $B(E)$, may not be reliable enough to completely remove all systematic errors. Some alternative methods are needed to deal with such problems. A baseline correction to modelling of

spectra with least-squares fitting is proposed in eqns. 4.18–4.20. In eqn. 4.18 a simple linear baseline is added to the model. The parameter, p_1 , is scaling parameter for the background, $B(E)$. The fitting parameters to ionization core-losses are $[p_2, \dots, p_{k-2}]$. The baseline given by $p_{k-1}E + p_k$, is of the slope-intercept linear form, $mx + c$. The terms p_{k-1} and p_k determines the slope and intercept respectively.

$$S(E) = p_1 B(E) \cdot E^{p_2} + \begin{bmatrix} p_3 \\ \cdot \\ \cdot \\ p_{k-2} \end{bmatrix}^\top \left\{ S_{PSF}(E) * \frac{\partial}{\partial E} \begin{bmatrix} \sigma_1(E, \beta, E_0) \\ \cdot \\ \cdot \\ \sigma_n(E, \beta, E_0) \end{bmatrix} \right\} + p_{k-1}E + p_k \quad (4.19)$$

Eqn. 4.19 not only scales the background but multiplies it with the term E^{p_2} . If $B(E)$ is an inverse power-law function as in eqn. 2.2 the effective exponent in the power-law background becomes $(-r + p_2)$. The parameters $[p_3, \dots, p_{k-2}]$ are the fitting parameters of reference spectra and can be used to get relative quantification of the core-losses.

$$S(E) = p_1 B(E)^{p_2} + \begin{bmatrix} p_3 \\ \cdot \\ \cdot \\ p_{k-2} \end{bmatrix}^\top \left\{ S_{PSF}(E) * \frac{\partial}{\partial E} \begin{bmatrix} \sigma_1(E, \beta, E_0) \\ \cdot \\ \cdot \\ \sigma_n(E, \beta, E_0) \end{bmatrix} \right\} + p_{k-1}E + p_k \quad (4.20)$$

Eqn. 4.20 has the additional fitting parameter p_2 used in a different way, as an exponent to the background model, $B(E)$. If $B(E)$ is an inverse power-law function as in eqn. 2.2, then its exponent are scaled by a factor p_2 i.e. $(-r \cdot p_2)$. The parameters $[p_3, \dots, p_{k-2}]$ are the fitting parameters to the reference ionization core-losses and p_{k-1} and p_k model the slope-intercept baseline. A list of the above descriptions of eqns. 4.16–4.20 is shown in table 4.1. All the fitting parameters, $p_k \forall k$, from eqns. 4.16–4.18, are linear in nature. Hence, these models are commonly known as MLLS methods of quantification of EELS (Leapman et al., 1988). However, models in eqns. 4.19 and 4.20 have a non-linear fitting parameter p_2 . Hence, they are known as non-linear least-squares (NLLS) method of quantification of EELS. The models all seem similar but, surprisingly, the quantification of ionization cross-section depends heavily on the type of model chosen. This is illustrated in all three regions 3, 5 and 8 of the GaAs on Ge based multi-junction solar cell with 950 eV offset for joint fitting of Cu L_{2,3}, Ga L_{2,3} and As L_{2,3} in tables 4.2–4.4. The Cu L_{2,3} is dominant only in region 2, however, Since the edge detection algorithm would have

TABLE 4.1: The attributes associated with each formulas from eqn. 4.16 to 4.19.

Eqn.	S ⁽¹⁾	S _{Res} ⁽²⁾	Scale Back ⁽³⁾	Back Power ⁽⁴⁾	pdfc ⁽⁵⁾	Baseline
4.16		✓			✓	✓
4.17	✓		✓		✓	
4.18	✓		✓		✓	✓
4.19	✓		✓	✓ (Add powers)	✓	✓
4.20	✓		✓	✓ (Multiply powers)	✓	✓

- (1) Spectrum; (2) Residue Spectrum;
(3) Scaled background; (4) Non-linear background;
(5) Plural scattered theoretical differential cross-sections.

detected all three ionization edges in the SI, it is necessary to include all of them to fit the core-losses. In the three regions of the multi-junction solar cell where Cu should not be present. It is expected that the quantification of Cu in these region should have a mean value close to zero. Regions 3 and 8 are GaAs doped with Si. Hence, it is expected that Ga and As should each reach ~ 50 at.%. Region 5 has AlGaInP doped with As Note that the Al K edge at 1560 eV is very faint and therefore buried in the noise dominated by gain correction irregularities of the CCD (ref: fig. 3.8). The Hartree-Slater ioniza-

TABLE 4.2: Relative quantification of elemental maps at region 3 as shown in fig. 4.7(D) (GaAs).

Eqn.	Cu L _{2,3}		Ga L _{2,3}		As L _{2,3}		Cu L _{2,3}	Ga L _{2,3}	As L _{2,3}
	Mean	Std	Mean	Std	Mean	Std	at. %	at. %	at. %
4.16	-2.47	3.45	39.70	8.74	51.65	14.95	-2.78	44.67	58.11
4.17	2.75	2.47	41.87	10.67	63.76	27.58	2.54	38.63	58.83
4.18	-6.79	3.09	30.26	5.34	38.71	8.72	-10.92	48.67	62.26
4.19	-2.42	1.49	31.45	5.78	37.95	8.84	-3.61	46.95	56.66
4.20	-0.28	1.17	28.51	4.71	31.63	6.34	-0.47	47.63	52.84

tion cross-sections of Cu L_{2,3}, Ga L_{2,3} and As L_{2,3} have been convoluted with the low-losses and fitting parameters used according eqns. 4.16–4.20 to fit these theoretical cross-sections to the experimental intensities. These terms

TABLE 4.3: Relative quantification of elemental maps at region 5 as shown in fig. 4.7(D) (GaAs).

Eqn.	Cu L _{2,3}		Ga L _{2,3}		As L _{2,3}		Cu L _{2,3} at.%	Ga L _{2,3} at.%	As L _{2,3} at.%
	Mean	Std	Mean	Std	Mean	Std			
4.16	-6.80	1.97	20.45	5.73	11.43	4.24	-27.11	81.54	45.57
4.17	-0.45	1.28	23.47	6.40	28.33	7.43	-0.88	45.70	55.18
4.18	-2.97	1.75	19.58	6.13	6.58	2.63	-12.79	84.41	28.38
4.19	-1.63	1.17	19.44	6.26	5.68	2.89	-6.95	82.77	24.18
4.20	-1.79	1.25	19.16	6.66	5.11	3.38	-7.96	85.24	22.72

TABLE 4.4: Relative quantification of elemental maps at region 8 as shown in fig. 4.7(D) (GaAs).

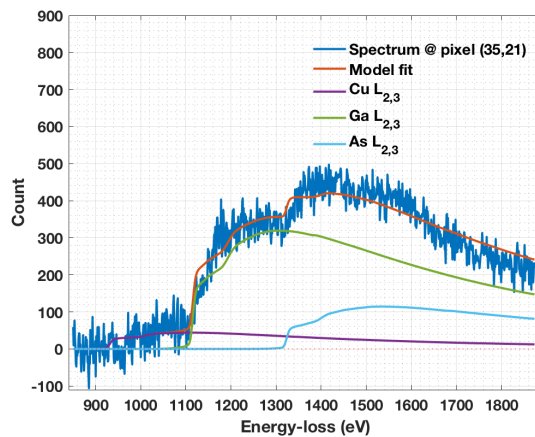
Eqn.	Cu L _{2,3}		Ga L _{2,3}		As L _{2,3}		Cu L _{2,3} at.%	Ga L _{2,3} at.%	As L _{2,3} at.%
	Mean	Std	Mean	Std	Mean	Std			
4.16	-6.16	3.09	33.04	4.46	51.55	3.61	-7.86	42.13	65.73
4.17	1.62	1.91	36.35	5.91	71.67	12.27	1.48	33.15	65.37
4.18	-6.44	2.30	26.99	5.85	41.14	2.99	-10.44	43.75	66.68
4.19	-2.50	1.85	26.47	5.48	38.94	3.11	-3.98	42.07	61.90
4.20	-1.85	1.40	23.68	6.58	34.24	3.27	-3.29	42.23	61.06

are deduced and are shown in eqn. 4.21.

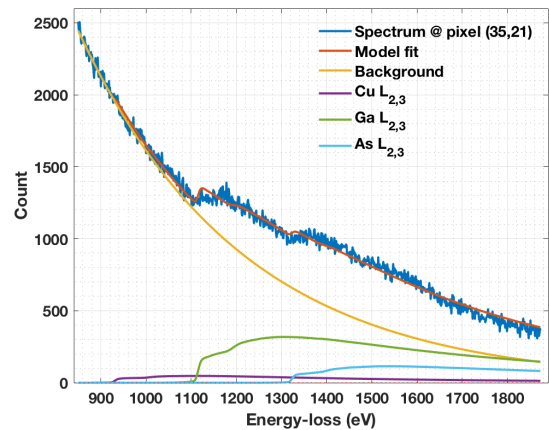
$$\begin{bmatrix} p_1 \\ p_2 \\ p_3 \end{bmatrix}^\top \left\{ S_{PSF}(E) * \frac{\partial}{\partial E} \begin{bmatrix} \sigma_{CuL_{2,3}}(E, \beta, E_0) \\ \sigma_{GaL_{2,3}}(E, \beta, E_0) \\ \sigma_{AsL_{2,3}}(E, \beta, E_0) \end{bmatrix} \right\} \quad (4.21)$$

It is evident that the reliability of relative quantification among Cu, Ga and As has increased from eqn. 4.16 through eqn. 4.20. Although, the relative quantification of Ga and As is not precisely at 50 at.%, the quantification from are close to the expected at.% values and the error in quantification of Cu has significantly reduced. This is due to minimization of systematic errors. It is worth noting that eqns. 4.19 and 4.20 are similar and the only difference is placement of the fitting parameter p_2 . However, the relative quantification values from eqn. 4.20 in regions of GaAs are slightly better with respect to eqn. 4.19. One can also argue that the overall coefficient of residuals, R^2 , might have improved (including the background while calculating R^2) but adjusted R^2 , (a.k.a R^2_{adj}) will drop. However, R^2_{adj} values are of consequence if the number of fitting parameters are comparable to the

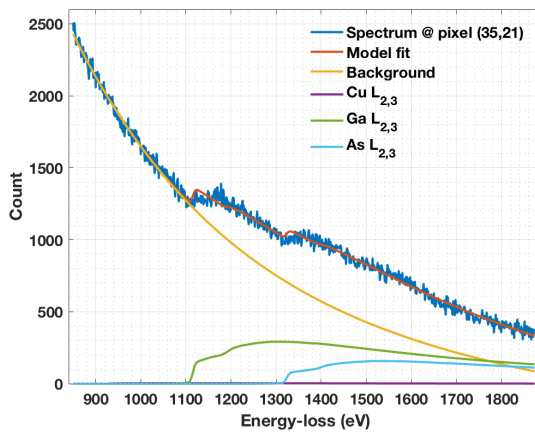
number of data points (number of channels). Fig. 4.6 show individual fits of all the models from eqn. 4.16 through eqn. 4.20 for pixel (35, 21) in region 3 (GaAs) and 950 eV spectrum offset. It is important to note that the R^2 mentioned below the images are calculated after subtracting the background. Hence while calculating R^2 , only weighted Hartree-Slater cross-sections are used from each models. The R^2 values are decreasing where as the quantification has improved through eqns. 4.16–4.20. This significantly suggesting that only modelling net core-loss intensity to best R^2 would not produce best results. The quality of background model plays significant role in determination of quantification. Modelling single background for one ionization edge and stacking the theoretical models also would not consider the background successive ionization edges. The eqns. 4.16 and 4.17 are significantly overestimating the Cu content (~ 6.5 at.%). The As edge intensity is underestimated (~ 33.7 at.%), while eqns. 4.18–4.20 have estimated Cu $\lesssim 2.2$ at.% and Ga and As within 5 at.% error. The values are not ideal, but are significant improvements over eqn. 4.16 and 4.17. The elemental maps calculated by eqn. 4.20 with offsets of 80 eV, 250 eV and 950 eV EELS SI are shown in fig. 4.7. It is interesting to note that Al $L_{2,3}$ map is not only noise (intensity in region 2 is noise) even though a distortion (at channel number $\sim \#100$ due to ZLP which was acquired before) is present, as shown in fig. 3.12. When Al $L_{2,3}$ is included, the relative quantification in region 5 is $\text{Al}_{0.48}\text{In}_{0.31}\text{Ga}_{0.21}\text{P}:\text{As}$. In section 3.4, it was quantified using Al L_1 edge, which had underestimated as $\text{Al}_{0.09}\text{In}_{0.37}\text{Ga}_{0.54}\text{P}:\text{As}$. The table 4.5, lists the relative quantification of region 3, 5 and 8 from GaAs multi-junction solar cell. As there is no model reliable for partial cross-section for L_1 edges, Al $L_{2,3}$ edge is considered. In all the regions listed in table 4.5, do not have any quantification value that is going large negative or large positive as was the case in traditional background subtraction method. Hence in table 3.2, those outlying negative values were clipped at zero to calculate the relative quantification, however, this was not the case here. The values again are not perfectly describing the stoichiometry of the material, this is due to the fact that all the SI were acquired independently with different exposure time (τ), dispersion (eV/channel) and pixel sizes. This causes, the background to be different in each SIs. This is the major drawback in quantification of EELS. The core-losses are far apart and to quantify the core-losses reliably, all the edges must be on the same background which is difficult to obtain when there are various edges at different energy onsets. The errors in calculation of theoretical cross-section also plays an important role in reliability of quantification in least-squares methods.



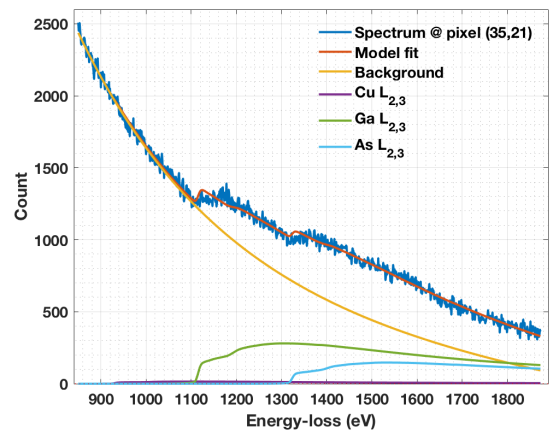
(A) Cu = 6.31%, Ga = 59.92%, As = 33.77% and $R^2 = 0.9553$.



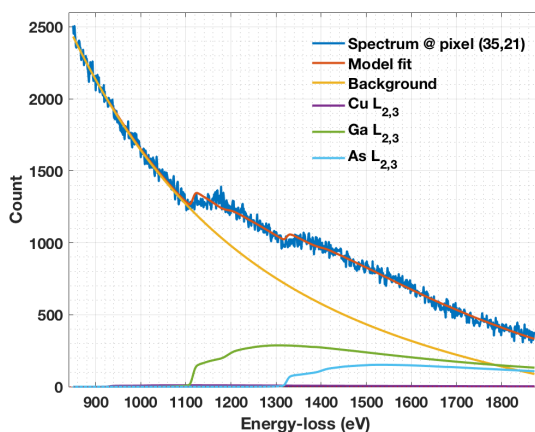
(B) Cu = 6.74%, Ga = 59.53%, As = 33.73% and $R^2 = 0.9548$.



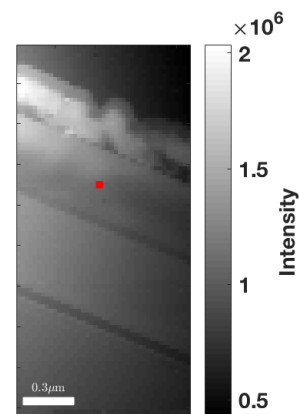
(C) Cu = 0.56%, Ga = 53.76%, As = 45.68% and $R^2 = 0.9551$.



(D) Cu = 2.19%, Ga = 53.59%, As = 44.23% and $R^2 = 0.9544$.



(E) Cu = 1.40%, Ga = 53.76%, As = 44.84% and $R^2 = 0.9486$.



(F) Pixel (35, 21) location in region 3.

FIGURE 4.6: Least-squares fits for all the proposed models. (A) eqn. 4.16. (B) eqn. 4.17. (C) eqn. 4.18. (D) eqn. 4.19 and (E) eqn. 4.20. (F) Location of pixel (35, 21) in region 3 shown in STEM image.

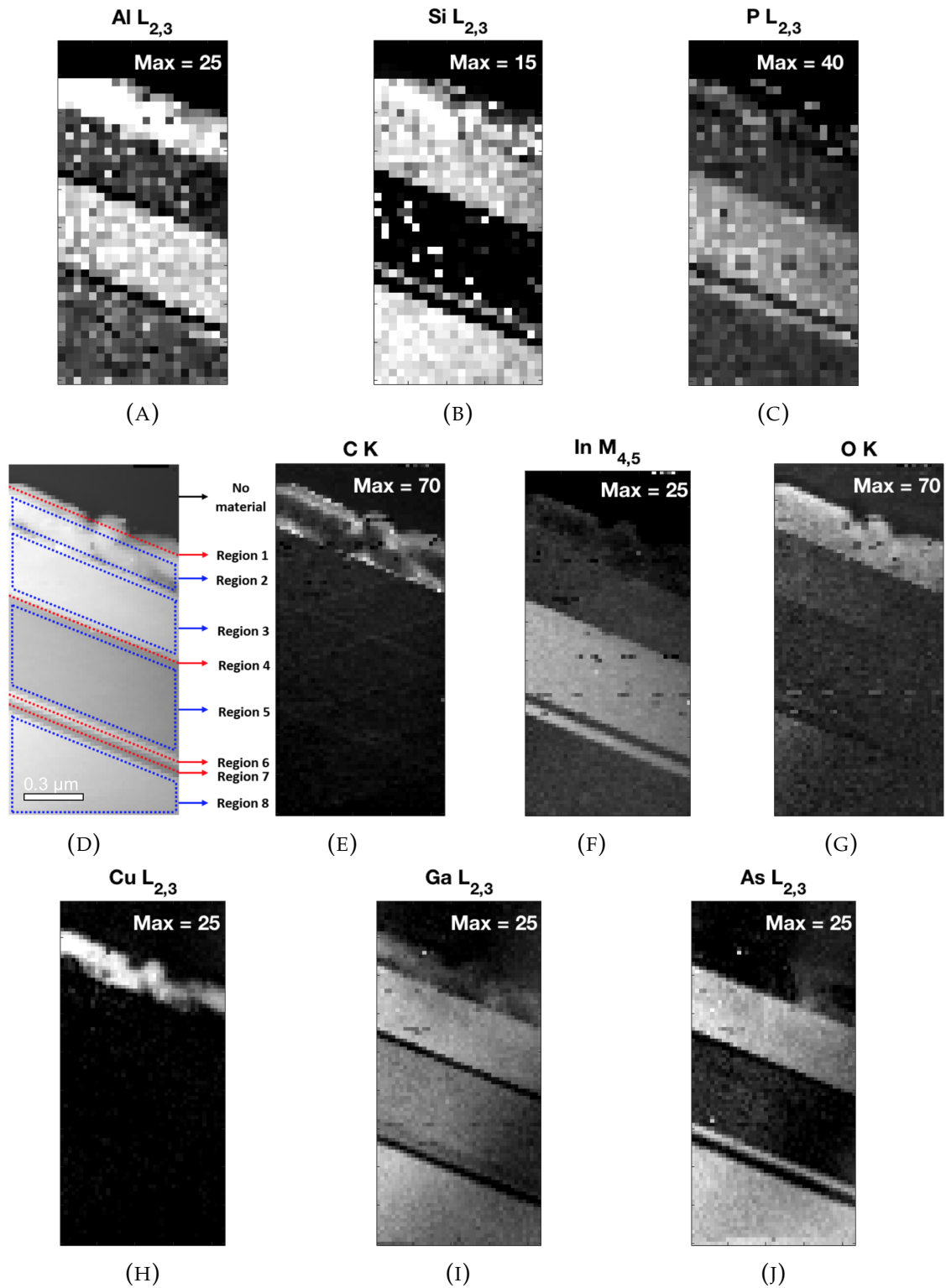


FIGURE 4.7: Elemental maps obtained from baseline corrected eqn. 4.20. (A–C) maps are from EELS SI with 80 eV offset. (D–F) from EELS SI with 250 eV offset and (G–I) from EELS SI with 950 eV offset.

TABLE 4.5: Quantification in atomic percent (at.%) of region 3, 5 and 8 of the three GaAs multi-junction solar cell SIs recorded as discussed in section A.1. The sum of all concentrations has been normalised to 100% according to eqn. 3.17.

Dispersion (eV/channel)	Exposure time (τ) (s)	t/λ	80 eV offset			250 eV offset			950 eV offset		
			Si L _{2,3}	Al L _{2,3}	P L _{2,3}	C K	In M _{4,5}	OK	Cu L _{2,3}	Ga L _{2,3}	As L _{2,3}
Region 3	0.95	11.92	6.65	8.21	9.16	5.12	15.49	-0.23	14.00	15.59	
Region 5	1.01	-1.74	21.15	23.27	6.11	14.05	12.00	-0.92	9.20	2.66	
Region 8	1.11	11.64	7.95	10.15	1.96	5.59	12.39	-1.03	11.62	17.35	

The error associated with K edges (hydrogenic models) is $\sim 5\%$, L edges and M and N edges (Hartree-Slater models) is $\sim 10 - 20\%$ and $\gtrsim 20\%$ (Egerton et al., 1979, 1993; Gatan, 2016; Rez, 1982).

4.6.1 Comparison with standard routines

The quantified values from eqn. 4.20 for Ga and As are still far from perfect 50 : 50 in regions 3 and 5. This is due to systematic errors are still getting cascaded for overlapping edges. The values quantified by eqn. 4.20 are compared with the standard available routines like Hyperspy and Gatan's DigitalMicrograph™. Thomas et al., (2012) have proposed that core-losses can be independently fitted by dividing the spectrum into different regions. Thomas et al., (2012)'s algorithm uses combination of MLLS as well as standard integral method. Their algorithm need pre-edge region for each edge and integration range as in case of integral method of quantification. The same is implemented in DigitalMicrograph™(Gatan, 2015). The values of quantification in baseline corrected least-squares fitting are better in region 3 and region 5. However, DigitalMicrograph™provide better results for As in region 8. However, in regions 5 As is a largely underestimated and large error bars. The expected Ga content in region 5 with respect to Cu and As is 100%. Hyperspy is not producing the results close to the expected value. However, the baseline corrected least-squares fit is estimating Ga content at $\sim 85\%$ as shown in table 4.7 and not producing large outliers. When the

TABLE 4.6: Relative quantification of Cu, Ga and As elemental maps with Hyperspy, DigitalMicrograph™and EELSAnalyser in region 3 shown in fig. 4.7(D) (GaAs).

Region 3 (0:50:50)	Cu L _{2,3} at.%	Ga L _{2,3} at.%	As L _{2,3} at.%
Hyperspy	8.76 ± 15.34	49.53 ± 5.20	41.72 ± 14.04
DigitalMicrograph™	3.39 ± 2.33	57.27 ± 4.7	36.60 ± 5.89
EELSAnalyser	-0.47 ± 12.27	47.63 ± 13.09	52.84 ± 13.76

relative quantification is applied to all the three SIs (80 eV, 250 eV and 950 eV spectrum offsets as described in table A.1) for GaAs solar cell, as shown in table 4.5 the values describe similar discrepancies as in table 3.2.

TABLE 4.7: Relative quantification of Cu, Ga and As elemental maps with Hyperspy, DigitalMicrograph™ and EELSAnalyser in region 5 shown in fig. 4.7(D) (GaAs).

Region 5 (0:100:0)	Cu L _{2,3} at.%	Ga L _{2,3} at.%	As L _{2,3} at.%
Hyperspy	9.63 ± 362.14	301.31 ± 4885.24	-210.93 ± 4587.24
DigitalMicrograph™	3.09 ± 5.26	78.83 ± 7.47	-40.95 ± 25.06
EELSAnalyser	-7.96 ± 11.35	85.24 ± 13.10	22.72 ± 11.78

TABLE 4.8: Relative quantification of Cu, Ga and As elemental maps with Hyperspy, DigitalMicrograph™ and EELSAnalyser in region 8 shown in fig. 4.7(D) (GaAs).

Region 8 (0:50:50)	Cu L _{2,3} at.%	Ga L _{2,3} at.%	As L _{2,3} at.%
Hyperspy	-33.81 ± 25.86	52.92 ± 12.34	80.89 ± 15.99
DigitalMicrograph™	2.25 ± 1.73	43.46 ± 3.18	52.37 ± 3.72
EELSAnalyser	-3.29 ± 11.33	42.23 ± 13.03	61.06 ± 11.71

4.7 Summary

In chapter 4, the limitations of the traditional background model based on an inverse power-law are shown. The mathematical inferences on why the inverse power-law tends to cross the spectrum at high-loss are discussed in section 4.1. A crossing of the background model will systematically underestimate the net core-loss intensity. Modelling the background by extrapolating the inverse power-law function to the post edge region and shifting it down to the ionization onset is giving an overestimate of the net core-loss intensity. Hence, an optimal fit is proposed where the model passes through the intersection of error bars of both under- and over-estimated background extrapolations. Some considerations for modelling the background without crossing the spectrum are mentioned. If the Ga L_{2,3} and As L_{2,3} edges were quantified only from the 950 eV offset GaAs sum spectrum in region 3 (without taking into account other SIs with 250 eV and 80 eV offsets) using pre-edge regions identified in fig. 3.14, the Ga to As ratio would be 1.41. After applying the optimal fit, the ratio has improved to 1.28. This just shows the disadvantages of quantification using background subtraction methods. Quantifying overlapping core-losses is always difficult in the traditional background subtraction method. An inverse power-law is only considered if the pre-edge region lies within the first #100 channels. Higher core-losses are modelled using an exponential decay function. The behaviour of RL deconvolution is tested for a

simulated hydrogenic ionization core-loss as an example. The RL deconvolution perfectly recovers the single scattering distribution if the spreading function is pure Poissonian. The MSE calculated on the residue between original and reconstructed hydrogenic edge is almost zero, as shown in fig. 4.3(B). The artefacts associated with the RL deconvolution are studied with respect to number of iterations on two different PSFs used to simulate the low-loss function. The first is a ZLP only which is modelled using a pure Gaussian kernel and the second a low-loss simulated as a mixture of a Gaussian and several Lorentzians weighted according to Poissonian statistics (where $t/\lambda = 1$). It is interesting to see that the amplitude and position of the ringing artefacts become almost linear on a log-scale as a function of number of iterations and as the ringing artefacts can be modelled, they can be subtracted. Other causes of ringing artefacts are discussed, such as the intensity at which tail is truncated. i.e where the core-loss is ending at the right (and left) end of the spectrum abruptly for not having a wide enough detection ranges. Apart from already existing extrapolation methods, such as Hann window (cosine window) and inverse power-law, flipping over (mirroring over the energy-loss axis) of the spectrum has been suggested. Mirroring of the continuous core-loss and low-loss spectrum before applying deconvolution will make the spectrum and its derivatives continuous at both beginning and end of the spectrum. If any kink is present, then a Gaussian filter can be used so that its n^{th} derivative is also continuous. Baseline corrections to improve quantification by a linear least-squares model has been proposed. An example spectra from GaAs in regions 3 and 8 of the multilayer solar cell are considered and all the models described in eqns. 4.16–4.20 are compared. From table 4.2, 4.3 and 4.4, it is clear that the relative quantification is improving from eqn. 4.16 to 4.20. The Ga:As quantification is approaching 50 : 50 at.% in regions 3 and 8. The advantage of a baseline correction is flexibility in modelling the background. From chapter 3, once the core-losses are identified, a pre-edge region for the left-most ionization is sufficient to model the background for an entire spectrum. The baseline correction model proposed using eqn. 4.20 does not need a large pre-edge region either. The pre-edge region can be as narrow as ~ 5 to 10 channels which is enough to model and quantify the ionization edges. The baseline takes care of the systematic errors due to extrapolation of background modelled either using inverse power-law or exponential functions at higher energies. It is important to notice that the R^2 values calculated between background subtracted residual spectrum and the weighted theoretical cross-section are decreasing

from 0.9553 to 0.9486 (fig. 4.6(A–E)), while the relative quantification of Cu, Ga and As are improving. This is an indication that the EELS quantification is severely affected by the quality of the background model. The h -parameter proposed Egerton, (1982) determines the extent of systematic errors and recommends the length of integration ranges based on the length of pre-edge regions. However, if overlapping (plural scattered) edges, such as for Ga and As, are present this parameter fails to quantify latter edges reliably. The proposed baseline corrected quantification by least-squares modelling is a novel approach of reliable quantification of overlapping core-loss edges. Applying relative quantification to independently acquired SIs with different exposure time (τ), dispersion (eV/channel) and SI pixel size would not produce consistent results. This is because the background on top of which the ionization core-losses reside are different. The cross-section models for each ionization edge type will have inherent approximation errors (K edges $\sim 5\%$, L edges $\sim 10 - 15\%$ and M and N edges $\gtrsim 20$)(Hofer, 1987; Hofer et al., 1988a,b). The statistical noise differs because it depends on exposure times. Note that in table 3.2, Al L₁ is used for the quantification whereas in table 4.5, Al L₃ is used. This is also one of the major reasons why both results do not match. It is interesting to observe the elemental map from the Al L₃ edge. Even though there is an artefact present at channel number #100 (due to previous ZLP acquisition), the baseline corrected model could produce an elemental map, although its values might be biased and are noisy, as shown in fig. 4.7(A). The same Al L₃ data, when the traditional background subtraction method is applied, produce an elemental map that is completely noise and has no clear structure, as shown in fig. 3.13(A).

Chapter 5

Automated low-loss analysis

5.1 Introduction

Phase separation in $\text{In}_x\text{Ga}_{1-x}\text{N}$ (Ho et al., 1996) has been studied using high-energy core-loss edges in chapter 3 for a field of view of ~ 7 nm. Phase separation of In and Ga in a ternary alloy of $\text{In}_x\text{Ga}_{1-x}\text{N}$ is not desirable in manufacturing of LEDs. The phase separation causes the device to emit light at multiple wavelengths. Hence, a homogeneous ternary alloy is desirable. The behaviour of In phase separation in $\text{In}_x\text{Ga}_{1-x}\text{N}$ ternary alloy is extended to larger field of view (ref: fig. A.3). The ADF image of the area investigated is shown in fig. A.3(A). The phase separation is studied by jointly fitting plasmons and core-losses of In $\text{N}_{4,5}$, Ga $\text{M}_{4,5}$ and the pure ternary alloy at energies in the range of 13 eV to ~ 23 eV. Then the fit ranges are extended to check the reliability of quantification at higher fit ranges. However, the experimental reference spectra of In $\text{N}_{4,5}$ edge is only present until ~ 23 leading to inclusion of step function in the extended fit ranges from 13 eV to 27 eV. Hence a truncation correction factor is later introduced to extrapolate the missing experimental reference spectrum of In $\text{N}_{4,5}$ edge to recover the effect of fitting abnormalities in calculation effective In content in EELS SI. In other EELS SI such as multi-junction solar cell (GaAs) where the bulk plasmons and core-losses can be independently modelled. Hence the profile of position and FWHM of bulk plasmons are studied to check the sanity of quantification done in the high-loss quantification in sections 3.4 and 3.6 for GaAs and AlN:Tb , respectively. The widening of FWHM of bulk plasmon is studied due to formation of amorphous surface oxides on the surface and due to formation Tb-O complexes in AlN crystal structures.

5.2 Modelling $\text{In}_x\text{Ga}_{1-x}\text{N}$ low-loss EELS

5.2.1 Modelling bulk plasmons of $\text{In}_x\text{Ga}_{1-x}\text{N}$

The bulk plasmon peaks can be modelled with a Lorentz function, $L(E, E_p, W_p, x)$, as shown in eqn. 5.1. $E_p(x)$ and $W_p(x)$ are the bulk plasmon peak position and FWHM as a function of x . In a phase separated ternary alloy like $\text{In}_x\text{Ga}_{1-x}\text{N}$, the effective bulk plasmon will be a weighted sum of three bulk plasmons due to InN, GaN and homogeneous $\text{In}_x\text{Ga}_{1-x}\text{N}$. Hence, eqn. 5.2 describes the model for quantifying phase separation through only plasmon peak positions.

$$L(E, E_p, W_p, x) = \frac{2}{\pi} \cdot \frac{W_p(x)}{4 \cdot (E - E_p(x))^2 + W_p(x)^2} \quad (5.1)$$

In eqn. 5.2, $x \in \mathbb{R} \mid 0 \leq x \leq 1$ values in the Lorentz functions act as a fitting parameter to determine the peak position of pure $\text{In}_x\text{Ga}_{1-x}\text{N}$ material. $[p_1, p_2, p_3]$ are the free fitting parameters of the individual Lorentz functions. These fitting parameters can later be normalised to weights that sum up to unity. In $L(E, E_p, W_p, x)$, x monitors the concentration of In in the ternary alloy $\text{In}_x\text{Ga}_{1-x}\text{N}$. $L(E, E_p, W_p, 1)$ indicates the bulk plasmon model for InN. Similarly, $L(E, E_p, W_p, 0)$ indicates the bulk plasmon model for GaN. Parameters $[p_1, p_2, p_3]$ and x are the unconstrained and constrained fitting parameters in eqn. 5.2. This is because the total intensity of Lorentz functions is unity.

$$L_{eff}(E, E_p, W_p, x) = \begin{bmatrix} p_1 \\ p_2 \\ p_3 \end{bmatrix}^\top \begin{bmatrix} L(E, E_p, W_p, 1) \\ L(E, E_p, W_p, x) \\ L(E, E_p, W_p, 0) \end{bmatrix} \quad (5.2)$$

The plasmon peak position (E_p) for $\text{In}_x\text{Ga}_{1-x}\text{N}$ is a function of In concentration, x . If $x = 0$, then ternary alloy is a pure GaN whose plasmon peak position is known to lie at $E_p(x = 0) = 19.35$ eV. The value of $E_p(x = 0) = 19.35$ eV is valid when the ZLP of spectra is perfectly calibrated. The $\text{In}_x\text{Ga}_{1-x}\text{N}$ low-loss EELS SI acquired using monochromator (Browning et al., 2006) as shown in fig. A.3, the ZLP is distorted and does not have a bell shape to model/calibrate the spectra, as shown in fig. 5.1. However, the calibration from plasmon peak of GaN can be achieved. Hence, while modelling MLLS fit, $E_p(x = 0) \approx 19.35$ eV and changes slightly (observed to be ≈ 19.55 eV) to accommodate better calibration. Similarly, the value of plasmon peak position for InN is $E_p(x = 1) = 15.5$ eV (Wang et al., 2015). These plasmon

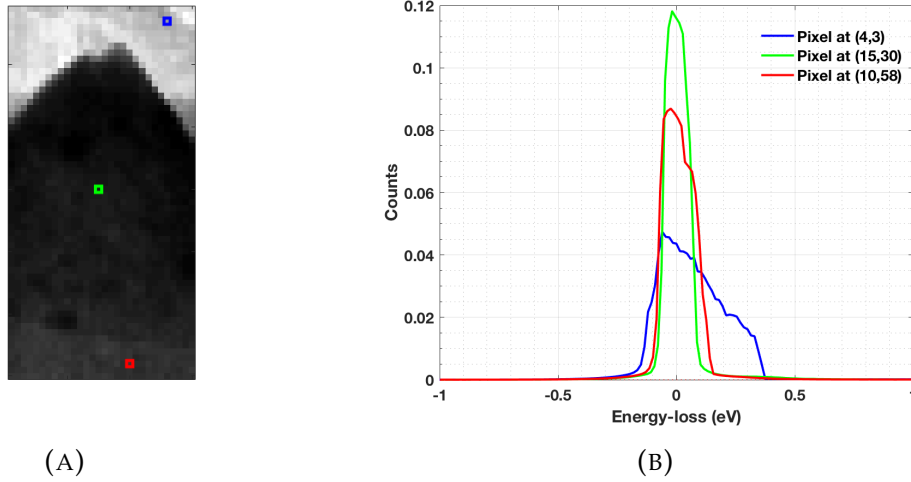


FIGURE 5.1: $\text{In}_x\text{Ga}_{1-x}\text{N}/\text{GaN}$ layers overview image with coloured boxes in (A) indicating location of extracted spectra in (B).

peaks can be determined by applying fourier-log deconvolution to low-loss spectra (Egerton et al., 1985). Wang et al., (2015) have compared the relationship between x and plasmon peak position and FWHM in ternary alloys of $\text{In}_x\text{Ga}_{1-x}\text{N}$ with the literature from Bosman et al., (2009), Egerton, (2009), Jinschek et al., (2006), Kong et al., (2012) and Specht et al., (2006) and have used a linear least-squares fit for the expression for $E_p(x)$ as shown in eqn. 5.3 (ref: to fig. 3 from Wang et al., (2015)). A similar linear relation has also been proposed by Trampert et al., (2014).

$$E_p(x) = E_p(x = 0) - 4.02 \cdot x \quad (5.3)$$

Similarly, the FWHM of the plasmons for various x values has been modelled by fitting the Lorentz functions, $L(E, E_p, W_p, x)$ to ternary alloy $\text{In}_x\text{Ga}_{1-x}\text{N}$ and plotting them against x , as shown in fig. 5.2. The FWHM of bulk plasmon (W_p) for $\text{In}_x\text{Ga}_{1-x}\text{N}$ is observed to be maximal when $x \approx 0.5$ and lowest when $x = 0$ or 1. Hence, a 2nd order polynomial of the form $a + b \cdot x + c \cdot x^2$ can be used to model W_p as a function of x , as shown in eqn. 5.4.

$$W_p(x) = 4.187 + 4.73727 \cdot x - 5.09438 \cdot x^2 \quad (5.4)$$

The Lorentzian models for bulk plasmons of InN , GaN and $\text{In}_x\text{Ga}_{1-x}\text{N}$ are shown in fig. 5.3(A).

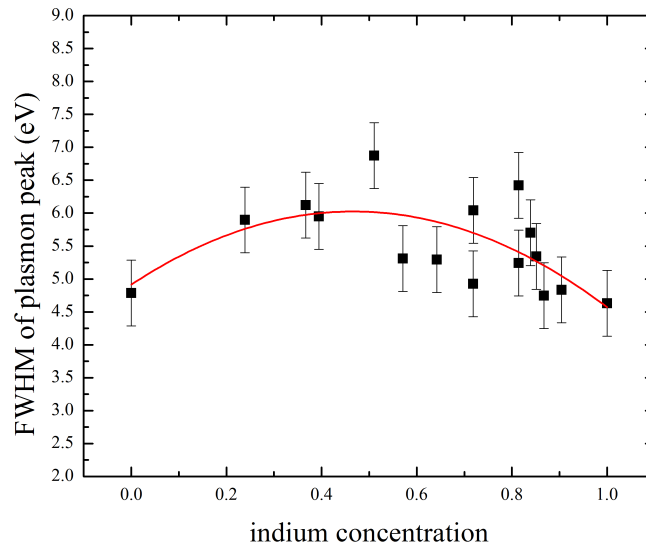


FIGURE 5.2: The FWHM of bulk plasmon peak of ternary alloy as a function of x (Wang et al., 2016).

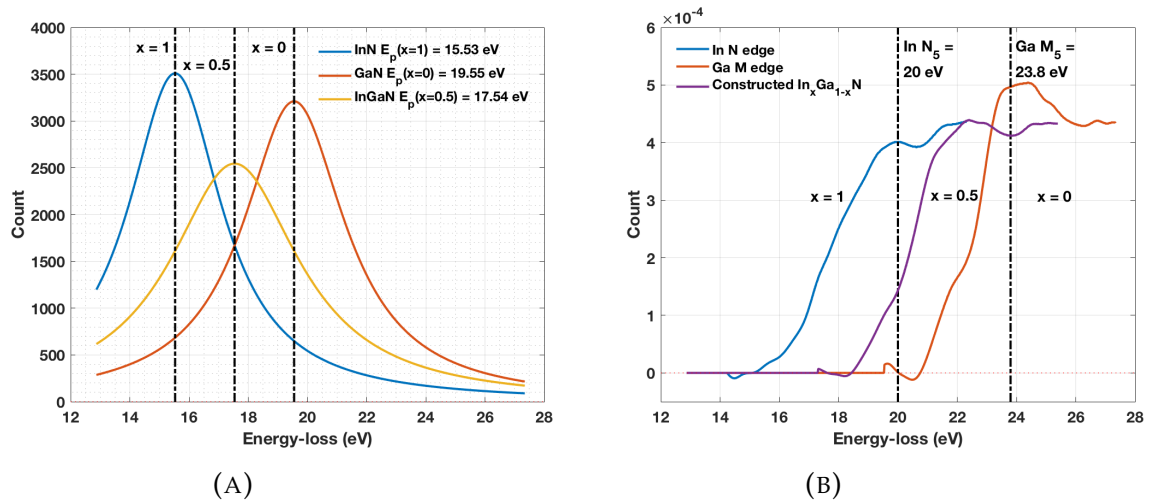


FIGURE 5.3: (A) Lorentzian functions which model the bulk plasmons for InN [$E_p(x = 1) = 15.53$ eV, $W_p(x = 1) = 3.83$ eV], GaN [$E_p(x = 0) = 19.55$ eV, $W_p(x = 0) = 4.19$ eV] and $\text{In}_x\text{Ga}_{1-x}\text{N}$ [$E_p(x = 0.5) = 17.54$ eV, $W_p(x = 0.5) = 5.28$ eV]. (B) Core-losses of In N_5 , Ga M_5 and simulated $\text{In}_{0.5}\text{Ga}_{0.5}\text{N}$, as shown in eqn. 5.7. The truncation of In $N_{4,5}$ and $\text{In}_x\text{Ga}_{1-x}\text{N}$ core-losses can be observed.

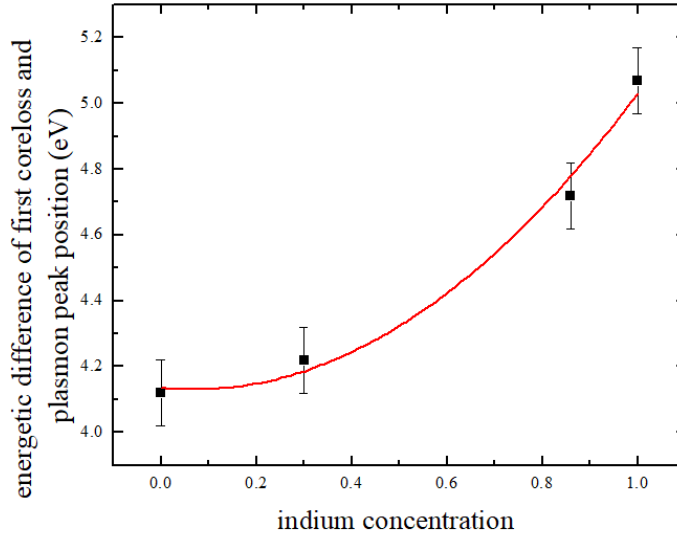


FIGURE 5.4: The offset energy, ΔE , in eV between plasmon and the first core-loss (Wang et al., 2016).

5.2.2 Modelling core-losses of $\text{In}_x\text{Ga}_{1-x}\text{N}$

The reference low-energetic core-losses for Ga ($3d$ transition) was acquired from pure GaN region (ref: region 5 in fig. A.3(B)). However, the In reference spectrum is extracted from $\text{In}_x\text{Ga}_{1-x}\text{N}$ region and the onset is moved to 20 eV. The extracted In is actually pure $\text{In}_x\text{Ga}_{1-x}\text{N}$ reference and is only considered until the onset of Ga $3d$ transition in $\text{In}_x\text{Ga}_{1-x}\text{N}$ core-loss spectrum. The pure InN spectrum is then extracted from pure $\text{In}_x\text{Ga}_{1-x}\text{N}$ spectrum by subtracting the weighted $(1-x)$ Ga reference spectrum. Hence, the reference In core-loss is available for analysis only until $\lesssim 23$ eV. For both reference spectra the bulk plasmon and ZLP are subtracted and are normalised for thickness and total intensity of the low-loss spectra. To synthesis the $\text{In}_x\text{Ga}_{1-x}\text{N}$ core-loss, the In and Ga core-losses are superimposed according to the weighting x for In and $(1-x)$ for GaN. The energetic difference (ΔE) between plasmon peak position and low-energetic ionization core-losses for a ternary $\text{In}_x\text{Ga}_{1-x}\text{N}$ alloy is not linear as could be assumed. Wang et al., (2016) investigated the plasmon peak positions for four $\text{In}_x\text{Ga}_{1-x}\text{N}$ samples ($x = 0, 0.3, 0.86$ and 1). The difference between the first core-loss and plasmon peak varied from ~ 4.14 eV to ~ 5.3 eV as shown in fig. 5.4. A 2nd degree polynomial (of the form $a+bx+cx^2$) is used to model the chemical shift $\Delta E(x)$ as a function of x , as shown in eqn. 5.5.

$$\Delta E(x) = 4.136 + 0.143 \cdot x + 1.036 \cdot x^2 \quad (5.5)$$

Hence, the relationship between the ionization edge onset, $E_i(x)$, and x values can be parametrized as in eqn. 5.6. This determines the core-loss ionization onsets for ternary alloy as a function of x .

$$E_i(x) = E_p(x) + \Delta E(x) \cdot x \quad (5.6)$$

The Ga $3d$ (Ga $M_{4,5}$ edge at 23.8 eV and 28.5 eV) (Keast et al., 2001, 2002) and In $4d$ (In $N_{4,5}$ edge at 20.0 eV and 25.9 eV) (Cardona et al., 1970; Mkhoyan et al., 2003) transitions are close to the plasmon peak. The plasmons and the core-losses in an experimental spectrum of $\text{In}_x\text{Ga}_{1-x}\text{N}$ as one broad peak with shoulders and are difficult to analyse individually. Modelling the superposition of bulk plasmons along with the corresponding core-loss spectra of pure InN, pure GaN and $\text{In}_x\text{Ga}_{1-x}\text{N}$ can be used to decompose experimental low-loss spectra of $\text{In}_x\text{Ga}_{1-x}\text{N}$ into components. However, in fig. A.3(A), the field of view of SI does not have any area of pure InN. Hence, the In $N_{4,5}$ edge is extracted from In rich $\text{In}_x\text{Ga}_{1-x}\text{N}$ ternary alloy and the core-losses are considered only until the onset of Ga $M_{4,5}$, as shown in fig. 5.3(B). The bottom part in fig. A.3(A) is the GaN buffer layer indicated as region 5 in fig. A.3(B) from which the Ga $M_{4,5}$ reference core-loss can be extracted by subtracting the bulk plasmon and ZLP. The $\text{In}_x\text{Ga}_{1-x}\text{N}$ core-loss, $S_{\text{InGaN}}(E, x)$, can be constructed from reference core-losses of InN and GaN by using weight of (x) and $(1 - x)$, respectively, as shown in eqn. 5.7. This additive superposition of core-losses and linear plasmon shifts are valid only in case of binary alloys such as $\text{In}_x\text{Ga}_{1-x}\text{N}$.

$$S_{\text{InGaN}}(E, x) = x \cdot S_{\text{InN}}(E) + (1 - x) \cdot S_{\text{GaN}}(E) \quad (5.7)$$

All the reference spectra constructed are normalised to the low-loss intensity and relative thickness. This makes sure that the cross-sections are normalised and the fitting parameters can directly be used to calculate the weights and hence, can be compared. Note that the In $N_{4,5}$ edge is present until ~ 23 eV, whereas the Ga $M_{4,5}$ edge is present in full range until ~ 27 eV. This is due to the fact that when extracting In reference spectrum, there was no pure InN region present in the field of view. Hence, In $4d$ transition is extracted from In rich region of $\text{In}_{0.95}\text{Ga}_{0.05}\text{N}$ core-loss until the onset of Ga $3d$ transition which is at ~ 23 eV. This will also affect the estimation of pure $\text{In}_x\text{Ga}_{1-x}\text{N}$ core-loss. This effect has not been considered by Walther et al., (2017) and Wang et al., (2015, 2016), where the analysis of bulk plasmon and core-losses was restricted to the range from ~ 13 eV to ~ 23 eV. This means that only near

edge structures of Ga M_5 ($E_i(x) = 23.8$ eV) are considered along with In $N_{4,5}$ in the construction of the $\text{In}_x\text{Ga}_{1-x}\text{N}$ spectra. However, the contrast of the InN core-loss distribution in the field of view are physical but not the quantification of core-losses, as shown in fig. 5.8. The GaN buffer region had the best R^2 but the range of fitting did not include all major components of reference core-losses, as seen in fig. 5.6(B). This also means that the quantification of Ga content in GaN buffer region was only due to near edge structures at ~ 23 eV. Hence, there is a need to increase the fitting range to include the complete Ga M_5 edge. Also the steps of x for which $\text{In}_x\text{Ga}_{1-x}\text{N}$ reference spectra have been calculated was $\Delta x = 0.05$. Hence, all the maps shown in figs. 5.8 have a quantization error due to finite step size of x . The experimental spectra can be modelled with three reference spectra for In $N_{4,5}$, Ga $M_{4,5}$ and pure $\text{In}_x\text{Ga}_{1-x}\text{N}$ over a larger fit range from 13 eV to 27 eV to include all the components of GaN $3d$ transitions, as shown in eqn. 5.8.

$$S_{CLeff}(E, x) = \begin{bmatrix} p_1 \\ p_2 \\ p_3 \end{bmatrix}^T \begin{bmatrix} S_{\text{InGaN}}(E, x = 1) \\ S_{\text{InGaN}}(E, x) \\ S_{\text{InGaN}}(E, x = 0) \end{bmatrix} \quad (5.8)$$

$S_{\text{InGaN}}(E, x)$ are the reference core-loss spectra constructed according to eqn. 5.7. Hence, $S_{\text{InGaN}}(E, x = 1)$ and $S_{\text{InGaN}}(E, x = 0)$ are effectively In $N_{4,5}$ and Ga $M_{4,5}$ reference spectra. Parameters $[p_1, p_2, p_3]$ are free fitting parameters. The ionization edge onsets of In $N_{4,5}$ and Ga $M_{4,5}$ are fixed. However, the onset of $\text{In}_x\text{Ga}_{1-x}\text{N}$, $E_i(x)$ from eqn. 5.6, is a function of x . Hence, eqn. 5.5, the chemical shift is incorporated in determination of ionization edge onset. $E_i(x = 0)$ is the edge onset of Ga M_5 edge at 23.8 eV. The onset of Ga M_4 is at 28.5 eV and is not recorded completely while conducting the experiments due to the finite detector size (1024 channels) and the choice of dispersion (0.015 eV/channel) and the need to keep ZLP away from the CCD edges. Hence, the Ga reference spectrum, $S_{\text{InGaN}}(E, x = 0)$, only has the Ga M_5 edge.

5.2.3 Joint fitting of bulk plasmons and core-losses

For the determination of phase separation in $\text{In}_x\text{Ga}_{1-x}\text{N}$ ternary alloy, it is almost impossible to determine solely through bulk plasmon fitting by three Lorentz functions as in eqn. 5.2. Hence, there is a need to fit all six functions (three bulk plasmon models and three experimental core-loss spectra). Each function can act as a basis function in modelling by MLLS fitting, as shown

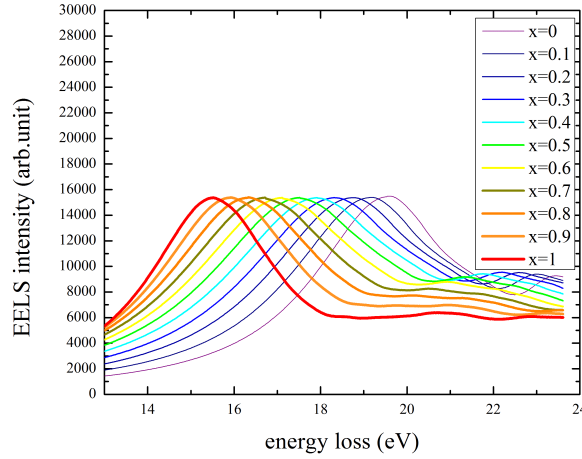


FIGURE 5.5: Simulated $\text{In}_x\text{Ga}_{1-x}\text{N}$ spectra for $x \in [0, 1]$ for step size, $\Delta x = 0.1$. The reference spectra for In and Ga edges are extracted from EELS data acquired from Nion USTEM (Walther et al., 2017).

in eqn. 5.9.

$$S_{eff}(E, x) = \begin{bmatrix} p_1 \\ p_2 \\ p_3 \\ p_4 \\ p_5 \\ p_6 \end{bmatrix}^T \begin{bmatrix} L(E, E_p, W_p, 1) \\ L(E, E_p, W_p, x) \\ L(E, E_p, W_p, 0) \\ S_{\text{InGaN}}(E, x = 1) \\ S_{\text{InGaN}}(E, x) \\ S_{\text{InGaN}}(E, x = 0) \end{bmatrix} \quad (5.9)$$

Parameters $[p_1, \dots, p_6]$ are the MLLS free fitting parameters. Eqn. 5.9, is optimised with linear least-squares fit for best $R^2 \in [0, 1]$. The value of x is changed to $(x + \Delta x) \forall x \in [0, 1]$ and the process is repeated until the limit of x is reached, i.e. 1. The simulated low-loss spectra for $x \in [0, 1] \mid \Delta x = 0.1$ is shown in fig. 5.5. Among $R^2(x) \forall x \in [0, 1]$, the effective model that is describing the experimental spectrum with highest $R^2(x)$ value is the best solution.

$$R_{eff}^2 = \|R^2(x)\|_{\infty} = \max R^2(x) \quad (5.10)$$

The effective R^2 for the best fit over all the x values chosen in $L(E, E_p, W_p, x)$ and $S_{\text{InGaN}}(E, x)$. The step size of Δx determines the quality of quantification. This is due to the fact that large step sizes, Δx , introduces quantization errors and the R^2 values will be lower. To reduce quantization error, the value of Δx should be as small as possible. All the individual fits in fig. 5.6 are fitted in the range 13 eV to ~ 23 eV, which is the full available range for In core-loss. The fits are very good with an $R^2 = 0.9709$ in fig. 5.6(A) and $R^2 = 0.9871$ in fig. 5.6(B). However, the fits do not include most of Ga $M_{4,5}$ edge. In fig. 5.7 for comparison, the fit range is 13 eV to 27 eV. Hence, these fits include Ga

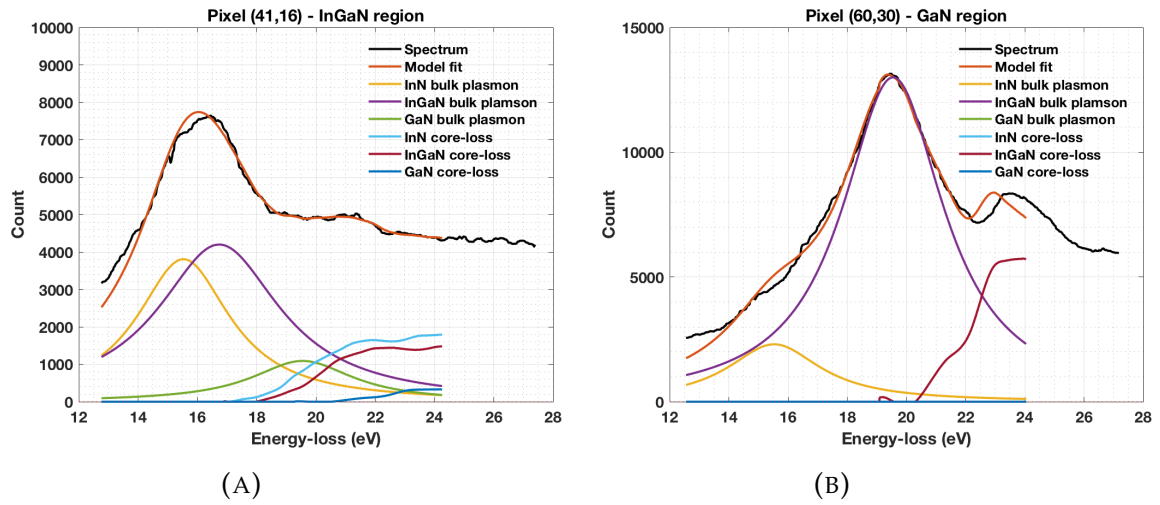


FIGURE 5.6: Model fit in the range of 13 eV to ~ 23 eV and individual components of three bulk plasmons and three core-losses in (A) $\text{In}_x\text{Ga}_{1-x}\text{N}$ region at pixel (41, 16) (region 2 in fig. A.3(B)) with $R^2 = 0.9709$ and (B) GaN buffer layer at pixel (60, 30) (region 5 in fig. A.3(B)) with $R^2 = 0.9871$.

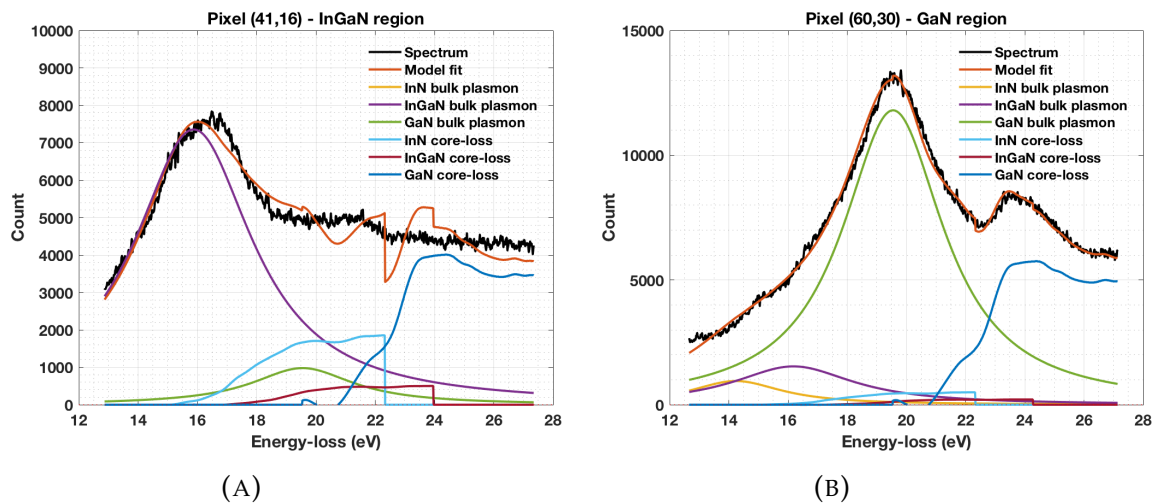


FIGURE 5.7: Model fit in the range of 13 eV to 27 eV and individual components of three bulk plasmons and three core-losses in (A) $\text{In}_x\text{Ga}_{1-x}\text{N}$ region at pixel (41, 16) (region 2 in fig. A.3(B)) with $R^2 = 0.9709$ and (B) GaN buffer layer at pixel (60, 30) (region 5 in fig. A.3(B)) with $R^2 = 0.9871$.

M_5 edge. It is evident from the model fit in $\text{In}_x\text{Ga}_{1-x}\text{N}$ region from fig. 5.7(A) that it includes step functions (discontinuities) in the MLLS basis functions. This is due to truncated $\text{In N}_{4,5}$ edge and constructed $\text{In}_x\text{Ga}_{1-x}\text{N}$ edge. The model fit in $\text{In}_x\text{Ga}_{1-x}\text{N}$ region has $R^2 = 0.87$ and in GaN region $R^2 = 0.99$. The weighting of each bulk plasmon needs to be normalised as shown in eqns. 5.11–5.13. w_{pInN} , w_{pInGaN} and w_{pGaN} are the weighting factors for bulk plasmons of InN, $\text{In}_x\text{Ga}_{1-x}\text{N}$ and GaN respectively. $[p_1, p_2, p_3]$ are the free fitting parameters for bulk plasmon losses obtained by joint fitting of bulk plasmons and core-losses obtained from eqn. 5.9.

$$w_{\text{pInN}} = \frac{p_1 \cdot \int^E L(E, E_p, W_p, 1)}{\begin{bmatrix} p_1 \\ p_2 \\ p_3 \end{bmatrix}^\top \begin{bmatrix} \int^E L(E, E_p, W_p, 1) \\ \int^E L(E, E_p, W_p, x) \\ \int^E L(E, E_p, W_p, 0) \end{bmatrix}} \quad (5.11)$$

$$w_{\text{pInGaN}} = \frac{p_2 \cdot \int^E L(E, E_p, W_p, x)}{\begin{bmatrix} p_1 \\ p_2 \\ p_3 \end{bmatrix}^\top \begin{bmatrix} \int^E L(E, E_p, W_p, 1) \\ \int^E L(E, E_p, W_p, x) \\ \int^E L(E, E_p, W_p, 0) \end{bmatrix}} \quad (5.12)$$

$$w_{\text{pGaN}} = \frac{p_3 \cdot \int^E L(E, E_p, W_p, 0)}{\begin{bmatrix} p_1 \\ p_2 \\ p_3 \end{bmatrix}^\top \begin{bmatrix} \int^E L(E, E_p, W_p, 1) \\ \int^E L(E, E_p, W_p, x) \\ \int^E L(E, E_p, W_p, 0) \end{bmatrix}} \quad (5.13)$$

The weightings for core-losses are also normalised to compare them with weightings of bulk plasmons as shown in eqns. 5.14–5.16.

$$w_{\text{cInN}} = \frac{p_4 \cdot \int^E S_{\text{InGaN}}(E, x = 1)}{\begin{bmatrix} p_4 \\ p_5 \\ p_6 \end{bmatrix}^\top \begin{bmatrix} \int^E S_{\text{InGaN}}(E, x = 1) \\ \int^E S_{\text{InGaN}}(E, x) \\ \int^E S_{\text{InGaN}}(E, x = 0) \end{bmatrix}} \quad (5.14)$$

$$w_{\text{cInGaN}} = \frac{p_5 \cdot \int^E S_{\text{InGaN}}(E, x)}{\begin{bmatrix} p_4 \\ p_5 \\ p_6 \end{bmatrix}^\top \begin{bmatrix} \int^E S_{\text{InGaN}}(E, x = 1) \\ \int^E S_{\text{InGaN}}(E, x) \\ \int^E S_{\text{InGaN}}(E, x = 0) \end{bmatrix}} \quad (5.15)$$

$$w_{\text{cGaN}} = \frac{p_6 \cdot \int^E S_{\text{InGaN}}(E, x = 0)}{\begin{bmatrix} p_4 \\ p_5 \\ p_6 \end{bmatrix}^\top \begin{bmatrix} \int^E S_{\text{InGaN}}(E, x = 1) \\ \int^E S_{\text{InGaN}}(E, x) \\ \int^E S_{\text{InGaN}}(E, x = 0) \end{bmatrix}} \quad (5.16)$$

All the weightings calculated in eqns. 5.11–5.16 are normalised to be in the interval $[0, 1]$. Hence, the weightings calculated from bulk plasmons and referenced core-losses can be compared to observe and verify the consistency in the determination of phase separation in $\text{In}_x\text{Ga}_{1-x}\text{N}$ ternary alloys. The maps of all the weighting calculated at each pixel are shown in figs. 5.8 for fitting range from 13 eV to ~ 23 eV and figs. 5.9 for fitting range from 13 eV to 27 eV. The statistics of weightings in both short and extended fit ranges are listed in tables 5.1 and 5.2, respectively.

5.3 Effective composition in $\text{In}_x\text{Ga}_{1-x}\text{N} / \text{GaN}$

The phase separation in an $\text{In}_x\text{Ga}_{1-x}\text{N}$ ternary alloy can be observed in spatial distribution of plasmon peak positions. If at all there is a phase separation, In is present as InN and $\text{In}_x\text{Ga}_{1-x}\text{N}$. Hence, the effective In content can be determined by normalised weights calculated in eqns 5.11–5.13 from Lorentz functions (which are determined by fitting parameters) as shown in eqn. 5.17.

$$x_p = w_{p\text{InN}} \cdot 1 + w_{p\text{InGaN}} \cdot x + w_{p\text{GaN}} \cdot 0 \quad (5.17)$$

The determination of In content from plasmon peak positions is straight forward as they can be modelled using Lorentz functions and the values can be modelled at all energy-loss ranges. Hence, in joint fitting of plasmon peaks and core-losses, the phase separation determined by plasmons can be compared to that determined from low-energetic core-losses:

$$x_c = w_{c\text{InN}} \cdot 1 + w_{c\text{InGaN}} \cdot x + w_{c\text{GaN}} \cdot 0 \quad (5.18)$$

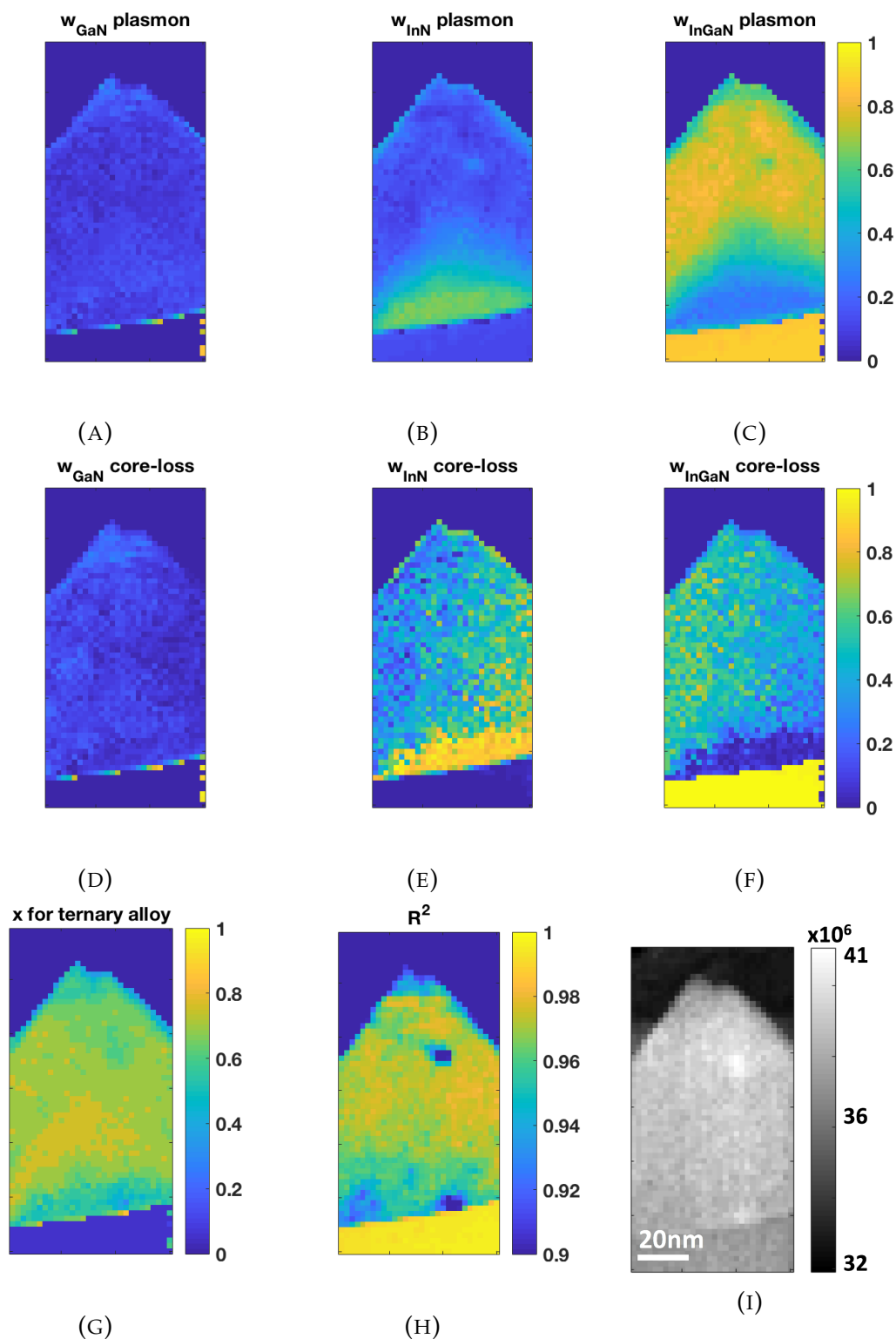


FIGURE 5.8: Results from fitting each spectrum from the SI in fig. A.3(B) by a linear superposition of three reference spectra, one for GaN, one for InGa_N and one for InN film. Shown are the weight parameters attributed to (A,D) GaN, (B,E) InN and (C,F) In_xGa_{1-x}N where x was varied from 0.05 to 0.95 in steps of 0.05 ($\Delta x = 0.05$). Top row: fit for plasmons, middle row: fit for core losses. (G) plots the best fitting x value of the ternary component only. (H) shows the R^2 parameter of the fit for each spectral data point. (I) Rotated ADF image of the area investigated where the apparent slight tilt from vertical growth is due to drift during the acquisition of SI.

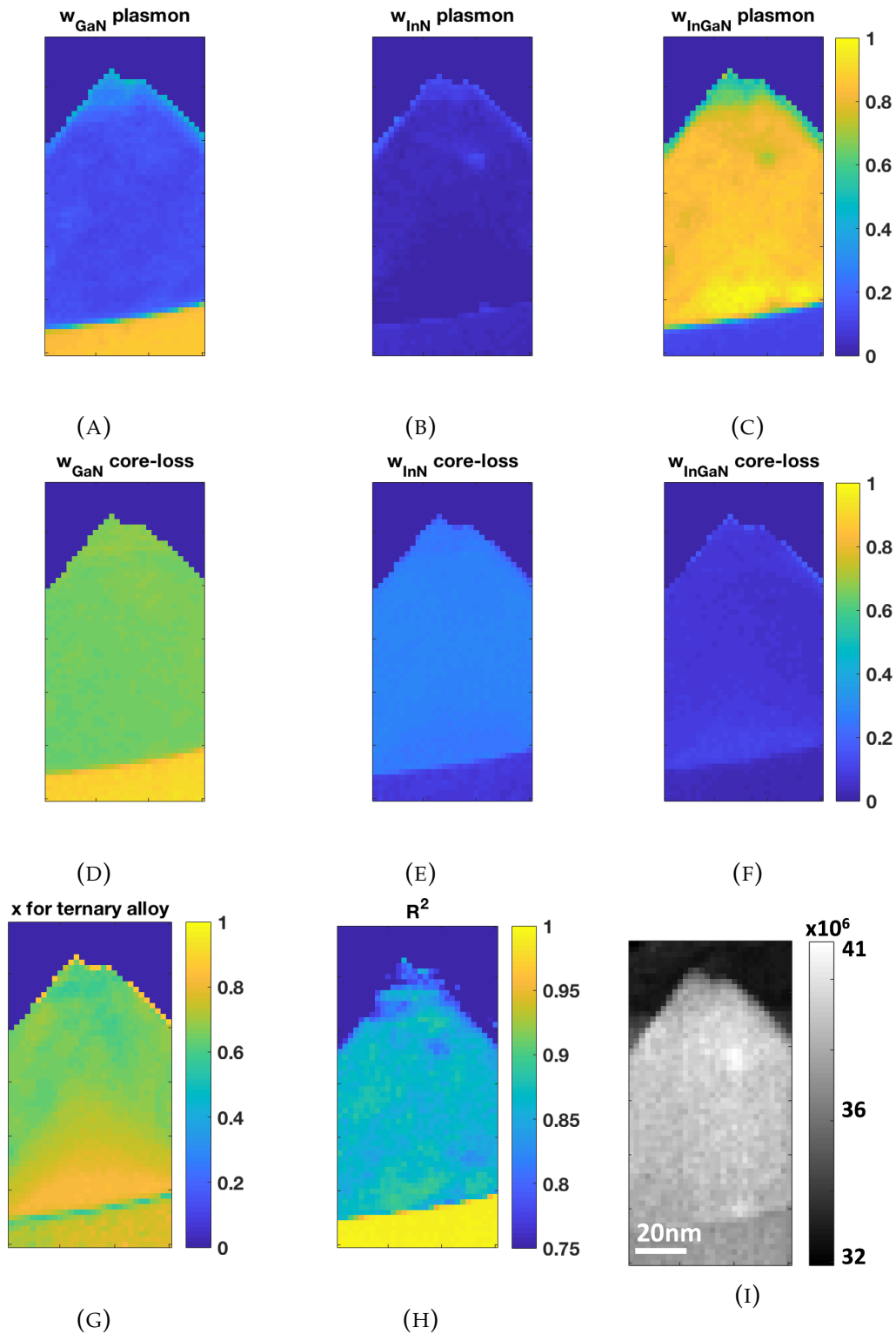


FIGURE 5.9: Results from fitting each spectrum from the SI in fig. A.3(B) by a linear superposition of three reference spectra, one for GaN, one for InGaN and one for InN film. Shown are the weight parameters attributed to (A,D) GaN, (B,E) InN and (C,F) $\text{In}_x\text{Ga}_{1-x}\text{N}$ where x was varied from 0.001 to 0.999 in steps of 0.001 ($\Delta x = 0.001$). Top row: fit for plasmons, middle row: fit for core losses. (G) plots the best fitting x value of the ternary component only. (H) shows the R^2 parameter of the fit for each spectral data point. (I) Rotated ADF image of the area investigated where the apparent slight tilt from vertical growth is due to drift during the acquisition of SI.

Similarly, the Ga content of $\text{In}_x\text{Ga}_{1-x}\text{N}$ from bulk plasmons ($1 - x_p$) and core-losses ($1 - x_c$) can be determined as shown in eqns. 5.19 and 5.20.

$$(1 - x_p) = w_{p\text{InN}} \cdot 0 + w_{p\text{InGaN}} \cdot (1 - x) + w_{p\text{GaN}} \cdot 1 \quad (5.19)$$

$$(1 - x_c) = w_{c\text{InN}} \cdot 0 + w_{c\text{InGaN}} \cdot (1 - x) + w_{c\text{GaN}} \cdot 1 \quad (5.20)$$

The determination of phase separation from core-losses is similar to that from plasmon losses if the reference spectra cover a sufficiently large range. However, in this case, the reference spectra for InN and synthesised $\text{In}_x\text{Ga}_{1-x}\text{N}$ spectra are truncated, as shown in fig. 5.3(B). As mentioned earlier in subsection 5.2.3 smaller fitting ranges (13 eV to ~ 23 eV) can be used to get the fits and the fitted model almost perfectly agree with experimental spectrum, as shown by Wang et al., (2015, 2016) in fig. 5.8 (Walther et al., 2017). However, the Ga M_5 edge with an edge onset of 23.8 eV (and Ga M_4 at 28.5 eV) is almost not included in the fitting, the fitting range is from 13 eV to 23 eV. The determination of In content from core-losses (as shown in fig. 5.10(B)) in $\text{In}_x\text{Ga}_{1-x}\text{N}$ region (and GaN buffer region) will always be a slight overestimate of $\sim 10\%$ as shown in table 5.1. The In content determ-

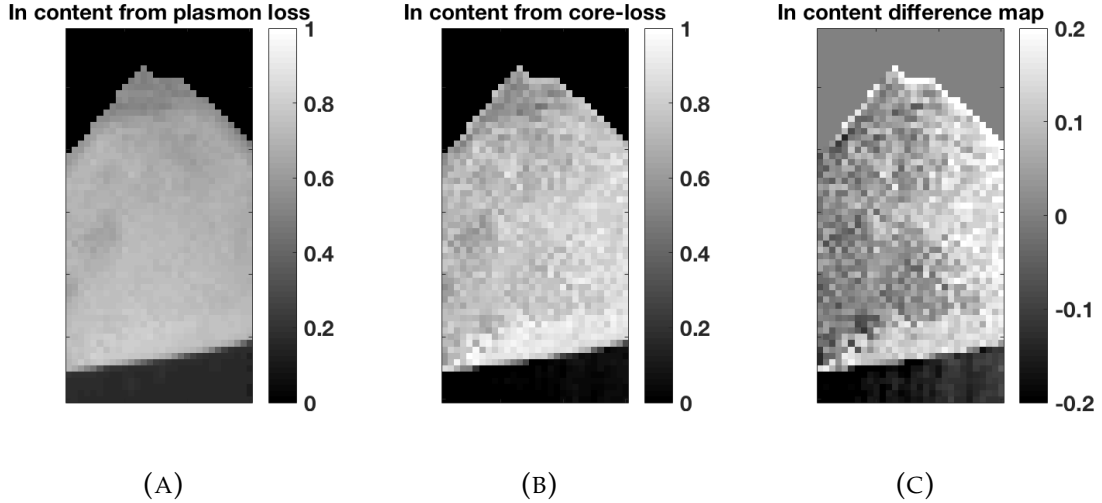


FIGURE 5.10: Maps of In content, x , calculated for data from fig. 5.8(G) from weights of fitting (A) plasmon losses, (B) low core-losses, (C) difference map (B)–(A).

ined in Ga buffer layer are slightly biased as well due to almost non existence of Ga $M_{4,5}$ edge in the shorter fitting range from 13 eV to ~ 23 eV. However, if the larger range of fitting is considered from 13 eV to ~ 27 eV, then due to truncation of reference InN and synthesised $\text{In}_x\text{Ga}_{1-x}\text{N}$ references spectra (as

TABLE 5.1: Comparison of effective In content from different regions identified in fig. A.3(B) for fitting range from 13 eV to ~ 23 eV.

	Regions				
	1	2	3	4	5
w_{pInN}	0.18 ± 0.08	0.22 ± 0.11	0.23 ± 0.10	0.64 ± 0.03	0.12 ± 0.01
w_{pInGaN}	0.74 ± 0.09	0.67 ± 0.13	0.67 ± 0.11	0.26 ± 0.02	0.85 ± 0.15
w_{pGaN}	0.13 ± 0.02	0.14 ± 0.02	0.13 ± 0.01	0.13 ± 0.01	0.87 ± 0.01
w_{cInN}	0.33 ± 0.13	0.43 ± 0.13	0.60 ± 0.12	0.85 ± 0.11	-0.02 ± 0.02
w_{cInGaN}	0.56 ± 0.10	0.47 ± 0.10	0.34 ± 0.10	0.08 ± 0.09	0.99 ± 0.18
w_{cGaN}	0.12 ± 0.04	0.11 ± 0.04	0.06 ± 0.03	0.08 ± 0.03	0.03 ± 0.01
x_p	0.70 ± 0.03	0.69 ± 0.04	0.70 ± 0.02	0.78 ± 0.02	0.14 ± 0.02
x_c	0.72 ± 0.06	0.75 ± 0.07	0.84 ± 0.05	0.89 ± 0.05	0.02 ± 0.01

shown in fig. 5.3(B)) the weighting for Ga is larger. The Ga content is overestimated and In content is underestimated from core-losses, as tabulated in table 5.2 and shown in fig. 5.11(B), under the influence of dominant bulk plasmon models on the left and Ga M_5 at the right side in $\text{In}_x\text{Ga}_{1-x}\text{N}$ region as shown in fig. 5.7(A). In GaN buffer layer, the GaN content is more reliable

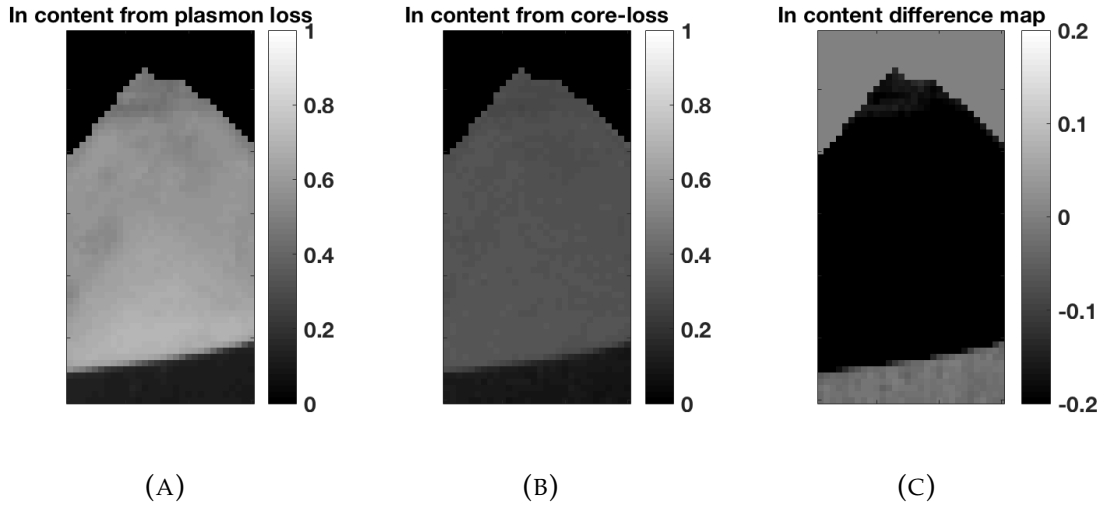


FIGURE 5.11: Maps of In content, x , calculated for data from fig. 5.9(G) from weights of fitting (A) plasmon losses, (B) low core-losses, (C) difference map (B)–(A).

as the predominant Ga M_5 is included. The underestimation of In content is systematic and a correction can be proposed. The phase separation calculated from core-losses can be compared with In content determined through bulk plasmons.

TABLE 5.2: Comparison of effective In content from different regions identified in fig. A.3(B) for fitting range from 13 eV to 27 eV.

	Regions				
	1	2	3	4	5
$w_{p\text{InN}}$	0.03 ± 0.01	0.02 ± 0.03	0.01 ± 0.02	-0.08 ± 0.02	0.03 ± 0.01
$w_{p\text{InGaN}}$	0.84 ± 0.02	0.84 ± 0.04	0.85 ± 0.02	0.95 ± 0.03	0.10 ± 0.01
$w_{p\text{GaN}}$	0.13 ± 0.02	0.14 ± 0.02	0.13 ± 0.01	0.13 ± 0.01	0.87 ± 0.01
$w_{c\text{InN}}$	0.28 ± 0.01	0.28 ± 0.01	0.28 ± 0.01	0.25 ± 0.01	0.07 ± 0.01
$w_{c\text{InGaN}}$	0.07 ± 0.01	0.07 ± 0.01	0.06 ± 0.01	0.11 ± 0.01	0.02 ± 0.01
$w_{c\text{GaN}}$	0.65 ± 0.01	0.66 ± 0.01	0.66 ± 0.01	0.65 ± 0.01	0.91 ± 0.01
x_p	0.60 ± 0.03	0.60 ± 0.05	0.61 ± 0.03	0.70 ± 0.01	0.11 ± 0.01
x_c	<i>0.33 ± 0.01</i>	<i>0.32 ± 0.01</i>	<i>0.32 ± 0.01</i>	<i>0.34 ± 0.01</i>	<i>0.09 ± 0.01</i>

5.4 Results from joint fitting

While jointly fitting the core-losses and bulk plasmons, the fitting ranges affect the quantification. This is even more so when part of the reference In N_{4,5} is not completely available in range considered (i.e. from 13 eV to 27 eV). The quantification of In content in regions as defined by fig. A.3(B) are shown in table 5.2 for an extended fit range. It is worth noting that the R^2 values of the fit are < 0.90 in fitting range of 13 eV to 27 eV, only In_xGa_{1-x}N region as shown in fig. 5.9(H). The lower R^2 is due to larger range and inclusion of In N_{4,5} edge in the MLLS fit and has a step included in the fit as shown in fig. 5.7(A). We need a model that relates the quality of quantification to goodness of fits, i.e. R^2 in the extended fit ranges. In previous model for shorter fit ranges (i.e. 13 eV to ~ 23 eV), the R^2 were > 0.90 in In_xGa_{1-x}N region but the Ga quantification might be unreliable. The quantification of effective In content from bulk plasmons, x_p is shown in table 5.2. The quantification of In content from bulk plasmons, x_p , in both ranges (shorter and extended) are similar. From tables 5.1 and 5.2, a systematic error of $\sim 10\%$ in all regions for x_p is due to truncation of reference In N edge might cause error while joint fitting. However, the changes of x_p in all regions for both fitting ranges are same. But are offset by $\sim 10\%$. The quantification of effective In content from core-losses by extended fit range look completely erroneous as shown in italicised row of table 5.2. But the source of error is known, which is the truncation of In N_{4,5} edge. Hence, a truncation correction for the core-loss quantification can be proposed.

5.5 Truncation correction for core-losses

The quantification values of effective In for extended fit ranges in table 5.2 are indicating severe systematic errors. The reference spectrum for In was generated by considering the first peak of the experimental core-loss as the edge onset. There are no definite models present for the representation of $4d$ transitions. The left tail of the reference In core-loss is very much dependent on the quality of background removal such as Fourier-log deconvolution and bulk plasmon subtractions from Lorentz function fitting. The low-loss joint MLLS fit applied by Wang et al., (2016) have chosen the value of x manually to fit the model to the experimental spectra. However, the proposed automated joint fitting here constructs the $\text{In}_x\text{Ga}_{1-x}\text{N}$ core-loss on the fly while fitting for best R^2 . The best R^2 is chosen among all the models constructed at a step size of $\Delta x = 0.001$. The truncated In and $\text{In}_x\text{Ga}_{1-x}\text{N}$ core-losses at $x = 0.5$ are shown in fig. 5.12(A). The intensity that is lost by the In

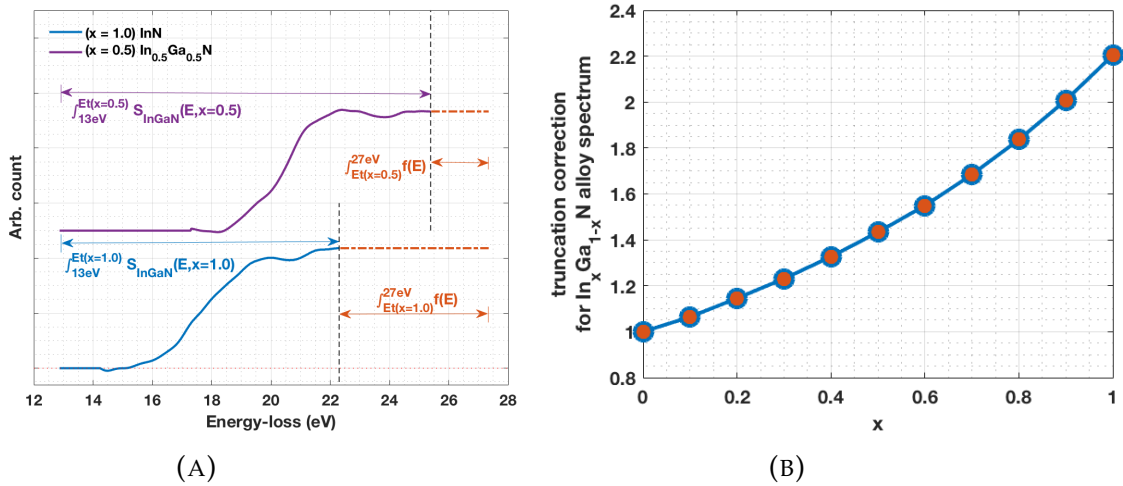


FIGURE 5.12: (A) In and constructed $\text{In}_x\text{Ga}_{1-x}\text{N}$ at $x = 0.5$ reference spectra. The constant extrapolation after the truncation is shown in orange dotted horizontal line. The black dotted vertical line is bifurcating the available spectra and the extrapolated spectra. (B) Truncation correction for $\text{In}_x\text{Ga}_{1-x}\text{N}$ as a function of x .

reference core-loss spectrum can be retrieved by modelling an extrapolation for the core-loss. The theoretical models do not describe well the $3d$ and $4d$ transitions for Ga and In core-losses, respectively. Hence, a new strategy is needed for extrapolation. The In $N_{4,5}$ and Ga $M_{4,5}$ edges do not possess sharp onsets. A constant extrapolation, $f(E) = \text{constant}$, at the end of the In truncation is the best approximation in the range from $\sim 23\text{eV}$ to 27eV . The total intensity of the InN ($\int_{13\text{eV}}^{E_t(x=1)} S_{\text{InGaN}}(E, x = 1)$) and synthesised $\text{In}_{0.5}\text{Ga}_{0.5}\text{N}$

($\int_{13\text{ eV}}^{E_t(x=0.5)} S_{\text{InGaN}}(E, x = 0.5)$) spectra are shown in fig. 5.12(A). The total extrapolated intensity as a function of x is $\int_{E_t(x)}^{27\text{ eV}} f(E)$, which is the area of a rectangle of width from $\sim 23\text{ eV}$ to 27 eV and height $S_{\text{InGaN}}(E_t(x=1), x=1)$. A truncation correction is proposed which can be used to correct the weights of the core-losses for InN, w_{InN} , and $\text{In}_x\text{Ga}_{1-x}\text{N}$, w_{InGaN} , core-losses and is calculated as shown in eqn. 5.21.

$$f_{\text{cor}}(x) = \frac{\left[\int_{13\text{ eV}}^{E_t(x)} S_{\text{InGaN}}(E, x) + \int_{E_t(x)}^{27\text{ eV}} f(x) \right]}{\int_{13\text{ eV}}^{E_t(x)} S_{\text{InGaN}}(E, x)} \quad (5.21)$$

The truncation correction, $f_{\text{cor}}(x)$, is a function of x . This is because the total intensity of the synthesised $\text{In}_x\text{Ga}_{1-x}\text{N}$ increases with decrease in x , as shown in table 5.3. It means that as the value of x approaches 1, the total intensity is that from GaN which has a full range from 13 eV to 27 eV . The trunca-

TABLE 5.3: The total intensity of the reference spectrum of InN, synthesised $\text{In}_x\text{Ga}_{1-x}\text{N}$ and the extrapolated spectrum are used to calculate the truncation correction at each value of x .

x	$\int_{13\text{ eV}}^{E_t(x)} S_{\text{InGaN}}(E, x)$	$\int_{E_t(x)}^{27\text{ eV}} f(x)$	$f_{\text{cor}}(x)$
1.0	0.127	0.153	2.204
0.9	0.131	0.132	2.008
0.8	0.135	0.113	1.837
0.7	0.138	0.095	1.684
0.6	0.142	0.078	1.549
0.5	0.146	0.063	1.433
0.4	0.150	0.049	1.327
0.3	0.153	0.035	1.231
0.2	0.157	0.023	1.145
0.1	0.161	0.010	1.064
0.0	0.163	0.000	1.000

tion correction factor is used to correct the weights of InN and constructed $\text{In}_x\text{Ga}_{1-x}\text{N}$ core-losses calculated in eqns. 5.14–5.15. The InN, $S_{\text{InGaN}}(E, x=1)$, reference core-loss has been truncated the most. Hence, it will have the largest correction factor, $f_{\text{cor}}(x=1)$, as shown in fig. 5.12(B). However, the truncation correction is not needed in GaN buffer layer as GaN reference spectrum is available for fitting in full range till 27 eV . InN and $\text{In}_x\text{Ga}_{1-x}\text{N}$ will

have almost no influence on the quality of fits in GaN buffer layer as is evident from fig. 5.7(B) but Ga $M_{4,5}$ is overestimated in $\text{In}_x\text{Ga}_{1-x}\text{N}$ layer to compensate for In $N_{4,5}$ truncation. Hence, the weights in eqns. 5.14–5.16 can be corrected as shown in eqns. 5.22–5.24 only in $\text{In}_x\text{Ga}_{1-x}\text{N}$ region. Hence the maps of $f_{cor}(x)$ are shown in figs. 5.13. Note that the value of $f_{cor}(x)$ in GaN buffer region is always unity.

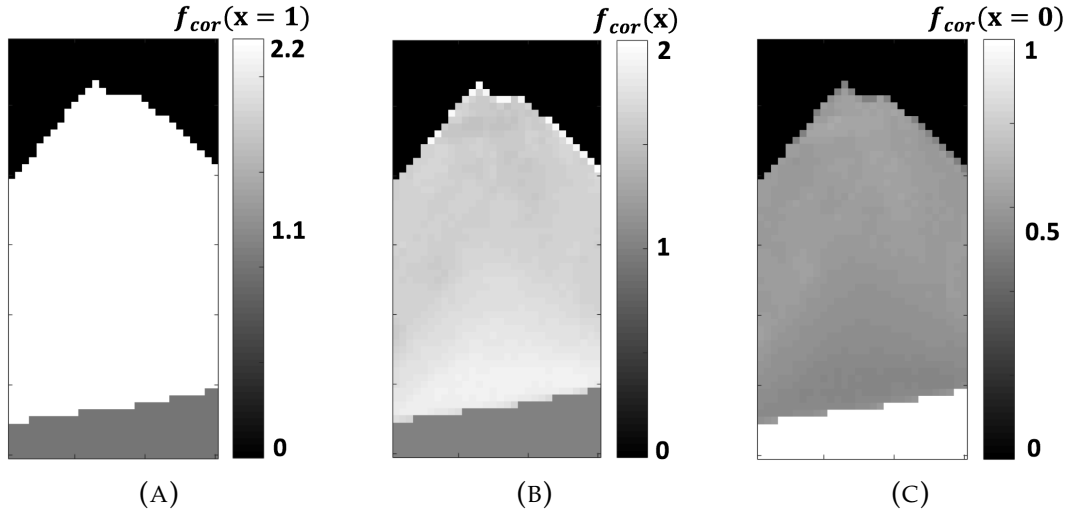


FIGURE 5.13: The maps of truncation correction factors for (A) reference InN spectrum, $f_{cor}(x = 1)$. (B) constructed $\text{In}_x\text{Ga}_{1-x}\text{N}$ spectrum, $f_{cor}(x)$ and (C) reference GaN spectrum, $f_{cor}(x = 0)$.

$$w'_{cInN} = w_{cInN} \cdot f_{cor}(x = 1) \quad (5.22)$$

$$w'_{cInGaN} = w_{cInGaN} \cdot f_{cor}(x) \quad (5.23)$$

$$w'_{cGaN} = w_{cGaN} \cdot \frac{1}{f_{cor}(x = 1)} \quad (5.24)$$

With these corrected weightings, as shown in figs. 5.14(A–C), the effective In and Ga content from core-losses can be determined by eqns. 5.25–5.26. The truncation corrected effective In content is shown in fig. 5.15(B).

$$x'_c = w'_{cInN} \cdot 1 + w'_{cInGaN} \cdot x + w'_{cGaN} \cdot 0 \quad (5.25)$$

$$(1 - x'_c) = w'_{cInN} \cdot 0 + w'_{cInGaN} \cdot (1 - x) + w'_{cGaN} \cdot 1 \quad (5.26)$$

The truncation factor value is higher in In rich region near the interface because the local x value in that region is higher. Hence, the onset of the synthesised $\text{In}_x\text{Ga}_{1-x}\text{N}$ core-loss will be shifted towards InN core-loss. This

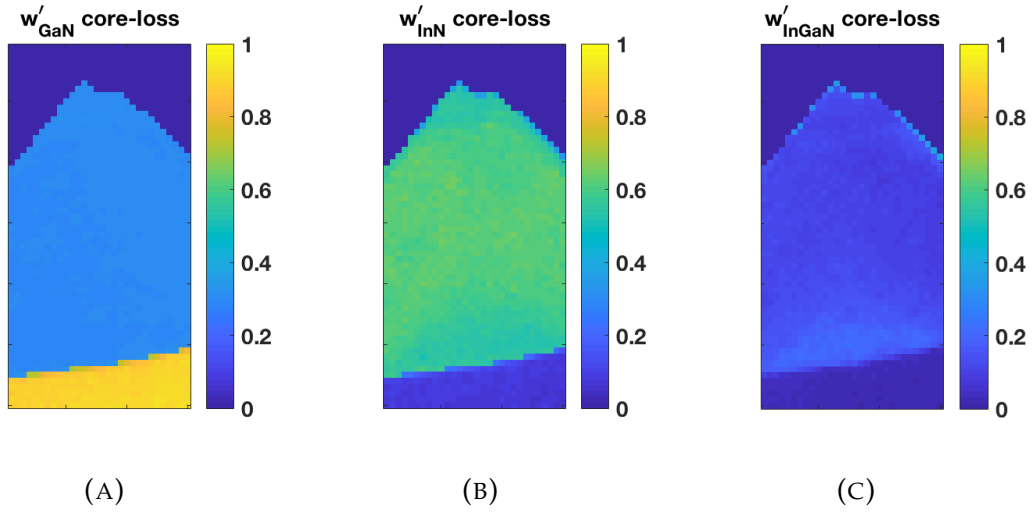


FIGURE 5.14: Truncation corrected weights calculated in eqns. 5.22–5.24 for (A) GaN (B) InN and (C) $\text{In}_x\text{Ga}_{1-x}\text{N}$ core-loss.

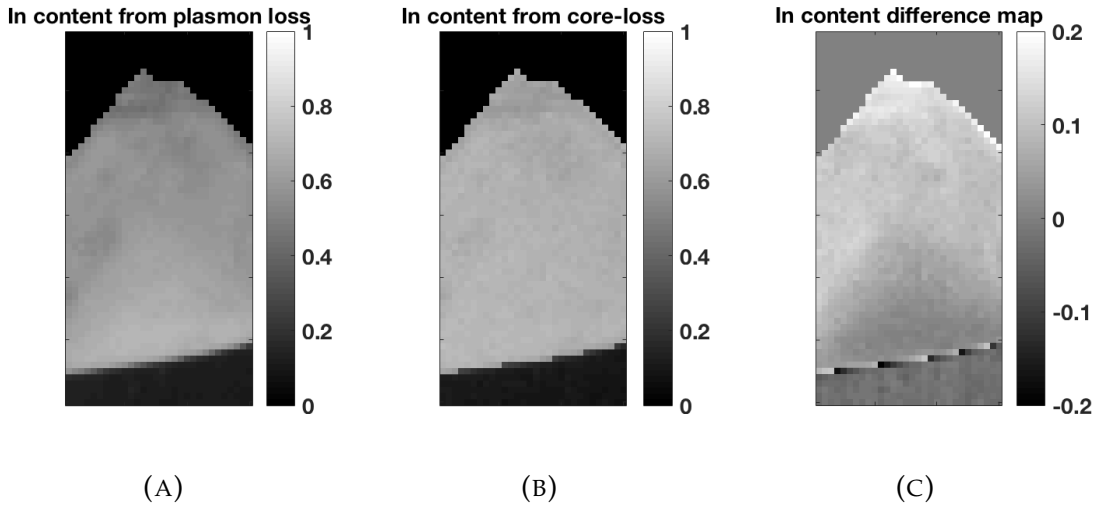


FIGURE 5.15: Maps of In content, x , calculated for data from fig. 5.9(G) from truncation corrected weights from fig. 5.14 of fitting (A) plasmon losses, (B) low core-losses, (C) difference map (B)–(A).

TABLE 5.4: Comparison of effective In content from different regions identified in fig. A.3(B) for fitting range from 13 eV to ~ 23 eV.

	Regions				
	1	2	3	4	5
w'_{cInN}	0.62 ± 0.01	0.61 ± 0.02	0.61 ± 0.02	0.54 ± 0.01	0.07 ± 0.01
w'_{cInGaN}	0.12 ± 0.01	0.12 ± 0.02	0.11 ± 0.02	0.20 ± 0.01	0.02 ± 0.01
w'_{cGaN}	0.30 ± 0.01	0.30 ± 0.01	0.30 ± 0.01	0.30 ± 0.01	0.91 ± 0.01
x_p	0.60 ± 0.03	0.60 ± 0.05	0.61 ± 0.03	0.70 ± 0.01	0.11 ± 0.01
x'_c	0.69 ± 0.02	0.69 ± 0.02	0.69 ± 0.01	0.71 ± 0.01	0.09 ± 0.01

indicates that more intensity is lost which needs a higher correction factor to recover the correct value. Similar effects can be observed in weighting maps from fig. 5.14(C). The w_{InN} core-loss map from fig. 5.9(E) will have a constant correction factor of $f_{cor}(x = 1)$, as shown in fig. 5.13(A). The contrast of w'_{InGaN} core-loss map in fig. 5.14(C) in the $In_xGa_{1-x}N/GaN$ interface region is higher. In fig. 5.9(H), the R^2 values in GaN buffer layers are almost unity, indicating that the model is almost perfectly describing the experimental spectrum as evident from fig. 5.7(B). Hence, the correction factor in GaN buffer region should be unity. This is indicated in truncation correction map, $f_{cor}(x)$, in fig. 5.13(A–C). A similar analysis can be done with Ga content. The amount of Ga that is overestimated in $In_xGa_{1-x}N$ region is due to truncation of $In N_{4,5}$ core-loss. Hence, the weighting of GaN, w_{GaN} core-loss, must be divided by the truncation factor, $f_{cor}(x = 1)$. The step size, Δx , for reference spectra considered by Walther et al., (2017) was only 0.05. However, the larger Δx cause quantization errors in the maps. Hence, introducing larger error bars in the quantification in table 5.1. The proposed method introduces an automated $In_xGa_{1-x}N$ reference spectra construction at a step size of $\Delta x = 0.001$. It is also worth noting that without truncation correction the weighting of the Ga $M_{4,5}$ edge, w_{GaN} core-loss in fig. 5.9(A), was increased systematically to compensate for truncated $In N_{4,5}$ edge. After corrections made in eqns. 5.22–5.24, the quantification from core-loss and bulk plasmons are now comparable. The advantage of using extended fitting ranges is to get In and Ga quantification within a error bars.

5.6 Quantification from plasmon peaks

In previous sections, the quantification for $In_xGa_{1-x}N/GaN$ layers has been attempted by joint fitting of both bulk plasmons and core-losses of In and Ga. The bulk plasmons are characteristic of a material and can be modelled independently using Lorentz functions, $L(E, E_p, W_p)$. The maps of plasmon peak position, E_p , and width, W_p , can be studied to cross check with the quantification carried out using high-loss ionization edges. In some case, like $In_xGa_{1-x}N$, it is difficult to model the bulk plasmons independently due to the overlap of the low-energetic core-losses and bulk plasmons and possible broadening of bulk plasmon due to phase separation. However, in cases like the multi-junction solar cell and Tb doped AlN, the bulk plasmons can be quantified independently and quantification can be verified for high energy-losses and vice-versa. The bulk plasmon modelling is done with Lorentz

functions as shown in eqn.5.27. The parameters E_p and W_p define the peak position and the FWHM of bulk plasmons.

$$L(E, E_p, W_p) = \frac{A_p}{\pi} \cdot \frac{(W_p/2)}{(E - E_p)^2 + (W_p/2)^2} \quad (5.27)$$

where A_p is a scaling factor. The Lorentz function, $L(E, E_p, W_p)$, can be fitted to a bulk plasmon over the range from $E_p - W_p/2$ to $E_p + W_p/2$. However, sometimes core-losses overlap with the bulk plasmon peaks on the right side and the tails of the ZLP with the left side shoulder of the bulk plasmons. Hence, the FWHM calculated without taking these other effects into account will always be an overestimate. The fit range for bulk plasmon are therefore chosen from $(E_p - 0.2 \cdot W_p)$ to $(E_p + 0.15 \cdot W_p)$. The results from Lorentz fits for bulk plasmons of layers in the multi-junction solar cell are shown in fig. 5.16(B) and fig. 5.17. The maps of plasmon peak position, E_p , and FWHM, W_p , are shown in figs. 5.18(A,C) and their profiles are shown in figs. 5.18(B,D). The profiles of E_p and W_p shown in figs. 5.18(B,D) are ob-

TABLE 5.5: The modelled bulk plasmon position, E_p , from Lorentz function described in eqn. 5.27 for the low-loss EELS of multi-junction solar cell in fig. 5.16(A).

	Region 2	Region 3	Region 5	Region 8
E_p [eV]	21.67 ± 0.14	15.53 ± 0.02	15.09 ± 0.02	15.53 ± 0.02
W_p [eV]	20.14 ± 1.01	5.48 ± 0.04	5.67 ± 0.14	5.48 ± 0.04

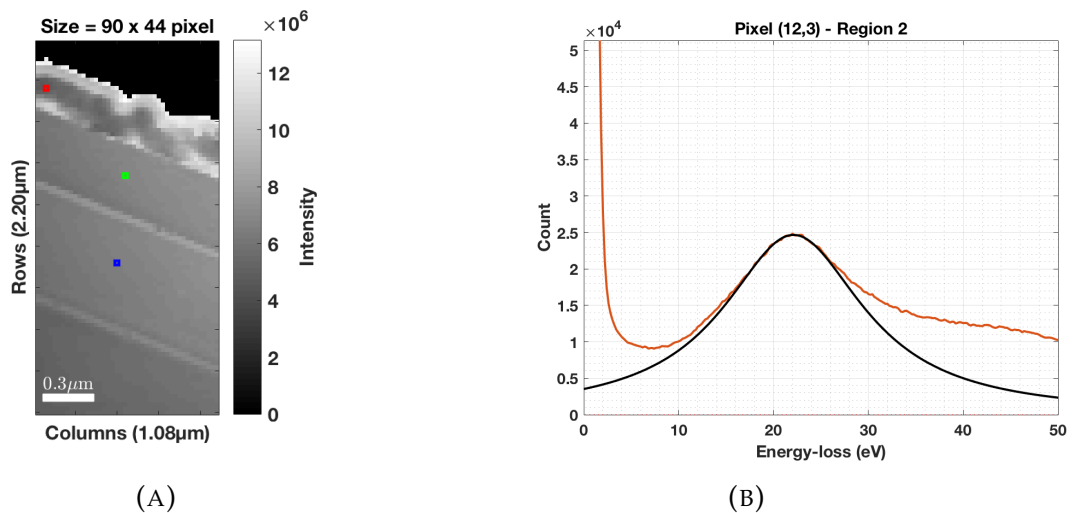


FIGURE 5.16: (A) The locations of random spectrum extracted from regions 2 (red), 3 (green) and 4 (blue) of multi-junction solar cell. (B) Spectrum extracted from region 2 of multi-junction solar cell (Cu) and a Lorentz function is fitted to the bulk plasmons. $E_p = 22.11$ eV and $W_p = 18.07$ eV.

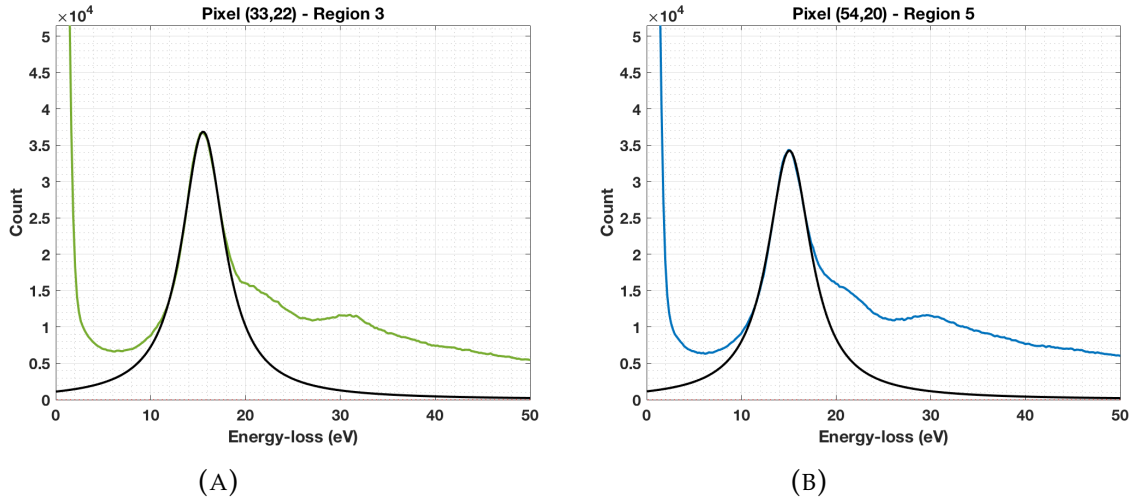


FIGURE 5.17: Lorentz function is fitted to the bulk plasmons from (A) region 3 (GaAs), ($E_p = 15.54$ eV and $W_p = 5.50$ eV) and (B) region 5 (AlGaInP), ($E_p = 15.08$ eV and $W_p = 5.61$ eV) of multi-junction solar cell.

tained by integrating over the map across the line marked on the maps. It is a clear indication of all regions having similar plasmon peak positions, E_p , and FWHM, W_p . Regions 3 and 8 thick are GaAs layers doped with Si, hence, only one representative spectrum is taken from region 3. The values of E_p and W_p for regions 2 (Cu was reported at $E_p = 20.40$ eV by Mikoushkin, (2012) and Ngantcha et al., (2005)), 3 and 8 (GaAs was reported at $E_p = 15.66$ eV, $W_p = 4$ eV by Stöger–Pollach et al., (2006), $E_p = 15.80$ eV by Egerton, (2011b) and $E_p = 16$ eV, $W_p = 5.48$ eV by Ahn, (2005)) are in agreement with the literatures within error margin of ± 0.2 eV for E_p . The large FWHM of bulk plasmon in region 2 is due to the formation of oxides on the top layer. The oxides do not have proper crystal orientation to have resonance, hence, the W_p values are wider for oxides. A similar phenomenon is observed in the W_p map of AlN doped with Tb as shown in fig. 5.18(F). Tb–O complexes formed due to Tb and O co-segregation is observed (Angadi et al., 2017). The statistics of E_p and W_p for AlN doped with Tb are shown in table 5.6. The values of E_p and W_p for AlN reported at $E_p = \sim 21.20$ eV, $W_p = \sim 8.30$ eV by Magnan et al., (1999) and Serin et al., (1998) and for Si reported at $E_p = \sim 16.75$ eV, $W_p = \sim 4.80$ eV by Batson, (1991), Cheynet et al., (2004), Pantel et al., (2006) and Stöger–Pollach et al., (2006) and are within error of ± 0.04 for E_p . The W_p map from fig. 5.18(F) of AlN doped with Tb can be correlated with O K elemental map calculated from core-losses in fig. 3.16(D). The maps are positively correlated in AlN region which also confirms the wider FWHM of bulk plasmons for oxides. At the interface of AlN and Si, SiO_2 has been formed. This is reflected in the W_p map, as well as the O K map at high-loss map in

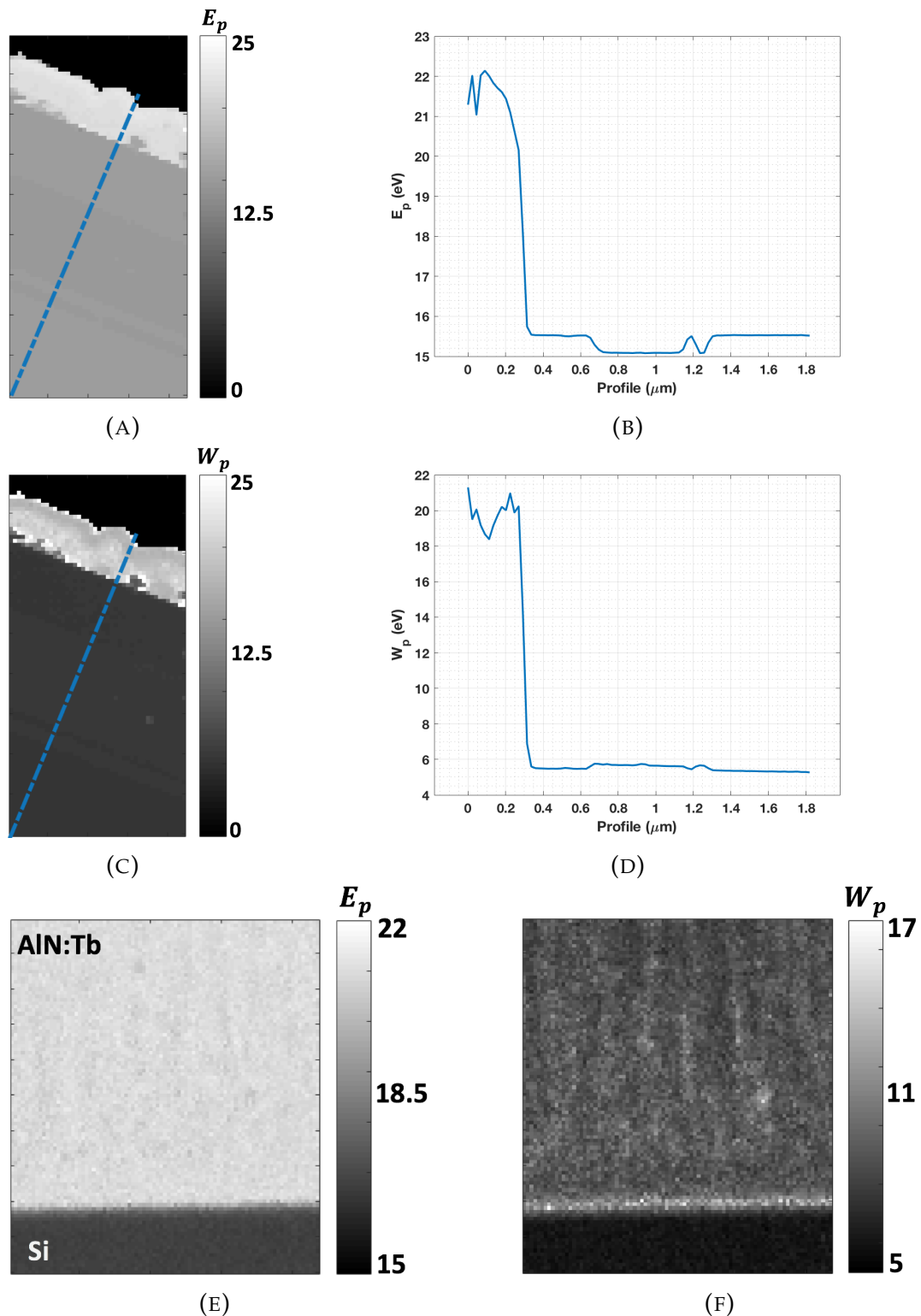


FIGURE 5.18: (A,C) maps and (B,D) profiles of bulk plasmon peak position, E_p (in eV), and FWHM, W_p (in eV), determined by Lorentz fitting. (E) and (F) are maps of bulk plasmon peak position, E_p (in eV), and FWHM, W_p (in eV), determined by Lorentz fitting.

TABLE 5.6: The modelled bulk plasmon position, E_p , from Lorentz function described in eqn. 5.27 for the low-loss EELS of AlN doped with Tb in fig. A.4(B).

	Box 1	Box 2
E_p [eV]	20.99 ± 0.17	16.82 ± 0.08
W_p [eV]	8.91 ± 0.77	6.08 ± 0.24

fig. 3.16(D).

5.7 Relative specimen thickness from modelling

The relative specimen thickness is defined as the natural log of the ratio of total intensity, I_t , to intensity of ZLP, I_0 , as shown in eqn. 5.28.

$$\frac{t}{\lambda} = \ln \left(\frac{I_t}{I_0} \right) \quad (5.28)$$

where I_0 is approximately determined by integrating the intensity of spectrum from channel #1 until minimum point between ZLP and bulk plasmon peak position. An alternative and more accurate ways to measure t/λ would include fitting the bulk plasmon with a Lorentz function, $L(E, E_p, W_p)$, (eqn. 5.27) and the ZLP with a Gaussian function, $\mathcal{N}(E, E_0, W_0)$, (eqn. 5.29) and then weighting both according to a Poisson distribution, $P(n, t/\lambda)$, (eqn. 2.20) simultaneously, as shown in eqn. 5.30.

$$\mathcal{N}(E, E_0, W_0) = \left[\frac{A_0}{W_0 \sqrt{2\pi}} \right] \cdot \left(2\sqrt{2 \ln 2} \right) \exp \left(\left[-\frac{(E - E_0)^2}{2W_0^2} \right] \cdot \left(2\sqrt{2 \ln 2} \right)^2 \right) \quad (5.29)$$

$$S(E, t/\lambda, E_0, W_0, E_p, W_p) = P(0, t/\lambda) \mathcal{N}(E, E_0, W_0) + \sum_{k=1}^n P(k, t/\lambda) L(E, k \times E_p, W_p) \quad (5.30)$$

where $n = \lfloor E_{max}/E_p \rfloor \in \mathbb{N}$ is the integer number of plasmon losses considered. t/λ , position (E_0) and FWHM (W_0) of the ZLP, position (E_p) and FWHM (W_p) of bulk plasmon are the fitting parameters. Eqn. 5.28 can be used as an initial estimate of t/λ in MLLS fitting of the low-loss in eqn. 5.30. The bulk plasmon peaks are ideally Lorentzian function if there is no spreading by

the spectrometer. However, the detector of the spectrometer has its own PSF which is convolved with the low-loss spectrum. Hence, instead of using pure Lorentzian, a Voigt function can be used. Voigt function, $V(E, E_p, W_p, W_0)$, is the convolution of both a Gaussian and a Lorentzian function, as shown in eqn. 5.31.

$$V(E, E_p, W_p, W_0) = A_v \cdot \{\mathcal{N}(E, 0, W_0) * L(E, E_p, W_p)\} \quad (5.31)$$

where W_0 , E_p and W_p are the fitting parameters along with A_0 (eqn. 5.29) and A_p (eqn. 5.27). The Gaussian kernel, $\mathcal{N}(E, 0, W_0)$, is centred at 0 eV, (hence, $E_0 = 0$). This is to avoid Sifting property of convolution. The Sifting property convolution with a delta function, $\delta(E)$, is shown in eqn. 5.32.

$$f(E) * \delta(E - E_0) = \int_{k=-\infty}^{+\infty} f(E - k)\delta(k - E_0)dk = f(E - E_0) \quad (5.32)$$

Hence, the location of Voigt function, $V(E, E_p, W_p, W_0)$, is entirely dictated by the location of the Lorentz function, E_p . Then, the low-loss model would be as shown in eqn. 5.33.

$$S(E, t/\lambda, E_0, W_0, E_p, W_p) = P(0, t/\lambda) \mathcal{N}(E, E_0, W_0) + \sum_{k=1}^n P(k, t/\lambda) V(E, k \times E_p, W_p, W_0) \quad (5.33)$$

Modelling Voigt functions is computationally expensive. Hence, sometimes an approximation of the Voigt function, called Pseudo-Voigt function, is used. A pseudo-Voigt function, $V_p(E, E_p, W_p, W_0)$, is a weighted sum of a Gaussian and a Lorentzian, as shown in eqn. 5.34, where $\eta \in [0, 1]$ is the weighting factor as well as the fitting parameter.

$$V_p(E, E_p, W_p, W_0) = \eta \cdot \mathcal{N}(E, 0, W_0) + (1 - \eta) \cdot L(E, E_p, W_p) \quad (5.34)$$

The modelled spectrum is shown in fig. 5.19, where the Voigt functions fit for bulk plasmons is slightly broadened. However, the Lorentz functions fit the bulk plasmons almost perfectly. The low-loss modelling can be extended to an entire SI, which provides average t/λ values of $\overline{t/\lambda} = 0.31$, ($\overline{R^2} = 0.992$) based on multiple scattering statistics as shown in table 5.7. The relative thickness map of AlN doped with Tb calculated using this method is shown

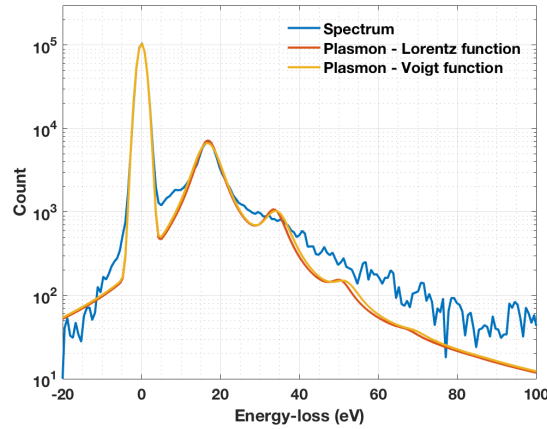


FIGURE 5.19: The AlN:Tb spectrum from EELS SI in fig. A.4(A) is chosen as an example and fits described in eqns. 5.30 & 5.33 are shown on log-scale. Orange line: spectrum modelled using bulk plasmons as Lorentz functions. Yellow line: Voigt function is used to model the bulk plasmons. In both cases, ZLP is modelled using a Gaussian function.

TABLE 5.7: AlN doped with Tb

	t/λ	R^2	t/λ		R^2
	All region		1	2	1 & 2
Eqn. 5.28	0.32 ± 0.05	–	0.36 ± 0.03	0.26 ± 0.01	–
Eqn. 5.30	0.31 ± 0.04	~ 1	0.35 ± 0.02	0.25 ± 0.01	0.99 ± 0.01
Eqn. 5.33	0.31 ± 0.04	0.99 ± 0.01	0.35 ± 0.02	0.25 ± 0.01	0.99 ± 0.01

in fig. A.4(C). The inelastic mean free paths (λ) calculated in table 3.5 are relatively constant in all regions. Hence, the t/λ value can be directly related to absolute thickness of the sample which we got ~ 16 nm. The R^2 map of Lorentz function fits shown in fig. 5.20(D) indicate that the spreading from spectrometer will have very little effect of broadening of bulk plasmons. Hence, the R^2 values are almost unity in fig. 5.20(D) when compared to fig. 5.20(F). The t/λ maps calculated from the three methods described by eqns. 5.28, 5.30 and 5.33 are almost the same within error bars. It is also worth mentioning that t/λ values calculated from eqn. 5.28 are always slight overestimates of 0.01 in case of the AlN:Tb EELS SI. The I_t values include ionization core-loss intensity, DOS, Fowler-Nordheim and Maxwell-Boltzmann distributions, surface plasmons and phonon scattering. The models described in eqns. 5.30 & 5.33 fit only the ZLP, bulk plasmon and multiple scattering. The t/λ values from Lorentz and Voigt function are exactly the same, with a MSE of difference between eqn. 5.30 and eqn. 5.33 are 0. However, the MSE of R^2 for the same is 0.0064 ± 0.0046 .

5.8 Summary

In chapter 5, a novel approach of measuring phase separation in $\text{In}_x\text{Ga}_{1-x}\text{N}$ by jointly fitting bulk plasmons and low energetic core-losses is described. The values of bulk plasmon width, peak positions, core-loss onsets and chemical shifts of InN, GaN and $\text{In}_x\text{Ga}_{1-x}\text{N}$ ternary alloys are interpolated from Wang et al., (2015, 2016). Pure InN was not present in our acquired EELS SI, hence the In $4d$ core-loss was extracted from a specimen of known x value in the area of In rich $\text{In}_x\text{Ga}_{1-x}\text{N}$ region. The extracted core-loss onset was moved to In $4d$ transition onset and normalised to thickness and total intensity of low-loss as described by Wang et al., (2016). Initially, the range of 13 eV to ~ 23 eV had been used to jointly fit six basis functions (three bulk plasmons and three core-losses for GaN, InN and $\text{In}_x\text{Ga}_{1-x}\text{N}$) with a step size of $\Delta x = 0.05$. The weighted maps of bulk plasmon and core-losses shown in figs. 5.8 indicate high noise ($\sim \pm 10\%$) as tabulated in table 5.1. This is due to the large step size chosen for increments of x for ternary phase. The effective In content measured from both bulk plasmons and the core-losses are comparable. The In content is overestimated by core-loss weightings by $\lesssim 10\%$ with respect to the In content calculated by weightings from bulk plasmons. This could be due to the fact that in the fitting range from 13 eV to ~ 23 eV, the reference for Ga $M_{4,5}$ is not completely included, leading to an overestimation of overall In

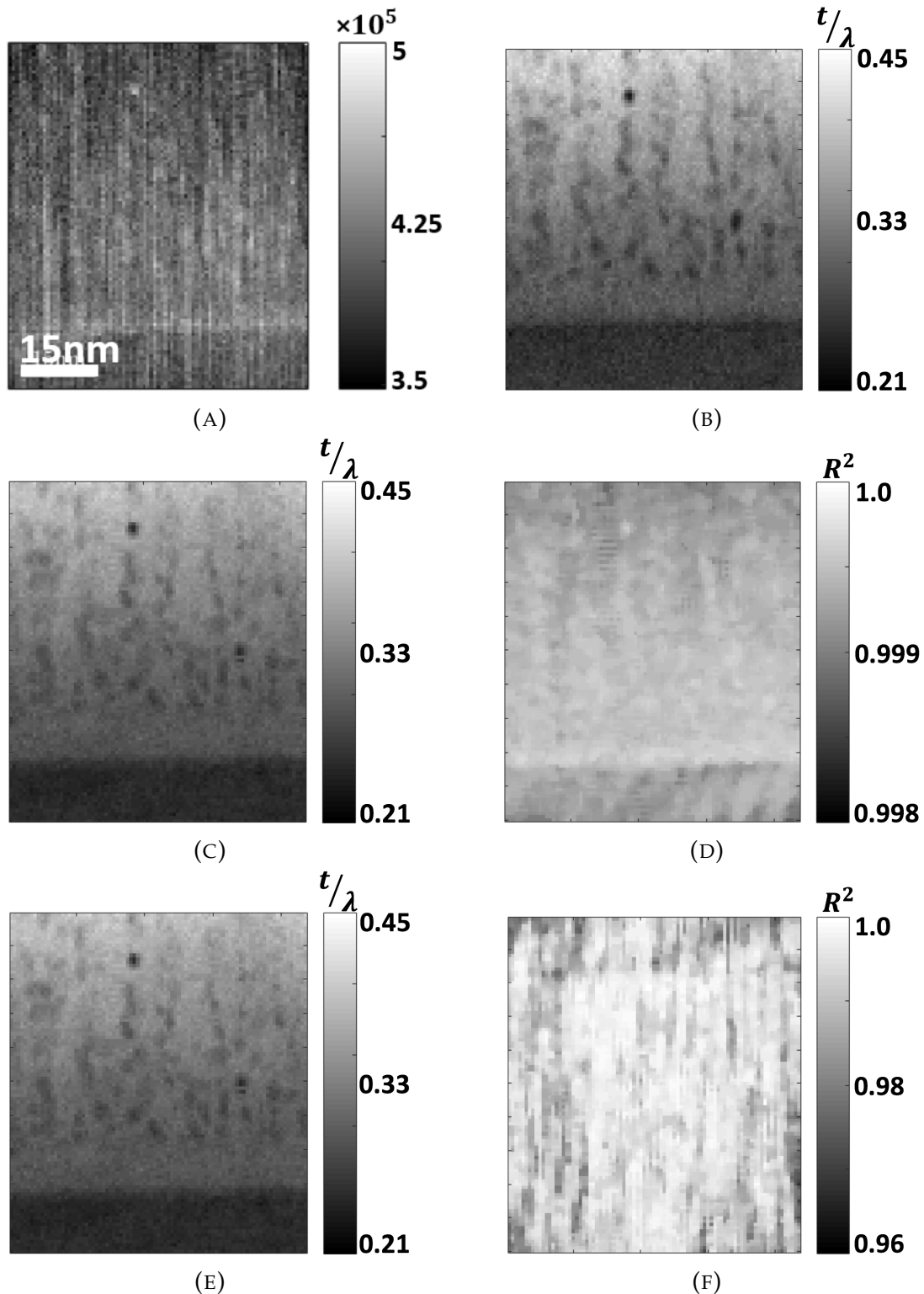


FIGURE 5.20: (A) HAADF. t/λ values calculated using (B) eqn. 5.28, (C) low-loss fitting as described in eqn. 5.30 and the R^2 values of both the fit using Lorentzian and Voigt as bulk plasmons are described in (D). Similarly, (E, F) are the t/λ and R^2 values calculated from low-loss fit using eqn. 5.33.

content by core-losses. To include the full Ga $3d$ ($M_{4,5}$) transition, the fitting range was increased from ~ 23 eV until 27 eV. However, as the experimental reference spectrum for InN only extended until ~ 23 eV, it was necessary to include a step function in our fitting from 13 eV to 27 eV, as shown in figs. 5.7. The weight maps thus obtained in figs. 5.9 by increasing the fit range could not be interpreted physically as the values of In and $\text{In}_x\text{Ga}_{1-x}\text{N}$ maps were completely different from those from the smaller fit range e.g. the mean value of In content in different regions identified in fig. A.3(B) where in the range of $\sim 0.32 \pm 0.01$. This is almost half the value of estimated by the quantification from bulk plasmons. Hence, a truncation correction has been proposed to compensate for the intensity that is lost by the experimental reference spectrum for InN not fully covering the In $N_{4,5}$ edge from ~ 23 eV to ~ 27 eV. It is also important to note that there are no models present in the literature to extrapolate a $4d$ transition, so a simple horizontal extrapolation was assumed. The truncation corrected maps showed contrast in agreement with the extended fit ranges, however, the correct In content can be recovered only within $\sim 7\%$ error considering the In content quantified by bulk plasmon for short fit range as the reference. The In content quantified in both fit ranges using bulk plasmons differ by $\sim 10\%$ (observe x_p in both table 5.1 and 5.4). This difference in quantification is because of the step function being present in the fitting which will affect the fitting coefficients of Lorentz function, and the truncation correction is not applied to x_p but only to x_c . The difference in the contrast of weights in short and larger fit ranges in figs. 5.8 and 5.9 are only due to different fitting ranges and the anomalies in the fitting coefficients due to inclusion of a step function. However, when the In content is calculated the results are comparable. Hence, it can be concluded that while fitting low-loss spectra with low energetic core-losses and bulk plasmon losses for quantification, it is always preferable to have reference spectra covering the same energy ranges for fitting. In other materials (such as solar cell and AlN:Tb) the bulk plasmons have been individually modelled using Lorentz functions. Since the bulk plasmon peak position is characteristic for a given material, and in the systems considered shifts with stoichiometry the initial quantification can be estimated from the bulk plasmon peak position, E_p or the can be used to verify with the already quantified core-losses. It was interesting to note that the width of the bulk plasmon was increased near the interface of AlN and Si substrate. This is presumably due to the formation of SiO_2 which has a plasmon peak both higher and wider in energy. The formation of Tb and O co-segregation by forming Tb–O complexes as suggested

by Benz et al., (2013b). A novel approach of determining relative thickness by distribution fitting to low-loss is proposed. The ZLP and bulk plasmon are modelled using a Gaussian and several Lorentzian functions weighed according to Poissonian statistics, the t/λ in the Poisson function being a fitting parameter which provides the relative thickness. The Lorentz functions were replaced with Voigt functions to check the variation in the estimation of t/λ . The t/λ values from both techniques were found to be identical and are compared with t/λ estimated using Egerton's method. The values are found to be similar within error margin. The elemental quantification based purely on bulk plasmon peak position is impossible. If the end-members are well defined, as was in case of $\text{In}_x\text{Ga}_{1-x}\text{N}$, x can be quantified. The same method can be extended to study the other ternary and quaternary alloys, when the end-members are well defined.

Chapter 6

Automated VEELS for bandgap measurements

6.1 Introduction

Precise determination of the electronic bandgap is important for semiconductor research. It is possible but not straight-forward to determine the location of the onset of the DOS from low-loss EELS rather than by optical spectroscopy. For example determination of bandgap from Tauc plot (Davis et al., 1970; Dolgonos et al., 2016; Stenzel, 2005; Tauc, 1968; Tauc et al., 1966) that describes the optical absorption spectrum and the onset of a linear onset provides the direct bandgap of the semiconductor material. The problem with the Tauc plot is the linear extrapolation is very subjective and slight variation in the fit window for linear extrapolation will alter the bandgap determination. The other computational methods such as support vector regression computational intelligence (SVRCI) based model for estimation of direct bandgap of ZnO is proposed by Owolabi et al., (2016). A square-root function fit to the low-loss EELS spectrum may work for direct bandgaps (Rafferty et al., 1998) but will be affected by the presence of a strong and asymmetric ZLP (Lazar et al., 2003; Rafferty et al., 2000; van Benthem et al., 2001), phonons (Stöger-Pollach et al., 2007), Čerenkov effects (Horák et al., 2015; Stöger-Pollach, 2008; Stöger-Pollach et al., 2006), guided light modes and possibly even surface plasmons. One solution (Erni et al., 2005) would be to use a monochromator where the energy-resolution can be as good as ~ 0.015 eV (Krivanek et al., 2013). Deconvolution methods can be applied to remove or reduce effects from ZLP tails (Egerton, 2011b). Also, the tail of the bulk plasmon will affect the determination of bandgap (Walther et al., 2017). The determination of DOS onset for wide-bandgap materials has been studied extensively (Amari et al., 2011; Bangert et al., 1997b; Lakner et al., 1999; Park et al., 2009) still the reliability required for electronics ($\ll 0.1$ eV)

is difficult to achieve quantitatively when the material is unknown. Fourier-log and RL deconvolution methods are routinely used for one-dimensional (1D) spectra but they tend to enhance noise. However, with proper pre-processing by extrapolation of tails at both ends and embedding the spectrum into twice as wide empty spectrum and padding both ends, noise can be reduced. Lot of work has been done qualitatively in analysing the low-loss region by applying Fourier-log deconvolution (Hage et al., 2013). The deconvoluted spectrum can then be used to get the energy-loss function using Kramers–Kronig analysis to reveal the complex dielectric function (Dorneich et al., 1998; Morales–Rodríguez et al., 2012; Pokrant et al., 2005; Potapov et al., 2009; Schamm et al., 2003; Stöger–Pollach, 2008). Morales-Cruz et al., (2017) have used the energy-loss function to determine bandgap onset for $\text{Bi}_2\text{Mo}_x\text{W}_{1-x}\text{O}_6$ by manually selecting the fit ranges. An alternative method is two-dimensional (2D) deconvolution of a spatially resolved EELS (Gloter et al., 2003). In this method the deconvolution is applied to a spatially (Walther, 2003; Walther et al., 1999) or angular resolved EELS or 2D EELS, reducing the size of the extended ZLP to almost a single point. By this way of deconvolution, even weak information which is hidden by the wide PSF of the ZLP can be made visible. In this study, different ways to determine the bandgap of wide-bandgap materials such as GaN are compared using RL deconvolution of 1D and 2D EELS. For this, starting from the same 2D EELS, the effect of changing the sequence of projection (from 1D to 2D) and deconvolution is compared. A Gaussian model of the ZLP is considered as an initial PSF in both cases.

6.2 Limitations in determination of bandgap onset

The DOS onset is usually buried between the tails of the dominant ZLP on the left and the bulk/surface plasmon on the right. To identify the bandgap, the underlying background must be subtracted. The latter can be modelled pretty straight forward using Lorentz functions from eqn. 5.27. In ternary alloy systems, like $\text{In}_x\text{Ga}_{1-x}\text{N}$, the bulk plasmons can be modelled along with core-losses using joint fitting from eqn. 5.9 (Walther et al., 2017). Eccles et al., (2008) and Gu et al., (2007) have discussed the difficulty in measuring bandgap using a monochromator in the presence of Čerenkov effects and have also discussed the effects of specimen thickness in measuring the

bandgap. However, modelling of ZLP is not straight forward as it is a combination of elastic scattering, phonon scattering, Fowler-Nordheim distribution in the case of FEG- emitters (Fowler et al., 1928) and Maxwell-Boltzmann distribution combined with the PSF of the spectrometer. A ZLP acquired using a monochromator can have a FWHM of $W_0 \approx 0.015$ eV. However, the ZLP of the $\text{In}_x\text{Ga}_{1-x}\text{N}$ low-loss SI from table A.2 which has been acquired with monochromator are distorted as shown in fig. 5.1, probably due to misalignment while acquisition. It will be difficult to model the ZLP with a single Gaussian or Lorentzian functions. The fit above FWHM of the ZLP will have the highest R^2 values. But fail to model the tails of ZLP (Bangert et al., 1997a). (Bangert et al., 1997b) have modelled Fowler-Nordheim distribution along with a Gaussian or a Lorentzian to model the energy-loss side tail of the ZLP, but fitting an entire ZLP with two functions only will create fitting errors in the very low intensity tails side of the ZLP. Voigt function seems ideal as it has Lorentzian like tail with Gaussian like FWHM. The expression described by Rafferty et al., (2000), includes Gaussian (instabilities in the spectrometer), Poissonian (electron scattering model) and Fowler-Nordheim due to cold-FEG emission. The fit optimization R^2 will not be very meaningful if the model is crossing the spectrum at low intensities. This will then have uncertainties at the tail side of the ZLP due to insensitivity of fit optimization parameters, which is where the presumed DOS is expected to rise. In literature there isn't much work done on automated determination of bandgaps. Although there are studies more or less successfully who have fitted square-root functions to multiple semiconductor crystals whose direct bandgap onset was known a-priori, the fit quality and the fitting parameters such as fit-ranges were often not mentioned. Figs. 6.1 show the bandgap onset, E_g plotted vs R^2 for GaN. Short fit ranges of 0.5 eV to 3 eV with 0.5 eV increments have been chosen and calculated every 0.5 eV between 0 eV to 10 eV. All the determined E_g values are plotted against their respective R^2 . It is clear that the spread of E_g values is large and does not converge to ~ 3.44 eV. There are few E_g values at $E_g \approx 3.44$ eV but the R^2 is no better. Hence there are no criteria to determine which E_g measurement is best without previous knowledge of the material. Short fitting ranges with best R^2 will obviously not provide the most accurate E_g . Hence, investigating various generic methodologies is important for a reliable determination of bandgaps.

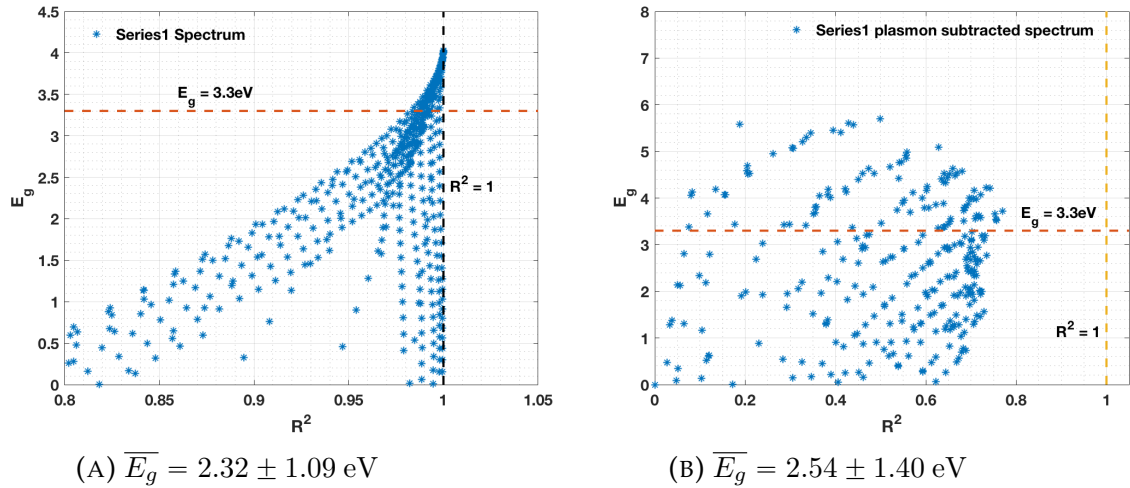


FIGURE 6.1: Clusters of E_g vs. R^2 for EELS of GaN Series 1. The square-root fitting is applied to the raw experimental spectrum in fig. A.5(B) with varying fit ranges from 0.5 eV to 3 eV between 0–10 eV at every 0.5 eV increment, (A) without subtracting any background and (B) and with bulk-plasmon subtraction.

6.3 Modelling ZLP

For any iterative deconvolution methods, a good estimation of the PSF is needed. In EELS, the PSF can be approximated by a broadened ZLP. For the ZLP of a spectrum acquired using a cold-FEG, one needs to consider modelling it by a superposition of a Fowler-Nordheim distribution for field emission (taking into account tunneling of the slowest electrons through the surface states), a Maxwell-Boltzmann distribution for thermal emission (taking into account a tail of high-energy electrons due to thermal fluctuations at high temperatures) and Gaussian instrument broadening due to the spectrometer and instabilities in the high voltage supply (Arslan et al., 2006). Bangert et al., (1997b) have demonstrated a model for ZLP fitting using a Fowler-Nordheim distribution for electron distribution from the gun, a Lorentzian function for the PSF due to lens aberrations (Egerton et al., 1995) and a Gaussian function for instrument instabilities. Gloter et al., (2003) have applied, for the first time, RL 2D deconvolution to improve the energy-resolution to observe ELNES at ionization edge structures and compared the results with a set of standard spectra. A similar approach can be utilized to compare the reliability of bandgap determination in 2D deconvoluted spectra.

6.3.1 Modelling ZLP in 1D

For a standard 1D spectrum of intensity vs. energy-loss, the top half of the ZLP can be approximated by a Gaussian function, $\mathcal{N}(E, E_0, W_0)$, as in eqn. 5.29. This can be used to calibrate the energy-loss axis to sub-channel accuracy by way of interpolation to a finer sampling grid. A pure Gaussian function cannot model the tails of ZLP, although a Voigt function, $V(E, E_p, W_0, W_p)$, (eqn. 5.31) can provide better approximation of ZLP, as shown in fig. 6.2. Due to the complexity of ZLP, a simple but sufficient model can be an extrapolation of the right tail of the ZLP (Batson et al., 1987). This could probably be the best possible way to remove background for determining the DOS. The combination of Gaussian and Fowler-Nordheim distribution is a simple exponential at higher energies. The simple extrapolation of the right tail of the ZLP is shown in fig. 6.2. The range of fitting for the exponentials was $3 \times W_0$ to $3.3 \times W_0$, where W_0 is the FWHM of the ZLP, which means that only the right most tail end of the ZLP has been used to extrapolate the ZLP. It is observed that, approximately $3.5 \times W_0$ is usually near the energy where a spectrum from the JEOL 2010F will have a minimum point between bulk plasmon and ZLP. Whereas in UltraSTEM (a monochromator), the energy resolution is superior. Hence the local minima at $3.5 \times W_0$ may not be true for that particular case. Hence, we need to model the exponentials left of that minima. That is also the approximate region where the DOS rises in many wide-bandgap semiconductors. If the FWHM of ZLP, W_0 , is too large then it is possible that the DOS is buried deep inside and cannot be retrieved. Hence while acquiring the low-loss spectrum for determination of bandgap, ideally $W_0 \ll 1$ eV. There are alternative frugal method used by DigitalMicrograph™ software (Gatan, 2015) that can be reliable in subtracting ZLP in case of monochromated spectra. The method uses flipping the left shoulder of the ZLP on to right side and extrapolating the right tail with an inverse power-law function (eqn. 2.2) or an exponential function (eqn. 2.3). The mirroring of ZLP works best when the ZLP is symmetric and the contributions of Fowler-Nordheim and Maxwell-Boltzmann distributions are either minimal (which is the case for spectra acquired using monochromator) or of similar extension. From fig. 6.2 it is clear that, a Gaussian distribution decays too rapidly towards zero and does not fit the tails of a ZLP, while a Voigt function can follow the tails of ZLP more closely. The simple two-exponential term extrapolation (eqn. 2.3, where $k = 2$), however, provides almost perfect approximation of the background.

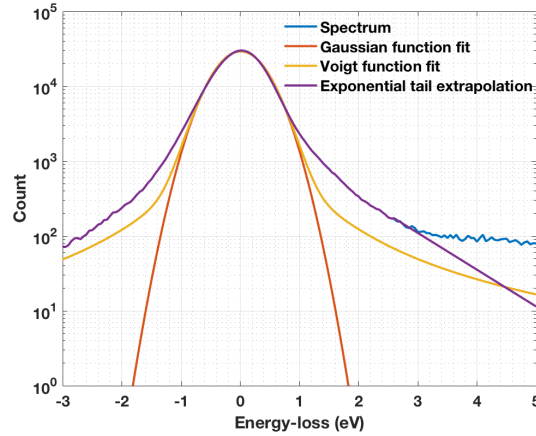


FIGURE 6.2: 1D modelling of ZLP of EELS for (GaN from fig. A.5(B) and $t/\lambda = 0.25$) by distribution fitting of Gaussian ($R^2 = 0.995$) and Voigt ($R^2 = 0.998$) functions in the fitting range -5 eV to 5 eV or exponential tail extrapolation.

6.3.2 Modelling ZLP in 2D

A 2D EELS or spatially resolved EELS use 2 detector and retain image or reciprocal co-ordinate in non-dispersive direction operating TEM in imaging or diffraction mode. In this case, the image was operated at imaging mode for GaN material using 0.6 mm aperture. The details of the experimental conditions conducted by Dr. Thomas Walther are described in section A.4. For deconvolution, we need an improved approximation of the multivariate function (2D PSF). Similar to a 1D spectrum, a 2D spectrum can be modelled using a multivariate normal (MVN) distribution function as described in eqn. 6.1.

$$\mathcal{N}(\mathbf{x}, \mu, \Sigma) = \frac{A_0}{\sqrt{|\Sigma|}(2\pi)^2} \exp\left(-\frac{1}{2}(\mathbf{x} - \mu)^\top \Sigma^{-1}(\mathbf{x} - \mu)\right) \quad (6.1)$$

where $\mathbf{x} = [x_1, \dots, x_k]$, $\forall k \in \mathbb{N}^+$ is a k -dimensional random vector, $\mu \in \mathbb{R}^k$ are the mean values and $\Sigma \in \mathbb{R}^{k \times k}$ values are the square-root of the covariance matrix. Mean values of the distribution from a multivariate Gaussian fit are subtracted from the 2D spectrum to get calibrated axes in both dispersive and non-dispersive direction. The energy-loss axis can be calibrated in 2D by using multivariate Gaussian distribution. The modelled μ and Σ for 2D SI of GaN Series 1 from table A.4 are shown in table 6.1. These pixel values of μ are used as reference to calibrate the ZLP to 0 eV in the energy-dispersive axis. A multivariate Voigt function as shown in eqn. 6.2 can be used to model the ZLP tails, however a standard Voigt function is computationally expensive. Hence, some software routines tend to use modified approximations

TABLE 6.1: Modelling multivariate Gaussian function to experimental 2D EELS of GaN. The values of μ and Σ are in pixels and not in eV.

	μ	Σ
Series 1	$\begin{bmatrix} 64.66 \\ 73.80 \end{bmatrix}$	$\begin{bmatrix} 8.36 & 0 \\ 0 & 7.15 \end{bmatrix}$

of the multivariate Voigt function called multivariate pseudo-Voigt function which lends different weights to both Gaussian and Lorentzian as described in eqn. 6.3. The expression for a 2D modelled ZLP with multivariate pseudo-Voigt function is shown in fig. 6.3.

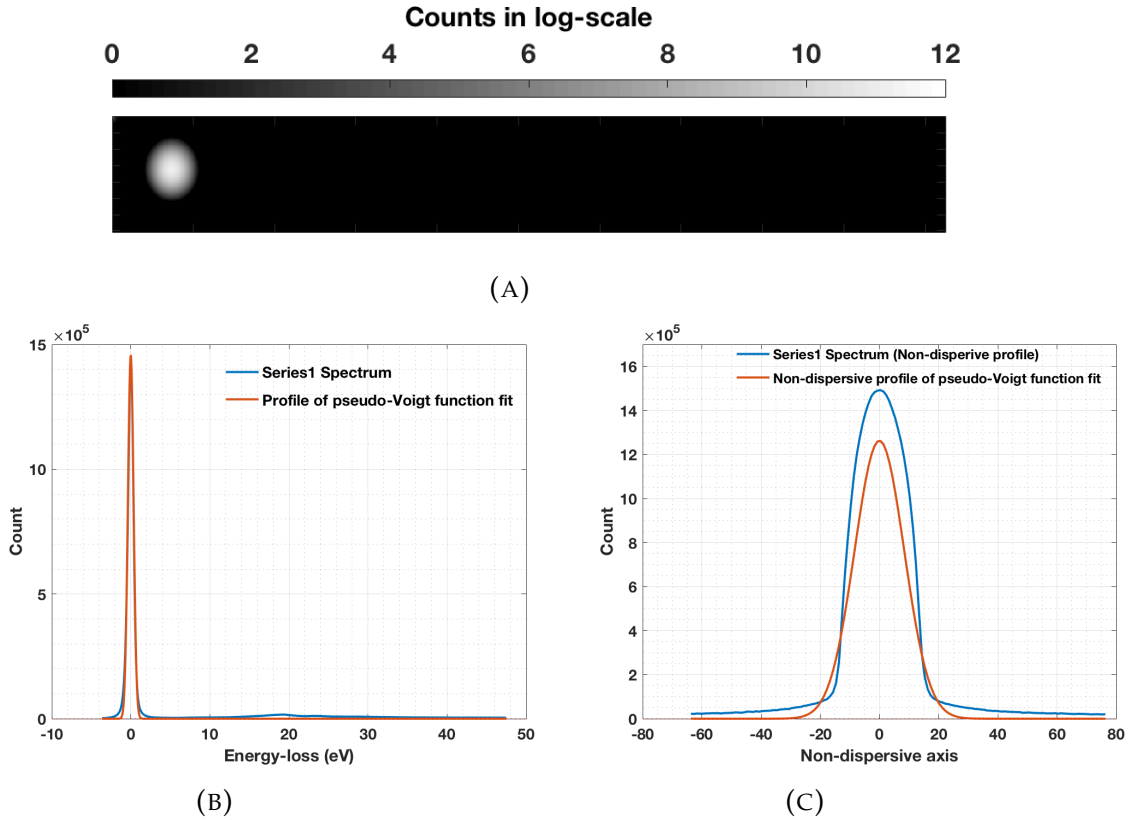


FIGURE 6.3: (A) Modelled 2D ZLP with multivariate pseudo-Voigt function ($V_p(\mathbf{x}, \mu, \Sigma, \mathbf{C})$) to experimental GaN 2D EELS Series 1 shown in fig. A.5(A). (B) Profiles of spectrum and multivariate pseudo-Voigt function model. (C) Non-dispersive axis profile of multivariate pseudo-Voigt function model to ZLP.

$$V(\mathbf{x}, \mu, \Sigma, \mathbf{C}) = p_1 \cdot \{\mathcal{N}(\mathbf{x}, \mu, \Sigma) * L(\mathbf{x}, \mathbf{C})\} \quad (6.2)$$

$$V_p(\mathbf{x}, \mu, \Sigma, \mathbf{C}) = p_1 \cdot \mathcal{N}(\mathbf{x}, \mu, \Sigma) + p_2 \cdot L(\mathbf{x}, \mathbf{C}) \quad (6.3)$$

where, $L(\mathbf{x}, \mathbf{C})$ is the multivariate Lorentz function. There is no straightforward form of a multivariate Lorentzian function. A Student t -distribution (a.k.a multivariate t -distribution) as shown in eqn. 6.4 with a special case of one degree of freedom in 2D takes the form of a multivariate Cauchy-Lorentz distribution, eqn. 6.5. i.e. $L(\mathbf{x}, \mathbf{C}) = M_t(\mathbf{x}, \mu, \mathbf{C}, \nu = 1, k = 2)$.

$$M_t(\mathbf{x}, \mu, \mathbf{C}, \nu, k) = \frac{\Gamma\left(\frac{\nu+k}{2}\right)}{\Gamma\left(\frac{\nu}{2}\right) \nu^{k/2} \pi^{k/2} |\mathbf{C}|^{1/2}} \left[1 + \frac{1}{\nu} (\mathbf{x} - \mu)^\top \mathbf{C}^{-1} (\mathbf{x} - \mu)\right]^{-\frac{\nu+k}{2}} \quad (6.4)$$

$$L(\mathbf{x}, \mathbf{C}) = \frac{1}{2\pi |\mathbf{C}|^{-1} (1 + \mathbf{x}^\top \mathbf{C}^{-1} \mathbf{x})^{\frac{3}{2}}} \quad (6.5)$$

For Cauchy distribution, mean and standard deviation are not defined. \mathbf{C} is the $k \times k$ symmetric matrix and not a covariance matrix. The diagonal elements of the \mathbf{C} contains the half-width at half maximum (HWHM) of the distribution in k dimensions. Γ is a Gamma function of integers, which is a factorial function shifted down by 1 and is given by $\Gamma(n) = (n-1)!, \forall n \in \mathbb{N}^+$ and for $\mathbb{R}[z] > 0$, it is defined as shown in eqn. 6.6.

$$\Gamma(z) = \int_0^{\infty} x^{z-1} e^{-x} dx \quad (6.6)$$

6.3.3 Deconvolution of 1D ZLP

The RL deconvolution method has been consistently used in improving the energy resolution of low-loss EELS. As discussed in subsection 4.4, RL deconvolution works perfectly if the spreading function has pure Poissonian statistics, but it cannot make the ZLP to a δ -function. The iterative method is used only to improve energy resolution at the expense of heightened noise. The major disadvantage of any iterative deconvolution method is the need for an initial estimate of the PSF, $S_{est}^{(0)}(E)$, which determines the rate of deconvolution per iterations. The rate of deconvolution is attributed to the number of iterations it takes to get an estimated PSF. If the initial estimate is far from the actual PSF, then more number of iterations are required for the desired deconvolution. All standard implementations of RL deconvolution methods in MATLAB R2017b and Hyperspy v1.3 assume that the spreading function is positive and pure Poissonian in nature. Hence if the number of iterations is increased, then any intensity counts that could become negative will be replaced by zeros. A work around could be by adding and subtracting a large positive offset before and after applying RL deconvolution. However,

this contradicts the principle of RL deconvolution. RL deconvolution is only designed to deal with Poissonian spread function (Fish et al., 1995; Laasmaa et al., 2011; Lucy, 1974; Richardson, 1972; Shepp et al., 1982). It is also worth noting in fig. 6.4(A) that the deconvoluted spectrum with 20 iterations is getting clipped very close to the bandgap onset region. Hence it is best to avoid higher iterations for RL deconvolutions. Ringing artefacts then also start to creep in and will affect the determination of bandgap. The tails of the

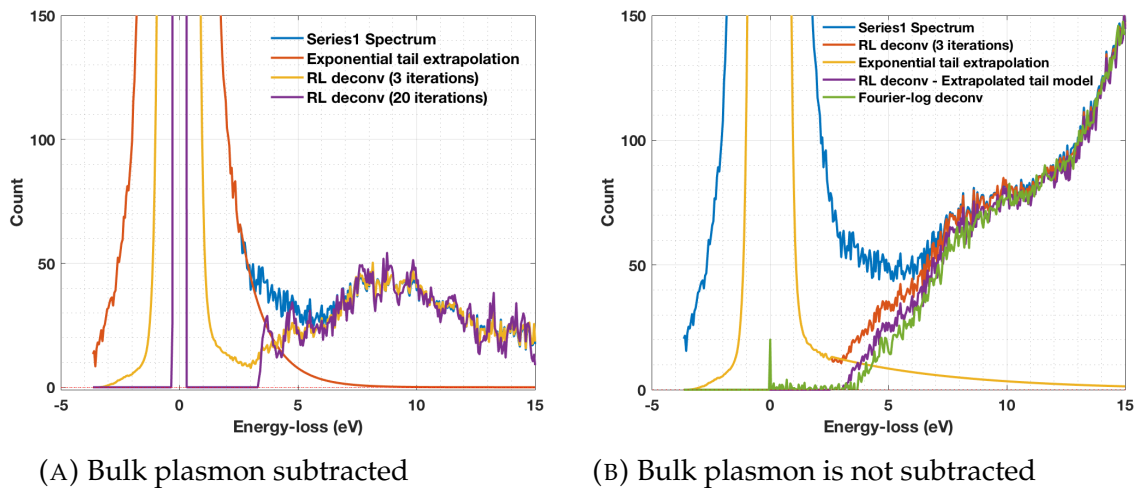


FIGURE 6.4: (A) RL deconvolution applied to bulk plasmon subtracted to GaN low-loss EELS from fig. A.5(B) at different iterations to demonstrate the effects of ringing artefacts and non-negative nature due to Poissonian statistics. (B) ZLP background removal for DOS using RL and Fourier-log deconvolution. RL deconvolution is applied for 3 iterations then an exponential function is used to extrapolate the tail and subtract with RL deconvoluted spectrum.

Lorentz function modelling the bulk plasmon do not decay towards zero as fast as a Gaussian would. Hence whenever subtracting the background for bandgap onset determination, it is important to always subtract the plasmon first before modelling the contribution of the ZLP. After RL deconvolution, the tails of ZLP are close to 0. The remaining background that is left after deconvolution can be removed by modelling the ZLP again by tail extrapolation method. An alternative deconvolution method of removing the ZLP is standard Fourier-log deconvolution. Fig. 6.4(B) compares ZLP background removal for DOS using RL and Fourier-log deconvolution methods.

6.4 Determination of Bandgap from 1D Spectra

The direct bandgap can be modelled with a square-root function. The square-root model to fit the DOS for direct bandgap can take different forms depending upon the type of pre-processing done to the low-loss EELS to model the background. The various models considered are listed in eqns. 6.7 and 6.8.

$$D(E) = a \cdot (E - E_g)^{0.5} \quad (6.7)$$

$$D(E) = a \cdot (E - E_g)^{0.5} + c \quad (6.8)$$

where a is a scaling parameter, c is the offset or a constant and E_g is the location of bandgap onset. All a , c and E_g are fitting parameters. The function $D(E) \in \mathbb{C}$, i.e. these models are only defined for $E \geq E_g$. Hence for fitting the DOS a discontinuous function, $f(E, E_g) \in \mathbb{R}$, is defined as shown in eqn. 6.9.

$$f(E, E_g) = \begin{cases} a \cdot (E - E_g)^{0.5}, & : E \geq E_g \\ 0, & : E < E_g \end{cases} \quad (6.9)$$

The eqn. 6.8 has an additional constant term, c . It is used when the EELS still has some background, the offset parameter modelling a constant background. Determination of bandgap onset for very wide-bandgap materials, such as AlN or AlGaIn, is mostly forward as the effects of Čerenkov radiation will be minimum at higher energy and the tails of the ZLP be less at higher energy-losses. The authors Amari, (2011) and Amari et al., (2011) have studied the relation between R^2 and E_g by fitting a straight line to the squared spectrum near bandgap region without removing ZLP or bulk plasmons. As the bandgap tends to narrow, their fitting of the EELS starts to become affected by dominant ZLP. Hence, a monochromator is needed to get better energy resolution. Walther et al., (2017) have observed that the DOS of the region wasn't exactly square-root function in shape as expected. The bandgap onset had a steep rise and flattened at higher energy-loss, as shown in figs. 6.5. The authors have determined the bandgap onset by using three different methods: first, by extracting the low-loss spectrum between 0.7 eV (onset of InN direct bandgap) to 4 eV (>3.4 eV, onset of GaN direct bandgap), smoothing the spectrum with spline functions and get the peak position of the first derivative (or gradient), as described in eqn. 3.3. In a second method, the background was modelled purely by an offset and the residue spectrum was modelled using eqn. 6.7 in the range 0.7 eV to 5 eV, which is equivalent

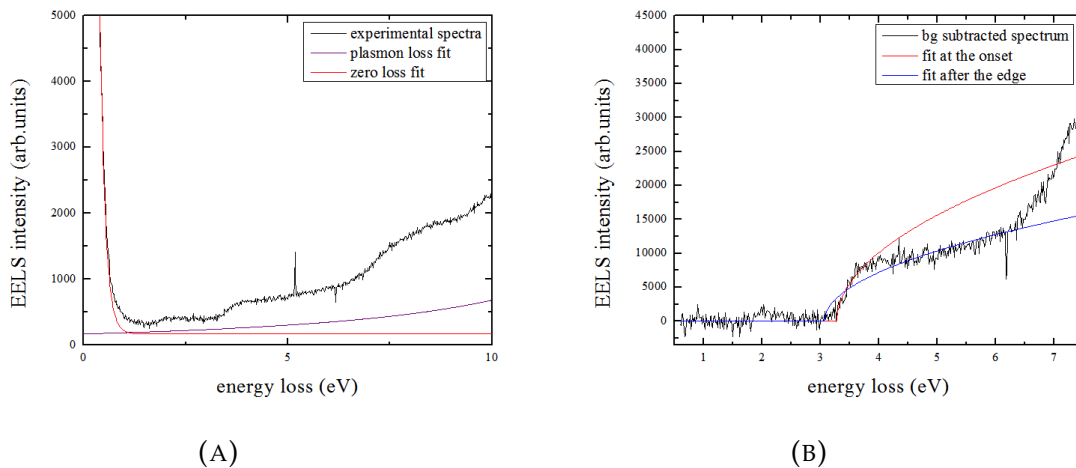


FIGURE 6.5: (A) The background is by three exponentials extrapolation and the bulk plasmon by a Lorentz function. (B) The difficulty in choosing the fit range for reliable determination of bandgap is illustrated by fitting a $300 \times \sqrt{E - E_g}$ function fit at onset and a square-root function after the edge.

to eqn. 6.8. The third method was fitting a square-root function as in eqn. 6.7 in the same range as the second method but after ZLP and plasmon had been subtracted. The ZLP was subtracted by fitting three exponential functions to the tail of ZLP before 0.7 eV. The bulk plasmons were subtracted by joint fitting as described in eqn. 5.9. The maps of bandgap determined from monochromated low-loss are presented in figs. 6.6. If the data had been acquired in the non-monochromator, the energy resolution is limited. However, with the proper methodologies listed in the following subsections, the bandgap onset can be determined reliably. The fit ranges from 0 eV to 12 eV, hence covering a range suitable for both narrow and wide bandgap materials. In the following, 5 methods of background, ZLP and bulk plasmon removal are compared.

6.4.1 Method I

1. model ZLP by exponential tail extrapolation (method);
2. subtract the modelled ZLP from the experimental low-loss EELS;
3. fit a square-root function as in eqn. 6.7 to the residual spectrum.

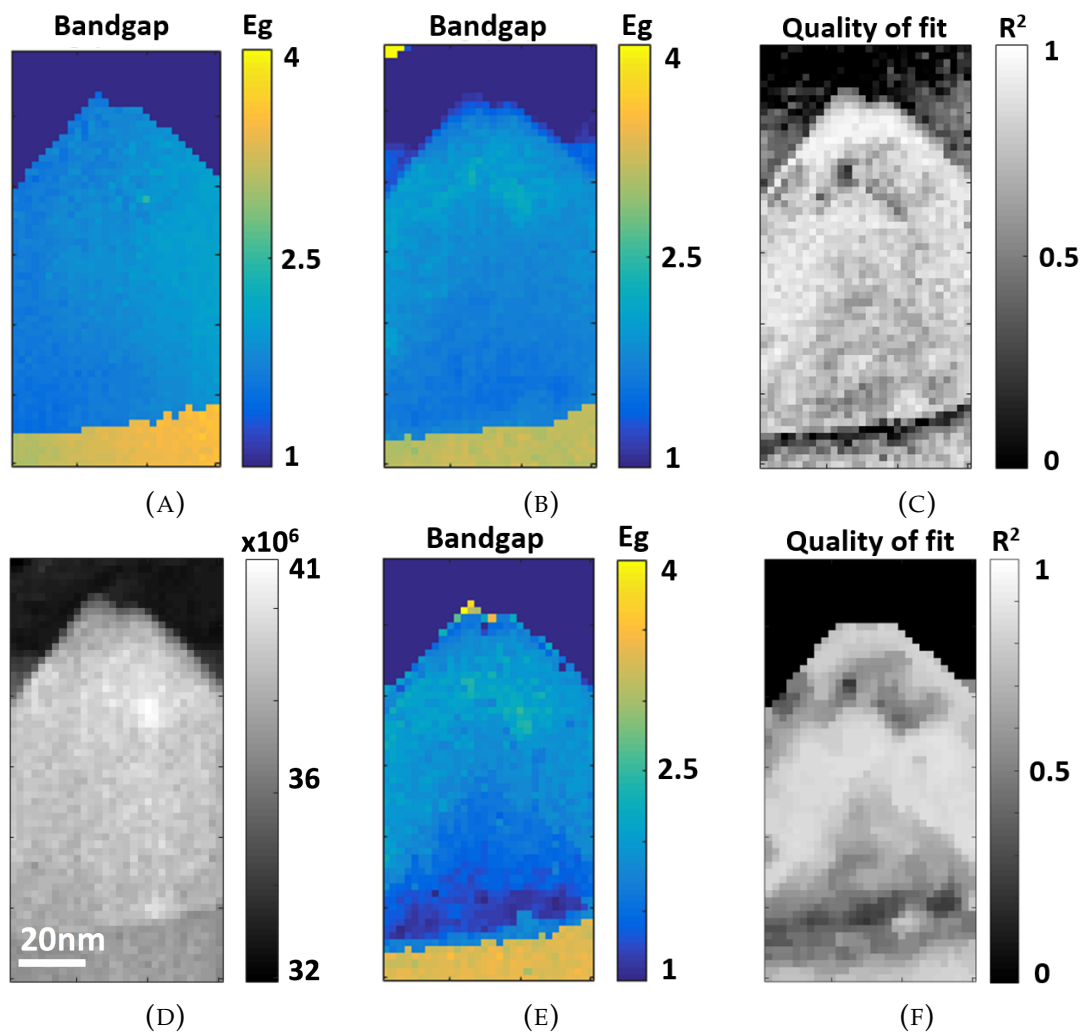


FIGURE 6.6: Bandgap maps of $\text{In}_x\text{Ga}_{1-x}\text{N}$ determined by (A) derivative method. (B) modelling background as an offset and fitting eqn. 6.7. (D) Rotated ADF image of the area investigated where the apparent slight tilt from vertical growth is due to drift during the acquisition of SI. (E) subtracting ZLP and bulk plasmons, and modelling the residual spectrum with eqn. 6.7. (C,F) are R^2 maps of eqn. 6.7 fitting (B,E) respectively.

6.4.2 Method II

1. model bulk-plasmon peak using Lorentz function and subtract it from the spectrum;
2. model ZLP by exponential tail extrapolation method and subtract it from the spectrum;
3. fit a square-root function as in eqn. 6.7 to the residual spectrum.

6.4.3 Method III

1. model ZLP by exponential tail extrapolation method;
2. consider modelled ZLP as initial estimate, apply RL deconvolution;
3. model ZLP again and subtract from the spectrum;
4. fit a square-root function as in eqn. 6.7 to the residual spectrum.

6.4.4 Method IV

1. apply Fourier-log deconvolution;
2. fit a square-root function as in eqn. 6.7 to the deconvoluted spectrum.

6.4.5 Method V

1. model bulk-plasmon peak using Lorentz function and subtract it from the spectrum;
2. apply Fourier-log deconvolution;
3. fit a square-root function as in eqn. 6.7 to the residual spectrum.

6.4.6 Discussion of 1D spectrum processing

The tail extrapolation by fitting multiple exponentials has been used as default to model the ZLP in all the proposed methods in subsections 6.4.1-6.4.5. The distribution modelling of ZLP discussed in subsection 6.3.1 leaves a residual background which will severely affect the determination of bandgaps.

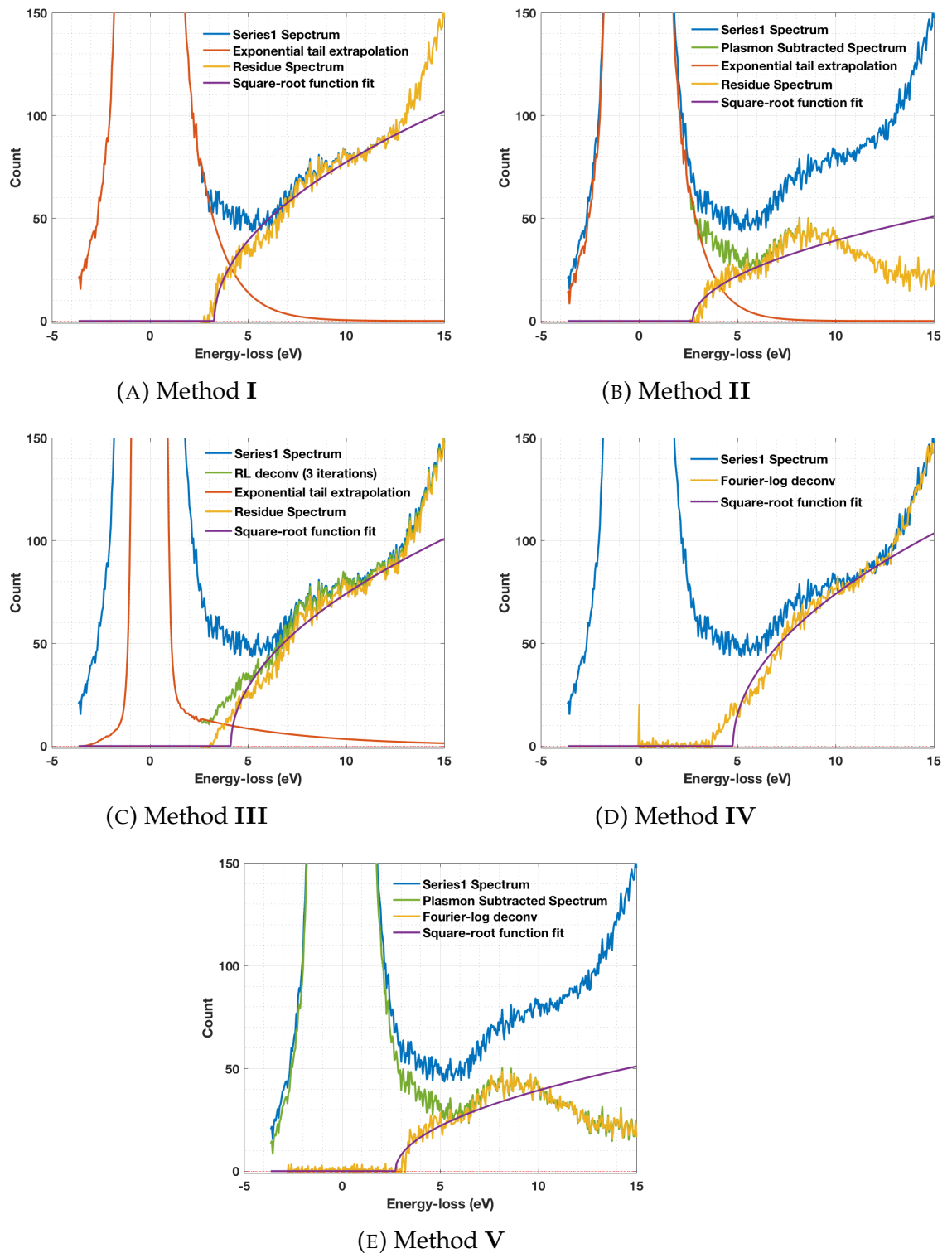


FIGURE 6.7: The square-root function fit applied to residual spectrum of GaN (A–E) Series 1. The fit range is from 0 eV to 12 eV.

TABLE 6.2: Bandgap determined by all the proposed methods for 1D GaN spectrum.

	Square-root fit		Differential Method
	E_g	R^2	
Method I	3.28	0.91	3.31
Method II	2.72	0.91	3.26
Method III	4.12	0.98	3.56
Method IV	4.78	0.98	4.21
Method V	2.71	0.89	3.26

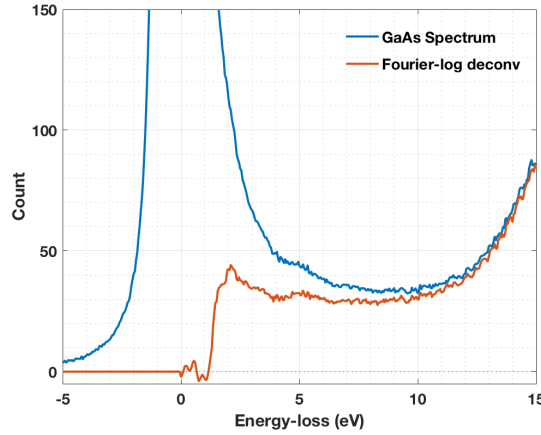
Hence, the extrapolation method is ideal as it will leave almost no background contribution from the ZLP for the DOS. Method I is a very simple model where only ZLP is subtracted. The bandgap values determined for GaN Series 1 through method I are in close proximity of the theoretical bandgap value of ~ 3.44 eV (Brockt et al., 2000; Davydov et al., 2002a,b; Davydov et al., 2002c; Mánuel et al., 2016; Schamm et al., 2003) Method I also gave an $E_g = 3.28$ eV with an $R^2 = 0.91$. Since the E_g values are the fitting parameters in square-root functions, the error margin can be related to R^2 values. However, in this situation, we cannot compare R^2 as a measure of error in the determined bandgap value. It is merely stating the quality of fit. The quality of E_g lies in the quality of background subtraction and not on the square-root fitting. This indicates that method I in this experimental spectrum describes the background well. In method II and method V, bulk plasmon has been subtracted and a square-root function modelled from 0 eV to 12 eV. The bandgap onset values obtained for this range are an underestimate of the true bandgap, as shown in table 6.2. The plasmon subtracted residual spectrum in figs. 6.7(B,E) is dipping at ~ 10 eV. The R^2 values are lower because the residual spectrum dips after ~ 10 eV and the E_g values are underestimated due to the overall fitting flattens. However, if the fit range is adjusted from 0 eV to peak position of the residue around ~ 10 eV, then better E_g and R^2 values are obtained for methods I and V, as shown in table 6.3. It is worth noting that the quality of fit is increased as R^2 values have been increased and E_g values are in proximity to the theoretical value of bandgap for GaN. It is also interesting to know that any deconvolution (RL or Fourier-log) that is applied to low-loss EELS without subtracting the plasmon (i.e. methods III or IV) is giving an overestimate of the bandgap onset. However, applying deconvolution after the bulk plasmon has been subtracted

TABLE 6.3: Bandgap determined for method II and method V for adjusted fit range of 0 eV to 10 eV for 1D GaN spectrum.

	Square-root fit		Differential Method
	E_g	R^2	
Method II	3.01	0.97	3.26
Method V	3.01	0.95	3.26

(i.e. method V with fitting range 0 eV to 10 eV) is giving an underestimate of values, $E_g = 3.01$ eV. The differential method is a very simple but reliable form of bandgap determination. This is evident even for $\text{In}_x\text{Ga}_{1-x}\text{N}$ as shown in fig. 6.6(A). The bandgap determination by square-root functions heavily relies on the quality of background subtraction. If a bandgap onset is clearly visible, then the differential method can detect it quite reliably. Although this hasn't been the case in method IV. The apparent onset of the bandgap after applying Fourier-log deconvolution has been diminished until ~ 4.5 eV. This could be due to bulk plasmon not being subtracted. In all other methods, determination of the bandgap onset by differentiation is superior to fitting square-root functions. Note that RL deconvolution is not applied to plasmon subtracted spectrum, because RL deconvolution cannot be applied to a spectrum whose intensity (in this case near bulk plasmon which has been subtracted) has negative values. Hence, only Fourier-log deconvolution is considered for plasmon subtracted spectrum. It will be difficult to determine the onset of any small bandgap with precision, using a square-root function. If the spectrum is acquired using a monochromator, this should be straightforward. Consider the case of GaAs where the direct bandgap is ~ 1.42 eV (Xiang et al., 2017), and EELS have been acquired in JEOL 2010F FEG-TEM in diffraction mode (beam energy = 197 keV, $\alpha = 10$ mrad, $\beta = 20$ mrad, dispersion = 0.05 eV/channel, exposure time = 1 s, condenser aperture = 20 mm and entrance aperture = 0.6 mm). The FWHM of ZLP, W_0 , was 0.93 eV. This means that the onset of the DOS is completely buried in ZLP. Hence, the only method that is suitable for determination of bandgap for GaAs would be Fourier-log deconvolution, as shown in fig. 6.8. However, the deconvoluted spectrum is not following a square-root function although there is an onset at ~ 1.4 eV. For direct bandgap semiconductors the square-root function seems not ideal for determining the onset, however, with differential method applied to method IV in subsection 6.4.4, the onset of DOS for GaAs

is found to be exactly at 1.40 eV^1 which is in closest proximity to theoretical value of $\sim 1.424 \text{ eV}$ (El Allali et al., 1993; Kolhatkar et al., 2014; Shan et al., 1999; Vatanparast et al., 2017).



(A)

FIGURE 6.8: Fourier-log deconvolution applied to GaAs low-loss spectrum. The onset of DOS could be seen at $\sim 1.40 \text{ eV}$.

6.5 Determination of bandgap from 2D SI

In modelling the background from 2D SI, the tail extension method cannot be used due to the presence of large noise in spectrum at different non-dispersive locations where the count in the spectrum are low. Hence the only way to model the background is by multivariate distributions as discussed in subsection 6.3.2. The first step in Methods I and II is ZLP modelling. However, a 2D ZLP modelled by pseudo-Voigt function cannot be subtracted straight away. The residual spectrum would still have a large offset remaining. Hence, deconvolution is the only way to model ZLP in 2D. RL deconvolution is applied for 3 iterations with the initial estimate of the 2D ZLP being pseudo-Voigt function model as shown in fig. 6.9(A). It is evident from the profiles of the 2D deconvoluted spectra, shown in fig. 6.9(B), that the tails of the ZLP are not precisely modelled. If the number of iterations increased to more than 3, then the deconvoluted spectrum is clipping off at zero. Hence even only 3 iterations used.

¹The dispersion for the GaAs spectrum is 0.05 eV/channel . Hence with differential method, the bandgap determination is limited by the energy dispersion. This method cannot interpolate the values between pixels as was in case of square-root fit. Hence $E_g = 1.40 \text{ eV}$ is the closest one could get with differentiation method with 0.05 eV/channel energy dispersion.

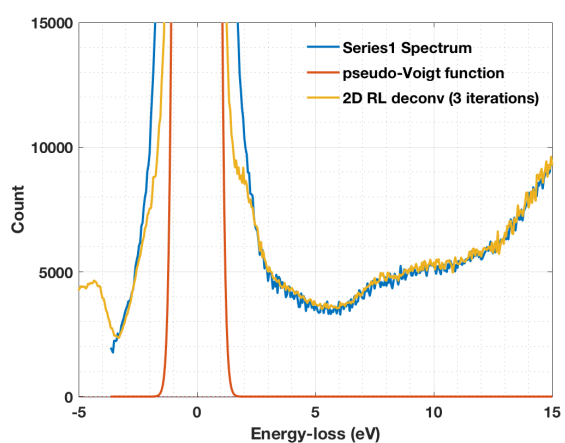
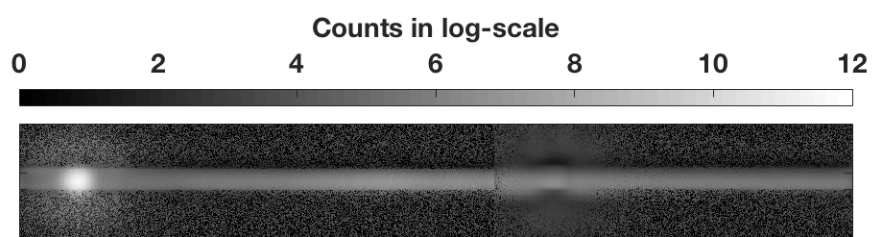


FIGURE 6.9: (A) 2D RL deconvolution applied to 2D EELS SI of GaN Series 1. (B) Profiles of GaN Series 1, pseudo-Voigt function model to ZLP and 2D deconvoluted spectrum.

6.5.1 Discussion of 2D spectrum processing

Applying 2D RL deconvolution as in fig. 6.9(B), it can be seen that the bandgap region was unaffected. However, the ZLP was sharpened from 0.81 eV to 0.78 eV. Although this is not a significant increase in energy resolution, higher iterations are introducing artefacts by clipping the deconvoluted spectrum to zero near the DOS. Further, the profile of the 2D deconvoluted spectrum was again subjected to all the methods described in subsections 6.4.1-6.4.5. The resulting values of the bandgap were exactly the same. This was because the deconvoluted and original spectra are same at the bandgap region. Hence as per the extensive investigation, it is difficult to observe the improvements in energy resolution near the DOS as was carried out in high-loss region by Gloter et al., (2003).

6.6 Bandgap determination by cluster analysis

It is evident from figs. 6.1 that a smaller fit window for square-root function does not clearly give a unique solution for bandgap. However, there are clusters that appear to converge to certain values close to the known bandgap value of ~ 3.44 eV for GaN. The clustered E_g values may not have the highest R^2 values. A standard k -means clustering algorithms can be applied assuming there are 4 clusters. Higher number of clusters can be assumed. Assuming lower number of cluster results in centroid value calculated at lower value. Also note later in the section that there is always one cluster detected at zero. The negative E_g values determined by ill conditioned fitting were clipped at zero. Hence it is always assumed that number of clusters must 3 – 6. Clustering of E_g values is shown in figs.6.10(A,C,E) for the GaN 1D spectrum. Each data point in the plots is an E_g value determined by square-root fitting as shown in eqn. 6.7. The square-root fit in the window, w , is moved between 0 eV to 10 eV for all combinations of fit window size increased at every 0.5 eV and moved at every 0.5 eV step across the energy-loss axis. This is to comprehensively analyse the bandgap values for every possible fit window. While applying k -means clustering, only $E_g > 0$ are considered. Four k -means algorithm classifies the clusters of E_g based on Euclidean distances. A centroid for each clusters can be determined. Among the 4 centroids (due to 4 clusters), the centroid with highest R^2 value could be considered the best estimation of the bandgap. In

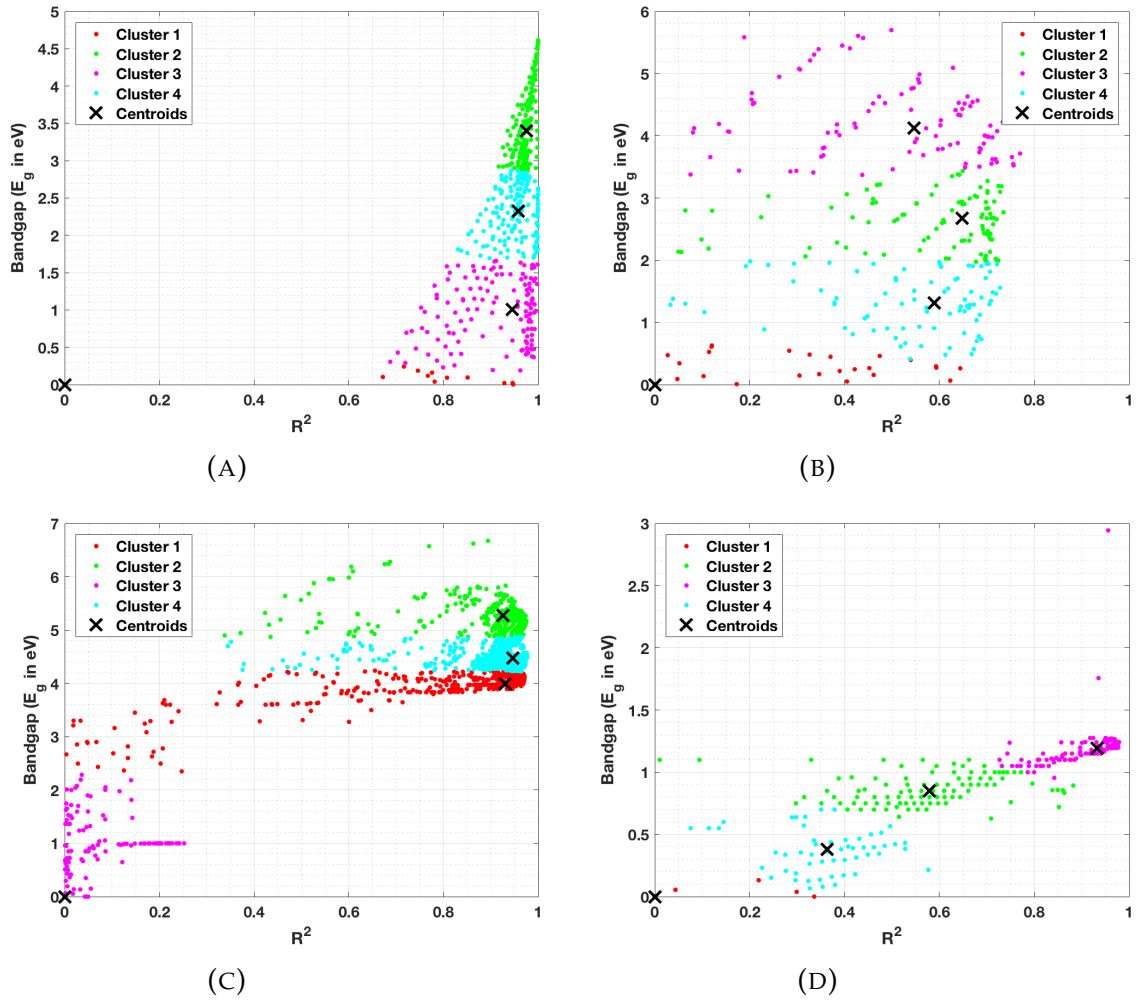


FIGURE 6.10: k -means cluster assignments and centroids for bandgap determination by square-root fits for all possible fit windows with a change in step window of 0.5 eV for GaN 1D (A) raw (B) plasmon subtracted (C) Fourier-log deconvoluted spectrum. The limits of the fit range are 0 eV to 10 eV. The similar fitting analysis is used to get the cluster for (D) Fourier-log deconvoluted GaAs spectrum.

TABLE 6.4: The co-ordinates of the centroids with highest R^2 .

EELS	Process	R^2	E_g (eV)
GaN Series 1	raw spectrum	0.98	3.40
	plasmon subtracted	0.65	2.68
	Fourier-log deconvolution	0.95	4.48
GaAs	Fourier-log deconvolution	0.93	1.20

figs. 6.10(A), the spectrum was not processed, i.e. only a profile of 2D spectrum was taken and no ZLP or plasmon subtracted or deconvolved. It can be seen that in such cases, E_g values calculated for smaller fit windows are forming clusters close to bandgap. The centroid with highest R^2 gives an estimate of the GaN bandgap of 3.40 eV with $R^2 = 0.98$ (median = 3.35 eV, mean = 3.38 eV and std = 0.33 eV). For plasmon subtracted GaN Series 1 1D spectrum, there are no dense clusters are formed (fig. 6.10(B)), though k -means has identified four clusters based on Euclidean distances. Clearly, the estimated bandgap, $E_g \approx 2.68$ eV (median = 2.68 eV, mean = 2.64 eV and std = 0.40 eV), is not close to the expected value. This could be due to the presence of Čerenkov effects which makes it difficult to determine bandgaps for smaller fit windows. For Fourier-log deconvoluted spectra of GaN Series 1 (fig. 6.10(C)), the estimated bandgaps are a strong overestimate as was the case in method IV in subsection 6.4.4. In case of GaAs 1D spectrum, since the initial energy-resolution of the spectrum is of the order of the bandgap, the bandgap is submerged in the ZLP. Hence, determining E_g by square-root function and clustering on unprocessed and plasmon subtracted spectrum would not provide any meaningful estimate. For any low energy-resolution spectrum with narrow(er) direct bandgap, Fourier-log must be applied to remove the ZLP first. The Fourier-log deconvoluted GaAs spectra is used to estimate the bandgap using clustering process as shown in fig. 6.10(D). The value of bandgap based on the centroid with highest R^2 is $E_g \approx 1.20$ eV (median = 1.20 eV, mean = 1.19 eV and std = 0.19 eV), which underestimates the expected direct bandgap of GaAs by ~ 0.22 eV.

6.7 Summary

In chapter 6, the reliability of bandgap measurement in EELS is studied. This means to determine the onset of the DOS. Some studies based on square-root fitting claim to be able to measure the onset to a precision of < 0.1 eV (Eljarrat et al., 2012). However, the the semiconductor under observation is already known (Eljarrat et al., 2016; Granerød et al., 2018). Here, a generic solution to blindly measure the bandgap of an unknown material by EELS is proposed. The traditional square-root fitting is applied to ZLP subtracted or ZLP deconvoluted and bulk plasmon subtracted EELS of GaN. A spatially resolved EELS was also used to check if it could be used for any improvements in the measurement of bandgap. For a normal EELS (1D spectrum), the bandgap measured from a residue spectra are tabulated in table 6.2. The statistics of

the measured bandgap with square-root fitting gave 3.52 ± 0.91 eV and the approach using derivative method 3.52 ± 0.41 eV. Although the mean value of the bandgap determined is correct to $\lesssim 0.1$ eV with respect to the theoretical value of 3.44 eV, the spread of the statistics is too large (± 0.91 eV and ± 0.41 eV) to be useful in practice. There was no significant improvement in measurement of bandgap observed in deconvolution applied to 1D and 2D EELS spectra. Large outliers were produced by Fourier-log deconvolution ($E_g = 4.78$ eV, $R^2 = 0.98$ for square-root fitting and $E_g = 4.21$ eV for derivative method) applied to GaN low-loss EELS spectrum. Considering only the rest of the methods for wide-bandgap material, the bandgap was measured at $E_g = 3.37 \pm 0.70$ eV for square-root fitting and $E_g = 3.38 \pm 0.14$ eV for derivative method. Hence, for determination of the bandgap for wide-bandgap semiconductors, the derivative method applied to ZLP subtracted spectrum is more suitable as it can give precision within $\lesssim 0.14$ eV. However, for bandgap onset values that are too low and are partially submerged in the dominant ZLP (i.e. $E_g \lesssim W_0$, where W_0 is FWHM of ZLP), then Fourier-log methods provide much better statistics. An example of GaAs was used whose nominal bandgap is at 1.424 eV. The onset cannot be retrieved by any ZLP subtraction methods, hence, Fourier-log deconvolution method has been used to remove the ZLP. The deconvoluted spectrum in fig. 6.8 does not resemble a square-root function. Hence, the only available derivative method is used to determine the onset and gives a bandgap measurement of 1.40 eV. A novel approach of bandgap measurement using k -means clustering is proposed and bandgap measurement from cluster analysis was found to be showing similar statistics as determination by square-root fitting. The k -means cluster measured bandgap centroid with highest R^2 for raw spectra of GaN gave $E_g = 3.40 \pm 0.33$ eV with an $R^2 = 0.98$. Again bandgap measurement with k -means cluster analysis for wide-bandgap materials using Fourier-log methods are providing outliers. Hence for wide-bandgap materials, k -means should be applied to raw spectra without removing any background for DOS. However for GaAs, the k -means cluster analysis applied to Fourier-log deconvoluted spectra gives an apparent bandgap value of $E_g = 1.20 \pm 0.19$ eV which is an under-estimate of ~ 0.22 eV. Hence in general, if the energy resolution of the low-loss EELS spectrum (FWHM of ZLP) is $\gtrsim 1$ eV (with bandgap assumed to be hidden in ZLP), then all three proposed methods (square-root fitting, derivative and cluster analysis) applied to Fourier-log deconvoluted spectra will provide relatively reliable results. But the precision with which EELS can measure bandgaps is not good

enough for applications in electronics where optical spectroscopy methods can provide more reliable results and precision to typically ± 0.02 eV. In low-loss EELS, if a direct bandgap can be measured with more precision then the doping levels can be measured as shifts in the onset of the bandgap.

Chapter 7

Conclusion

Automated and unbiased EELS quantification has been carried out for high and low energy-losses. Various EELS example spectra such as from a GaAs based multilayer solar cell on a Ge substrate, $\text{In}_x\text{Ga}_{1-x}\text{N}$ ternary alloy deposited on top of GaN substrate and AlN doped with Tb have been considered. The tested methodologies include non monochromated as well as monochromated spectra.

In chapter 3, two novel automated ionization core-loss edge detection algorithms have been proposed. The detected core-losses are then used for automated pre-edge and post-edge regions for modelling background and integrating residue intensity respectively.

In chapter 4, an alternative modelling of background in post-edge region is explored for quantification of overlapping edges such as GaAs. An improvement in Ga/As quantification ratio from 1.41 to 1.28 is observed (ideally ~ 1) w.r.t to traditional pre-edge region background fitting with an inverse power-law. RL deconvolution has been proposed to core-loss edges to retrieve single scattering distribution when the low-loss is spectra is not present. An NLLS fitting with baseline correction model is proposed to quantify core-losses. The quantification of simultaneous fitting for Cu $L_{2,3}$, Ga $L_{2,3}$ and As $L_{2,3}$ show significant improvement within ± 3 at.% and the values are close to the expected values (0:50:50) are achieved (−0.5:47.6:52.8) when compared to standard packages such as Hyperspy (8.8:49.5:41.7) and DigitalMicrograph™ (3.4:57.3:36.6).

In chapter 5, quantification of $\text{In}_x\text{Ga}_{1-x}\text{N}$ is studied in low-loss region by jointly fitting of bulk plasmons and low-energetic core-losses. The In content quantified from both bulk-plasmons and low-energetic core-losses agree within ± 0.2 error. A novel method of measuring relative thickness, t/λ , is proposed by fitting the low-loss with Gaussian and Lorentzian (or Voigt) functions weighed according to Poissonian statistics. The proposed measurements agree with the traditional log-ratio method with ± 0.01 .

In chapter 6, a novel direct bandgap measurement method is proposed by k -means clustering for GaN ($E_g \approx 3.44$ eV) and the measurement has a spread of 3.40 ± 0.33 eV when compared to similar measurements by derivative method (3.52 ± 0.41 eV) and square-root fitting (3.52 ± 0.91 eV).

7.1 Future work

A fresh signal processing and machine learning perspective of EELS is explored. An automated, unbiased and improved EELS quantification methodologies of EELS at different energy-losses is studied.

The automated ionization edge detection by counting positive slope-angles uses look-up table to detect ionization edge onset. The look-up table needs to be more comprehensive and should include all semiconductors and their ionization edges. The edge detection by peak detection could be improved so that its sensitivity to gain correction anomalies and EXELFS can be minimized.

The background modelling at post-edge region could be extended to multiple overlapping ionization edges to study the statistics of the quantification. The NLLS fittings can be extended to fit for energy shifts of onset of the core-loss ionization edges.

Low-loss modelling of bulk plasmon and low-energetic core-losses can be extended to study phase separation in other alloys. Fowler-Nordheim and Maxwell-Boltzmann distributions can be modelled along with surface plasmon and phonons as a pre-processing step before measuring direct bandgaps. More advanced clustering techniques such as DBSCAN algorithms which are density based clustering can be explored to measure the bandgaps.

Appendix A

EELS experiments

EELS SI data have been acquired from a germanium (Ge) based multiple junction solar cell test sample (Angadi et al., 2016), indium gallium nitride ($\text{In}_x\text{Ga}_{1-x}\text{N}$) thin films with islands (Walther et al., 2017; Wang et al., 2015, 2016), terbium (Tb) doped aluminium nitride (AlN) films (Angadi et al., 2016; Benz et al., 2013b) and spatially resolved EELS from gallium nitride (GaN). The details of the preparation of these materials and experimentations have been described in Angadi et al., (2016, 2017) and Walther et al., (2017), respectively. The summary of all the experimentation carried out by Dr. Thomas Walther and Dr. Toshihiro Aoki (for $\text{In}_x\text{Ga}_{1-x}\text{N}$) are stated in following sections with overview ADF images, relative thickness maps and the regions of interest in each material.

A.1 Multi-layer solar cell

Four EELS SIs using different energy offsets and dispersions were acquired from the same area of a cross-sectioned semiconductor heterostructure designed to be used for multi-junction solar cells. On top of a Ge substrate (not shown due to limited field of view) several GaAs based layers of different thicknesses had been deposited. The SIs have been acquired in a JEOL 2010F field emission transmission electron microscope operated in STEM mode at 197 kV and equipped with a Gatan Imaging Filter (GIF200) with parameters as shown in table A.1. Fig. A.1(A) is an ADF overview image of the heterostructure obtained with 55–170 mrad collection semi-angle (β) in which the SI and spatial drift regions used are indicated. The SI shows eight distinctive regions as labelled in fig. A.1(B). The thicker layers labelled by numbers 3, 5 and 8 clearly differ in their scattering power due to their different chemistry, which are of interest and are investigated further in the chapters.

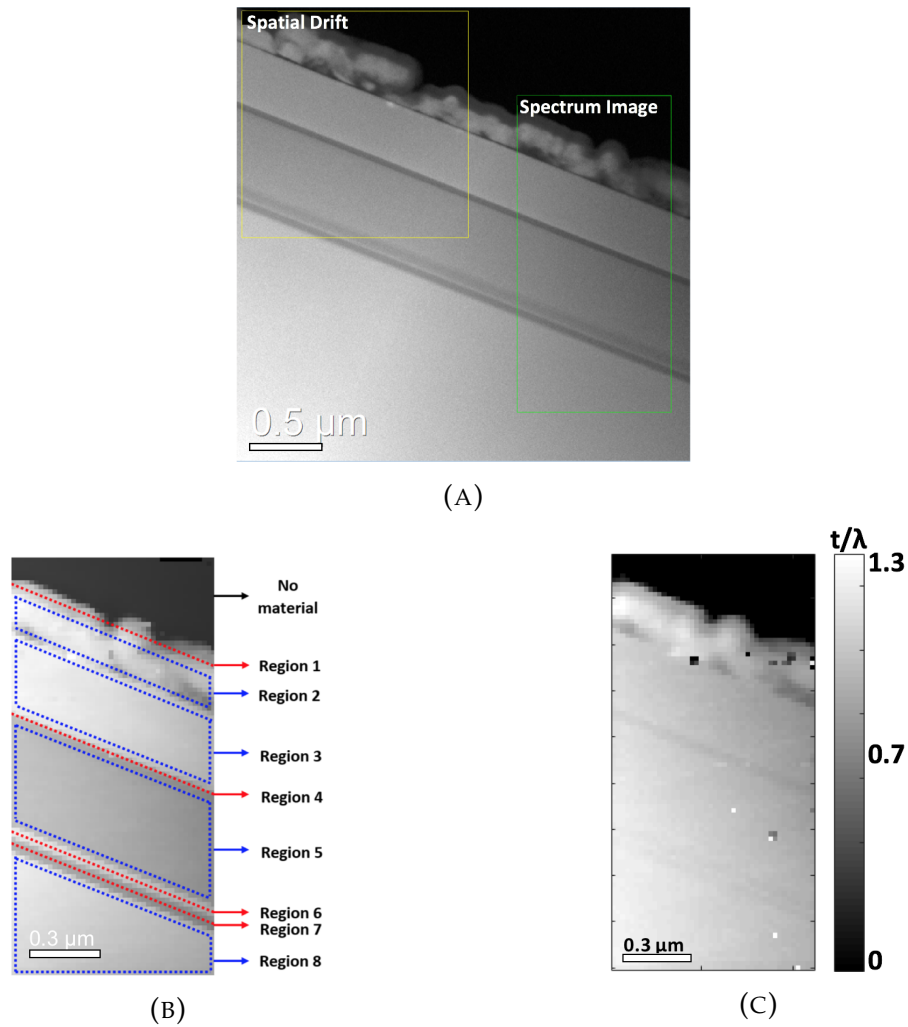


FIGURE A.1: (A) An ADF image showing an overview of the layer structure analysed and indicating the rectangular regions selected for spatial drift (yellow) and SI acquisition (green). (B) Definition of regions in the EELS SI. Regions indicated by blue dotted lines are thicker regions, while red lines denote interfaces. A sum spectrum is extracted from each region for further quantification in table 3.2. (C) Relative thickness map (t/λ).

TABLE A.1: EELS data acquisition parameters for the four SIs acquired from the same area, indicated by the green rectangle in fig. A.1(A).

Attributes	EELS SI_0	EELS SI_1	EELS SI_2	EELS SI_3
Spatial image size (pixels)	90 × 44	45 × 22	90 × 44	92 × 43
Real-space pixel size (nm)	24.4	48.8	24.4	23.9
Spectrum channels	1024	1024	1024	1024
Dispersion (eV/channel)	0.2	0.1	0.5	1
Height of FoV (μm)	2.2	2.2	2.2	2.2
Width of FoV (μm)	1.1	1.1	1.1	1.1
Conv. semi-angle (α)(mrad)	16.6	16.6	16.6	16.6
Coll. semi-angle (β)(mrad)	15	15	15	15
Spectrum offset (eV)	0	80	250	950
Exposure time (s)	1×10^{-1}	5×10^{-1}	5×10^{-1}	2
Acceleration voltage (kV)	197	197	197	197
Total acquisition time (min)	~ 9	~ 11	~ 44	~ 176

Note: Actual acquisition commenced in reverse order, starting with the highest energy losses. The SI sizes give pixel numbers along *rows* × *columns* directions and channel number along the energy-loss coordinate. FoV is abbreviation for field of view.

A.2 InGaN thin films

The EELS experiments for $\text{In}_x\text{Ga}_{1-x}\text{N}$ were carried out using a Nion UltraSTEM 100 (Nion Co., Kirkland, Washington) with Gatan Enfium ER energy-loss spectrometer, aberration corrector and HERMESTM monochromator (Krivanek et al., 2009, 2013, 2014, 2015) installed within the LeRoy Eyring Center for Solid State Science at Arizona State University, Tempe, AZ, USA. The microscope was operated with 30 mrad convergence semi-angle (α) at 100 kV (not monochromated for high core-losses, with 0.5 eV/channel dispersion) or 60 kV (monochromated for low-losses, with 0.015 eV/channel dispersion). The collection semi-angle (β) was >90 mrad for high-angle ADF imaging, 30 mrad with 2 mm entrance aperture for EELS (used at 60 kV), and 45 mrad with 3 mm entrance aperture for EELS (used at 100 kV). The energy resolution was better than 0.35 eV without and ~0.15 eV with monochromator (FWHM values, including the PSF of the detector). A ~ 0.12 nm probe size with ~300 pA beam current (20–30 pA after monochromation) was set up and spectra were acquired with the CCD detector in single read-out vertical integration mode and binning for fast acquisition to avoid electron beam-induced damage of the sample. The apparent waviness of the lattice planes at high resolution is due to slight thermal drift during the acquisition.

TABLE A.2: EELS data acquisition parameters for the two SIs acquired from InGaN, indicated by fig. A.2(A) and fig. A.3(A).

Attributes	High loss SI	Low-loss SI
Spatial image size (pixels)	128 × 128	60 × 30
Real-space pixel size (Å)	0.547	20
Spectrum channels	1024	2048
Dispersion (eV/channel)	1	0.015
Height of FoV (nm)	7	120
Width of FoV (nm)	7	60
Conv. semi-angle (α)(mrad)	30	30
Coll. semi-angle (β)(mrad)	45	45
Spectrum offset (eV)	280	0
Exposure time (ms)	50	500
Acceleration voltage (kV)	100	60
Total acquisition time	~ 13 min 40 s	~ 15 min

Note: The SI sizes give pixel numbers along x and y directions and channel number along the energy-loss coordinate.

Drift correction was not used as this would have necessitated additional reference image collection and thus would have slowed down acquisition and increased the total dose. All images and maps shown were acquired and rotated through almost 90° so that the growth direction points upwards, and the fine vertical stripes visible in parts of fig. A.2(A) are due to emission fluctuations typical of the cold field emitter. Fig. A.2(B) is a relative thickness map of the area calculated from the intensity log-ratio of the ZLP to the total intensity, and when we use a value of $\lambda = 55 \pm 9$ nm for the inelastic mean free path extrapolated from tabulated semiconductor values recorded at 100 kV for different acquisition angles (table 5.2 on page 296 of Egerton, 2011b) the value of $t/\lambda = 0.69 \pm 0.03$ measured for this sample region would indicate the specimen area investigated here is slightly less than 40 nm thin. The above inelastic mean free path is smaller than typical values for most semiconductors at 100 kV or 200 kV because of the large entrance aperture used (45 mrad reduces λ to $3/4^{\text{th}}$ of the value for 10 mrad listed in Egerton, 2011b), and the heavy In atoms in $\text{In}_{0.6}\text{Ga}_{0.4}\text{N}$ reduce it even further.

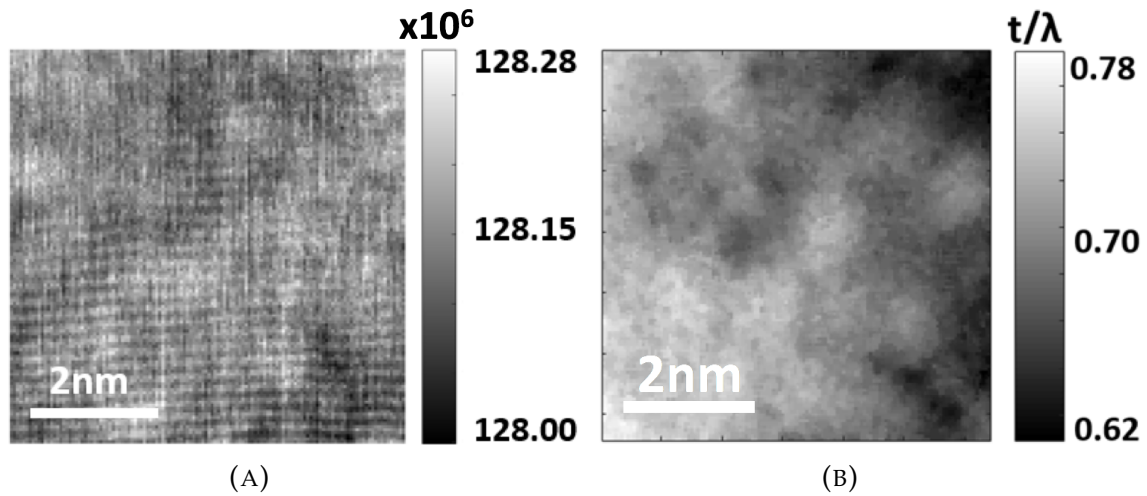


FIGURE A.2: (A) Rotated HAADF-STEM image of cross-sectioned $\text{In}_{0.62}\text{Ga}_{0.38}\text{N}$ film at high magnification, about 10 nm above the GaN substrate, showing (0002) lattice fringes. Growth direction points upwards. (B) Relative thickness map (t/λ) in multiples of the inelastic mean free path, λ .

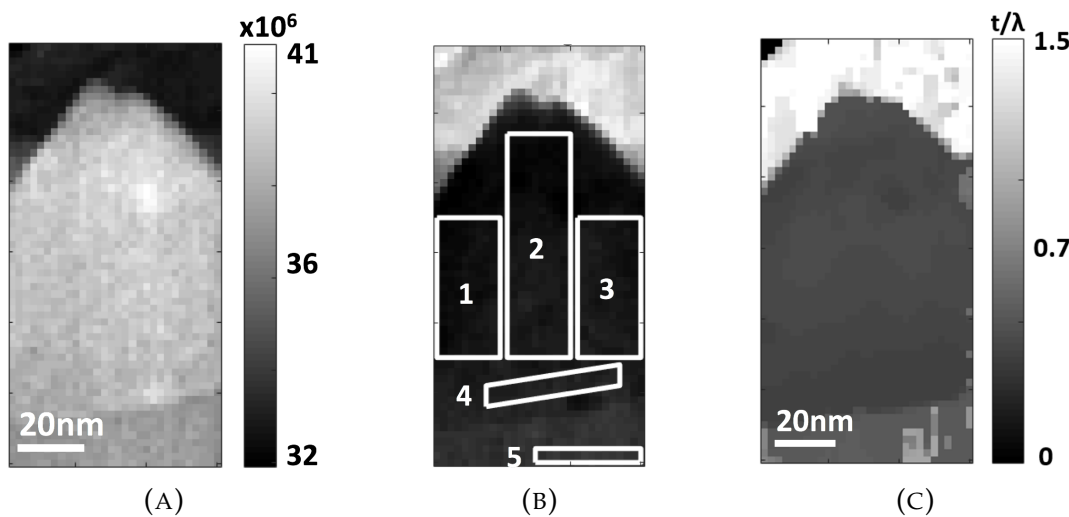


FIGURE A.3: (A) Rotated ADF image of the area investigated where the apparent slight tilt from vertical growth is due to drift during the acquisition of SI. (B) Definition of regions 1–4 in the InGaN and region 5 in the GaN buffer used later in analysis. (C) Relative thickness map for spectrum imaging at 60 kV, with mean values of $t/\lambda = 1.52 \pm 0.14$ in the top carbon region, 0.43 ± 0.02 in the InGaN layer (which is, hence, almost uniformly thin) and 0.59 ± 0.13 in the GaN buffer.

A.3 AlN thin film doped with Tb

Further STEM experiments were carried out using the Nion UltraSTEM 100. The microscope was operated at 60 kV with 30 mrad beam convergence semi-angle (α). No energy-selecting slit in the dispersive plane of the monochromator was used, providing 0.12 nm probe size (nominal spot size of 20i), with ~ 300 pA beam current at an energy resolution better than 0.35 eV, as given by the characteristics of the cold field emitter electron gun (cold-FEG). The collection semi-angle (β) was >90 mrad for high-angle annular dark field (HAADF) imaging and <45 mrad with 3 mm entrance aperture for EELS. Spectra were acquired with the CCD detector in single read-out, vertical integration mode and a binning factor of 2 for fast acquisition to avoid electron beam-induced damage of the sample. This gave an effective energy dispersion of 0.7 eV/channel where the apparent width of the ZLP was limited by the detector PSF rather than the actual energy spread of the electrons. The acquisition parameters of two EELS SI are listed in table A.3. The acquired

TABLE A.3: EELS data acquisition parameters for the two SIs acquired from the same area.

Attributes	Low-loss SI	High loss SI
Spatial image size (pixels)	100×87	100×87
Real-space pixel size (\AA)	7	7
Spectrum channels	2048	512
Dispersion (eV/channel)	0.7	2.8
Height of FoV (nm)	70	70
Width of FoV (nm)	61	61
Conv. semi-angle (α)(mrad)	30	30
Coll. semi-angle (β)(mrad)	45	45
Spectrum offset (eV)	0	310
Acceleration voltage (kV)	60	60
Exposure time (s)	8×10^{-5}	1×10^{-1}
Total acquisition time	~ 700 ms	~ 14 min 30 s

SI has a field of view of 70 nm and has been rotated through $\sim 90^\circ$ so that the growth direction in all maps points upwards (AlN on top of Si). A HAADF image is shown in fig. A.4(A). The vertical lines in the HAADF image are artefacts due to emission current fluctuations of the cold-FEG. A relative thickness map is shown in fig. A.4(C).

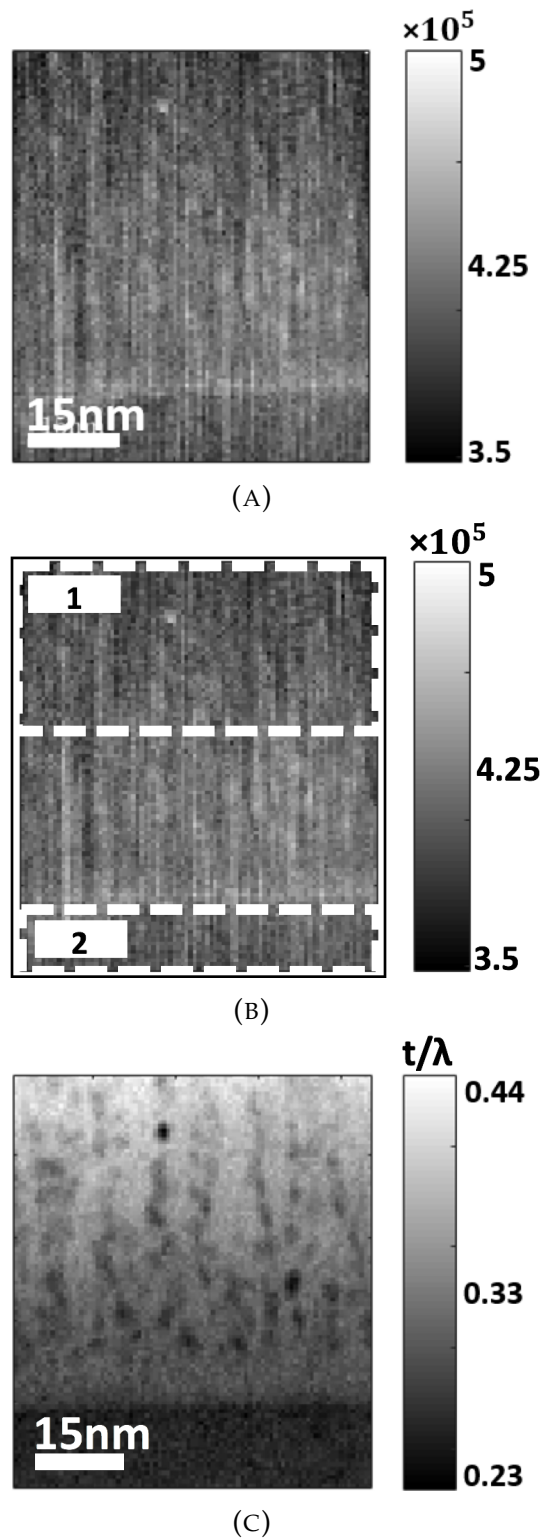


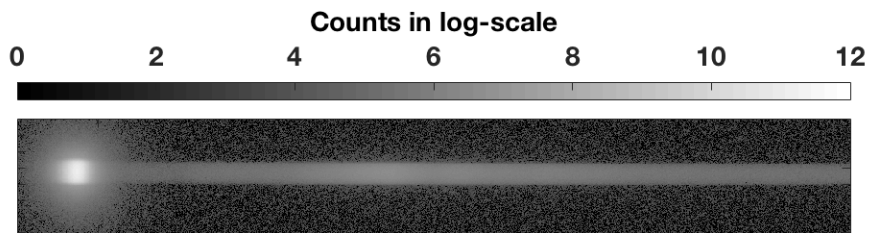
FIGURE A.4: (A) HAADF. (B) Box 1 area in AlN used for the calculation of cross-correlation between elemental maps. Box 2 includes the Si substrate. (C) Relative thickness map (t/λ).

A.4 GaN

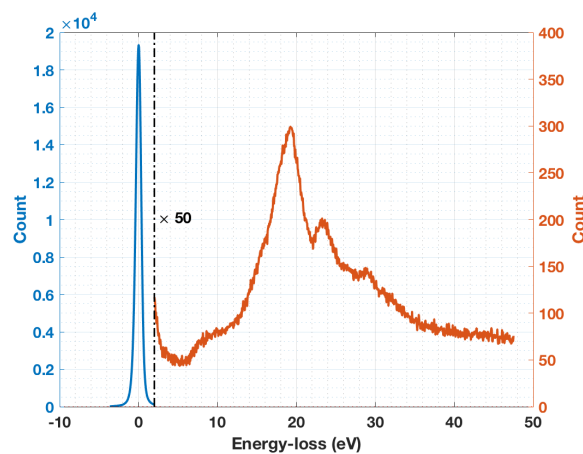
A spatially resolved EELS spectrum of GaN has been acquired in the JEOL 2010F, where the horizontal direction is the dispersive energy-loss axis (in eV) and the vertical direction is a non-dispersive axis which can be a real or reciprocal space co-ordinate depending on whether the electron microscope is operated in imaging or diffraction mode. Since the spatially resolved EELS is acquired in TEM mode, the non-dispersive direction is a real space co-ordinate. By integrating along (profile) the vertical non-dispersive direction, a standard 1D spectrum can be obtained. Hence a spatially resolved EELS spectrum as shown in fig. A.5, can be viewed as a stack of 1D spectra along the non-dispersive direction. The dispersion along the energy-loss axis was measured by offsetting the ZLP using drift-tube (40 eV). The dispersion was found to be uniform (0.0502 ± 0.0002 eV/channel) along the CCD energy-loss axis. The spatially resolved EELS has been acquired in a JEOL 2010F field emission TEM operated in TEM and image mode at 197 kV and equipped with a Gatan Imaging Filter (GIF200) with parameters as shown in table A.4. The spatially resolved EELS low-loss, called Series 1, was acquired using 0.6 mm entrance aperture, 20 mrad objective aperture. Initially, the acquired image size was 1024×1024 . However, to reduce noise while applying deconvolution (which is discussed later in chapter 6), only 141 pixels along non-dispersive axis are considered (retaining the ZLP as centre as shown in fig. A.5(A)). While integrating (or taking profile of spatially resolved EELS), only 40 rows of non-dispersive axis were considered. Hence, the 1D spectrum shown in fig. A.5(C) has higher SNR. The data has been acquired in series, i.e. spatially resolved EELS data were acquired by adding 25 images with exposure time of 1 s, acquired every 7 s interval.

TABLE A.4: EELS low-loss data acquisition parameters for the 2D SI acquired in TEM mode.

Attributes	Series 1
Spatial image size (pixels)	141 × 1024
Spectrum channels	1024
Dispersion (eV/channel)	0.0502 ± 0.0002
Entrance aperture (mm)	0.6
Condenser aperture (mm)	20
Conv. semi-angle (α)(mrad)	10
Coll. semi-angle (β)(mrad)	20
Drift tube offset (eV)	10
Exposure time (s)	1
Acquisition interval time (s)	7
Acceleration voltage (kV)	197
Total acquisition time	~3 min 20 s



(A)



(B)

FIGURE A.5: The spatially resolved EELS (Counts on log-scale) acquired with a drift tube offset of (A) 10 eV with a 0.6 mm entrance aperture. (B) is the profile of spatially resolved EELS integrated across 40 non-dispersive channels from (A).

Appendix B

User manual for the EELSAnalyser

EELSAnalyser is a set of MATLAB codes (.m files) to visualise and quantify EELS data. The codes are available to use on GitHub (url : https://github.com/vcangadi1/EELS_Matlab).

B.1 Import EELS data into EELSAnalyser

```
1 EELS = readEELSdata('/path/to/file');
```

The supported files are .dm3, .msa, .mat, .hdf5, .hspy. The .hdf5 and .hspy are data exported from **Hyperspy** (de la Peña et al., 2017a). This makes it flexible to work with Gatan's **DigitalMicrograph** and **Hyperspy**. `readEELSdata()` is combines the codes written by **Robert McLeod** (for .dm3 format).

```
1 si_struct = DM3Import('/path/to/file');
```

and **Joshua Taillon** (for .hdf5 and .hspy).

```
1 [data, ax_scales, ax_units, ax_names, ax_sizes, ax_offsets, ...
   ax_navigates] = readHyperSpyH5('/path/to/file');
```

EELS data could be SI, ADF image or a 1D spectrum. The EELS data structure from `readEELSdata()` contains following fields:

- EELS Spectrum Image (3-D Spectrum Image)
-

```

1 EELS
2 |
3 |-----Fullpathname : '/path/to/file.ext'
4 |-----E0_eV : [ ]
5 |-exposure_time_sec : [ ]
6 |-----SI_y : [ ]
7 |-----SI_x : [ ]
8 |-----SI_z : [ ]
9 |-----SImage : [ ] % 3-D Array
10 |-----dispersion : [ ]
11 |-----offset_eV : [ ]
12 |-----probe_size_nm : [ ]
13 |---conv_angle_mrad : [ ]
14 |---coll_angle_mrad : [ ]
15 |-----mag : [ ]
16 |--energy_loss_axis : [ ]
17 |-----S : [1x1 Unknown]
18 |-step_size
19 0 |
20 |   |--xunit : ' '
21 |   |--yunit : ' '
22 |   |-----x : [ ]
23 |   |-----y : [ ]
24 |   0

```

- EELS Image (2-D Image)

```

1 EELS
2 |
3 |--Fullpathname : '/path/to/file.ext'
4 |-----Image_y : [ ]
5 |-----Image_x : [ ]
6 |-----Image : [ ] % 2-D Array
7 |-scale
8 0 |
9 |   |--xunit : ' '
10 |   |--yunit : ' '
11 |   |-----x : [ ]
12 |   |-----y : [ ]
13 |   0

```

- EELS Spectrum (1-D Spectrum)

```

1 EELS
2 |
3 |-----Fullpathname : '/path/to/file.ext'
4 |-----dispersion : [ ]
5 |-----spectrum : [ ] % 1-D Array
6 |--energy_loss_axis : [ ]
7 0

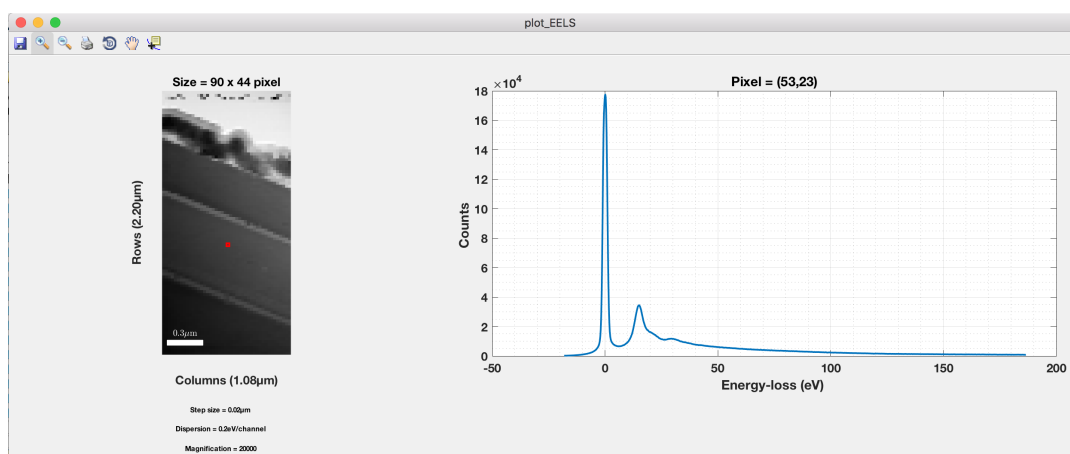
```

B.2 Visualization in *EELSAnalyser*

The visualization of EELS SI is inspired by Hyperspy. [link](#). The command in *EELSAnalyser* for plotting EELS data is:

```
1 plotEELS(EELS)
```

Simply plots the EELS data irrespective of whether the data is EELS SI, Image or a spectrum.








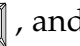



```
1 plotEELS(EELS, 'stem')
```

plots only the image of EELS SI by integrating the spectrum.

```
1 plotEELS(I, 'map')
```

Elemental map *I* can be visualised as an image. The colour maps can be changed as per the standard MATLAB documentation for e.g. `colormap jet` or `colormap gray`. The limits of colormaps can be changed using command `colormapeditor` in the command window of MATLAB.

The additional advantage of visualizing EELS SI in *EELSAnalyser* is that there are navigational advantages using arrow keys. The location of the spectrum being displayed is the red box on the image. Use following keys to navigate , , , , , , , and . Use  key to close the image object.

The spectrum axes can be put on hold to observe a particular energy-loss axis range in the spectrum.

The inputs for `stem_map_mlls_fit_modified()` are:

- `EELS` EELS structure obtained from `readEELSdata()`.
- `model_begin_eV` background model begin in eV.
- `model_end_eV` background model end in eV.
- `Diff_cross_sections` Differential cross-sections models for the respective ionization core-loss edges.
- `Fit_Type` provide options form modelling methods described in section 4.6. The inputs A to E uses models from eqns. 4.16 to 4.20.
- `Optional_EELS_low_loss` low-loss EELS structure obtained from `readEELSdata()`.

A similar MATLAB routine has been developed by Schmidt et al., (2017) called ‘Spectrum image analysis tool’ which has a MATLAB GUI to visualise EELS and cathodoluminescence (CL) SIs. But the advantage of `EELSAnalyser` is in its capability of multitasking the work on to multi-core processors. The routine `stem_map_back_sub.m` uses MATLAB parallel computing toolbox to distribute the code among multi-core processor. It also matrixises the all the spectra in the rows. The task scheduling (Martin, 2016) of quantification of Ga elemental maps from multi-junction solar cell EELS SI on to two physical core of the CPU with respect to time is shown in fig. B.1. Each chunk of the bar shows row number along with the total number of

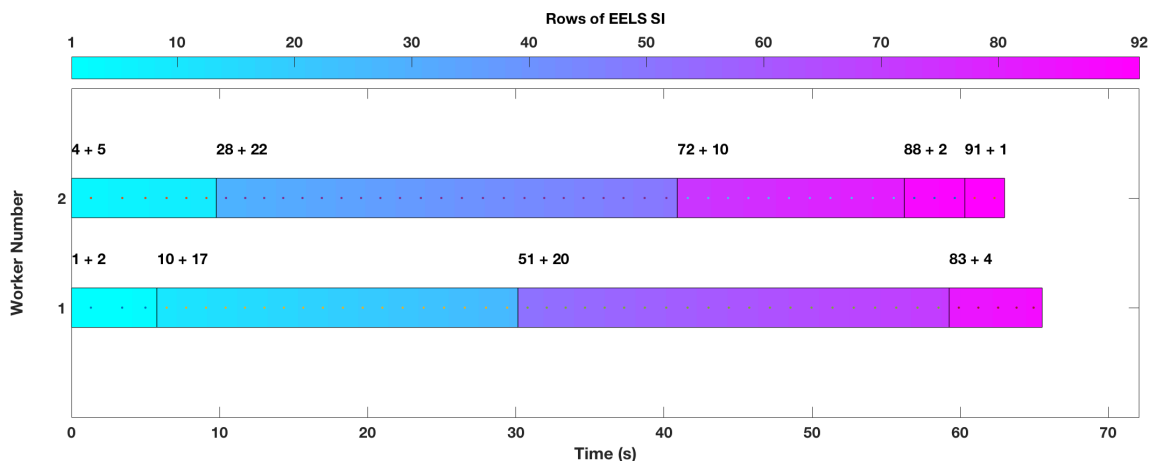


FIGURE B.1: Visual time report of distributed tasks using two workers on MacBook Pro.

rows assigned to a particular worker for quantification ($r + \Delta r$, where r is

the row number and Δr is the number of rows). In fig. B.1 at time zero, the scheduler assigns first 3 rows from row numbers #1 till #3 to worker **A** and next 5 rows from #4 till #9 to worker **B**. The worker **A** finishes its task ahead of worker **B** and gets the next 17 bulk of rows to quantify from row number #10 till #27. Meanwhile worker **B** gets task from row number #28 till #50. This can be extended to high performance computing for larger data sets of EELS SI.

Bibliography

- Ahmad, M. and Sundararajan, D. (1987). 'A Fast Algorithm for Two-Dimensional Median Filtering'. *IEEE Trans. Circ. Sys.* **34**:11, pp. 1364–1374. DOI: [10.1109/TCS.1987.1086059](https://doi.org/10.1109/TCS.1987.1086059).
- Ahn, C. C. (2005). 'Transmission Electron Energy-loss Spectrometry in Materials Science and the EELS Atlas'. Wiley, Weinheim, pp. 97–126.
- Ahn, C. C. et al. (1983). *EELS Atlas: A Reference Guide of Electron Energy-loss Spectra Covering All Elements*. Center for Solid State Science, Arizona State University, USA.
- Aitasalo, T. et al. (2003). 'Persistent Luminescence Phenomena in Materials Doped with Rare Earth Ions'. *J. Sol. St. Chem.* **171**:1-2, pp. 114–122. DOI: [10.1016/S0022-4596\(02\)00194-9](https://doi.org/10.1016/S0022-4596(02)00194-9).
- Amari, H. (2011). 'Characterization of AlGaN and InGaN Thin Films and Quantum Wells by Analytical Transmission Electron Microscopy'. PhD thesis. University of Sheffield, UK.
- Amari, H. et al. (2011). 'Nanoscale EELS Analysis of Elemental Distribution and Bandgap Properties in AlGaN Epitaxial Layers'. *J. Phys. Conf. Ser.* **326**:1. DOI: [10.1088/1742-6596/326/1/012039](https://doi.org/10.1088/1742-6596/326/1/012039).
- Amari, H. et al. (2012). 'Measurement of the Al Content in AlGaN Epitaxial Layers by Combined Energy-dispersive X-ray and Electron Energy-loss Spectroscopy in a Transmission Electron Microscope'. *Phys. St. Sol. (C)* **9**:3–4, pp. 1079–1082. DOI: [10.1002/pssc.201100165](https://doi.org/10.1002/pssc.201100165).
- Angadi, V. C., Abhayaratne, C. and Walther, T. (2016). 'Automated Background Subtraction Technique for Electron Energy-loss Spectroscopy and Application to Semiconductor Heterostructures'. *J. Microsc.* **262**:2, pp. 157–166. DOI: [10.1111/jmi.12397](https://doi.org/10.1111/jmi.12397).
- Angadi, V. C. et al. (2017). 'Evidence of Terbium and Oxygen Co-segregation in Annealed AlN:Tb'. *Appl. Phys. Lett.* **110**:22, p. 222102. DOI: [10.1063/1.4984237](https://doi.org/10.1063/1.4984237).
- Arenal, R. et al. (2008). 'Extending the Analysis of EELS Spectrum Imaging Data, from Elemental to Bond Mapping in Complex Nanostructures'. *Ultramicroscopy* **109**:1, pp. 32–38. DOI: [10.1016/j.ultramicro.2008.07.005](https://doi.org/10.1016/j.ultramicro.2008.07.005).
- Arslan, I. and Browning, N. D. (2006). 'Atomic Scale Defect Analysis in the Scanning Transmission Electron Microscope'. *Microsc. Res. Tech.* **69**:5, pp. 330–342. DOI: [10.1002/jemt.20289](https://doi.org/10.1002/jemt.20289).
- Ataman, E., Aatre, V. and Wong, K. (1980). 'A Fast Method for Real-time Median Filtering'. *IEEE Trans. Acous. Speech Sig. Process.* **28**:4, pp. 415–421. DOI: [10.1109/TASSP.1980.1163426](https://doi.org/10.1109/TASSP.1980.1163426).

- Baden, A. D. et al. (1981). 'Observation of Surface Optical Phonons on SrTiO₃(100)'. *J. Phys. C. Sol. St. Phys.* 14:34. DOI: [10.1088/0022-3719/14/34/003](https://doi.org/10.1088/0022-3719/14/34/003).
- Baier, V. N. and Katkov, V. M. (1999). 'Multiphoton Effects in Energy-loss Spectra'. *Phys. Rev. D* 59:5, p. 056003. DOI: [10.1103/PhysRevD.59.056003](https://doi.org/10.1103/PhysRevD.59.056003).
- Bangert, U., Harvey, A. J. and Keyse, R. (1997a). 'Assessment of Electron Energy-loss Spectroscopy below 5 eV in Semiconductor Materials in a VG STEM'. *Ultramicroscopy* 68:3, pp. 173–180. DOI: [10.1016/S0304-3991\(97\)00025-9](https://doi.org/10.1016/S0304-3991(97)00025-9).
- Bangert, U. et al. (1997b). 'Highly Spatially Resolved Electron Energy-loss Spectroscopy in the Bandgap Regime of GaN'. *J. Microsc.* 188:3, pp. 237–242. DOI: [10.1046/j.1365-2818.1997.2640821.x](https://doi.org/10.1046/j.1365-2818.1997.2640821.x).
- Batson, P. E. (1991). 'Current Trends for EELS Studies in Physics'. *Microsc. Microanal. Microstr.* 2:2-3, pp. 395–402. DOI: [10.1051/mm:0199100202-3039500](https://doi.org/10.1051/mm:0199100202-3039500).
- Batson, P. E. et al. (1987). 'Local Bonding and Electronic Structure Obtained from Electron Energy-loss Scattering'. *Ultramicroscopy* 22:1-4, pp. 89–101. DOI: [10.1016/0304-3991\(87\)90053-2](https://doi.org/10.1016/0304-3991(87)90053-2).
- Benz, F., Walther, T. and Strunk, H. P. (2013a). 'Towards the Structure of Rare Earth Luminescence Centres – Terbium Doped Aluminium Nitride as an Example System'. *J. Phys. Conf. Ser.* 471:2016, p. 012032. DOI: [10.1088/1742-6596/471/1/012032](https://doi.org/10.1088/1742-6596/471/1/012032).
- Benz, F. et al. (2013b). 'Tuning the Emission Colour by Manipulating Terbium-Terbium Interactions: Terbium Doped Aluminium Nitride as an Example System'. *J. Appl. Phys.* 114:7, p. 073518. DOI: [10.1063/1.4818815](https://doi.org/10.1063/1.4818815).
- Bertoni, G. et al. (2006). 'Quantification of Crystalline and Amorphous Content in Porous TiO₂ Samples from Electron Energy-loss Spectroscopy'. *Ultramicroscopy* 106:7, pp. 630–635. DOI: [10.1016/j.ultramic.2006.03.006](https://doi.org/10.1016/j.ultramic.2006.03.006).
- Bertoni, G. and Verbeeck, J. (2008). 'Accuracy and Precision in Model Based EELS quantification'. *Ultramicroscopy* 108:8, pp. 782–790. DOI: [10.1016/j.ultramic.2008.01.004](https://doi.org/10.1016/j.ultramic.2008.01.004).
- Bevington, P. R. and Robinson, D. K. (1969). *Data Reduction and Error Analysis for the Physical Sciences*. 3rd ed. McGrawHill, New York.
- Biggs, D. S. C. and Andrews, M. (1997). 'Acceleration of Iterative Image Restoration Algorithms'. *Appl. Optics* 36:8, pp. 1766–1775. DOI: [10.1364/AO.36.001766](https://doi.org/10.1364/AO.36.001766).
- Blumenthal, G. R. and Gould, R. J. (1970). 'Bremsstrahlung, Synchrotron Radiation, and Compton Scattering of High-Energy Electrons Traversing Dilute Gases'. *Rev. Mod. Phys.* 42: (2), pp. 237–270.
- Bosman, M. et al. (2009). 'Nanoscale Band Gap Spectroscopy on ZnO and GaN-based Compounds with a Monochromated Electron Microscope'. *Appl. Phys. Lett.* 95:10, p. 101110. DOI: [10.1063/1.3222974](https://doi.org/10.1063/1.3222974).
- Boyle, R. D. and Thomas, R. C. (1988). *Computer Vision: A First Course*. Blackwell Scientific, Oxford, p. 210.

- Brockt, G. and Lakner, H. (2000). 'Nanoscale EELS Analysis of Dielectric Function and Bandgap Properties in GaN and Related Materials'. *Micron* **31**:4, pp. 435–440. DOI: [10.1016/S0968-4328\(99\)00121-3](https://doi.org/10.1016/S0968-4328(99)00121-3).
- Browning, N. D. et al. (2006). 'Monochromators and Aberration Correctors: Taking EELS to New Levels of Energy and Spatial Resolution'. *J. Phys. Conf. Ser.* **26**:1, pp. 59–64. DOI: [10.1088/1742-6596/26/1/014](https://doi.org/10.1088/1742-6596/26/1/014).
- Browning, N. D. et al. (2011). 'Low-Loss EELS in the STEM'. *Scanning Transmission Electron Microscopy*. Springer, New York, pp. 659–688. DOI: [10.1007/978-1-4419-7200-2_16](https://doi.org/10.1007/978-1-4419-7200-2_16).
- Brydson, R. and Royal Microscopical Society (2001). *Electron Energy-loss Spectroscopy*. 48th ed. Bios in association with the Royal Microscopical Society, Oxford.
- Cardona, M. et al. (1970). 'Core Transitions and Density of Conduction States in the III–V Semiconductors'. *Phys. Rev. Lett.* **25**:10, pp. 659–661. DOI: [10.1103/PhysRevLett.25.659](https://doi.org/10.1103/PhysRevLett.25.659).
- Cheyne, M. C. and Epicier, T. (2004). 'Structural and Chemical Analysis of a Model Si—SiO₂ Interface using Spatially Resolved Electron Energy-loss Spectroscopy'. *Phil. Mag.* **84**:17, pp. 1753–1771. DOI: [10.1080/14786430310001659507](https://doi.org/10.1080/14786430310001659507). URL: <http://www.tandfonline.com/doi/abs/10.1080/14786430310001659507>.
- Colliex, C. et al. (1994). 'Electron Energy-loss Spectrometry Mapping'. *Mikrochimica Acta* **114-115**:1, pp. 71–87. DOI: [10.1007/BF01244534](https://doi.org/10.1007/BF01244534).
- Colliex, Christian et al. (2010). 'Atomic Scale STEM-EELS Mapping Across Functional Interfaces'. *J. Microsc.* **62**:12, pp. 53–57. DOI: [10.1007/s11837-010-0181-9](https://doi.org/10.1007/s11837-010-0181-9).
- Cooper, D. et al. (2011). 'Field Mapping with Nanometer Scale Resolution for the Next Generation of Electronic Devices'. *Nano Letters* **11**:11, pp. 4585–4590. DOI: [10.1021/nl201813w](https://doi.org/10.1021/nl201813w).
- Craven, A. J. et al. (2016). 'Accurate Measurement of Absolute Experimental Inelastic Mean Free Paths and EELS Differential Cross-sections'. *Ultramicroscopy* **170**: pp. 113–127. DOI: [10.1016/j.ultramicro.2016.08.012](https://doi.org/10.1016/j.ultramicro.2016.08.012).
- Cueva, P., Hovden, R. and Muller, D. A. (2011). 'Cornell Spectrum Imager: Open Source Spectrum Analysis with ImageJ'. *Microsc. Microanal.* **17**:S2, pp. 792–793. DOI: [10.1017/S1431927611004831](https://doi.org/10.1017/S1431927611004831).
- Cueva, P. et al. (2012). 'Data Processing for Atomic Resolution Electron Energy-loss Spectroscopy'. *Microsc. Microanal.* **18**:04, pp. 667–675. DOI: [10.1017/S1431927612000244](https://doi.org/10.1017/S1431927612000244).
- Davies, E. R. (2012). *Computer and Machine Vision: Theory, Algorithms, Practicalities*. 4th ed. Academic Press, Oxford.
- Davis, E. A. and Mott, N. F. (1970). 'Conduction in Non-Crystalline Systems V. Conductivity, Optical Absorption and Photoconductivity in Amorphous Semiconductors'. *Phil. Mag.* **22**:179, pp. 903–922. DOI: [10.1080/14786437008221061](https://doi.org/10.1080/14786437008221061).
- Davydov, V. Y. et al. (2002a). 'Bandgap of Hexagonal InN and InGaN Alloys'. *Phys. St. Sol. (B) Basic Res.* **234**:3, pp. 787–795. DOI: [10.1002/1521-3951\(200212\)234:3<787::AID-PSSB787>3.0.CO;2-H](https://doi.org/10.1002/1521-3951(200212)234:3<787::AID-PSSB787>3.0.CO;2-H).

- Davydov, V. Y. et al. (2002b). 'Reply to Comment on 'Bandgap of InN and In Rich $\text{In}_x\text{Ga}_{1-x}\text{N}$ Alloys ($0.36 < x < 1$)'''. *Phys. St. Sol. (B)* **233**:3, R10–R11. DOI: [10.1002/1521-3951\(200210\)233:3<R10::AID-PSSB999910>3.0.CO;2-E](https://doi.org/10.1002/1521-3951(200210)233:3<R10::AID-PSSB999910>3.0.CO;2-E).
- Davydov, V. Yu et al. (2002c). 'Bandgap of InN and In Rich $\text{In}_x\text{Ga}_{1-x}\text{N}$ Alloys ($0.36 < x < 1$)'. *Phys. St. Sol. (B) Basic Res.* **230**:2. DOI: [10.1002/1521-3951\(200204\)230:2<R4::AID-PSSB99994>3.0.CO;2-Z](https://doi.org/10.1002/1521-3951(200204)230:2<R4::AID-PSSB99994>3.0.CO;2-Z).
- de la Peña, F. (2010). 'Advanced Methods for Electron Energy-loss Spectroscopy Core-loss Analysis'. PhD thesis. Université de Paris-Sud, Paris.
- de la Peña, F. et al. (2011). 'Mapping Titanium and Tin Oxide Phases using EELS: An Application of Independent Component Analysis'. *Ultramicroscopy* **111**:2, pp. 169–176. DOI: [10.1016/j.ultramicro.2010.10.001](https://doi.org/10.1016/j.ultramicro.2010.10.001).
- de la Peña, F. et al. (2017a). 'Electron Microscopy (Big and Small) Data Analysis with the Open Source Software Package HyperSpy'. *Microsc. Microanal.* **23**:S1, pp. 214–215. DOI: [10.1017/S1431927617001751](https://doi.org/10.1017/S1431927617001751).
- de la Peña, F. et al. (2017b). *hyperspy/hyperspy: HyperSpy 1.3*. DOI: [10.5281/zenodo.583693](https://doi.org/10.5281/zenodo.583693).
- den Dekker, A. J. and Van Aert, S. (2002). 'Quantitative High-Resolution Electron Microscopy and Fisher Information'. *Proc. 15th Int. Congr. Electron Microsc., Interdisciplinary Tech. Forum Abstracts*, pp. 185–186.
- Dobigeon, N. and Brun, N. (2012). 'Spectral Mixture Analysis of EELS Spectrum Images'. *Ultramicroscopy* **120**: pp. 25–34. DOI: [10.1016/j.ultramicro.2012.05.006](https://doi.org/10.1016/j.ultramicro.2012.05.006).
- Dolgonos, A., Mason, T. O. and Poepelmeier, K. R. (2016). 'Direct Optical Bandgap Measurement in Polycrystalline Semiconductors: A Critical Look at the Tauc Method'. *J. Sol. St. Chem.* **240**: pp. 43–48. DOI: [10.1016/j.jssc.2016.05.010](https://doi.org/10.1016/j.jssc.2016.05.010).
- Door, R. and Gängler, D. (1995). 'Multiple Least-Squares Fitting for Quantitative Electron Energy-loss Spectroscopy - An Experimental Investigation using Standard Specimens'. *Ultramicroscopy* **58**:2, pp. 197–210. DOI: [10.1016/0304-3991\(94\)00198-V](https://doi.org/10.1016/0304-3991(94)00198-V).
- Doppalapudi, D. et al. (1998). 'Phase Separation and Ordering in InGaN Alloys Grown by Molecular Beam Epitaxy'. *J. Appl. Phys.* **84**:3, pp. 1389–1395. DOI: [10.1063/1.368251](https://doi.org/10.1063/1.368251).
- Dorneich, A. D. et al. (1998). 'Quantitative Analysis of Valence Electron Energy-loss Spectra of Aluminium Nitride'. *J. Microsc.* **191**:3, pp. 286–296. DOI: [10.1046/j.1365-2818.1998.00370.x](https://doi.org/10.1046/j.1365-2818.1998.00370.x).
- Eccles, J. W. L. and Bangert, U. (2008). 'Analysis of VEEL Spectra of Diamond Using a Dedicated STEM: Isolation of Čerenkov loss Contributions'. *J. Phys. Conf. Ser.* **126**: p. 012004. DOI: [10.1088/1742-6596/126/1/012004](https://doi.org/10.1088/1742-6596/126/1/012004).
- Egerton, R. F. (1978). 'Formulae for Light-element Micro Analysis by Electron Energy-loss Spectrometry'. *Ultramicroscopy* **3**: pp. 243–251. DOI: [10.1016/S0304-3991\(78\)80031-X](https://doi.org/10.1016/S0304-3991(78)80031-X).
- (1982). 'A Revised Expression for Signal/Noise Ratio in EELS'. *Ultramicroscopy* **9**:4, pp. 387–390. DOI: [10.1016/0304-3991\(82\)90101-2](https://doi.org/10.1016/0304-3991(82)90101-2).

- (1989). 'Quantitative Analysis of Electron Energy-loss Spectra'. *Ultramicroscopy* **28**:1-4, pp. 215–225. DOI: [10.1016/0304-3991\(89\)90299-4](https://doi.org/10.1016/0304-3991(89)90299-4).
- (2009). 'Electron Energy-loss Spectroscopy in the TEM'. *Rep. Progr. Phys.* **72**:1, p. 016502. DOI: [10.1088/0034-4885/72/1/016502](https://doi.org/10.1088/0034-4885/72/1/016502).
- (2011a). *Computer Programs for Electron Energy-loss Spectroscopy in the Electron Microscope*. URL: <https://sites.google.com/site/temsemeels/home/matlab-programs-from-eels-in-the-electron-microscope-3rd-edition> (visited on 10/01/2018).
- (2011b). *Electron Energy-Loss Spectroscopy in the Electron Microscope*. 3rd ed. Springer, New York. DOI: [10.1007/978-1-4419-9583-4](https://doi.org/10.1007/978-1-4419-9583-4).
- Egerton, R. F. and Kenway, D. (1979). 'An Acquisition, Storage, Display and Processing System for Electron Energy-loss Spectra'. *Ultramicroscopy* **4**:2, pp. 221–225. DOI: [10.1016/S0304-3991\(79\)90247-X](https://doi.org/10.1016/S0304-3991(79)90247-X).
- Egerton, R. F., Williams, B. G. and Sparrow, T. G. (1985). 'Fourier Deconvolution of Electron Energy-loss Spectra'. *Proc. R. Soc. Lond. Ser. A, Math. Phys. Sci.* Vol. **398**. 1815, pp. 395–404. DOI: [10.1098/rspa.1985.0041](https://doi.org/10.1098/rspa.1985.0041).
- Egerton, R. F. and Wang, Z. L. (1990). 'Plural Scattering Deconvolution of Electron Energy-loss Spectra Recorded with an Angle Limiting Aperture'. *Ultramicroscopy* **32**:2, pp. 137–147. DOI: [10.1016/0304-3991\(90\)90032-H](https://doi.org/10.1016/0304-3991(90)90032-H).
- Egerton, R. F., Yang, Y. Y. and Cheng, S. C. (1993). 'Characterization and Use of the Gatan 666 Parallel Recording Electron Energy-loss Spectrometer'. *Ultramicroscopy* **48**:3, pp. 239–250. DOI: [10.1016/0304-3991\(93\)90098-I](https://doi.org/10.1016/0304-3991(93)90098-I).
- Egerton, R. F. and Wong, K. (1995). 'Some Practical Consequences of the Lorentzian Angular Distribution of Inelastic Scattering'. *Ultramicroscopy* **59**:1-4, pp. 169–180. DOI: [10.1016/0304-3991\(95\)00026-W](https://doi.org/10.1016/0304-3991(95)00026-W).
- Egerton, R. F. et al. (2008). 'Fourier-Ratio Deconvolution and its Bayesian Equivalent'. *Micron* **39**:6, pp. 642–647. DOI: [10.1016/j.micron.2007.10.004](https://doi.org/10.1016/j.micron.2007.10.004).
- Egoavil, R. et al. (2014). 'Atomic Resolution Mapping of Phonon Excitations in STEM-EELS Experiments'. *Ultramicroscopy* **147**: pp. 1–7. DOI: [10.1016/j.ultramicro.2014.04.011](https://doi.org/10.1016/j.ultramicro.2014.04.011).
- El Allali, M. et al. (1993). 'Experimental Determination of the GaAs and Ga_{1-x}Al_xAs Bandgap Energy Dependence on Temperature and Aluminum Mole Fraction in the Direct Bandgap Region'. *Phys. Rev. B* **48**:7, pp. 4398–4404. DOI: [10.1103/PhysRevB.48.4398](https://doi.org/10.1103/PhysRevB.48.4398).
- Eljarrat, A. et al. (2012). 'Optoelectronic Properties of InAlN/GaN Distributed Bragg Reflector Heterostructure Examined by Valence Electron Energy-loss Spectroscopy'. *Microsc. Microanal.* **18**:5, pp. 1143–1154. DOI: [10.1017/S1431927612001328](https://doi.org/10.1017/S1431927612001328).
- Eljarrat, A. et al. (2016). 'Quantitative Parameters for the Examination of In-GaN QW Multilayers by Low-loss EELS'. *Phys. Chem. Chem. Phys.* **18**:33, pp. 23264–23276. DOI: [10.1039/C6CP04493J](https://doi.org/10.1039/C6CP04493J).
- Erni, R. and Browning, N. D. (2005). 'Valence Electron Energy-loss Spectroscopy in Monochromated Scanning Transmission Electron Microscopy'.

- Ultramicroscopy* 104:3-4, pp. 176–192. DOI: [10.1016/j.ultramic.2005.03.009](https://doi.org/10.1016/j.ultramic.2005.03.009).
- Fish, D. A. et al. (1995). ‘Blind Deconvolution by Means of the Richardson–Lucy Algorithm’. *J. Optical Soc. America A* 12:1, p. 58. DOI: [10.1364/JOSAA.12.000058](https://doi.org/10.1364/JOSAA.12.000058).
- Fowler, R. H. and Nordheim, L. (1928). ‘Electron Emission in Intense Electric Fields’. *Proc. R. Soc. A, Math. Phys. Eng. Sci.* Vol. 119. 781, pp. 173–181. DOI: [10.1098/rspa.1928.0091](https://doi.org/10.1098/rspa.1928.0091).
- Fuggle, J. C. and Inglesfield, J. E. (1991). *Unoccupied Electronic States*. Vol. 69. Topics in Applied Physics. Springer, Berlin, p. 362. DOI: [10.1007/3-540-54162-4](https://doi.org/10.1007/3-540-54162-4).
- Fukunaga, K. (2013). *Introduction to Statistical Pattern Recognition*. 2nd ed. Academic press, London.
- Gatan (1996). *Gatan Imaging Filter - User Manual*. URL: <http://www.gatan.com/products/tem-imaging-spectroscopy/gif-quantum-energy-filters#resources> (visited on 10/01/2018).
- (2015). *Gatan Microscopy Suite Software : GMS3*. URL: <http://www.gatan.com/products/tem-analysis/gatan-microscopy-suite-software> (visited on 10/01/2018).
- (2016). *EELSinfo - Quantify Extracted Signal*. URL: <http://www.eels.info/how/quantification/quantify-extracted-signal> (visited on 05/01/2018).
- Gloter, A. et al. (2003). ‘Improving Energy Resolution of EELS Spectra: An Alternative to the Monochromator Solution’. *Ultramicroscopy* 96:3–4, pp. 385–400. DOI: [10.1016/S0304-3991\(03\)00103-7](https://doi.org/10.1016/S0304-3991(03)00103-7).
- Graham, C. (2009). *A Cross-sectional, Simplified Diagram of a TEM*. URL: http://commons.wikimedia.org/wiki/File:Electron_Microscope.png (visited on 10/01/2018).
- Granerød, C. S., Zhan, W. and Prytz, Ø. (2018). ‘Automated Approaches for Bandgap Mapping in STEM-EELS’. *Ultramicroscopy* 184: pp. 39–45. DOI: [10.1016/j.ultramic.2017.08.006](https://doi.org/10.1016/j.ultramic.2017.08.006).
- Gu, L. et al. (2007). ‘Bandgap Measurements of Direct and Indirect Semiconductors using Monochromated Electrons’. *Phys. Rev. B* 75:19, p. 195214. DOI: [10.1103/PhysRevB.75.195214](https://doi.org/10.1103/PhysRevB.75.195214).
- Hage, F. S. et al. (2013). ‘Topologically Induced Confinement of Collective Modes in Multilayer Graphene Nanocones Measured by Momentum Resolved STEM–VEELS’. *Phys. Rev. B Conden. Matt. Mater. Phys.* 88:15, pp. 1–12. DOI: [10.1103/PhysRevB.88.155408](https://doi.org/10.1103/PhysRevB.88.155408).
- Härdle, W. K. and Simar, L. (2012). ‘Multivariate Distributions’. *Applied Multivariate Statistical Analysis*. Springer, Berlin, pp. 107–165. DOI: [10.1007/978-3-642-17229-8_4](https://doi.org/10.1007/978-3-642-17229-8_4).
- Harris, L. A. (1968). ‘Analysis of Materials by Electron Excited Auger Electrons’. *J. Appl. Phys.* 39:3, pp. 1419–1427.
- Ho, I. H. and Stringfellow, G. B. (1996). ‘Solid Phase Immiscibility in GaInN’. *Appl. Phys. Lett.* 69:18, pp. 2701–2703. DOI: [10.1063/1.117683](https://doi.org/10.1063/1.117683).

- Hofer, F. (1987). 'EELS Quantification of M Edges by using Oxidic Standards'. *Ultramicroscopy* 21:1, pp. 63–68. DOI: [10.1016/0304-3991\(87\)90007-6](https://doi.org/10.1016/0304-3991(87)90007-6).
- Hofer, F., Golob, P. and Brunegger, A. (1988a). 'EELS Quantification of the Elements Sr to W by Means of M45 Edges'. *Ultramicroscopy* 25:1, pp. 81–84. DOI: [10.1016/0304-3991\(88\)90409-3](https://doi.org/10.1016/0304-3991(88)90409-3).
- Hofer, F. and Golob, P. (1988b). 'Quantification of Electron Energy-loss Spectra with K and L Shell Ionization Cross-sections'. *Micron Microsc. Acta* 19:2, pp. 73–86. DOI: [10.1016/0739-6260\(88\)90002-0](https://doi.org/10.1016/0739-6260(88)90002-0).
- Hofer, F. and Kothleitner, G. (1993). 'Quantitative Microanalysis using Electron Energy-loss Spectrometry. I. Li and Be in oxides'. *Microsc. Microanal. Microstr.* 4:6, pp. 539–560. DOI: [10.1051/mmm:0199300406053900](https://doi.org/10.1051/mmm:0199300406053900).
- Horák, M. and Stöger-Pollach, M. (2015). 'The Čerenkov Limit of Si, GaAs and GaP in Electron Energy-loss Spectrometry'. *Ultramicroscopy* 157: pp. 73–78. DOI: [10.1016/j.ultramicro.2015.06.005](https://doi.org/10.1016/j.ultramicro.2015.06.005).
- Horita, Z., Sano, T. and Nemoto, M. (1989). 'Energy Dispersive X-ray Microanalysis in the Analytical Electron Microscope'. *ISIJ International* 29:3, pp. 179–190. DOI: [10.2355/isijinternational.29.179](https://doi.org/10.2355/isijinternational.29.179).
- Hovden, R. et al. (2013). 'The Open Source Cornell Spectrum Imager'. *Microsc. Today* 21:01, pp. 40–44. DOI: [10.1017/S1551929512000995](https://doi.org/10.1017/S1551929512000995).
- Hunt, J. A. et al. (1995). 'Electron Energy-loss Chemical Imaging of Polymer Phases'. *Ultramicroscopy* 58:1, pp. 55–64. DOI: [10.1016/0304-3991\(94\)00178-P](https://doi.org/10.1016/0304-3991(94)00178-P).
- Ilin, A. and Raiko, T. (2010). 'Practical Approaches to Principal Component Analysis in the Presence of Missing Values'. *J. Mach. Learn. Res.* 11: pp. 1957–2000.
- Ishizuka, K. (1993). 'Analysis of Electron Image Detection Efficiency of Slow Scan CCD Cameras'. *Ultramicroscopy* 52:1, pp. 7–20. DOI: [10.1016/0304-3991\(93\)90018-S](https://doi.org/10.1016/0304-3991(93)90018-S).
- Jablonski, A. (1987). 'Effects of Auger Electron Elastic Scattering in Quantitative AES'. *Surface Science* 188:1–2, pp. 164–180.
- Jackson, J. E. (1991). *A User's Guide to Principal Components*. Vol. 410. Wiley Series in Probability and Statistics 1. John Wiley & Sons, Inc., Hoboken, pp. 135–44. DOI: [10.1002/0471725331](https://doi.org/10.1002/0471725331).
- Jinschek, J. R. et al. (2006). 'Local Indium Segregation and Bandgap variations in high efficiency green light emitting InGaN/GaN diodes'. *Sol. St. Communi.* 137:4, pp. 230–234. DOI: [10.1016/j.ssc.2005.10.030](https://doi.org/10.1016/j.ssc.2005.10.030).
- Johnson, D. W. and Spence, J. C.H. (1974). 'Determination of the Single Scattering Probability Distribution from Plural Scattering Data'. *J. Phys. D, Appl. Phys.* 7:6, pp. 771–780. DOI: [10.1088/0022-3727/7/6/304](https://doi.org/10.1088/0022-3727/7/6/304).
- Jolliffe, I. (2002). 'Principal Component Analysis and Factor Analysis'. *Principal Component Analysis*. Springer, New York. Chap. 7, pp. 150–166. DOI: [10.1007/0-387-22440-8_7](https://doi.org/10.1007/0-387-22440-8_7).
- Justusson, B. I. (1981). 'Median Filtering: Statistical Properties'. *Two-Dimensional Digital Signal Processing II*. Vol. 43. Springer, Berlin. Chap. 5, pp. 161–196. DOI: [10.1007/BFb0057597](https://doi.org/10.1007/BFb0057597).

- Keast, V. J. et al. (2001). 'Electronic Structure of GaN Studied with Electron Energy-loss Spectroscopy and Density Functional Theory'. *Inst. Phys. Conf. Ser.* 168, pp. 441–444.
- Keast, V. J. et al. (2002). 'Electronic Structure of GaN and $\text{In}_x\text{Ga}_{1-x}\text{N}$ Measured with Electron Energy-loss Spectroscopy'. *Phys. Rev. B* 66:12, pp. 1253191–1253197. DOI: [10.1103/PhysRevB.66.125319](https://doi.org/10.1103/PhysRevB.66.125319).
- Keenan, M. R. and Kotula, P. G. (2004). 'Accounting for Poisson Noise in the Multivariate Analysis of ToF-SIMS Spectrum Images'. *Surf. Interf. Anal.* 36:3, pp. 203–212. DOI: [10.1002/sia.1657](https://doi.org/10.1002/sia.1657).
- Keizer, J. G., McKibbin, S. R. and Simmons, M. Y. (2015). 'The Impact of Dopant Segregation on the Maximum Carrier Density in Si:P Multilayers'. *ACS nano* 9:7, pp. 7080–7084. DOI: [10.1021/acsnano.5b01638](https://doi.org/10.1021/acsnano.5b01638).
- Kenyon, A. J. (2002). 'Recent Developments in Rare-earth Doped Materials for Optoelectronics'. *Prog. Quantum Electron.* 26:4-5, pp. 225–284. DOI: [10.1016/S0079-6727\(02\)00014-9](https://doi.org/10.1016/S0079-6727(02)00014-9).
- (2003). 'Quantum Confinement in Rare-earth Doped Semiconductor Systems'. *Curr. Opin. Sol. St. Mater. Sci.* 7:2, pp. 143–149. DOI: [10.1016/S1359-0286\(03\)00043-3](https://doi.org/10.1016/S1359-0286(03)00043-3).
- Kimoto, K., Sekiguchi, T. and Aoyama, T. (1997). 'Chemical Shift Mapping of Si L and K Edges using Spatially Resolved EELS and Energy Filtering TEM'. *J. Electr. Microsc.* 46:5, pp. 369–374. DOI: [10.1093/oxfordjournals.jmicro.a023532](https://doi.org/10.1093/oxfordjournals.jmicro.a023532).
- Knuth, D. E. (1973). *The Art of Computer Programming. Vol.1, Fundamental Algorithms*. 2nd ed. Addison-Wesley, London.
- Kolhatkar, G. et al. (2014). 'Growth Optimization and Optical Properties of AlGaNaNs Alloys'. *J. Appl. Phys.* 115:16. DOI: [10.1063/1.4873169](https://doi.org/10.1063/1.4873169).
- Kong, X. et al. (2012). 'Plasmon Excitation in Electron Energy-loss Spectroscopy for Determination of Indium Concentration in (In, Ga)N/ GaN Nano-wires'. *Nanotechnology* 23:48, p. 485701. DOI: [10.1088/0957-4484/23/48/485701](https://doi.org/10.1088/0957-4484/23/48/485701).
- Krivanek, O. L. et al. (2009). 'High Energy Resolution Monochromator for Aberration Corrected Scanning Transmission Electron Microscopy/Electron Energy-loss Spectroscopy'. *Philos. Trans. Ser. A Math. Phys. Eng. Sci.* 367:1903, pp. 3683–97. DOI: [10.1098/rsta.2009.0087](https://doi.org/10.1098/rsta.2009.0087).
- Krivanek, O. L. et al. (2013). 'Monochromated STEM with a 30 meV Wide, Atom Sized Electron Probe'. *Microscopy* 62:1, pp. 3–21. DOI: [10.1093/jmicro/dfs089](https://doi.org/10.1093/jmicro/dfs089).
- Krivanek, O. L. et al. (2014). 'Towards Sub-10 meV Energy Resolution STEM-EELS'. *J. Phys. Conf. Ser.* 522:1. DOI: [10.1088/1742-6596/522/1/012023](https://doi.org/10.1088/1742-6596/522/1/012023).
- Krivanek, O. L., Lovejoy, T. C. and Dellby, N. (2015). 'Aberration Corrected STEM for Atomic Resolution Imaging and Analysis'. *J. Microsc.* 259:3, pp. 165–172. DOI: [10.1111/jmi.12254](https://doi.org/10.1111/jmi.12254).
- Krzanowski, W. (2000). *Multivariate Statistical Methods: A Primer*. 2nd ed. Oxford University Press, Oxford.

- Kundmann, M. K. and Krivanek, O. L. (1991). 'Automated Processing of Parallel Detection EELS Data'. *Microsc. Microanal. Microstr.* 2:2-3, pp. 245–256. DOI: [10.1051/mmm:0199100202-3024500](https://doi.org/10.1051/mmm:0199100202-3024500).
- Laasmaa, M., Vendelin, M. and Peterson, P. (2011). 'Application of Regularized Richardson-Lucy Algorithm for Deconvolution of Confocal Microscopy Images'. *J. Microsc.* 243:2, pp. 124–140. DOI: [10.1111/j.1365-2818.2011.03486.x](https://doi.org/10.1111/j.1365-2818.2011.03486.x).
- Lakner, H., Rafferty, B. and Brockt, G (1999). 'Electronic Structure Analysis of (In, Ga, Al) N Heterostructures on the Nanometre Scale using EELS'. *J. Microsc.* 194:1, pp. 79–83. DOI: [10.1046/j.1365-2818.1999.00453.x](https://doi.org/10.1046/j.1365-2818.1999.00453.x).
- Lazar, S. et al. (2003). 'Materials Science Applications of HREELS in Near Edge Structure Analysis and Low Energy-loss Spectroscopy'. *Ultramicroscopy* 96:3-4, pp. 535–546. DOI: [10.1016/S0304-3991\(03\)00114-1](https://doi.org/10.1016/S0304-3991(03)00114-1).
- Leapman, R. (2005). 'EELS Quantitative Analysis'. *Transmission Electron Energy-loss Spectrometry in Materials Science and The EELS Atlas*. 2nd ed. Vol. 161. Wiley, Weinham, pp. 49–96. DOI: [10.1002/3527605495.ch3](https://doi.org/10.1002/3527605495.ch3).
- Leapman, R. D. and Swyt, C. R. (1988). 'Separation of Overlapping Core Edges in Electron Energy-loss Spectra by Multiple Least Squares Fitting'. *Ultramicroscopy* 26:4, pp. 393–403. DOI: [10.1016/0304-3991\(88\)90239-2](https://doi.org/10.1016/0304-3991(88)90239-2).
- Lichtert, S. and Verbeeck, J. (2013). 'Statistical Consequences of Applying a PCA Noise Filter on EELS Spectrum Images'. *Ultramicroscopy* 125: pp. 35–42. DOI: [10.1016/j.ultramic.2012.10.001](https://doi.org/10.1016/j.ultramic.2012.10.001).
- Lim, J. S. (1990). 'Two-dimensional Signal and Image Processing'. *Prentice Hall, Englewood Cliffs, New Jersey* 1: p. 694.
- Lin, Y. et al. (2000). 'Dependence of Composition Fluctuation on Indium Content in InGaN/GaN Multiple Quantum Wells'. *Appl. Phys. Lett.* 77:19, pp. 2988–2990. DOI: [10.1063/1.1323542](https://doi.org/10.1063/1.1323542).
- Liu, H., Shah, S. and Jiang, W. (2004). 'On-line Outlier Detection and Data Cleaning'. *Comp. Chemi. Engi.* 28:9, pp. 1635–1647. DOI: [10.1016/j.compchemeng.2004.01.009](https://doi.org/10.1016/j.compchemeng.2004.01.009).
- Lucy, L. B. (1974). 'An Iterative Technique for the Rectification of Observed Distributions'. *Astronomical J.* 79: p. 745. DOI: [10.1086/111605](https://doi.org/10.1086/111605).
- Magnan, J., Weatherly, G. C. and Cheynet, M. C. (1999). 'The Nitriding Behavior of Ti-Al Alloys at 1000°'. *Metal. Mater. Trans. A* 30:1, pp. 19–29. DOI: [10.1007/s11661-999-0192-8](https://doi.org/10.1007/s11661-999-0192-8).
- Malis, T., Cheng, S. C. and Egerton, R. F. (1988). 'EELS Log-ratio Technique for Specimen Thickness Measurement in the TEM'. *J. Electron. Microsc. Tech.* 8:2, pp. 193–200. DOI: [10.1002/jemt.1060080206](https://doi.org/10.1002/jemt.1060080206).
- Manly, B. F. J. and Alberto, J. A. N. (2016). *Multivariate Statistical Methods: A Primer*. 4th ed. CRC Press, Florida.
- Mánuel, J. M. et al. (2016). 'Inline Electron Holography and VEELS for the Measurement of Strain in Ternary and Quaternary (In,Al,Ga)N Alloyed Thin Films and its Effect on Bandgap Energy'. *J. Microsc.* 261:1, pp. 27–35. DOI: [10.1111/jmi.12312](https://doi.org/10.1111/jmi.12312).

- Martin, J. (2016). *Visual Timing Report for Distributed Tasks*. URL: <https://uk.mathworks.com/matlabcentral/fileexchange/7751-visual-timing-report-for-distributed-tasks> (visited on 10/01/2018).
- MathWorks (2017). *MATLAB R2017b*. URL: https://uk.mathworks.com/products/new_products/latest_features.html?s_tid=hp_release_2017b (visited on 10/01/2018).
- Mayer, J. and Pitzko, J. M. (1996). 'Mapping of ELNES on a Nanometre Scale by Electron Spectroscopic Imaging'. *J. Microsc.* **183**:1, pp. 2–8. DOI: [10.1046/j.1365-2818.1996.07370.x](https://doi.org/10.1046/j.1365-2818.1996.07370.x).
- Michel, J. et al. (1991). 'Impurity Enhancement of the 1.54 μm Er^{3+} Luminescence in Silicon'. *J. Appl. Phys.* **70**:5, pp. 2672–2678. DOI: [10.1063/1.349382](https://doi.org/10.1063/1.349382).
- Mikoushkin, V. (2012). 'Nitridation of GaAs Surface by Low Energy Ion Implantation with In-Situ Control of Chemical Composition'. *Ion Implantation*. InTech, Rijeka. Chap. 9. DOI: [10.5772/34863](https://doi.org/10.5772/34863).
- Mkhoyan, K. A. et al. (2003). 'Measuring Electronic Structure of Wurtzite InN using Electron Energy-loss Spectroscopy'. *Appl. Phys. Lett.* **82**:9, pp. 1407–1409. DOI: [10.1063/1.1559660](https://doi.org/10.1063/1.1559660).
- Morales-Rodríguez, H. J. and Espinosa-Magaña, F. (2012). 'Experimental and Theoretical Determination of the Low-loss Electron Energy-loss Spectroscopy of Nanostructured ZnO'. *Micron* **43**:2-3, pp. 177–182. DOI: [10.1016/j.micron.2011.07.010](https://doi.org/10.1016/j.micron.2011.07.010).
- Morales-Cruz, D. et al. (2017). 'Bandgap Measurement of $\text{Bi}_2\text{Mo}_x\text{W}_{1-x}\text{O}_6$ by Low-loss Electron Energy-loss Spectroscopy'. **63**: pp. 184–189. DOI: [10.1016/j.mssp.2017.02.016](https://doi.org/10.1016/j.mssp.2017.02.016).
- Muller, D. A. et al. (2008). 'Atomic Scale Chemical Imaging of Composition and Bonding by Aberration Corrected Microscopy'. *Science* **319**:5866, pp. 1073–1076. DOI: [10.1126/science.1148820](https://doi.org/10.1126/science.1148820).
- Ngantcha, J P et al. (2005). 'Correlation between Micro-structure and Mechanical Spectroscopy of a Cu–Cu₂O alloy between 290 K and 873 K'. *Euro. Phys. J. Appl. Phys.* **29**:1, pp. 83–89. DOI: [10.1051/epjap:2004200](https://doi.org/10.1051/epjap:2004200).
- Oliveira, J. C. et al. (2004). 'The Influence of Erbium Doping of Al-N Sputtered Coatings on their Optical properties'. *Thin Solid Films* **446**:2, pp. 264–270. DOI: [10.1016/j.tsf.2003.09.055](https://doi.org/10.1016/j.tsf.2003.09.055).
- Otten, M. T. and Coene, W. M. J. (1993). 'High Resolution Imaging on a Field Emission TEM'. *Ultramicroscopy* **48**:1-2, pp. 77–91. DOI: [10.1016/0304-3991\(93\)90173-U](https://doi.org/10.1016/0304-3991(93)90173-U).
- Owolabi, T. O. et al. (2016). 'Computational Intelligence Method of Determining the Energy Bandgap of Doped ZnO Semiconductor'. *Mater. Design* **101**: pp. 277–284. DOI: [10.1016/j.matdes.2016.03.116](https://doi.org/10.1016/j.matdes.2016.03.116).
- Pal, M. et al. (2012). 'Effects of Crystallization and Dopant Concentration on the Emission Behavior of $\text{TiO}_2\text{:Eu}$ Nanophosphors'. *Nanosc. Res. Lett.* **7**:1, p. 1. DOI: [10.1186/1556-276X-7-1](https://doi.org/10.1186/1556-276X-7-1).
- Pantel, R., Cheynet, M. C. and Tichelaar, F. D. (2006). 'Comparison of Si and Ge Low-loss Spectra to Interpret the Ge Contrast in EFTEM Images of

- $\text{Si}_{1-x}\text{Ge}_x$ Nanostructures'. *Micron* 37:7, pp. 657–665. DOI: [10.1016/j.micron.2006.01.008](https://doi.org/10.1016/j.micron.2006.01.008).
- Park, I. K. et al. (2005). 'Enhancement of Phase Separation in the InGaN Layer for Self Assembled In Rich Quantum Dots'. *Appl. Phys. Lett.* 87:6. DOI: [10.1063/1.2008365](https://doi.org/10.1063/1.2008365).
- Park, J. et al. (2009). 'Bandgap Measurement of Thin Dielectric Films using Monochromated STEM-EELS'. *Ultramicroscopy* 109:9, pp. 1183–1188. DOI: [10.1016/j.ultramicro.2009.04.005](https://doi.org/10.1016/j.ultramicro.2009.04.005).
- Pearson, K. (1901). 'LIII. On Lines and Planes of Closest Fit to Systems of Points in Space'. *Philos. Mag. Series 6* 2:11, pp. 559–572. DOI: [10.1080/14786440109462720](https://doi.org/10.1080/14786440109462720).
- Penilla, E. H., Kodera, Y. and Garay, J. E. (2013). 'Blue Green Emission in Terbium Doped Alumina ($\text{Tb}:\text{Al}_2\text{O}_3$) Transparent Ceramics'. *Adv. Funct. Mater.* 23:48, pp. 6036–6043. DOI: [10.1002/adfm.201300906](https://doi.org/10.1002/adfm.201300906).
- Pennycook, T. J. et al. (2011). 'Seeing Oxygen Disorder in YSZ/ SrTiO_3 Colossal Ionic Conductor Heterostructures using EELS'. *Euro. Phys. J. Appl. Phys.* 54:3, p. 33507. DOI: [10.1051/epjap/20111100413](https://doi.org/10.1051/epjap/20111100413).
- Perreault, S. and Hebert, P. (2007). 'Median Filtering in Constant Time'. *IEEE Trans. Image Proces.* 16:9, pp. 2389–2394. DOI: [10.1109/TIP.2007.902329](https://doi.org/10.1109/TIP.2007.902329).
- Pokrant, S. et al. (2005). 'Chemical Analysis of Nanometric Dielectric Layers using Spatially Resolved VEELS'. *Ultramicroscopy* 104:3-4, pp. 233–243. DOI: [10.1016/j.ultramicro.2005.05.001](https://doi.org/10.1016/j.ultramicro.2005.05.001).
- Potapov, P. (2016). 'Why Principal Component Analysis of STEM Spectrum Images Results in Abstract, Uninterpretable Loadings?' *Ultramicroscopy* 160: pp. 197–212. DOI: [10.1016/j.ultramicro.2015.10.020](https://doi.org/10.1016/j.ultramicro.2015.10.020).
- Potapov, P. L. et al. (2009). 'Measuring the Dielectric Constant of Materials from Valence EELS'. *Micron* 40:2, pp. 262–268. DOI: [10.1016/j.micron.2008.07.006](https://doi.org/10.1016/j.micron.2008.07.006).
- Pratt, W. K. (2007). 'Geometrical Image Modification'. *Digital Image Processing*. 4th ed. Wiley, New Jersey, pp. 386–393.
- Raether, H. (1980). *Excitation of Plasmons and Interband Transitions by Electrons*. Vol. 88. Springer, Berlin.
- Rafferty, B. and Brown, L. M. (1998). 'Direct and Indirect Transitions in the Region of the Bandgap using Electron Energy-loss Spectroscopy'. *Phys. Rev. B* 58:16, pp. 10326–10337. DOI: [10.1103/PhysRevB.58.10326](https://doi.org/10.1103/PhysRevB.58.10326).
- Rafferty, B., Pennycook, S. J. and Brown, L. M. (2000). 'Zero-loss Peak Deconvolution for Bandgap EEL Spectra'. *J. electron microsc.* 49:4, pp. 517–524. DOI: [10.1093/oxfordjournals.jmicro.a023838](https://doi.org/10.1093/oxfordjournals.jmicro.a023838).
- Rastogi, C. K. et al. (2015). 'Kinetically Stabilized Aliovalent Europium-doped Magnesium Oxide as a UV Sensitized Phosphor'. *Phys. Chem. Chem. Phys.* 17:6, pp. 4600–4608. DOI: [10.1039/c4cp05205f](https://doi.org/10.1039/c4cp05205f).
- Reilman, R. F. and Manson, S. T. (1979). 'Photoabsorption Cross-sections for Positive Atomic Ions with Z Equal to or Less than 30'. *Astrophys. J. Suppl. Ser.* 40: p. 815. DOI: [10.1086/190605](https://doi.org/10.1086/190605).

- Reimer, L. (1995). *Energy-Filtering Transmission Electron Microscopy*. Vol. 71. Springer Series in Optical Sciences. Springer, Berlin. DOI: [10.1007/978-3-540-48995-5](https://doi.org/10.1007/978-3-540-48995-5).
- Rez, P. (1982). 'Cross-sections for energy loss spectrometry'. *Ultramicroscopy* 9:3, pp. 283–287. DOI: [10.1016/0304-3991\(82\)90213-3](https://doi.org/10.1016/0304-3991(82)90213-3).
- Richardson, W. H. (1972). 'Bayesian Based Iterative Method of Image Restoration'. *J. Opti. Soc. America* 62:1, p. 55. DOI: [10.1364/JOSA.62.000055](https://doi.org/10.1364/JOSA.62.000055).
- Saloman, E. B., Hubbell, J. H. and Scofield, J. H. (1988). 'X-ray Attenuation Cross-sections for Energies 100 eV to 100 keV and Elements $Z = 1$ to $Z = 92$ '. *Atomic Data and Nuclear Data Tables* 38:1, pp. 1–196. DOI: [10.1016/0092-640X\(88\)90044-7](https://doi.org/10.1016/0092-640X(88)90044-7).
- Schamm, S. and Zanchi, G. (2003). 'Study of the Dielectric Properties Near the Bandgap by VEELS: Gap Measurement in Bulk Materials'. *Ultramicroscopy* 96:3-4, pp. 559–564. DOI: [10.1016/S0304-3991\(03\)00116-5](https://doi.org/10.1016/S0304-3991(03)00116-5).
- Scheinfein, M. and Isaacson, M. (1984). 'Design and Performance of Second Order Corrected Spectrometers for Use With the Scanning Transmission Electron Microscope'. *Scan. Electron. Microsc.* 4, pp. 1681–1696.
- Schmidt, F., Hofer, F. and Krenn, J. R. (2017). 'Spectrum Image Analysis Tool – A Flexible MATLAB Solution to Analyze EEL and CL Spectrum Images'. *Micron* 93: pp. 43–51. DOI: [10.1016/j.micron.2016.11.004](https://doi.org/10.1016/j.micron.2016.11.004).
- Scholl, J. A., Koh, A. L. and Dionne, J. A. (2012). 'Quantum Plasmon Resonances of Individual Metallic Nanoparticles'. *Nature* 483:7390, pp. 421–427. DOI: [10.1038/nature10904](https://doi.org/10.1038/nature10904).
- Scott, J. et al. (2008). 'Near-simultaneous Dual Energy Range EELS Spectrum Imaging'. *Ultramicroscopy* 108:12, pp. 1586–1594. DOI: [10.1016/j.ultramicro.2008.05.006](https://doi.org/10.1016/j.ultramicro.2008.05.006).
- Serin, V. et al. (1998). 'EELS Investigation of the Electron Conduction Band States in Wurtzite AlN and Oxygen Doped AlN(O)'. *Phys. Rev. B* 58:8, pp. 5106–5115. DOI: [10.1103/PhysRevB.58.5106](https://doi.org/10.1103/PhysRevB.58.5106).
- Shan, W. et al. (1999). 'Reduction of Bandgap Energy in GaNAs and Al-GaNAs synthesized by N^+ implantation'. *Appl. Phys. Lett.* 75:10, pp. 1410–1412. DOI: [10.1063/1.124951](https://doi.org/10.1063/1.124951).
- Shepp, L. A. and Vardi, Y. (1982). 'Maximum Likelihood Reconstruction for Emission Tomography'. *IEEE Tran. Medical Imaging* 1:2, pp. 113–122. DOI: [10.1109/TMI.1982.4307558](https://doi.org/10.1109/TMI.1982.4307558).
- Shuman, H. and Somlyo, A. P. (1987). 'Electron Energy-loss Analysis of Near Trace Element Concentrations of Calcium'. *Ultramicroscopy* 21:1, pp. 23–32. DOI: [10.1016/0304-3991\(87\)90004-0](https://doi.org/10.1016/0304-3991(87)90004-0).
- Singh, R. et al. (1997). 'Phase Separation in InGaN Thick Films and Formation of InGaN/GaN Double Heterostructures in the Entire Alloy Composition'. *Appl. Phys. Lett.* 70:9, pp. 1089–1091. DOI: [10.1063/1.118493](https://doi.org/10.1063/1.118493).
- Specht, P. et al. (2006). 'Local Band and Defect Transitions in InGaN Observed by Valence Electron Energy-loss Spectroscopy'. *Phys. B Cond. Mat.* 376–377:1, pp. 552–555. DOI: [10.1016/j.physb.2005.12.139](https://doi.org/10.1016/j.physb.2005.12.139).
- Spiegelberg, J. and Rusz, J. (2017a). 'Can we use PCA to Detect Small Signals in Noisy Data?' *Ultramicroscopy* 172: pp. 40–46. DOI: [10.1016/j.ultramicro.2016.10.008](https://doi.org/10.1016/j.ultramicro.2016.10.008).

- Spiegelberg, J. et al. (2017b). 'The Usage of Data Compression for the Background Estimation of Electron Energy-loss Spectra'. *Ultramicroscopy* **181**: pp. 117–122. DOI: [10.1016/j.ultramicro.2017.05.017](https://doi.org/10.1016/j.ultramicro.2017.05.017).
- Steele, J. D. et al. (1985). 'A Single Stage Process for Quantifying Electron Energy-loss Spectra'. *Ultramicroscopy* **17**:3, pp. 273–276. DOI: [10.1016/0304-3991\(85\)90095-6](https://doi.org/10.1016/0304-3991(85)90095-6).
- Stenzel, O (2005). *The Physics of Thin Film Optical Spectra*. Vol. **44**. Springer Series in Surface Sciences 9. Springer, Berlin, pp. 1689–1699. DOI: [10.1007/3-540-27905-9](https://doi.org/10.1007/3-540-27905-9).
- Stöger-Pollach, M. (2008). 'Optical Properties and Bandgaps from Low loss EELS: Pitfalls and Solutions'. *Micron* **39**:8, pp. 1092–1110. DOI: [10.1016/j.micron.2008.01.023](https://doi.org/10.1016/j.micron.2008.01.023).
- Stöger-Pollach, M. et al. (2006). 'Čerenkov Losses: A Limit for Bandgap Determination and Kramers—Kronig Analysis'. *Micron* **37**:5, pp. 396–402. DOI: [10.1016/j.micron.2006.01.001](https://doi.org/10.1016/j.micron.2006.01.001).
- Stöger-Pollach, M. and Schattschneider, P. (2007). 'The Influence of Relativistic Energy-losses on Bandgap Determination using Valence EELS'. *Ultramicroscopy* **107**:12, pp. 1178–1185. DOI: [10.1016/j.ultramicro.2007.01.015](https://doi.org/10.1016/j.ultramicro.2007.01.015).
- Suomela, J. (2014). 'Median Filtering is Equivalent to Sorting'. arXiv: [1406.1717](https://arxiv.org/abs/1406.1717). URL: <http://arxiv.org/abs/1406.1717>.
- Takahei, K. et al. (1994). 'Atomic Configuration of the Er-O Luminescence Center in Er-doped GaAs with oxygen Codoping'. *J. Appl. Phys.* **76**:7, pp. 4332–4339. DOI: [10.1063/1.357319](https://doi.org/10.1063/1.357319).
- Tauc, J. (1968). 'Optical Properties and Electronic Structure of Amorphous Ge and Si'. *Mater. Res. Bull.* **3**:1, pp. 37–46. DOI: [10.1016/0025-5408\(68\)90023-8](https://doi.org/10.1016/0025-5408(68)90023-8).
- Tauc, J., Grigorovici, R. and Vancu, A. (1966). 'Optical Properties and Electronic Structure of Amorphous Germanium'. *Phys. St. Sol. (B)* **15**:2, pp. 627–637. DOI: [10.1002/pssb.19660150224](https://doi.org/10.1002/pssb.19660150224).
- Tenailleau, H. and Martin, J. M. (1992). 'A New Background Subtraction for Low Energy EELS Core Edges'. *J. Microsc.* **166**:3, pp. 297–306. DOI: [10.1111/j.1365-2818.1992.tb01529.x](https://doi.org/10.1111/j.1365-2818.1992.tb01529.x).
- Thomas, P. J. (2001). 'Data Reduction Methods in EELS and EFTEM Spectrum Image Analysis'. *Inst. Phys. Conf. Ser.* **168**, pp. 235–238.
- Thomas, P. J., Midgley, P. A. and Spellward, P. (1999a). 'Compositional Mapping in the EFTEM using Image Spectroscopy'. *Inst. Phys. Conf. Ser.* **161**, pp. 239–242.
- Thomas, P. J. and Midgley, P. A. (1999b). 'Fourier Deconvolution of Image Spectre: The Removal of Plural Scattering from Energy Filtered Series'. *Inst. Phys. Conf. Ser.* **161**, pp. 179–182.
- (2001a). 'Image Spectroscopy - I. The Advantages of Increased Spectral Information for Compositional EFTEM Analysis'. *Ultramicroscopy* **88**:3, pp. 179–186. DOI: [10.1016/S0304-3991\(01\)00077-8](https://doi.org/10.1016/S0304-3991(01)00077-8).
- (2001b). 'Image Spectroscopy - II. The Removal of Plural Scattering from Extended Energy Filtered Series by Fourier Deconvolution'. *Ultramicroscopy* **88**:3, pp. 187–194. DOI: [10.1016/S0304-3991\(01\)00078-X](https://doi.org/10.1016/S0304-3991(01)00078-X).

- Thomas, P. J. and Midgley, P. A. (2002). 'An Introduction to Energy Filtered Transmission Electron Microscopy'. *Topics in Catalysis* 21:4, pp. 109–138. DOI: [10.1023/A:1021377125838](https://doi.org/10.1023/A:1021377125838).
- Thomas, P.J. and Twesten, R.D. (2012). 'A Simple, Model Based Approach for Robust Quantification of EELS Spectra and Spectrum Images'. *Microsc. Microanal.* 18:S2, pp. 968–969. DOI: [10.1017/S1431927612006691](https://doi.org/10.1017/S1431927612006691).
- Trampert, A. et al. (2014). *Microstructure of Group III-N Nanowires*. John Wiley & Sons, Inc., pp. 125–156. DOI: [10.1002/9781118984321.ch6](https://doi.org/10.1002/9781118984321.ch6).
- Trebbia, P. and Walther, T. (1996). 'Maxwell's Demon and Data Analysis [and Discussion]'. *Philos. Trans. R. Soc. Lond. A.* 354:1719, pp. 2697–2711. DOI: [10.1098/rsta.1996.0124](https://doi.org/10.1098/rsta.1996.0124).
- van Benthem, K., Elsässer, C. and French, R. H. (2001). 'Bulk Electronic Structure of SrTiO₃: Experiment and Theory'. *J. Appl. Phys.* 90:12, pp. 6156–6164. DOI: [10.1063/1.1415766](https://doi.org/10.1063/1.1415766).
- Vatanparast, M. et al. (2017). 'Bandgap Measurement of High Refractive Index Materials by Off Axis EELS'. *Ultramicroscopy* 182: pp. 92–98. DOI: [10.1016/j.ultramic.2017.06.019](https://doi.org/10.1016/j.ultramic.2017.06.019).
- Verbeeck, J. (2015). *EELSModel*. URL: <http://www.eelsmodel.ua.ac.be/documentation#tutorials> (visited on 10/01/2018).
- Verbeeck, J. and Van Aert, S. (2004). 'Model Based Quantification of EELS Spectra'. *Ultramicroscopy* 101:2-4, pp. 207–224. DOI: [10.1016/j.ultramic.2004.06.004](https://doi.org/10.1016/j.ultramic.2004.06.004).
- Verbeeck, J., Van Aert, S. and Bertoni, G. (2006). 'Model Based Quantification of EELS Spectra: Including the Fine Structure'. *Ultramicroscopy* 106:11, pp. 976–980. DOI: <https://doi.org/10.1016/j.ultramic.2006.05.006>.
- Verbeeck, J. and Bertoni, G. (2008a). 'Model-based Quantification of EELS: Is Standardless Quantification Possible?' *Microchimica Acta* 161:3-4, pp. 439–443. DOI: [10.1007/s00604-008-0948-7](https://doi.org/10.1007/s00604-008-0948-7).
- (2008b). 'Model-based Quantification of EELS Spectra: Treating the Effect of Correlated Noise'. *Ultramicroscopy* 108:2, pp. 74–83. DOI: [10.1016/j.ultramic.2007.03.004](https://doi.org/10.1016/j.ultramic.2007.03.004).
- (2009). 'Deconvolution of Core Electron Energy-loss Spectra'. *Ultramicroscopy* 109:11, pp. 1343–1352. DOI: [10.1016/j.ultramic.2009.06.010](https://doi.org/10.1016/j.ultramic.2009.06.010).
- Walther, T. (2003). 'Electron Energy-loss Spectroscopic Profiling of Thin Film Structures: 0.39 nm Line Resolution and 0.04 eV Precision Measurement of Near-edge Structure Shifts at Interfaces'. *Ultramicroscopy* 96:3-4, pp. 401–411. DOI: [10.1016/S0304-3991\(03\)00104-9](https://doi.org/10.1016/S0304-3991(03)00104-9).
- Walther, T. et al. (1995). 'A Correlation between Compositional Fluctuations and Surface Undulations in Strained Layer Epitaxy'. *Mater. Sci. Forum* 196-201: pp. 505–510. DOI: [10.4028/www.scientific.net/MSF.196-201.505](https://doi.org/10.4028/www.scientific.net/MSF.196-201.505).
- Walther, T. and Mader, W. (1999). 'Application of Spatially Resolved Electron Energy-loss Spectroscopy to the Quantitative Analysis of Semiconducting Layer Structures'. *Inst. Phys. Conf. Ser.* 164, pp. 22–25.

- Walther, T. et al. (2017). 'Study of Phase Separation in an InGaN Alloy by Electron Energy-loss Spectroscopy in an Aberration Corrected Monochromated Scanning Transmission Electron Microscope'. *J. Mater. Res.* **32**:05, pp. 983–995. DOI: [10.1557/jmr.2016.447](https://doi.org/10.1557/jmr.2016.447).
- Wang, X. et al. (2015). 'Combination of Electron Energy-loss Spectroscopy and Energy Dispersive X-ray Spectroscopy to Determine Indium Concentration in InGaN Thin Film Structures'. *Semicond. Sci. Tech.* **30**:11, p. 114011. DOI: [10.1088/0268-1242/30/11/114011](https://doi.org/10.1088/0268-1242/30/11/114011).
- (2016). 'Investigation of Phase Separation in InGaN Alloys by Plasmon-loss Spectroscopy in a TEM'. *MRS Advances* **1**:40, pp. 2749–2756. DOI: [10.1557/adv.2016.542](https://doi.org/10.1557/adv.2016.542).
- Wang, Y. et al. (1992). 'Optimization of Quantitative Electron Energy-loss Spectroscopy in the Low-loss Region: Phosphorus L Edge'. *Ultramicroscopy* **41**:1-3, pp. 11–31. DOI: [10.1016/0304-3991\(92\)90091-w](https://doi.org/10.1016/0304-3991(92)90091-w).
- Wang, Y. et al. (2018). 'Towards Atomically Resolved EELS Elemental and Fine Structure Mapping via Multi-frame and Energy Offset Correction Spectroscopy'. *Ultramicroscopy* **184**: pp. 98–105. DOI: [10.1016/j.ultramicro.2017.10.014](https://doi.org/10.1016/j.ultramicro.2017.10.014).
- Wieg, A. T. et al. (2012). 'Visible Photoluminescence in Polycrystalline Terbium Doped Aluminum Nitride (Tb:AlN) Ceramics with High Thermal Conductivity'. *Appl. Phys. Lett.* **101**:11, p. 111903. DOI: [10.1063/1.4751856](https://doi.org/10.1063/1.4751856).
- Wieg, A. T. et al. (2015). 'Thermomechanical properties of rare-earth-doped AlN for laser gain media: The role of grain boundaries and grain size'. *Acta Materialia* **86**: pp. 148–156. DOI: [10.1016/j.actamat.2014.11.045](https://doi.org/10.1016/j.actamat.2014.11.045).
- Williams, D. B. and Carter, C. B. (1996). *The Transmission Electron Microscope*. 1st ed. Springer, New York.
- Xiang, J. et al. (2017). 'Hot Electron Intraband Luminescence from GaAs Nanospheres Mediated by Magnetic Dipole Resonances'. *Nano Letters* **17**:8, pp. 4853–4859. DOI: [10.1021/acs.nanolett.7b01724](https://doi.org/10.1021/acs.nanolett.7b01724).
- Xie, E. Y. et al. (2012). 'Strain Relaxation in InGaN/GaN Micro-pillars Evidenced by High Resolution Cathodoluminescence Hyperspectral Imaging'. *J. Appl. Phys.* **112**:1. DOI: [10.1063/1.4733335](https://doi.org/10.1063/1.4733335).
- Yedra, L. et al. (2014). 'Oxide Wizard: An EELS Application to Characterize the White Lines of Transition Metal Edges'. *Microsc. Microanal.* **20**:3, pp. 698–705. DOI: [10.1017/S1431927614000440](https://doi.org/10.1017/S1431927614000440).
- Zavada, J. M. and Zhang, D. (1995). 'Luminescence Properties of Erbium in III-V Compound Semiconductors'. *Sol. St. Electron.* **38**:7, pp. 1285–1293. DOI: [10.1016/0038-1101\(94\)00286-0](https://doi.org/10.1016/0038-1101(94)00286-0).